

Simulation Studies on Polymer Gel-Polymer Solution Interfaces and Molecular Motor-Polymer Conjugates



JOHANNES GUTENBERG
UNIVERSITÄT MAINZ

Dissertation submitted for the award of the title
Doctor of Natural Sciences
to the Faculty of Physics, Mathematics and Computer Science
of Johannes Gutenberg University of Mainz

by

Jude Ann Vishnu

Born in : Ernakulam, Kerala, India
Date of Birth : 08 July 1997

Jude Ann Vishnu

Simulation Studies on Polymer Gel-Polymer Solution Interfaces and Molecular Motor-Polymer Conjugates

Oral Examination : 4th December 2024

Supervisors : Prof. Dr. Friederike Schmid [REDACTED]

Address: KOMET 1, INSTITUTE OF PHYSICS, JOHANNES GUTENBERG UNIVERSITY,
MAINZ

Abstract

This dissertation discusses two major projects, focusing on the computational modeling of core-shell microgels and molecular motor gels. The first project involves investigating the interface of core-shell microgels formed through micro-fluidic experiments. A deeper understanding of the processes at the boundaries of these two phase can be developed by using molecular dynamic simulations, which could help in optimizing the strategy for synthesizing core-shell particles. Here in our study, we use a simple and idealized model for a gel which has the topology of a diamond lattice, with the free polymer and strand length chosen to be equal, and to consist of the same type of monomers. In the simulations, the concentration of the polymer phase is varied to study the interpenetration of the gel and the polymer solution phases. The density profiles reveals that there are two time regimes, an initial compression of the gel followed by swelling of the gel. An analysis on the interpenetrating chains at the interface, given by "degree of interfacial integration", reveals that the interface locally equilibrates after around 100 chain relaxation times. At times greater than the local equilibration time for the interface, the free polymer chain configuration within the gel region reveals emerging percolating clusters, only if the chain concentration exceeds a certain threshold. This threshold concentration was found to be of the same order of magnitude as the overlap concentration of the chains. Finally, we studied the structures formed at the interface by applying the capillary wave theory on the locally equilibrated interfaces, which revealed a positive correlation between interfacial width and interfacial tension.

The second topic focused on the molecular machines, created by incorporating uni-directionally rotating light responsive rotors as cross-linkers in a polymer matrix. The winding of the chains, due to motor rotation leads to contraction of these gels. Because of this property, they are expected to be used as artificial muscles. Here in this study, we present the first coarse-grained molecular dynamics simulation of such gels, assuming a model motor that does not unwind even under large loads. We focus on simulating the limiting behaviour of these gels as observed in the contraction experiments, conducted by X.Yao et al. [326]. A regular diamond network with the model rotors as cross-linkers was chosen to represent the quasi-ideal network studied in the experiments. We demonstrate the success of our model, by qualitatively replicating the limiting behaviour observed in the experiments,

using a free regular gel and a periodically cross-linked regular gel under different loads. The simulation, in agreement with the experiments confirmed that the contraction ratios are independent of the strand-length and is limited mainly by the winding of the chain pairs attached to the motor. We examined the torque needed by these motors to sustain the contracted state and concluded that it is independent of the loads in the Hookean regime. However, the average torque for loads in the same regime shows a slight dependence on strand length. Further, the Gaussian linking number was used to analyze the local winding of the chain pairs that are connected to the same motors, revealing the regions of different linking. Finally, we studied the size ratio of "stiff gels", which showed a non-monotonic behaviour as we varied the stiffness.

Zusammenfassung

Diese Dissertation befasst sich mit zwei großen Projekten, die sich auf die rechnerische Modellierung von Kern-Schale-Mikrogelen und molekularen Motorgelen konzentrieren. Das erste Projekt befasst sich mit der Untersuchung der Grenzfläche von Kern-Schale-Mikrogelen, die durch mikrofluidische Experimente gebildet werden. Mit Hilfe von molekulardynamischen Simulationen kann ein tieferes Verständnis der Prozesse an den Grenzen dieser beiden Phasen entwickelt werden, was bei der Optimierung der Strategie für die Synthese von Kern-Schale-Partikeln helfen könnte. In unserer Studie verwenden wir ein einfaches und idealisiertes Modell für ein Gel, das die Topologie eines Diamantgitters aufweist, wobei die freie Polymer- und Stranglänge als gleich gewählt wurde und aus der gleichen Art von Monomeren besteht. In den Simulationen wird die Konzentration der Polymerphase variiert, um die gegenseitige Durchdringung der Gel- und der Polymerlösungsphase zu untersuchen. Die Dichteprofile zeigen, dass es zwei Zeitregime gibt, eine anfängliche Kompression des Gels gefolgt von einer Quellung des Gels. Eine Analyse der interpenetrierenden Ketten an der Grenzfläche, angegeben durch den "Grad der Grenzflächenintegration", zeigt, dass sich die Grenzfläche nach etwa 100 Kettenrelaxationszeiten lokal ausgleicht. Bei Zeiten, die größer sind als die lokale Gleichgewichtszeit für die Grenzfläche, zeigt die Konfiguration der freien Polymerketten innerhalb der Gelregion nur dann die Entstehung von Perkulationsclustern, wenn die Kettenkonzentration einen bestimmten Schwellenwert überschreitet. Diese Schwellenkonzentration liegt in der gleichen Größenordnung wie die Überlappungskonzentration der Ketten. Schließlich untersuchten wir die Strukturen, die sich an der Grenzfläche bilden, indem wir die Kapillarwellentheorie auf die lokal gleichgewichtigen Grenzflächen anwandten, was eine positive Korrelation zwischen Grenzflächenbreite und Grenzflächenspannung ergab.

Das zweite Thema konzentrierte sich auf die molekularen Maschinen, die durch den Einbau von unidirektional rotierenden, lichtempfindlichen Rotoren als Vernetzer in einer Polymermatrix entstehen. Das Aufwickeln der Ketten aufgrund der Motorrotation führt zu einer Kontraktion dieser Gele. Aufgrund dieser Eigenschaft wird erwartet, dass sie als künstliche Muskeln eingesetzt werden können. In dieser Studie stellen wir die erste

grobkörnige Molekulardynamiksimulation solcher Gele vor, wobei wir von einem Modellmotor ausgehen, der sich selbst unter großen Belastungen nicht abwickelt. Wir konzentrieren uns auf die Simulation des Grenzverhaltens dieser Gele, wie es in den von X.Yao et al. [326] durchgeführten Kontraktionsexperimenten beobachtet wurde. Ein regelmäßiges Diamantnetzwerk mit den Modellrotoren als Vernetzer wurde gewählt, um das in den Experimenten untersuchte quasi-ideale Netzwerk darzustellen. Wir demonstrieren den Erfolg unseres Modells, indem wir das in den Experimenten beobachtete begrenzende Verhalten qualitativ nachbilden, indem wir ein freies reguläres Gel und ein periodisch vernetztes reguläres Gel unter verschiedenen Belastungen verwenden. Die Simulation bestätigt in Übereinstimmung mit den Experimenten, dass die Kontraktionsverhältnisse unabhängig von der Stranglänge sind und hauptsächlich durch die Wicklung der am Motor befestigten Kettenpaare begrenzt sind. Wir haben das Drehmoment untersucht, das diese Motoren benötigen, um den kontrahierten Zustand aufrechtzuerhalten, und sind zu dem Schluss gekommen, dass es unabhängig von den Lasten im Hooke'schen Regime ist. Allerdings zeigt das durchschnittliche Drehmoment für Lasten im gleichen Regime eine leichte Abhängigkeit von der Stranglänge. Des Weiteren wurde die Gaußsche Verknüpfungszahl zur Analyse der lokalen Wicklung der Kettenpaare verwendet, die mit denselben Motoren verbunden sind, und dabei die Bereiche mit unterschiedlicher Verknüpfung aufgedeckt. Schließlich untersuchten wir das Größenverhältnis der "steifen Gele", das bei Variation der Steifigkeit ein nicht monotonen Verhalten zeigte.

Contents

Acknowledgements

Abstract

Zusammenfassung

Contents

List of Figures

List of Tables

1	Introduction	1
1.1	A short review on Gels	1
1.1.1	Hydrogels	2
1.1.1.1	Thermo-responsive hydrogels	2
1.1.1.2	Photo-responsive gels	3
1.1.2	Synthetic molecular machines	4
1.1.2.1	Molecular rotary motors	4
1.1.2.2	Polymeric gels as molecular machines	5
1.2	Aim	5
1.2.1	Core-shell microgels	6
1.2.1.1	Photo-Responsive Molecular-motor gels	7
1.3	Thesis Structure	7
2	Theory	9
2.1	Polymer Science	9
2.1.1	Summary of Ideal chains	10
2.1.2	Summary of Real Chains	12
2.2	Polymer Mixtures and Solutions	14
2.2.1	Flory-Huggins theory of mixing	14
2.2.2	Criterion for mixing and Phase separation	16
2.2.3	Phase diagram - polymer blend	18

2.2.3.1	Upper and Lower critical solution temperature	20
2.2.4	Summary of polymer solutions	23
2.3	Polymer Gels	26
2.3.1	Elasticity	27
2.3.1.1	Affine Network Model	27
2.3.1.2	Phantom network model	29
2.3.2	Summary of swelling of polymer gels	29
2.4	Capillary Wave theory	31
2.5	Summary	33
3	Computer simulations	35
3.1	Introduction	35
3.2	HOOMD Blue package	35
3.3	Molecular Dynamic Simulations	36
3.3.1	Walls	37
3.3.2	Boundary Conditions	38
3.3.2.1	Periodic Boundary conditions	38
3.3.2.2	Non-periodic boundary conditions	39
3.3.3	Force Calculation in MD	40
3.3.3.1	Verlet and Cell lists	40
3.3.3.2	Bounding Volume Hierarchies (LBVH)	41
3.3.3.3	Coarse grained potentials	42
3.3.4	Rigid Molecules	44
3.3.4.1	Euler Angles and Quaternions	45
3.3.4.2	Equation of motion of rigid bodies - quaternion representation	47
3.3.5	Integrating the equations of motion	48
3.3.5.1	Velocity Verlet and Leap-frog Integration Scheme	49
3.3.6	Brownian Dynamics	51
3.3.6.1	The Langevin Equations	51
3.3.6.2	Discretized Langevin equation	52
3.4	Summary	53
4	Structure and Dynamic Evolution of Interfaces between Polymer Solutions and Gels and Polymer Interdiffusion: A Molecular Dynamics Study	55
4.1	Introduction	56
4.2	Model and Simulation Details	57
4.3	Results	60
4.3.1	Dynamic Evolution of Gel-Solution Interfaces	61
4.3.1.1	Monomer Density Profiles	61
4.3.1.2	Connection between gel and solution	64

4.3.1.3	Percolation of free chains inside the gel	67
4.3.2	Structure of equilibrated interfaces	69
4.3.2.1	Local monomer motion and chain conformations	70
4.3.2.2	Interfacial width and interfacial tension	72
4.4	Conclusions and outlook	76
4.5	Appendix	77
4.5.1	Determination of interfacial width	77
4.5.2	Theoretical expression for capillary wave broadening	79
5	Molecular Motor gels	81
5.1	Introduction	81
5.1.1	Modeling and simulation details	83
5.1.1.1	The six bead rigid body motor model	83
5.1.1.2	Modeling uni-directional rotation	85
5.1.1.3	Current model for rotation	87
5.1.1.4	Gel model	88
5.1.1.5	Simulation Details	90
5.2	Results	91
5.2.1	Contraction of free motor gel	91
5.2.1.1	Angle distribution and Size ratio	92
5.2.2	Contraction of motor-gel attached to loads	96
5.2.3	Initializing the gel with load	96
5.2.3.1	Properties of passive gel	97
5.2.3.2	Load Test	98
5.2.3.3	Work and Torque	100
5.2.3.4	Measure of linking	103
5.2.4	Effect of stiffness on a free motor-gel	108
5.2.4.1	Size ratio	108
5.3	Conclusion and outlook	112
6	Tandem project - lab Work	115
6.1	Introduction	115
6.2	Brief explanation of Microfluidics	115
6.3	Aim	116
6.4	Methods	116
6.4.1	Shell-polymer synthesis	116
6.4.2	Fabrication of glass micro-fluidic device for core-gel preparation	117
6.4.3	Microfluidic Fabrication of Core gel particles	118
6.4.4	Microfluidic fabrication of core-shell particles	118
6.5	Result	119
6.6	Summary	120

7 Summary	121
A Appendix A : Supporting information for Chapter 4	125
A.1 Properties of free polymer solutions	125
A.1.1 Gyration radius of free chains in solution	125
A.1.2 Equation of state of free solution	125
A.1.3 Bulk modulus of bare swollen gel	126
A.2 Additional data for isotropic gels	127
A.2.1 Monomer density profiles	127
A.2.2 Percolation	128
A.2.3 Monomer motion profiles	128
A.2.4 Chain conformation profiles	129
A.3 Solution of diffusion equation for free polymers diffusing into a gel slab . .	131
Bibliography	133
List of Publications and Conferences	165

List of Figures

2.1	Bond vector representation of a coarse-grained polymer, with the end-to-end vector \vec{R}	10
2.2	Mixing two species A (magenta) and B (dark blue) with no volume change.	14
2.3	The free energy of a homogeneous solution is plotted as a function of solute concentration. Two scenarios are considered: (blue) the solute and solvent can mix at any composition, and (red) phase separation occurs. The magenta line indicates the line connecting the free energy at concentrations ϕ_1 and ϕ_2 . The free energy decreases after mixing for the first scenario, indicated by downward arrows from the magenta line. In the second scenario, the free energy increases indicated by the upward arrow from magenta line. The black line indicates the common tangent drawn between concentrations ϕ_a and ϕ_b which corresponds to minimas of free energy in red.	17
2.4	The free energy of mixing (in blue) and the binodal curve in $N\chi$ - ϕ plane (in solid red lines) is shown for a symmetric polymer blend. The left y axis (in red color) indicates the $N\chi$ values and the right y axis in blue color indicates scaled free-energy of mixing. The upper and bottom axis both indicates volume-fraction ϕ . The free-energy of mixing was drawn by choosing $N\chi = 2.7$. The pink/magenta colored vertical lines indicates the concentrations where $\partial^2 F/\partial\phi^2 = 0$, giving the spinodal volume fraction for the given free-energy curve. The green vertical lines are the volume fraction where the free energy has minimas, i.e., phase separated concentrations. The red dashed curve indicates spinodal for a symmetric mixture. Critical volume fraction ϕ_c and the scaled critical interaction parameter $N\chi_c$ is also shown here in black dashed lines.	20
2.5	Binodal diagrams for (a) LCST polymers, (b) UCST polymers depending on polymer fraction ϕ	21
2.6	Schematics of coil to globule transition in (a) LCST polymer PNIPAM and (b) UCST polymer PNAGA.	21
2.7	The phase diagram illustrates a polymer solution featuring an upper critical solution temperature. The solid red line depicts the binodal curve, indicating the threshold for phase separation. Meanwhile, the dashed blue line signifies the lower temperature limit of the semi-dilute good solvent region [252, 73].	23

2.8	Conformation of a dilute globule in a poor solvent, depicted as a random walk of thermal blobs up to the size of the globule.	24
2.9	(a -left) Schematic of a chain in a semi-dilute good solvent. The red colored circles mark the thermal blobs and the green colored circles represent the correlation blobs. The chain of interest is colored orange and the surrounding chains are blue in color. The black colored circles shows the correlation blobs from the near-by chains. (a-right) The plot shows the variation of end-to-end distance with the size of a chain subsection in a good solvent in logscale. (b) Log-scale plot of the concentration dependence of coil-size (solid red lines) and correlation length (dashed red lines) for a chain in intermediate good solvent. The figures (a)-(b) are plotted with the scaling exponent $\nu = 3/5$	26
4.1	Example of a regular bulk diamond network structure, constructed as described in the main text and not yet relaxed by a NPT simulation. The red beads indicate the cross-linking units, regular beads are gray. The network shown here is crosslinked across periodic boundary conditions in all directions and is smaller than that used in our simulation.	58
4.2	Setup of diffusive interpenetration study: A gel slab (gray) is sandwiched by free polymer chains (green) on either sides of it. The free chains permeate into the slab over time. The above snapshot is taken at 800τ at $\rho_{sol_f} = 0.168\sigma^{-3}$. The gel is anisotropic.	60
4.3	(a) Monomer density in the solution phase versus rescaled time t/τ_d for different final concentrations ρ_{sol_f} (in units of σ^{-3}) as indicated. (b,c): Monomer density profiles across the slab for free polymers (dashed orange), gel strands (solid green), and total (solid black) at different times as indicated for $\rho_{sol_f} = 0.168\sigma^{-3}$ (b) and $\rho_{sol_f} = 0.078\sigma^{-3}$ (c). Profiles corresponding to subsequent times are shifted upwards by $0.3\sigma^{-3}$ in (b) and $0.15\sigma^{-3}$ in (c). Thin dashed lines show corresponding baselines ($\rho = 0$). The gel is anisotropic. See Figure A.4 in the Appendix A for corresponding results for the isotropic gel.	61
4.4	Maximum gradient of the rescaled monomer density difference profiles $\psi(x)$ at the interface (see Equation (4.3)) vs. rescaled time t/τ_d (orange lines in Fig. 4.3) for solutions with different concentrations ρ_{sol_f} as indicated. The gel is anisotropic.	62
4.5	Monomer densities at the center of the gel slab versus rescaled time t/τ_d for (a) monomers belonging to free polymers, (b) gel monomers, and (c) all monomers, for different final concentrations in the outer solution ρ_{sol_f} (in units of σ^{-3}) as indicated. Inset in (a) shows equilibrium density of monomers belonging to free polymers inside the slab vs. ρ_{sol_f} , as extracted from a fit of the data in (a) to Eq. (4.4). The gel is anisotropic.	63

4.6	(a) DII vs scaled time t/τ_d for various concentrations ρ_{sol_f} . (b) Scaled areal density Σ of free chain monomers with connection to the interface vs scaled time t/τ_d . Dashed line indicates time after which Σ saturates. The gel is anisotropic.	65
4.7	Same as Figure (4.6) for the isotropic gel.	66
4.8	(a-c) Cluster formation of free chains within the gel region as viewed from top of the box (along z-axis) at different final polymer densities (ρ_{sol_f}) as indicated. Different clusters are colored differently in order to be distinguishable. The light gray color indicates solution region. (d-e) Characteristics of cluster distributions vs. (ρ_{sol_f}) at different times as indicated: (d) Average number of clusters; (e) Average cluster size (mean squared radius of gyration) of finite clusters; (f) Percolation strength (see text); (g) Fraction of free polymers inside gel that are part of the spanning cluster. The gel is anisotropic.	67
4.9	Profiles of monomer motion $\mathcal{M}_\alpha(x)$ in $\alpha = x$ (a), $\alpha = y$ (b) and $\alpha = z$ (c) direction vs. x -coordinate of monomers. The red symbols \oplus indicate the approximate position of interface, the red shading the gel regions. The gel is anisotropic.	70
4.10	Profiles of chain conformation parameters $\Delta^2 R_{g_\alpha}$ (see text) across the gel slab for different concentrations ρ_{sol_f} as indicated. The x coordinate refers to the center of mass of chains. Black dashed line indicates the position of the interface, shaded bands represents the error. The gel is anisotropic . . .	71
4.11	(a) Apparent squared interfacial width w^2 as a function of block size b (see text for explanation). The dashed lines represent the fit to Equation (4.20), see text for details. (b) Fitted value of interfacial tension γ vs polymer concentration ρ_{sol_f} . The dashed line shows a linear fit to the data. The gel is anisotropic.	74
4.12	Same as Figure 4.11 for the isotropic gel.	75
4.13	Schematics of the method use for extracting the total interfacial width from the gel monomer density profiles (a) and from the monomer density profiles for free polymers (b). After extracting δx_1 and δx_2 , we average over them to get w	78
5.1	Coarse grained representation of molecular motor. A-B-A' and D-C-D' represents the two rigid bodies which forms the molecular motor. The axis A-B-A' and D-C-D' rotates along B-C opposite to each other, such that relative cumulative angle between them in each half cycle is 180°	83
5.2	Two state switching potential as given by equation (5.5). State 1 corresponds to $n = -1$ and state 2 corresponds to $n = 1$	87
5.3	(a) Total dihedral potential energy in the relaxation step with $\phi_{ref} = 0$. (b) Total dihedral potential energy for rotation steps with $\phi_{ref} = 0$, for initially parallel subunits $n = 1$ (orange, solid) and anti-parallel sub-units $n = -1$ (orange, dot-dashed).	88

5.4	The four stages in the rotation cycle of a rotor molecule. The molecule rotates by switching the form of dihedral potential eq. (5.7), followed by thermal relaxation, then another potential switch and again a thermal relaxation. The bottom axis $D - C - D'$ is shown to be fixed in space, to facilitate the visualization of 180° rotation.	89
5.5	Initial structure of a small diamond network with 8 motors as crosslinkers .	90
5.6	(a)-(d) Autocorrelation function for the radius of gyration of the strands (Rg_s), measured at different relaxation steps, for the various strand lengths used in our simulations.	92
5.7	The swollen state of the gel on the left undergoes contraction as the molecules undergoes several rotation cycles to reach the contracted state on the right.	93
5.8	(a)-(d) Probability distribution of angle turned by the motors at the end of different rotation steps, for strand-length $N_s = 21 - 84$	94
5.9	(a) Fraction of motors rotating by 180° and (b) radius of gyration ratio of the gel, both as a function of rotation cycle (top x-axis) and simulation time (bottom x-axis), for gels with different strand-lengths.	95
5.10	The same as Figure 5.9 (a) rescaled in time, with logscale representation of the x axis. The inset shows the zoomed in portion of the plot where data for the strands do not collapse onto a single master curve.	95
5.11	Represents the gel attached to yellow rigid structures made of harmonically bonded WCA beads. These rigid structures acts like loads, similar to the 1D contraction experiments.	96
5.12	The relative extension $\langle \Delta L / \rangle \langle L_0 \rangle$ of the gel is plotted as a function of the applied load in the configuration illustrated in Figure 5.12 (a), where $\langle L_0 \rangle$ represents the initial extension of the gel. In panel (b), the density of gels under compression is shown as a function of compressive pressure. The dashed horizontal line represents the final density obtained in the one-dimensional contraction simulations after the molecular rotations were applied. In both panels (a) and (b), the simulations were conducted with molecular rotations turned off, while varying the strand lengths (N_s) as indicated.	98
5.13	(a) Simulation snapshot showing the initial equilibrium extended state under load and contracted state after motor rotations. (b) Graphs illustrating one-dimensional contraction (as percentage) and (c) density in the contracted state, both plotted against applied loads. The simulation data are presented in units of $k_B T$ and bead size σ	100
5.14	(a) The work done by the motors in pulling the load as a function of strand-length N_s , for different applied loads in Hookean regime. (b) The average torque applied by the motors in sustaining the contracted state as a function of N_s for different loads in Hookean regime. (c)-(f) shows the distribution of torques by the motor to sustain the system in the contracted state, for forces in the Hookean regime. The black dashed lines in (c)-(f) indicates the torque distribution at zero load.	101

5.15	(a) Mean torque for the non-Hookean forces as a function of strand-length N_s . (b)-(e) The distribution of torques by the motor to sustain the system in the contracted state for the two forces in the non-Hookean regime.	102
5.16	Calculation of the solid angle Ω_{IJ} between segments I and J , bounded by $I, I + 1$ and $J, J + 1$, respectively, involves the vectors $\mathbf{k}, \mathbf{m}, \mathbf{n}$, and \mathbf{l} shown in (a). The solid angle Ω_{IJ} formed at B in (b) is calculated using $\Omega(\mathbf{k}, \mathbf{l}, \mathbf{m})$ and $\Omega(\mathbf{k}, \mathbf{m}, \mathbf{n})$ as in Equation (5.14). "Reprinted figure with permission from Rasool Ahmad, Saptarshi Paul, and Sumit Basu, Phys. Rev. E, 101 , 022503(2020). Copyright (2020) by the American Physical Society." https://doi.org/10.1103/PhysRevE.101.022503	105
5.17	Definition of quantities involved in calculating Lk_G between segments of two chains I and J . "Reprinted figure with permission from Rasool Ahmad, Saptarshi Paul, and Sumit Basu, Phys. Rev. E, 101 , 022503(2020). Copyright (2020) by the American Physical Society." https://doi.org/10.1103/PhysRevE.101.022503	106
5.18	$\langle L_{K_G} \rangle$ in the contracted state for different applied loads for gels with $N_s = 21$ (top) and $N_s = 84$ (bottom). Loads $f = 87.48, 349.92k_B T \sigma^{-1}$ in (a)-(b) are in the Hookean regime, whereas loads $f = 2624.4, 4374k_B T \sigma^{-1}$ in (d)-(c) are in the non-Hookean regime.	107
5.19	(a)-(d) Time evolution of the size ratio of free motor-gels with different stiffness parameter k_{stiff} for $N_s = 21, 40, 62, 84$ respectively.	109
5.20	(a)-(d) shows the non-monotonic change of the final size ratio as a function k_{stiff} , for systems with different strand-length N_s . The x axis is in logscale. The black dashed lines represents the size ratio at $k_{\text{stiff}} = 0$ for a given N_s	110
5.21	(a)-(d) Distribution of normalized radius of gyration of polymer strands of the gel before it starts contracting and (e)-(h) distribution of normalized radius of gyration of polymer strands of the gel before after the gel contraction, for different k_{stiff} for systems with different strand length N_s	111
6.1	The in-house glass microfluidic device made for the core fabrication procedure.	117
6.2	(a)-(b) Different sample cores of size approximately $700\mu m$ produced during the micro-fluidic experiments.	119
A.1	Radius of gyration R_g of free polymers in solution vs. monomer density. Dashed lines indicates the expected power law scaling in the dilute regime ($R_g \propto \rho^0$) and in the semidilute regime ($R_g \propto \rho^{-1/8}$).	126
A.2	Pressure of the free polymer II solution vs. the solution density ρ . The dashed black lines shows a fit to the de Gennes scaling theory of polymers in a good solvent.	126
A.3	Bulk-modulus as a function of applied pressure.	127

A.4	(a) Time evolution of monomer density in the solution phase for different final concentrations ρ_{sol_f} (in units of σ^{-3}) as indicated. (b, c): Monomer density profiles across the slab for free polymers (dashed orange), gel strands (solid green), and total (solid black) at different times as indicated for different ρ_{sol_f} . For better readability, profiles corresponding to subsequent times are shifted upwards by $0.3\sigma^{-3}$ in (b) and $0.15\sigma^{-3}$ in (c). Thin dashed lines show corresponding baselines ($\rho = 0$). Data correspond to isotropic gels.	128
A.5	Monomer densities at the center of the gel slab versus rescaled time t/τ_d for (a) monomers belonging to free polymers, (b) gel monomers, (c) all monomers, for different final concentrations in the outer solution ρ_{sol_f} (in units of σ^{-3}) as indicated. The gel is isotropic.	128
A.6	(a-c) Snapshots showing cluster formation of free chains within the gel region as viewed from top of the box (along z-axis) at different final polymer densities (ρ_{sol_f}) as indicated. Different clusters are colored differently in order to be distinguishable. The light gray color marks the solution region. The gel is isotropic.	129
A.7	Characteristics of cluster distributions vs. (ρ_{sol_f}) at different times as indicated: (a) Average number of clusters; (b) Average cluster size (mean squared radius of gyration) of finite clusters; (c) Percolation strength (see text); (d) Fraction of free polymers inside gel that are part of the spanning cluster. The gel is isotropic.	130
A.8	Profiles of monomer motion $\mathcal{M}_\alpha(x)$ in $\alpha = x$ (a), $\alpha = y$ (b) and $\alpha = z$ (c) direction vs. x -coordinate of monomers. The red symbols \oplus indicate the approximate position of interface, the red shading the gel regions. The gel is isotropic.	130
A.9	Profiles of chain conformation parameters $\Delta^2 R_{g_\alpha}$ (see text) across the gel slab for different concentrations ρ_{sol_f} as indicated. The x coordinate refers to the center of mass of chains. Black dashed line indicates the position of the interface, shaded bands the error. The gel is isotropic.	131
A.10	Comparison of equation (A.4), describing the density of diffusing monomers at the center of the slab as a function of time (solid line), with the approximate expression Equation (A.5) (dashed line).	132

List of Tables

5.1	The table listing all the parameters used in our simulation	91
-----	---	----

Chapter 1

Introduction

1.1 A short review on Gels

A gel is a soft, squishy material that holds a lot of solvent. It resembles jellies found in desserts or the gels found in hair products, that stays in shape but are soft and flexible. Although gels are composed almost entirely of liquid by weight, their three-dimensional cross-linked structure imparts a solid-like behavior [333]. These cross-linking that forms in the liquid gives structure and tackiness (stickiness) to a gel [254, 211]. The term gel was introduced by a 19th-century Scottish chemist Thomas Graham [181] and is derived from the word "gelatin". Gelation is the mechanism by which a gel forms. Gelation is a broad category of processes where the molecules or particles interact with one another and the solvent and thus becomes spatially trapped, leading to the development of macroscopic rigidity. This solidification/ reinforcement could take place either by thermodynamic equilibrium transitions or dynamic non-equilibrium changes, and it can be thermally reversible or irreversible. Chemical cross-links are frequently encountered in several types of gels (e.g., rubbery materials), but cross-links can also arise from dynamic associations or topological interactions between extended anisotropic molecules and particles [254, 212, 129, 118]. Polymeric gels are formed when polymers connect to each other through cross-links in a solution. They are widely used in manufacturing. These cross-linked gels are generally resilient and are able to withstand large deformations. They are also able to absorb a large amount of solvent if the polymers and solvent are highly compatible. The nature of a cross-linked gel can be tailored by altering the chemical composition of the polymers and the conditions during their formation. The mechanical

strength of these gels are often increased by adding filler particles and other additives, which can form their own network within the polymer gel matrix.

1.1.1 Hydrogels

A subset of gels are the hydrogels known for their water absorbing capacity while retaining a solid structure. They are typically made of hydrophilic polymer chains that makes up a 3D framework which interacts favourably with surrounding aqueous solution, thus producing the effect of high water retaining capacity. Cross-linking points that connects the polymer strands in such networks, can be formed either covalently via chemical bonds [220, 277], or non-covalently through weaker interactions like ionic interactions, hydrogen bonds or van der Waals forces. A hydrogel's porous infrastructure can withstand a large amount of swelling without dissolution, due to the integrity of their structure established by their cross-linking pattern. Swelling of hydrogels depends on many attributes – cross-linking density, constituent polymers, environmental pH and ionic concentration, and sometimes any external triggers that alter its configuration. Such reactivity to changing surroundings, renders hydrogels "smart" platforms, whose properties can be tuned purposefully under certain conditions like temperature shifts, pH fluctuations or the local presence of ions and molecules. An attractive feature of hydrogels are their bio-compatibility because of their high water content, making them suitable for various biomedical uses [81, 321]. Similarly their degradability achieved through controlled polymer breakdown or enzymatic action can be manipulated to be used in applications like drug delivery or tissue regeneration.

The two types of the responsive gels which are important to understand this thesis are described below:

1.1.1.1 Thermo-responsive hydrogels

They are made of biological and engineered polymers whose properties can dynamically change based on temperature fluctuations. They respond to environmental cues and could potentially be used for targeted drug-delivery and tissue engineering. Thermo-responsive gels are known for their ability to undergo reversible phase transition owing to the critical solution temperatures of the constituent polymers. The lower critical solution temperature (LCST) represents the point above which the polymer becomes insoluble, inducing phase segregation. A typical example of polymers with LCST is poly(N-isopropylacrylamide)

(PNIPAm) that exhibits an LCST behaviour close to human body temperature, making it suitable for bio-medical uses [208, 226]. Another critical solution temperature which is also common for polymer solutions are the upper critical solution temperature (UCST), i.e., the temperature below which phase separation occurs. Gelatin is a very common example of material showing UCST, that has long been used in a variety of pharmaceutical products. For example, they are used as simple suppository which is required to liquefy at body temperature [31, 273]. They are also used as components in dermal creams, ointments, which could solidify after it has been applied on the body [209, 170]. Even though these gels have a wide range of applications, they face many obstacles due to their bio-incompatibility in some cases and the need for high concentration in some applications. Development of synthesis techniques like **reversible addition-fragmentation chain transfer (RAFT)** and **atomic transfer radical polymerization (ATRP)**, are broadening the range and sturdiness of these materials [293]. In addition to this, new polymeric material with both UCST and LCST behaviors are being discovered, unlocking new possibilities for a wider range of applications.

1.1.1.2 Photo-responsive gels

Photo-responsive polymer gels are fascinating materials that dynamically alter their form when exposed to light. These gels are comprised of polymer chains that are capable of undergoing reversible or irreversible physical or chemical transformations depending on the wavelengths of light [69, 94]. A major benefit of using light-sensitive polymers is the precise manipulation, afforded by the photonic trigger [94]. Their reactivity normally stems from a variety of degradation and bonding reactions, controlled by the equation connecting energy and frequency which was given by Planck [62, 158] and proven by Einstein [171]:

$$E = h\nu = \frac{hc}{\lambda} \quad (1.1)$$

where the E is the energy of light, h the Planck's constant, c the speed of light, λ the wavelength of light. The rates of photo-dependent reactions have shown strong correlations with the energy and irradiance of the light [74]. This, along with the precise control of light exposure, makes photo-catalyzed reactions an effective method for manipulating gels. However, using UV rays has its own disadvantages especially in in-vivo applications. This restricts the use of these materials to ex-vivo or skin level treatments. However with the recent advent of infrared sensitive materials, possibility of deeper tissue application have also emerged.

1.1.2 Synthetic molecular machines

Researchers have been able to create artificial/ synthetic molecular machines through the intricate arrangement of molecules or its components. The relative movements of these components are activated by external stimuli. The capability to execute precise mechanical motions by harnessing external energy provides these microscopic machines with vast potential applications, including complex actuators, manipulation of individual atoms and molecules, targeted drug delivery systems, and molecular electronic devices of the future. Many such prototypical machines are easily synthesized in laboratory, however they are regarded as simple switches rather than true machines because they are unable to produce useful work within a cycle, i.e., to say that they may produce only back and forth motion and not a uni-directional motion. Hence more research is still needed to reliably harness and amplify the minuscule nanoscale mechanical motions of synthetic molecular machines for practical applications. Recent advancements have allowed for the creation of machines which are part gel. The following sub-section will introduce the concept of molecular rotors and such polymeric gels, since we will be studying such soft-materials using coarse-grained simulations in this thesis.

1.1.2.1 Molecular rotary motors

The molecular rotors produce continuous uni-directional motion as a result of photo-induced and thermal reactions. Having uni-directional motion at the molecular scale is challenging due to a variety of reasons starting from thermal fluctuations, energy barriers and sometimes even friction. The creation of the very first artificial molecular rotor relied on light-induced isomerization of a chiral overcrowded alkenes [166]. As mentioned before these motors, function via sequence of photoinitiated and thermally driven steps. For example, in an overcrowded alkene motor, illumination can drive reversible E-Z isomerization while helical inversion proceeds irreversibly, leading to unidirectional rotation. So if we are able to continuously irradiate such molecules, they can produce autonomous continuous rotation at high frequencies even at room temperatures. Due to their robust nature, these motors are integrated into various materials and surfaces, making them suited for diverse technological applications. Other than the overcrowded alkenes, several other molecular designs using imines [177], indigos [122], and catenanes [63, 183], have also been explored for light-driven rotary motors.

1.1.2.2 Polymeric gels as molecular machines

Advancements in the field of molecular machines, has led to the development of responsive gels, where the molecular motors are incorporated into the gels. When Giuseppone and colleagues integrated Feringa's molecular motors into a polymeric gel, it exhibited macroscopic contraction under UV light [179]. This is achieved by linking alkyne-terminated ethylene glycol oligomeric legs and azide-ended PEG arms to the motor components, forming a polymer-motor conjugate that contracts irreversibly upon UV irradiation as the polymer chains wind up due to motor rotation.

To achieve reversible contraction, the group developed a motor-modulated-polymer conjugate gel by incorporating a photochromic dithienylethene modulator [103]. When UV light was used the modulator closed, activating the motor and thus creating contraction of the gel. However when white light was used, the modulator allowed for the reversal of the direction of rotation of the motor. This in turn expanded the gel back to its original size. In another study conducted by Harada [148], mechanically interlocked [c2] daisy chains were incorporated into a polymer gel, allowing it to exhibit reversible shrinking and expanding motions when exposed to alternating UV and visible light. They discovered that the dehydrated xerogels which were derived from the above mentioned [c2] daisy chain gels, responded even more rapidly to stimulations. The flexible material bent towards ultraviolet radiation, demonstrating its potential for applications like gripping objects.

These advancements illustrate the diverse capabilities of molecular machines in polymeric networks, paving the way for innovative applications in responsive and adaptive materials.

1.2 Aim

As we have already established the fundamental definitions and concepts regarding responsive gels, it is now appropriate to introduce the specific systems of our interest. As previously mentioned, we aim to study two primary gel systems: "core-shell micro-gels" and "photo-responsive molecular-motor gels" using coarse-grained molecular dynamics simulations.

1.2.1 Core-shell microgels

The research group under Sebastian Seiffert of Mainz University produced core-shell microgels, the structure of which corresponds to its name. These gels are unique because we can control how they behave mechanically and chemically. This is usually achieved by utilizing two different types of polymers for the core and the shell. With a double layered structure, the microgels can be tuned to respond dynamically to changes in temperature, pH and light.

We specifically address systems based on poly(N-isopropylacrylamide) (PNIPAM) [60, 324, 151]. These are polymers popular for their ability to respond to change in temperature. The gels made of these polymers are used as the core in the core-shell particle. The shell can be made from polyacrylamides which generally do not show any lower or upper critical solution temperature under typical conditions. Although, they may display such temperature-dependent behavior in the presence of specific co-solvents or under certain environmental conditions [25, 231, 58]. Other polymers like polyacrylates or polymethacrylates could also be used as shells since they are mechanically robust, chemically stable, and do not show thermoresponsive behavior in typical aqueous environments [67].

Prof. Seiffert's team has focused on the synthesis and characterization of these responsive core-shell microgels for a range of applications. In drug delivery systems, the core may encapsulate therapeutic agents while a diffusion barrier of shell material maintains or slows down the release of these therapeutic agents. Such control over drug release enables us to not only improve efficacy but also reduce side effects, thus making these microgels ideal for targeted therapies [176]. Besides the drug delivery, these responsive microgels are also being studied for smart materials and biomedical applications. Such as their use in the field of tissue engineering for applications such as; scaffolds (which respond to local environment, encouraging formations of cell adhesion and differentiation) [23]. Their ability to undergo reversible volume changes in response to environmental cues also makes them suitable for actuators [246] and sensors in soft robotics [314].

While core-shell particles hold promising applications, it remains unclear how core-shell connectivity shapes, product outcomes. This work deployed coarse-grained molecular dynamics simulations to explore the interfacial behavior between shell polymers and defect-free core gels. Specifically, we examined the interfacial dynamics between regular gel strands and a polymer solution where the chain length and the excluded volume interactions of the free chains and the strands are chosen to match with each other. This

work was published in ACS Macromolecules [303]. A reproduction of this publication can be found in the thesis in Chapter 4.

1.2.1.1 Photo-Responsive Molecular-motor gels

Incorporation of light-driven molecular motors into polymer networks represents a promising approach for developing dynamic and responsive materials. Through the development of molecular motor-polymer conjugates, Giuseppone and co-workers have made great strides in this area [109]. Building on this foundational work, Dr. Xuyang Yao working as a post-doc in the Walther group at Mainz, explored scalable and functional uses of these responsive gels [326]. In this way, he was able to control the molecular structure and block copolymer configuration in a highly non-intuitive manner, thus facilitating the design of new materials that could have applications in soft robotics or as artificial muscles.

Dr Yao's gels were able to undergo contraction due to braiding of the chains as the motors rotated. The free gel exhibited contraction ratios independent of the degree of polymerization. Even during the application of loads on such gels, they produced contraction independent of strand-length of the gels. We used molecular dynamics (MD) simulations of ideal networks with model motors as the cross-linking units to gain deeper insight into this contraction behavior. The purpose of these simulations were to reproduce the experimental results thereby increasing our ability to understand the system dynamics. Some core results from simulation were also published along with the experiments in reference [326]. In Chapter 5 of this thesis we will discuss on the simulation model and the results in more detail. Additional results on stiffer polymer gels will also be presented.

1.3 Thesis Structure

This thesis is structured as follows. In Chapter 2, I describe the theoretical aspects of polymers, polymer solutions and gels. Later in Chapter 3, I go back to the basics of computer simulation in soft-matter, focusing on molecular dynamics simulations. This is followed by two Chapters based on the two publications. Since the 1st paper [303] is purely theoretical, I have reproduced the entire paper as it is in Chapter 4. **Wherever new sentences/ paragraphs are added or when they are modified I mark them by purple color. If sentences or paragraphs are removed from the paper I**

mark it with [...]. The supporting information to this paper/ chapter can be found in Appendix [A](#). In Chapter [5](#), I discuss the simulation part of the paper [\[326\]](#) in detail and also add additional results in this chapter which were not published. In chapter [6](#), I discuss the micro-fluidic experiments done together with T.Linder, for my tandem project within the GRK 2516. The thesis ends with chapter [7](#), which summarises the main topics of my thesis.

Chapter 2

Theory

2.1 Polymer Science

For centuries, humans have been using naturally occurring polymers, without realizing they are dealing with macromolecules [252]. Prime examples of these include **starch**, derived from sources like corn, wheat and potatoes, that has been used for its thickening and binding properties in cooking and food preparation for centuries, **gelatin**, derived from animal collagen used to make food products like jelly and as a binding agent in traditional paints and glues. Other example include **natural rubber**, that comes from *Hevea brasiliensis*, the rubber-tree plant [127, 252].

In the year 1920 Staudinger proposed the **macromolecular hypothesis** [286, 228, 203] stating that polymers are molecules made of covalently bonded units, called monomers. Although initially met with suspicion, the gradual acceptance of this hypothesis in the following years, enabled significant progress in the field of polymers. In the 30 years that followed, main concepts in polymer-physics and chemistry were established. It also saw the development of synthesis tools and polymer refinement techniques [78, 252].

Although polymers can be made from a variety of molecules having different chemical properties, there are some universal behaviours associated with polymers which are independent of the chemistry of the monomers. These include, the scaling of the size of the polymers with degree of polymerization in dilute solutions, entropic elasticity of polymer materials [78, 155, 127]. Another example of such a generic property is the fact that two molecules cannot cross one another; this leads to the effect of entanglements, which produces dramatic visco-elastic effects in polymer melts and solutions. Polymer physics

thus explores the physical principles underlying the structure, dynamics, and mechanical properties of polymers, shedding light on their diverse applications across industries and scientific fields [78].

2.1.1 Summary of Ideal chains

The study of polymers involves a deep understanding of their structural and thermodynamic properties. One fascinating aspect is the concept of ideal chains, referring to polymers where monomers along the chain do not interact with each other. Since mea-

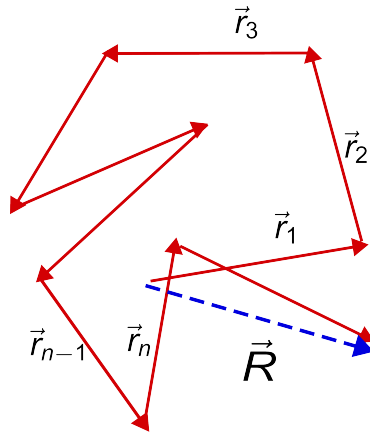


FIGURE 2.1: Bond vector representation of a coarse-grained polymer, with the end-to-end vector \vec{R}

suring the size of a polymer is needed and is useful in both experiments and theory, a quantity called the end-to-end vector (\vec{R}) has been used. The average end-to-end vector of a chain is defined as $\langle \vec{R} \rangle = \langle \sum_{i=1}^n \vec{r}_i \rangle$. Here, $\langle \dots \rangle$ denotes an average over all possible states of the system. In this case, the ensemble average corresponds to averaging over chains with n bonds in all possible orientations. With no preferred direction in this ensemble, the average end-to-end vector is zero [252, 191]. Therefore, a non-zero measure, the mean squared end-to-end distance ($\langle R^2 \rangle$), characterizes the chain dimensions. For an ideal chain with n main chain bonds of length l , the mean squared end-to-end distance is given by:

$$\langle R^2 \rangle = \langle \vec{R} \cdot \vec{R} \rangle = l^2 \sum_{i=1}^n \sum_{j=1}^n \langle \cos \theta_{ij} \rangle \quad (2.1)$$

Here θ_{ij} is the angle between bond vectors \vec{r}_i and \vec{r}_j . For polymer models like the "freely jointed chain", where the bond length is assumed to be constant ($|\vec{r}_i| = l$), with bond

vectors having no correlations with one another ($\langle \cos \theta_{ij} \rangle = 0$ for $i \neq j$), the mean squared end to end distance goes like:

$$\langle R^2 \rangle = nl^2 \quad (2.2)$$

It is to be noted that, typically in a polymer chain, the correlation between the bond vectors are not zero [252]. However for an ideal chain there is no interaction between monomers separated by a large distance along the chain contour, implying that there are no correlation between distant bond vectors. Hence $\langle \cos \theta_{ij} \rangle$ is zero in the limit of $|i - j| \rightarrow \infty$. Thus the sum over j for fixed i in equation (2.1) can be written as

$$C'_i = \sum_{j=1}^n \langle \cos \theta_{ij} \rangle, \quad (2.3)$$

which can be show to converge to a finite value C'_i , and thus the equation (2.1) reduces to [252]:

$$\langle R^2 \rangle = l^2 \sum_{i=1}^n C'_i = C_n nl^2, \quad (2.4)$$

where $C_n = \frac{1}{n} \sum_{i=1}^n C'_i$ is the Flory's characteristic ratio. For long chains, the characteristic ratio converges to C_∞ , simplifying the expression for the mean square end-to-end distance [73, 252, 149]:

$$\langle R^2 \rangle \cong C_\infty nl^2 \quad (2.5)$$

As mentioned in the introduction to this chapter, the flexible chains have many properties that are independent of the local chemical structures and hence a simple unified description of all ideal chains are provided by a "equivalent freely jointed chain". This equivalent chain has N Kuhn monomers of length b such that it's mean square end-to-end distance equals that of an ideal linear chain:

$$\langle R^2 \rangle = C_\infty nl^2 = Nb^2 \quad (2.6)$$

Note: Throughout this chapter we will use the "equivalent freely jointed chain" to describe all flexible polymers and will call N as either the degree of polymerization or number of monomers (instead of Kuhn monomers). Equivalently b will be referred to as monomer length instead of Kuhn monomer length.

Another critical quantity is the mean-square radius of gyration ($\langle R_g^2 \rangle$), representing the average squared distance of all monomers from the polymer's center of mass. For an ideal linear polymer, the mean-square radius of gyration is one-sixth of its mean-square end-to-end distance:

$$\langle R_g^2 \rangle = \frac{Nb^2}{6} \quad (2.7)$$

The distribution of size of ideal chains, $P(N, \vec{R})$ follows a Gaussian function:

$$P(N, \vec{R}) = \left(\frac{3}{2\pi Nb^2} \right)^{3/2} \exp \left(- \frac{3\vec{R}^2}{2Nb^2} \right) \quad \text{for } |\vec{R}| \ll Nb \quad (2.8)$$

The energy of an ideal chain $U(N, \vec{R})$ does not depend on the end-to-end vector \vec{R} because the monomers in an ideal chain do not interact. The free energy, accounting for entropic contributions, is expressed as:

$$F(N, \vec{R}) = \frac{3k_B T \vec{R}^2}{2Nb^2} \quad \text{for } |\vec{R}| \ll Nb \quad (2.9)$$

This equation shows that the entropic elasticity of an ideal chain obeys Hooke's law. Therefore, maintaining the chain at a fixed end-to-end distance requires equal and opposite forces proportional to \vec{R} acting on the chain ends [252, 149, 191]:

$$\vec{f} = \frac{3k_B T \vec{R}}{Nb^2} \quad \text{for } |\vec{R}| \ll Nb \quad (2.10)$$

2.1.2 Summary of Real Chains

In a real polymer chain, two monomers cannot occupy the same space as another. This volume which is unavailable to other molecules due to the presence of the first molecule is known as **excluded volume**. A polymer chain with excluded volume can also be modeled as self-avoiding walks (SAW) on a lattice. Unlike random walkers where the same sites could be visited multiple times, here the walker is not allowed to visit the sites which it has already visited.

Mathematically, the excluded volume (\mathbf{v}) is defined through the interaction potential $U(r)$ as follows [252]:

$$\mathbf{v} = - \int f(r) d^3r = \int (1 - \exp[-U(r)/k_B T]) d^3r \quad (2.11)$$

where f is the Mayer function. The excluded volume, $\mathbf{v} = 0$ when the monomer's attraction balances the hard-core repulsion effect, leading to the chains assuming nearly ideal conformations with $R_0 = bN^{1/2}$. Such a scenario with zero net excluded volume is called the θ -condition, and this corresponds to a specific temperature known as the θ -temperature for a given solvent.[73, 252].

At high temperatures, the Mayer f -function is influenced exclusively by hard-core repulsion. As a result, the excluded volume \mathbf{v} is approximately equal to b^3 and remains unaffected by temperature. Under these conditions, the polymer chain exhibits characteristics of a self-avoiding walk of monomers [260, 73, 252]. Hence:

$$R \approx bM^\nu \approx bN^{0.588} \quad \text{for athermal solvent} \quad (2.12)$$

When the attraction between monomers are weaker than the hard-core repulsion, it leads to the excluded volume being positive and the chain swells. This corresponds to a good solvent at a temperature above θ - temperature, and leads to a larger coil size than the ideal chain size. The size of such a chain is given by [73, 252]:

$$R_F \approx b \left(\frac{\mathbf{v}}{b^3} \right)^{2\nu-1} N^\nu \approx b \left(\frac{\mathbf{v}}{b^3} \right)^{0.18} N^{0.588} \quad \text{for good solvent} \quad (2.13)$$

The net excluded volume interaction becomes negative ($-b^3 < \mathbf{v} < 0$) for the cases where attraction between monomers is stronger than repulsion. This leads to the chain collapse. The temperature range for this to happen is below the θ - temperature, and corresponds to a poor solvent. In such a solvent, at length scales less than the thermal blob size ξ_T , the excluded volume attraction is larger than thermal energy kT . This results in the cohesive aggregation of thermal blobs, culminating in the formation of a compact and tightly knit globule. Assuming dense packing of such thermal blobs, we can calculate the size of the globule, which gives [252, 288]:

$$R_{gl} \approx |\mathbf{v}|^{-1/3} b^2 N^{1/3} \quad \text{for poor solvent} \quad (2.14)$$

We see here that the size of a globule is smaller than the ideal chain size.

2.2 Polymer Mixtures and Solutions

In this section we will look at the mean field ideas developed by Flory in-order to understand mixing and de-mixing in a polymer solutions [100, 145]. Furthermore, having the knowledge of phase-behaviour of polymer mixtures is essential in understanding the physics of volume phase transition (VPT) associated with thermo-responsive gels. We will also look at some terms and concepts for investigating polymer solutions, for example the overlap concentration which basically defines the border between dilute and semi-dilute solutions:

$$\phi^* \approx \frac{Nb^3}{R^3} \approx \left(\frac{b^3}{v}\right)^{6\nu-3} N^{1-3\nu} \quad (2.15)$$

where N , R and b are the degree of polymerisation, end to end distance and monomer diameter respectively. Chains begin to overlap when their volume fraction ϕ exceeds the volume fraction of monomers inside each isolated coil, called the overlap concentration ϕ^* . From Eq. (2.15) we can see that ϕ^* decreases rapidly with chain length ($\phi^* \approx N^{-0.76}$), compared to that in θ - solvent ($\phi_\theta^* \approx \frac{1}{\sqrt{N}}$) [252, 73]. A summary of all this will be discussed in the coming subsections.

2.2.1 Flory-Huggins theory of mixing

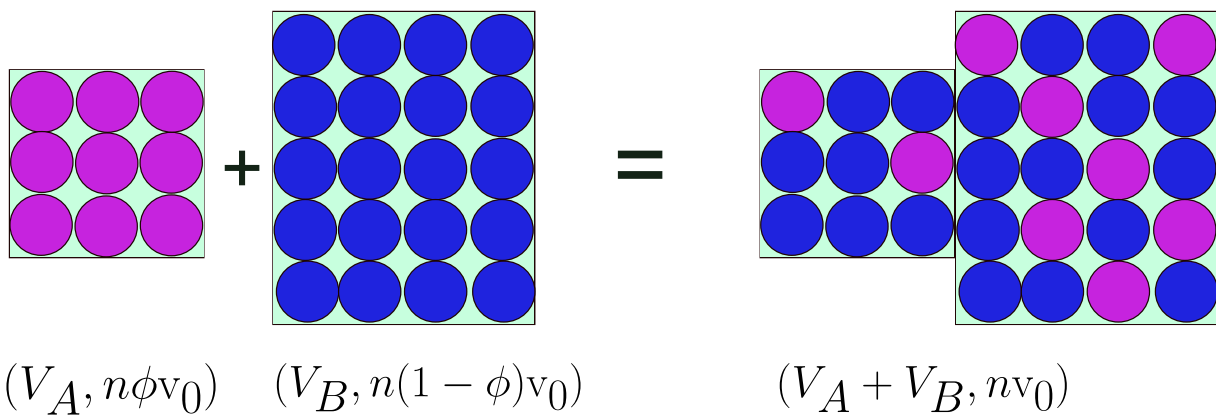


FIGURE 2.2: Mixing two species A (magenta) and B (dark blue) with no volume change.

The Flory-Huggins theory of mixing discusses the thermodynamics of binary mixtures in the framework of a lattice model. For simplicity we assume that [73, 252]:

1. The mixing of different components do no induce any change in the total volume.

2. Monomers of each species occupy the same volume v_0 .

Flory considered a binary mixture with total number n of monomers (sites) and a total volume $v_0 n$, where v_0 is the volume of a lattice site. The volume fraction of the two components in the binary mixture are ϕ_A and ϕ_B :

$$\phi_A = \frac{V_A}{V_A + V_B} = \phi \quad \text{and} \quad \phi_B = \frac{V_B}{V_A + V_B} = 1 - \phi \quad (2.16)$$

The number of translational states of a molecule in a mixture is the number of sites n :

$$\Omega_{AB} = \frac{V_A + V_B}{v_0} = n \quad (2.17)$$

The number of states of molecule A in a pure A phase is given by:

$$\Omega_A = \frac{V_A}{v_0} = n\phi \quad (2.18)$$

Now the Entropy change upon mixing of a molecule A is given by:

$$\Delta S_A = k_B \ln \Omega_{AB} - k_B \ln \Omega_A = -k_B \ln \phi \quad (2.19)$$

Similarly we can find the entropy of mixing of a B molecule. To calculate the total entropy of mixing we sum the contribution from each molecules:

$$\Delta S_{\text{mix}} = n_A \Delta S_A + n_B \Delta S_B = -k_B (n_A \ln \phi + n_B \ln (1 - \phi)) \quad (2.20)$$

Here n_A and n_B are the number of molecules of species A and B . Equation (2.20) can be rewritten as entropy per lattice site $\Delta \bar{S}_{\text{mix}} = \Delta S_{\text{mix}}/n$ through the relation $n_A = n\phi/N_A$ and $n_B = n(1 - \phi)/N_B$. The variables N_A and N_B , represent the number of lattice sites occupied by each molecule, respectively. So

$$\Delta \bar{S}_{\text{mix}} = -k_B \left(\frac{\phi}{N_A} \ln \phi + \frac{1 - \phi}{N_B} \ln (1 - \phi) \right) \quad (2.21)$$

We can also calculate the enthalpic contribution to the free-energy of mixing by mean-field approach. The energy per mixing of site is thus given by the difference between enthalpic contributions after (u_f) and before (u_i) mixing: $\Delta \bar{U}_{\text{mix}} = u_f - u_i$

$$\Delta \bar{U}_{\text{mix}} = \phi(1 - \phi)z \left[u_{AB} - \frac{u_{AA} + u_{BB}}{2} \right] = \phi(1 - \phi)k_B T \chi, \quad (2.22)$$

where $\chi = \frac{z}{k_B T} \left[u_{AB} - \frac{u_{AA} + u_{BB}}{2} \right]$. Here z is the coordination number of the regular lattice and u_{ij} , where $ij \in \{AA, BB, AB\}$ are the pair-wise interaction between molecules in adjacent lattice sites. This finally gives the Flory-Huggins free energy of mixing per site:

$$\begin{aligned} \Delta \bar{F}_{\text{mix}} &= k_B T \left[\frac{\phi}{N_A} \ln \phi + \frac{1-\phi}{N_B} \ln (1-\phi) + \chi \phi (1-\phi) \right] \text{ or in general,} \\ \Delta \bar{F}_{\text{mix}} &= k_B T \left[\frac{\phi_A}{N_A} \ln \phi_A + \frac{\phi_B}{N_B} \ln \phi_B + \chi \phi_A \phi_B \right] \end{aligned} \quad (2.23)$$

The first two terms in the free energy equation (2.23) have entropic origin and always act to promote mixing, although blends of long polymer chains have very less entropy of mixing. The last term in Eq. (2.23) can be positive (opposing mixing), negative (promotes mixing) or zero (ideal mixtures).

As mentioned in the beginning of this section, we assume that in Flory-Huggins theory that there is no volume change and the monomers of both species can fit on the lattice sites of the same lattice. In reality this is not the case and some monomers may pack well together with certain other monomers and hence there would be a volume change upon mixing [252]. We have not yet been able to completely understand these effects using a simple theory. However, it is known from experiments [49, 234, 256] that the interaction parameter depends on temperature. Therefore we can incorporate these unknown effects into the temperature dependence of χ as some additive constants. This enables us to correct for the deviations from the mean field Flory-Huggins theory. The relation connecting interaction parameter and temperature could then be written as: [252]

$$\chi \approx A + \frac{B}{T} \quad (2.24)$$

Here A is the temperature independent term and B the enthalpic term. Once we have added all the corrections into χ , we can use the Flory-Huggins equation to predict the equilibrium and meta-stable states of mixture, as we will discuss next.

2.2.2 Criterion for mixing and Phase separation

The free energy density can help us predict whether the system will remain in the homogeneous or phase separated state. Assuming a solution of species A having volume and concentration (V_1, ϕ_1) is allowed to be mixed with another solution of species B having (V_2, ϕ_2) , complete mixing of which will result in a solution having total volume $V_1 + V_2$

and a volume fraction [79]:

$$\begin{aligned}\phi_0 &= \frac{\phi_1 V_1 + \phi_2 V_2}{V_1 + V_2} = x\phi_1 + (1-x)\phi_2 \quad \text{where,} \\ x &= \frac{V_1}{V_1 + V_2}\end{aligned}\tag{2.25}$$

The total free energy of the system before mixing is $V_1 f(\phi_1) + V_2 f(\phi_2)$ (f is the free energy

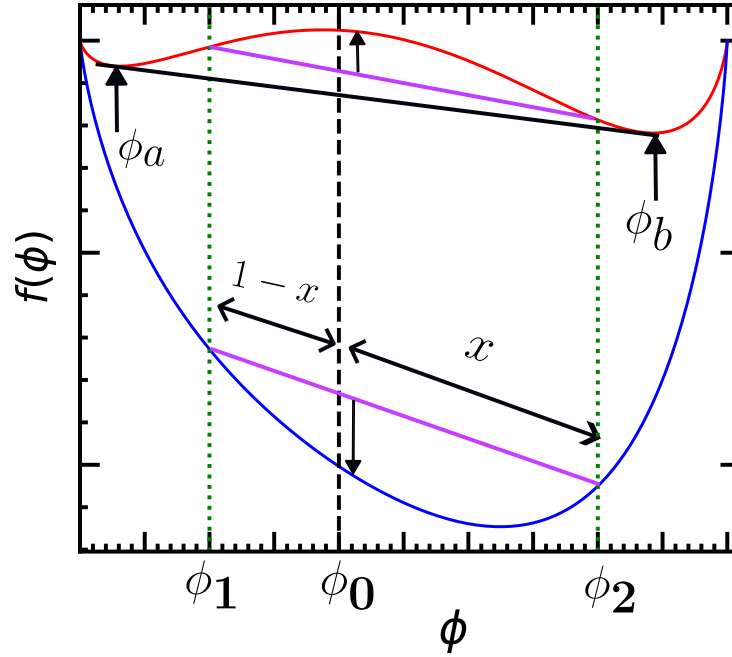


FIGURE 2.3: The free energy of a homogeneous solution is plotted as a function of solute concentration. Two scenarios are considered: (blue) the solute and solvent can mix at any composition, and (red) phase separation occurs. The magenta line indicates the line connecting the free energy at concentrations ϕ_1 and ϕ_2 . The free energy decreases after mixing for the first scenario, indicated by downward arrows from the magenta line. In the second scenario, the free energy increases indicated by the upward arrow from magenta line. The black line indicates the common tangent drawn between concentrations ϕ_a and ϕ_b which corresponds to minimas of free energy in red.

density function). Hence the free energy of the mixed system will be $(V_1 + V_2)f(\phi_0)$. To create a homogeneously mixed state, the free energy density of the mixed state must be less than the free energy density before mixing:

$$f(x\phi_1 + (1-x)\phi_2) < xf(\phi_1) + (1-x)f(\phi_2)\tag{2.26}$$

The above condition implies that $f(\phi)$ is an upper concave function in the region $\phi_1 < \phi < \phi_2$ (see Figure 2.3 (blue)), i.e., $\frac{\partial^2 f}{\partial \phi^2} > 0$ for $\phi_1 < \phi < \phi_2$. On the other hand if

free-energy density $f(\phi)$ has an upper convex part in the region between ϕ_1 and ϕ_2 as in Figure 2.3 (red), the solution phase separates into two concentrations ϕ_a and ϕ_b [78].

We know that the shape of the function $f(\phi)$ varies with temperature. In the temperature range where $f(\phi)$ has two local minima, a solution with concentration ϕ_0 ($\phi_a < \phi_0 < \phi_b$) will phase separate into two phases, ϕ_a and ϕ_b as mentioned before. One could find these concentrations from the free energy density curve using the common tangent criterion [79, 252]:

$$\left[\frac{\partial f}{\partial \phi} \right]_{\phi_a} = \left[\frac{\partial f}{\partial \phi} \right]_{\phi_b} = \frac{f(\phi_b) - f(\phi_a)}{\phi_b - \phi_a} \quad (2.27)$$

In order for a double local minimum to appear in the free energy density function, it should have the existence of a concave downward region positioned between ϕ_a and ϕ_b . As a consequence, within this range, there would exist two points C and D where the double derivative of free-energy density is zero. The locations of all such points in the $\phi-T$ curve defines the spinodal line. In the vicinity of the critical temperature, the points C and D comes closer, ultimately converging at the critical point. Beyond the critical point, $\frac{\partial^2 f}{\partial \phi^2}$ assumes a positive value. This, in turn, implies the fulfillment of a distinct set of equations precisely at the critical point [79], which can be used to determine it.

$$\begin{aligned} \frac{\partial^2 f}{\partial \phi^2} &= 0, \\ \frac{\partial^3 f}{\partial \phi^3} &= 0 \end{aligned} \quad (2.28)$$

2.2.3 Phase diagram - polymer blend

Here we summarize the phase behaviour of the mixture showing the regions of stability, instability and metastability. The free energy of mixing a polymer blend was given in Eq. (2.23). As mentioned before in the last part of the subsection 2.2.2, the common tangent to the free energy at the compositions ϕ_a and ϕ_b corresponds to equilibrium phases. For a simple symmetric polymer blend with $N_A = N_B = N$ the common tangent line is horizontal. So Eq. (2.27) can be solved for the interaction parameter corresponding to the phase-boundary. Hence the binodal (see Fig 2.4 (solid line in red color)) of a symmetric

blend is given by:

$$\chi_b = \frac{\ln(\phi/(1-\phi))}{(2\phi-1)N} \quad (2.29)$$

Using the empirical temperature dependence of the interaction parameter $\chi(T)$ (equation (2.24)), the relation in Eq. (2.29) can be transformed to that in $\phi - T$ space:

$$T_b = \frac{B}{\ln(\phi/(1-\phi))/(2\phi-1)N - A} \quad (2.30)$$

Now, solving the top equation in Eq. (2.28), the curve corresponding to the inflection point can be derived. This curve is called the spinodal (dashed red lines in Figure 2.4) which is the boundary between unstable and metastable region. [79, 252]:

$$\chi_s = \frac{1}{2} \left[\frac{1}{N_A\phi} + \frac{1}{N_B(1-\phi)} \right] \quad (2.31)$$

Applying the bottom equation of Eq. (2.28), the critical concentration is obtained; substituting it in Eq.(2.31) we get χ_c :

$$\begin{aligned} \phi_c &= \frac{\sqrt{N_B}}{\sqrt{N_B} + \sqrt{N_A}} \\ \chi_c &= \frac{1}{2} \left[\frac{1}{\sqrt{N_A}} + \frac{1}{\sqrt{N_B}} \right]^2 \end{aligned} \quad (2.32)$$

For a symmetric blend Eq. (2.32) simplifies to [78, 252]:

$$\begin{aligned} \phi_c &= \frac{1}{2} \\ \chi_c &= \frac{2}{N} \end{aligned} \quad (2.33)$$

When the interaction parameters χ falls below the critical threshold, the homogeneous mixture remains stable across all concentrations. However when χ becomes greater than χ_c , a phase separation gap called the miscibility gap, between the dual branches of the binodal, as illustrated in Figure 2.4 (blue) arises. For any composition in this miscibility gap, the equilibrium state corresponds to concentrations ϕ_a and ϕ_b , located on the two branches of the coexistence curve at the same value of χ [252].

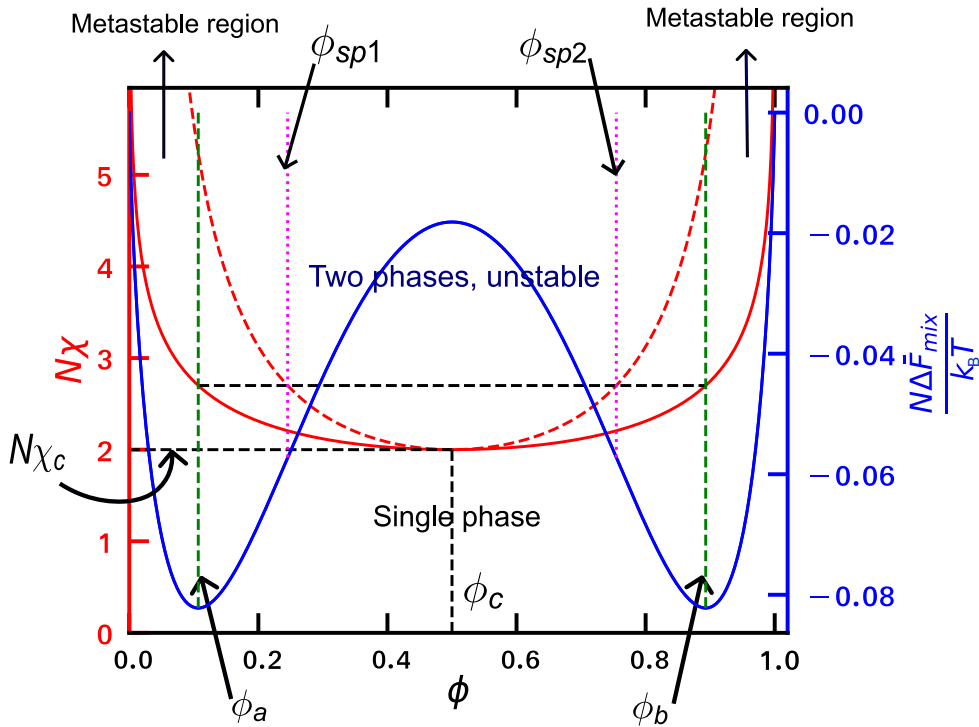


FIGURE 2.4: The free energy of mixing (in blue) and the binodal curve in $N\chi$ - ϕ plane (in solid red lines) is shown for a symmetric polymer blend. The left y axis (in red color) indicates the $N\chi$ values and the right y axis in blue color indicates scaled free-energy of mixing. The upper and bottom axis both indicates volume-fraction ϕ . The free-energy of mixing was drawn by choosing $N\chi = 2.7$. The pink/magenta colored vertical lines indicates the concentrations where $\partial^2 F / \partial \phi^2 = 0$, giving the spinodal volume fraction for the given free-energy curve. The green vertical lines are the volume fraction where the free energy has minimas, i.e., phase separated concentrations. The red dashed curve indicates spinodal for a symmetric mixture. Critical volume fraction ϕ_c and the scaled critical interaction parameter $N\chi_c$ is also shown here in black dashed lines.

2.2.3.1 Upper and Lower critical solution temperature

The understanding of how polymers interact with solvents dates back to the work of Flory [101] and Huggins [144, 224], who introduced the polymer-solvent interaction parameter χ . Their theory explained why the solubility of polymers behaved differently from that of small molecules. They also introduced the concept of free volume [225, 224] which was later used to explain the lower/upper critical solution temperature (LCST/UCST).

We can divide the thermoresponsive polymers into two categories based on their critical solution temperature, i.e. polymers having an upper critical solution temperature or the ones having a lower critical solution temperature. Figures 2.5 (a)-(b) depicts the phase diagram of LCST and UCST polymers respectively. Both types of polymers exhibit changes

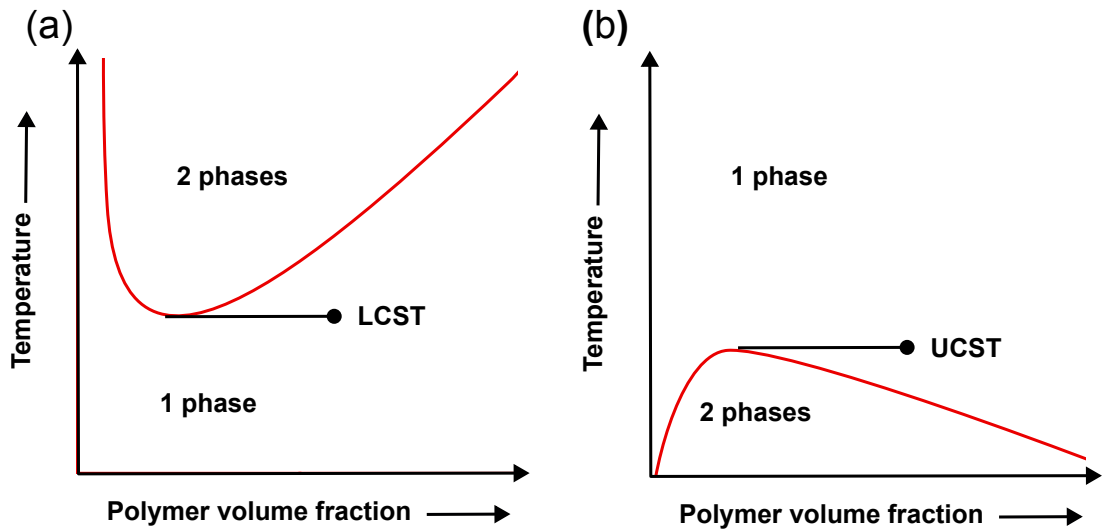


FIGURE 2.5: Binodal diagrams for (a) LCST polymers, (b) UCST polymers depending on polymer fraction ϕ .

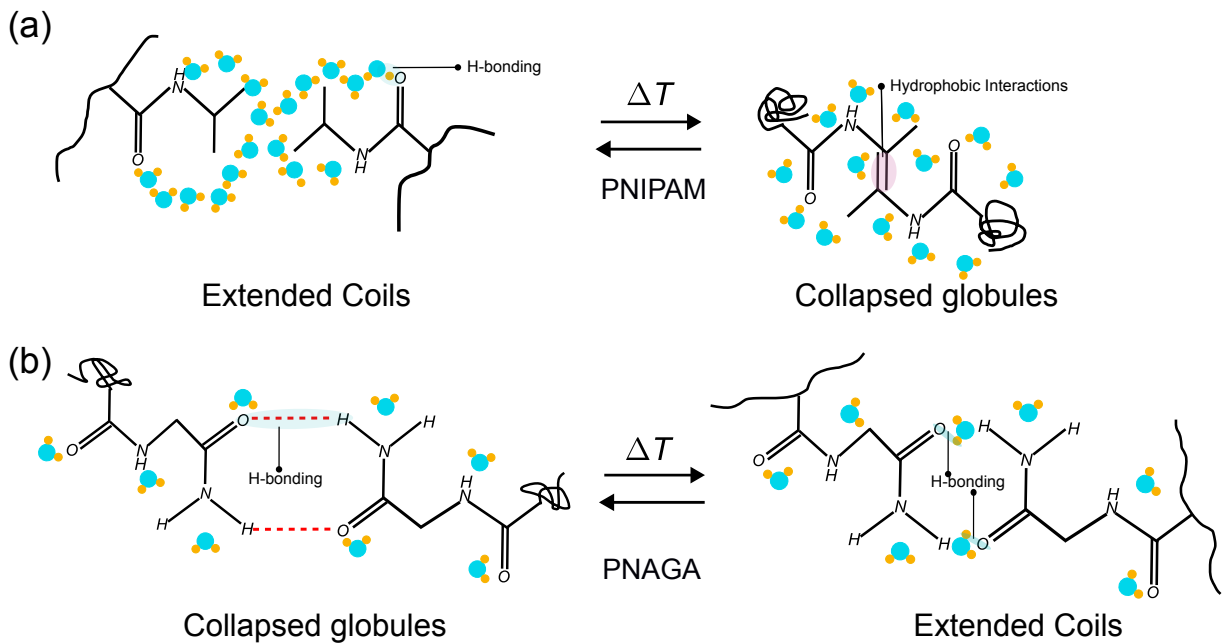


FIGURE 2.6: Schematics of coil to globule transition in (a) LCST polymer PNIPAM and (b) UCST polymer PNAGA.

in their properties at the critical solution temperature. UCST polymers are insoluble at low temperatures but become soluble above the UCST due to an enthalpy-driven process [292, 224]. In contrast, LCST polymers dissolve in solvent at low temperatures and are insoluble at high temperatures. The coil to globule transition in this case happens due to the increase in entropy, resulting in the polymers precipitating out of the solution. A possible reason for this behavior in water-based gels is the hydrophobic effect [285]. Such

gels can be described as a two-component system, consisting of the polymer and solvent (or solvent mixture), where their ability to mix depends on temperature and polymer concentrations.

The thermosensitive polymer poly(N-isopropylacrylamide) (PNIPAM) having LCST, is widely studied since its critical solution temperature is close to physiological temperature (32° C) [261, 224]. It undergoes entropic coil to globule transition in aqueous media [224, 130] as shown in Figure 2.6 (a). We can use the Gibbs free energy of mixing $\Delta G_{\text{mix}} = \Delta H_{\text{mix}} - T\Delta S_{\text{mix}}$ to understand the volume contraction in the PNIPAM gel [335, 224]. Below the LCST temperature, the enthalpy of mixing (ΔH_{mix}) is negative due to formation of hydrogen bonds between water and the amide groups. This also leads to a more ordered state where the entropy of mixing (ΔS_{mix}) is negative. The very negative enthalpic term dominates at the low temperatures and hence $\Delta G_{\text{mix}} < 0$, promoting mixing. As temperature increases and reaches values close to LCST, hydrogen bonds break. Above the LCST temperature, the endothermic breaking of hydrogen bonds leads to ΔH_{mix} being less negative and the entropy gain due to higher temperature causes the $T\Delta S_{\text{mix}}$ term to dominate leading to $\Delta G_{\text{mix}} > 0$ [224]. Thus at these temperatures we have coexistence of water and a collapsed polymer state.

Similarly we can also use the concept of free energy of mixing to explain the UCST behaviour in aqueous solutions. Poly(N-acryloyl glycinamide) (PNAGA) is an example of a non-ionic polymer that shows the UCST-type phase transition in aqueous solutions [28]. Figure 2.6 (b) show the schematics of this coil to globule transition for PNAGA polymers. This polymer is insoluble in water at low temperatures due to the strong polymer-polymer hydrogen bonds, which could be disrupted on heating the system. Hence at temperatures below UCST we have a positive ΔH_{mix} and the strong positive enthalpy of mixing dominates over the entropy of mixing ΔS_{mix} [269]. Consequently, the free energy of mixing, ΔG_{mix} is positive and thus at temperatures less than UCST we have phase separation. At temperatures above UCST, the interaction between the polymer chains get weakened and the interactions between water and polymer becomes energetically favorable. This leads to ΔH_{mix} being negative or less positive. However as the temperature increases, the entropy also increases and thus $T\Delta S_{\text{mix}}$ term of the free energy dominates over ΔH_{mix} , causing $\Delta G_{\text{mix}} < 0$. Thus for temperatures above UCST, these polymers mix with the solvent.

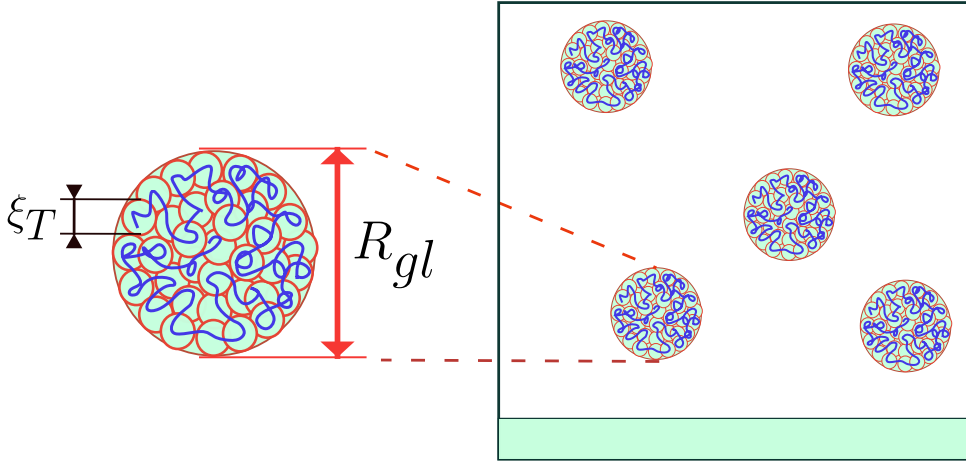


FIGURE 2.8: Conformation of a dilute globule in a poor solvent, depicted as a random walk of thermal blobs up to the size of the globule.

curve, the solution separates into a dilute phase of isolated globules and a concentrated sediment. The concentrations of the dilute phase (ϕ') and concentrated sediment (ϕ'') are given by the coexistence curve. The sediment concentration ϕ'' is determined by the balance of the second and third virial terms, $\phi'' \approx -\frac{\mathbf{v}}{b^3} \approx 2\chi - 1$. The globule size is thus given by:

$$R_{gl} \approx \frac{b^2 N^{1/3}}{|\mathbf{v}|^{1/3}} \quad (2.34)$$

If the temperature is high enough, the solvent becomes a good solvent and it exhibits three distinct regimes. The dilute good solvent regime exists at concentrations $\phi < \phi^* \approx \left(\frac{b^3}{\mathbf{v}}\right)^{6\nu-1} N^{1-3\nu}$. In this regime, the size of a swollen chain with excluded volume $\mathbf{v} > b^3/\sqrt{N}$, is similar to that of a self-avoiding walk of thermal blobs of size $\xi_T \approx b g_T^{1/2} \approx \frac{b^4}{|\mathbf{v}|^4}$. Here g_T represents the number of monomers within a thermal blob. Thus using the above idea the size of the coil can be given by

$$R_F \approx b \left(\frac{\mathbf{v}}{b^3}\right)^{2\nu-1} N^\nu \quad (2.35)$$

Chains begin to overlap for $\phi > \phi^*$. In the concentration range $\phi^* < \phi < \phi^{**} \approx \mathbf{v}/b^3$, we are at the semi-dilute good solvent regime. In this regime, since the polymer volume fractions are still quite low, each monomer can see only the solvent and few monomers of the same chain at shorter distances. Semi-dilute solutions are characterized by a length

scale ξ , where a given chain starts to interact with other chains. The correlation length is given by [252, 200]:

$$\xi \approx b \left(\frac{b^3}{\mathbf{v}} \right)^{(2\nu-1)/(3\nu-1)} \phi^{-\nu/(3\nu-1)} \quad (2.36)$$

On length scales larger than ξ , excluded volume interactions are screened by overlapping chains and hence on these scales the semi-dilute solution behaves like a melt of chains composed of correlation blobs. The size of the polymer chain in this regime is:

$$R \approx b \left(\frac{\mathbf{v}}{b^3 \phi} \right)^{(\nu-1/2)/(3\nu-1)} N^{1/2} \quad (2.37)$$

At length scales between thermal blob size and the correlation blob size ($\xi_T < r < \xi$), the chains are swollen, i.e., it exhibits self avoiding walks. It shows ideal chain statistics in the length scales where $r < \xi_T$ [230, 252]. Figure 2.9 (a) - left shows the schematics of a chain in semi-dilute good solvent in which both the correlation and thermal blobs are indicated. The right part of the same figure shows how the end to end distance of a subsection of the chain scales with number of monomers in the subsection. The concentration dependence of polymer size can be obtained using de-Gennes scaling theory [73, 252].

$$R \approx R_F \left(\frac{\phi}{\phi^*} \right)^{-(\nu-1/2)/(3\nu-1)} \approx R_0 \left(\frac{\phi}{\phi^{**}} \right)^{-(\nu-1/2)/(3\nu-1)} \quad (2.38)$$

The equation (2.38) shows that the chain size in semi-dilute good solvent decreases weakly with increasing concentration: Figure 2.9 (b) shows how the chain size and correlation length, scales with concentration ϕ in a good solvent.

Equation (2.36) indicates that the correlation length decreases with increasing concentration, while the thermal blob size ξ_T remains constant ($\xi_T \approx \frac{b^4}{|\mathbf{v}|}$) as shown in the Figure 2.9 (b). This implies that at a certain concentration ϕ^{**} , where $\xi_T \approx \xi$, the intermediate swollen region vanishes. Thus value $\phi^{**} = \frac{\mathbf{v}}{b^3}$ indicates the start of concentrated regime.

At concentrations exceeding the critical value ϕ^{**} , chains behave ideally at all length scales. This regime is an extension of the semi-dilute θ -solution region to higher temperatures. The correlation length also dictates the osmotic pressure and is given by $\Pi \approx \frac{kT}{\xi^3}$. This equation is valid for theta, good, and athermal solvents [252, 73, 200].

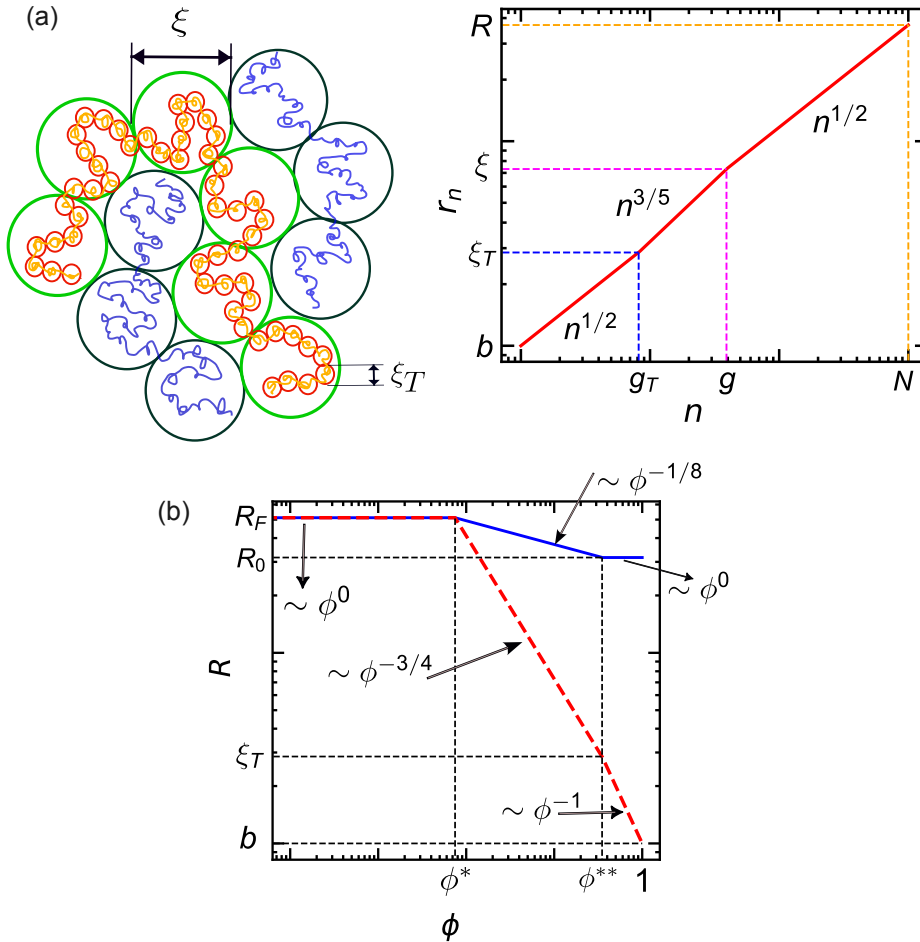


FIGURE 2.9: (a-left) Schematic of a chain in a semi-dilute good solvent. The red colored circles mark the thermal blobs and the green colored circles represent the correlation blobs. The chain of interest is colored orange and the surrounding chains are blue in color. The black colored circles shows the correlation blobs from the near-by chains. (a-right) The plot shows the variation of end-to-end distance with the size of a chain subsection in a good solvent in logscale. (b) Log-scale plot of the concentration dependence of coil-size (solid red lines) and correlation length (dashed red lines) for a chain in intermediate good solvent. The figures (a)-(b) are plotted with the scaling exponent $\nu = 3/5$

2.3 Polymer Gels

Polymer gels are an interesting class of soft matter. They are composed of polymer chains, which are cross-linked to form a network. They have high solvent retention capacity. When these network structures are made of hydrophilic polymers they can store a large amount of water. In addition to this they are soft, elastic and are porous. Due to their ability to absorb and release solvents or other substances they are considered extremely

versatile. Polymer gels are used in various applications like drug delivery [110, 76, 307], tissue engineering [68, 141, 44], eye health-related applications, including contact lenses and artificial corneas [59, 206, 146, 8], as well as an agricultural soil conditioners [281, 27, 32]. They have also found their way into commercial products e.g. diapers due to their exceptional absorbent property [50, 255, 334].

Physical gels and chemical gels represent the two fundamental types of polymer gels depending on their composition and structure. Physical gels are formed through physical interactions, such as hydrogen bonding [157, 64], van der Waals forces, or entanglement of polymer chains [237]. These are gels which under various external stimuli like temperature, pH or the concentration of surrounding solvent can change their structure reversibly along with their properties. Chemical gels or covalent gel are generated by permanent covalent bonds between polymer chains, which forms a 3-dimensional network. These gels are much stronger mechanically and structurally since they can form covalent bonds. The structure of a chemical gel is created when it is formed and will not easily be altered by environmental conditions. Their physical rigidity has made them suitable for tissue engineering, where they can serve as a scaffolds to promote cell proliferation and regeneration [310]. Both physical and chemical gels are characterized by their unique attributes and accompanying phenomena, so the choice between which one to employ is ultimately dictated by the application under consideration.

2.3.1 Elasticity

The phrase 'rubberlike elasticity' [102] characterizes the elastic response of substances comprising of polymers or polymer-like structures, essentially long-chain molecules. Initially observed in natural and vulcanized rubber, this behavior is now attributed to the entropic effects of the constituent polymer chains. When working with gels, this term is equally applicable. The objective of this section is to present fundamental models and principles for analyzing the elastic traits of the gel systems under investigation.

2.3.1.1 Affine Network Model

The impressive flexibility of polymer networks comes from the entropic elasticity of their polymer chains. In the affine network model, proposed by Kuhn [169], each strand's deformation is assumed to match the overall network's deformation.

For a rubber network with initial dimensions L_{x0} , L_{y0} , and L_{z0} , if deformed by factors λ_x , λ_y , and λ_z , the new dimensions are $L_x = \lambda_x L_{x0}$, $L_y = \lambda_y L_{y0}$, and $L_z = \lambda_z L_{z0}$. Each strand with N monomers has an end-to-end vector \vec{R}_0 , which transforms to \vec{R} with projections $R_x = \lambda_x R_{x0}$, $R_y = \lambda_y R_{y0}$, and $R_z = \lambda_z R_{z0}$ [252, 136].

The entropy of a chain with N Kuhn monomers and end-to-end vector \vec{R} is:

$$S(N, \vec{R}) = -\frac{3}{2}k_B \frac{\vec{R}^2}{Nb^2} + S(N, 0) \quad (2.39)$$

The change in entropy due to deformation is:

$$S(N, \vec{R}) - S(N, \vec{R}_0) = -\frac{3}{2}k_B \frac{(\lambda_x^2 - 1)R_{x0}^2 + (\lambda_y^2 - 1)R_{y0}^2 + (\lambda_z^2 - 1)R_{z0}^2}{Nb^2} \quad (2.40)$$

For n strands in the network, the total entropy change is:

$$\Delta S_{\text{net}} = -\frac{nk_B}{2}(\lambda_x^2 + \lambda_y^2 + \lambda_z^2 - 3) \quad (2.41)$$

The free energy change is:

$$\begin{aligned} \Delta F_{\text{net}} &= -T\Delta S_{\text{net}} \\ &= \frac{nk_B T}{2}(\lambda_x^2 + \lambda_y^2 + \lambda_z^2 - 3) \end{aligned} \quad (2.42)$$

For uni-axial deformation at constant volume, the product of deformation factors $\lambda_x \lambda_y \lambda_z = 1$. Hence, if $\lambda_x = \lambda$, the other two factors should be $\lambda_y = \lambda_z = \frac{1}{\sqrt{\lambda}}$ to keep the volume constant.

The free energy change for uni-axial deformation is:

$$\Delta F_{\text{net}} = \frac{nk_B T}{2} \left(\lambda^2 + \frac{2}{\lambda} - 3 \right) \quad (2.43)$$

The force required for deformation is:

$$\begin{aligned} f_x &= \frac{\partial \Delta F_{\text{net}}}{\partial L_x} \\ &= \frac{nk_B T}{L_{x0}} \left(\lambda - \frac{1}{\lambda^2} \right) \end{aligned} \quad (2.44)$$

The nominal stress given by, dividing f_x by the initial cross-sectional area, is [119]:

$$\sigma_{xx} = \frac{nk_B T}{V} \left(\lambda^2 - \frac{1}{\lambda} \right) \quad (2.45)$$

The shear modulus G is:

$$G = \frac{nk_B T}{V} = \nu k_B T \quad (2.46)$$

2.3.1.2 Phantom network model

Affine network model assumes that the network's endpoints remain anchored in space, moving in an affine manner along with the entire network. In reality the strands connect at cross-links, that constantly fluctuates rather than remain stationary. These fluctuations help in reducing the cumulative stretching of strands, lowering the system's free energy. This perspective is captured in a phantom network model [223, 83, 102, 128], envisioning the strands as ideal chains with ends connected at cross-links while the outer surface of the phantom network is fixed to a stable and immutable boundary. This anchoring stabilizes the volume of the phantom network, preventing any collapse. One can obtain the shear modulus of a phantom network from the modulus of affine network by substituting ν in equation 2.46 with $\nu(f - 2)/f$:

$$G = \nu k_B T \frac{f - 2}{f} \quad (2.47)$$

Here f refers to the functionality of the cross-linkers. The phantom network has the same number density of strands as the affine network but only the fraction $(f - 2)/f$ of the combined chain is the real strands that supports stress [128, 136, 252].

2.3.2 Summary of swelling of polymer gels

The polymer volume fraction ϕ in a swollen or partially swollen gel can be determined by measuring the volume V of the swollen gel (including the solvent) and the volume of the dry gel V_{dry} [252]:

$$\phi = \frac{V_{\text{dry}}}{V} \quad (2.48)$$

The volume fraction ϕ_0 of the polymers in the initial preparation state with volume V_0 remains constant as the amount of polymers doesn't change during swelling or de-swelling. The volume change is solely due to the solvent:

$$V_0\phi_0 = V\phi = V_{\text{dry}} \quad (2.49)$$

When a macroscopic network swells uniformly in a solvent, the swelling factor λ is the cube root of the volume ratio V/V_0 or the initial and final volume fractions ϕ_0/ϕ :

$$\lambda = \left(\frac{V}{V_0}\right)^{1/3} = \left(\phi_0/\phi\right)^{1/3} \quad (2.50)$$

Panyukov proposed the scaling of the elastic energy of gels during swelling/deswelling to be given by [222, 252, 136]:

$$\frac{F_{\text{el}}}{k_B T} \left(\frac{\phi}{Nb^3}\right) \approx \frac{G}{k_B T} \approx \frac{\phi}{Nb^3} \left(\frac{\lambda R_0}{R_{\text{ref}}}\right)^2 \quad (2.51)$$

Here, R_0^2 is the mean square end-to-end distance of the chains in the preparation state, and R_{ref}^2 is the mean square end-to-end distance of a free chain with the same number of monomers as the gel strand in the same solution and G is the modulus of the gel in swollen or partially swollen state.

During swelling equilibrium, the gel's elasticity is balanced by the osmotic pressure Π from a semi-dilute solution of uncrosslinked chains at a similar concentration. The equilibrium swelling ratio Q is the ratio of the fully swollen volume V_{eq} to the dry volume V_{dry} [70]:

$$Q = \frac{V_{\text{eq}}}{V_{\text{dry}}} \quad (2.52)$$

In θ and athermal solvents, the swelling ratio is $Q \approx \frac{N^{3/8}}{\phi_0^{1/4}}$ and $Q \approx \frac{N^{3(3\nu-1)/4}}{\phi_0^{1/4}}$, respectively [70]. In a good solvent for $\phi > \phi^{**}$, chains behave almost like an ideal chain, while for $\phi < \phi^{**}$, chains are swollen on intermediate scales. The network modulus and equilibrium swelling depends on the preparation and fully swollen concentrations (ϕ_0 and $1/Q$) relative to the crossover concentration ϕ^{**} . Since the swollen concentration is always

lower than the preparation concentration ($1/Q < \phi_0$), three cases are possible with the following swelling ratios [222, 252]:

$$\begin{aligned}
 Q &= (\mathbf{v}/b^3)^{0.4} N^{0.57} \phi_0^{-1/4} & 1/Q < \phi_0 < \phi^{**} \\
 &= (\mathbf{v}/b^3)^{0.53} N^{0.57} \phi_0^{-0.38} & 1/Q < \phi^{**} < \phi_0 \\
 &= N^{3/8} \phi_0^{-1/4} & \phi^{**} < 1/Q < \phi_0
 \end{aligned} \tag{2.53}$$

2.4 Capillary Wave theory

Understanding the interfacial properties of fluids is just as important as studying its bulk properties. In the early years of eighteen hundred's, scientists like Laplace and Gauss had made attempts to explain the interfaces and capillary phenomenon [250], which was later picked up by Maxwell in 1876, in his essay on "Capillary action" [193, 250]. However these early works, heavily relied on the assumption that the molecules or atoms at these interfaces are static. Secondly they assumed, that the gas-liquid interfaces are sharply defined, like a step function in density, which restricted their treatments near their critical triple point [250, 93]. Clearly, the first assumption is not true, as we now know that molecules are in constant thermal motion. A flaw in the assumption of sharp interface was also pointed out by Poisson in 1831 [232] and later corrected by Lord Rayleigh [184]. They argued that the molecules near to the interface would experience forces from the interface and because of this the density at the interface cannot be uniform. In 1893, van der Waals tried to address both these problems by developing a thermodynamic theory, where the density of molecules are continuous function of height [250, 245]. This was later re-derived in 1958 by Cahn and Hillard [43] using modern approaches, which replaced the step function for density by a continuous one

$$\rho(z) = \frac{1}{2} [\rho_1 + \rho_2 - (\rho_1 - \rho_2) \tanh(2z/w)] \tag{2.54}$$

where ρ_1 and ρ_2 are the densities of the two phases and w is the width of the interface.

Despite its conceptual simplicity, the infinitely sharp interface is still utilized in continuum frameworks like the Gibbs dividing surface model [319]. The major drawback of these continuous description of densities are that, they do not take into account fluctuations at the interface. Therefore, instead of assuming any random or uniform distribution of molecular densities, current theories of liquid focuses on correlation functions i.e., modern

theories of liquids is articulated in terms of the conditional probability of the occurrence of molecular pairs at specified positions in the system [3, 40].

For a fluid-fluid interface it is a well known fact that their interfaces are perturbed by long wavelength fluctuations parallel to the surface. These waves later called capillary waves are the oscillation of fluid under the influence of surface tension, in the absence of other external forces. Diving deeper into these oscillatory movements, Young discovered [328] a strong relationship between the wave's wavelength, velocity, and the surface tension acting upon it, given by :

$$\omega(k) = \sqrt{\frac{\gamma^3 k}{\rho} + gk} \quad (2.55)$$

Here, ω and k denote the frequency of the wave and wavenumber, respectively. The constants g , γ , and ρ represent gravitational acceleration, surface tension, and fluid density, respectively. Equation (2.55) comprises of two terms: the first captures capillary waves, and the second accounts for gravity waves. The capillary length serves as the scale where the transition between these regimes occurs. In this model, the shift between fluid/fluid phases is locally abrupt, characterized by a fluctuating height $h(x, y)$ along the surface normal.

The Capillary Wave Theory (CWT) [229, 40] incorporates these oscillations using the concept of an intrinsic surface $z = \xi(\mathbf{R})$, where $\mathbf{R} = (x, y)$, representing the microscopic boundary between liquid and vapor [51]. The intrinsic surface correlations, $\langle \xi(\mathbf{R}_1)\xi(\mathbf{R}_2) \rangle$, account for long-ranged transverse dependence. The CWT assumes statistical independence between $\tilde{\rho}(z)$ (intrinsic density) and $\xi(\mathbf{R})$. It also postulates that $\xi(\mathbf{R})$ follows a simple surface Hamiltonian, leading to uncorrelated Gaussian probabilities for each Fourier component, with $\langle |\hat{\xi}_q|^2 \rangle = \left(\gamma_0 A q^2 / k_B T \right)^{-1}$. Here, γ_0 is the macroscopic surface tension, $A = L_x^2$ is the finite transverse size, and periodic boundary conditions $q \geq 2\pi/L_x$ are applied [51]. The shape of the intrinsic profile is determined based on the definition of $\xi(\mathbf{R})$ and the upper limit $q_u \geq q$ for resolution [51, 229]. Thus under these assumptions, the shape of the intrinsic density profile is given by

$$\tilde{\rho}(z, q_u) = \left\langle \frac{1}{A} \sum_{i=1}^N \delta(z - z_i + \xi(\mathbf{R}_i)) \right\rangle \quad (2.56)$$

One could also compare the intrinsic density profile in Equation (2.56) with the mean density profile or the non-intrinsic density profile

$$\rho(z, q_u) = \left\langle \frac{1}{A} \sum_{i=1}^N \delta(z - z_i) \right\rangle \quad (2.57)$$

The difference here is that the intrinsic profile is measured with respect to an instantaneous local surface, whereas the non-intrinsic profile is measured with respect to an external fixed plane. Interestingly we have a relationship between the intrinsic density profiles $\hat{\rho}(z)$ and the non-intrinsic profile $\rho(z)$ [93, 53], i.e., non-intrinsic profiles can be expressed by the convolution of intrinsic profiles with Gaussian of width $\Delta_{\text{CW}}(q_u) = \sum_q \langle \xi_q^2 \rangle$ [52]

$$\rho(z, L_x) = \int dz' \frac{\tilde{\rho}(z' q_u)}{\sqrt{2\pi\Delta_{\text{CW}}}} \exp -\frac{(z - z')^2}{2\Delta_{\text{CW}}} \quad (2.58)$$

This a prediction from the Capillary Wave theory and can be used to check whether the theory is applicable to a particular system of interest [52, 93].

2.5 Summary

This chapter provides a comprehensive overview of the foundational concepts in polymer physics and gels. We begin with a brief history of polymer science, setting the stage for an introduction to ideal chain models. In this section, we cover fundamental concepts such as methods for describing the size of a polymer and the scaling relation to the number of bonds in a chain. We introduce the radius of gyration and its relationship to the end-to-end distance of a polymer chain. Additionally, we explore the free-energy and probability distributions associated with Gaussian chains. Moving forward, we provide a concise description of real polymer chains, focusing on the Meyer function and the concept of excluded volume. We then discuss the scaling laws governing polymer size in various solvents, including athermal, good, theta, and poor solvents. This discussion extends to polymer solutions, where we explain the Flory-Huggins theory of mixing and the criteria for phase separation, which are crucial for understanding the volume phase transition in thermo-responsive gels. We also examine how chain size varies with concentration in different concentration of polymer solutions and the solvent nature. The chapter transitions into a discussion on polymer gels, introducing two fundamental elastic theories. We

summarize the swelling behavior of these gels in different solvents, providing a clear understanding of swelling ratios. The chapter concludes with an introduction to Capillary-Wave theory, which will be utilized in Chapter 4 to derive interfacial tension. This theoretical framework sets the stage for the detailed analysis presented in the subsequent chapters.

Chapter 3

Computer simulations

3.1 Introduction

Computer simulations have a valuable role to play in providing exact solutions to problems in a variety of fields including economics, physics, chemistry, biology and engineering. The general approach of a simulation is to utilize models and algorithms to mimic the processes we are trying to learn. The results from a computer simulations can be compared with real experiments. In the first place this would act as a test for the underlying models used in the simulation. Later, if the model is a good one, the simulator can offer insights into difficult, expensive or impossible experiments, which can easily be done on a computer. They are also helpful in testing theories and hypothesis. Thus simulations plays a dual role by bridging the gap between models and theoretical predictions and also models and experimental results.

3.2 HOOMD Blue package

Since all the simulations in the presented thesis were performed with HOOMD package it seems rational to justify this choice and present the core features of this molecular dynamics package. HOOMD stands for Highly Optimized Object-Oriented Molecular Dynamics. We discuss a brief history of HOOMD based on this paper by Anderson [19] (<https://github.com/plotzerlab/hoomd-blue>).

HOOMD's development began in March 2007, arising from the need to have a highly efficient MD simulations package based on GPUs for coarse-grained simulations. It is the first fully GPU enabled simulation package and was made openly available since 2008. The implementation originated with a CUDA and C++ backend, offering Python scripting capabilities within an imperative programming paradigm. However, it required these scripts to be run through HOOMD-blue's modified interpreter that was responsible for managing its global state [41]. The Python front-end facilitated its broader use and proved to be more advantageous over its contemporary softwares like LAMMPS for which a python interface was only later developed (in 2010, as far as I know). Within the research community, HOOMD gained more notice as scholars utilized and referenced its abilities. Papers also emerged utilizing the platform, signaling its traction. HOOMD was renamed "HOOMD-blue", after University of Michigan acquired it, in August 2009. Later, certain improvements were incorporated into HOOMD-blue. Version 1.0 introduced in 2014 provided support for MPI domain decomposition followed by version 2.0 in 2016 which supported Monte Carlo techniques [114, 115] and discrete element molecular dynamics for rigid bodies [15]. Version 2.0 also allowed for the use of HOOMD-blue within the conventional python scripts. It also introduced 'SimulationContext' object which allowed for multiple autonomous simulations within a singular script. However this version only allowed partial access of users to global state and its python APIs were largely inspired from existing softwares like LAMMPS. In the later release like version 3.0, a complete change or re-design of the Pythonic interface was seen, making it more transparent and intuitive to the users. The concept of global object was removed and highly object oriented approaches was incorporated, giving the users the access to simulation configurations wherever possible [41].

3.3 Molecular Dynamic Simulations

Molecular dynamics (MD) simulations have become a powerful tool to study molecular systems, at coarse-grained levels. This computational approach enables us to understand the steady state properties and dynamical behavior of systems at those scales for which particle trajectories cannot be followed through experiments. MD simulation framework intends to solve Newtons equations of motion to examine how a system evolves with time. Information derived from MD simulations not only validates theoretical expectations but also enables us to generate fresh predictions in scenarios where theory is confined by its initial assumptions or the extent of its applicability. As described before, MD simulations

works by integrating the equations of motion and generally for a particle these equations look like the following:

$$\ddot{\vec{x}} = \frac{\vec{F}_i}{m_i} \quad (3.1)$$

here \vec{x}_i is the position of the particle i , \vec{F}_i is the net forces acting on the particle i , and m_i is the mass of the particle i . The dots on \vec{x}_i indicates second derivative with respect to time. To work with this method, it is necessary to define the initial conditions, which include the positions and velocities of all particles at a chosen time point, denoted as t_0 . A challenging aspect of MD simulation is calculating the forces acting on the particles; challenging because it is the most time consuming step in a simulation, which is of the order of $O(N^2)$. Here N is the number of particles. However several methods are used to overcome this issues, some of which will be discussed in the subsequent sub-sections [3.3.3.1](#) and [3.3.3.2](#).

3.3.1 Walls

Walls are oriented surfaces which interacts with the particles in the simulation box. These surfaces can be rough (made of particles) or ideal (made of interacting surfaces). HOOMD-blue allows for the creation of both rough and ideal walls. Rough walls can be created based on the requirement of the user and could possibly have a variety of shapes. After initializing the rough wall, the user can define the force field with which it interacts with the particles in the simulation box. HOOMD always uses periodic boundaries, so the users must ensure that the rough wall is defined in such a way that particles in the simulation box do not move between the allowed and the disallowed regions created by the walls, in either direction. Another aspect of caution is to set the width of the disallowed regions created by the rough walls and the simulation box length such that the particles do not interact across the periodic boundaries.

In HOOMD-blue, ideal or virtual walls have only limited pre-defined shapes and pair potentials to choose from. For example HOOMD-blue provides shapes like planes, spheres and cylinders. In contrast to the rough walls, the virtual walls only exist within the primary simulation box, however all cautions needed for the rough walls should also be applied to the virtual walls. Each of these virtual surfaces divides the space into two regions: one where particles are expected to be present, indicated by a positive signed distance from the surface, and one where particles are not expected, indicated by a

negative signed distance. Since particles are always wrapped into the primary simulation box, particles will interact only with the portions of the wall geometries that lie in (or just outside) the primary box image. The virtual walls provided by HOOMD-blue does not rescale under affine transformation of the simulation box or during constant pressure simulations. This rescaling of the virtual walls, have to be done by an external patch of code which updates the position of these walls as the simulation box size changes. However since the rough walls are made of particles they naturally get rescaled, if the particles that makes up the wall is also passed on to the integrator.

3.3.2 Boundary Conditions

Boundary conditions play a crucial role in simulation work. The choice between free, fixed, or periodic boundaries, or a combination thereof, should be tailored to the specific needs that are particular to your system. When one want to simulate a small number of particles, a major portion of them may accumulate at the surfaces. This would lead to wrong interpretation of the results, especially if we are looking at bulk properties, as surface effects would distort the results. Many, thus choose periodic boundary conditions to address this issue, thus simulating a system that behaves as if it continues beyond its apparent boundaries.

3.3.2.1 Periodic Boundary conditions

We can simulate bulk condensed phases and overcome the surface effects described before by using periodic boundary conditions [93, 9, 38]. Here the simulation cell, normally a cubical box, are replicated throughout the space to form an infinite lattice. One important property of PBC is that any shift in the particle position within the main box results in shifts of all mirrored replicates throughout repeated cells. This structure of an interconnected arrangement allows for interactions not only within the original cell but also with virtually infinite mirrored counterparts [160, 9]. In the models considered in the thesis, all the interactions are short ranged. So we work with the so-called minimum image convention [132], which means that for each particle in the primary simulation box, only the interactions from the nearest neighbor particles are taken into consideration. However, if we are working with long-range interacting potentials, we will need to retain several nearest particles.

3.3.2.2 Non-periodic boundary conditions

This is a broad term which encompasses several type of boundary conditions like fixed boundary, free boundary condition that do not use periodic wrapping and do not allow for interaction between particles across the boundaries. It is generally used to simulate a finite system.

- **Fixed boundaries** : Generally speaking fixed boundaries are a sub-class of non-periodic boundary condition, i.e., they do not allow for any wrapping of the particles that cross the box boundaries nor do they allow for interaction between particles across the boundaries. The position of the face of the boundaries are fixed and when the particles cross the boundary, they are typically removed from the simulation state in the next time step. Thus the number of particles in each time step may vary. This is problematic when we are trying to simulate a system in NVT ensemble. In such cases, fixed boundaries are generally combined with walls near to the boundaries so that the particles would not be removed from the simulation state. Unfortunately HOOMD-blue does not allow for fixed boundaries, but one could try to implement it using the custom action features in the newer versions of HOOMD-blue. A simpler way would be to use a very large simulation box to prevent interaction across the periodic boundaries and to use a wall to create a disallowed region. Ofcourse the width of the disallowed region and box length should also be controlled in order to prevent HOOMD-blue from applying pairwise interactions accounting for the periodic boundary conditions. Such boundaries are used for simulating finite sized systems under confinement [303, 134, 137], in some cases fixed boundaries combined with rigid-walls [137, 134] could serve as anchoring points or substrates [29, 268], they are also used to study interfaces and multi-layer systems [322, 272, 194, 125].
- **Free boundaries** : Free boundaries are again non-periodic boundary conditions. Here the position of the face of the boundaries are changed, so as to encompass the particles in the simulation state, no matter how far they move. Hence the simulation box gets extended or shrunk depending on the movement of the particle. One could also implement this boundary condition such that there is a bound on the position of the face of the boundaries. For example if the face of one of the x boundary was at 200σ (σ is the unit of length in simulation units) at the start of the simulation, the face will always be positioned at 200σ or above, even if the maximum extent of particle position in the x direction is less than 200σ . Many studies invoking the use of free boundaries are found in the literature; for example

the study of drug-diffusion from core-shell nano-particles [42], studies of deformation in finite gels/networks [161, 165, 161, 135] and nanoindentation studies done on crystal structures [322, 207].

HOOMD-blue does not support any kind of non-periodic boundary conditions. However as a work around for the free boundaries, one could typically start with a very large simulation box dimension in the direction of interest. Thus if the box dimension is sufficiently large, it would prevent particles from interacting across the boundary and would also encompass all the particles within the simulation box, thus creating the effect of free boundaries. We utilized this method for equilibration of our model network after relaxing the initial structure for our polymer-gel interface studies [303] and for the pulling simulation done to calculate work and contraction in the motor-gel studies [326].

3.3.3 Force Calculation in MD

As mentioned before in section 3.3, here we will discuss the method used to accelerate the calculation of forces used in our simulations, which is called the "bounding volume heirarchies". We will also describe, the other basic methods like Verlet and Cell-list which was also tried upon initially.

3.3.3.1 Verlet and Cell lists

We have focused on pairwise additive forces, which is what determines how the particles in our simulated system behaves. The next important step is to sum all these forces for every pair of particles individually. But the naive solution of iterating over all possible particle pairs cannot do better than give a speed of order $O(N^2)$, which means that the computational time required would grow in proportion to the square of the number of particles in the system. This would be a significant limiting factor on conducting feasible large-scale computer experiments.

Thankfully, for short-ranged pairs of additive interactions, one can optimize their code to make the simulations feasible. One key concept is the introduction of Verlet lists [104, 302, 117]. The idea is not to iterate through all the particle pairs at every step to calculate the pair interactions, instead we build for each (simulated) particle i a dedicated list containing only those particles which are present within the interaction range field at the very beginning of the simulation. That is, each particle j well within a sphere of radius

set to the cutoff value r_{cut} (beyond this distance, it is safe to truncate potentials) about the position of particle i will be separately itemized in an exclusive list corresponding to its source particle i . The number of neighbors corresponding to each particle i is also counted so that we can skip over the force calculations in case some particles do not have neighbors. The created neighbor list, should be updated at the appropriate intervals in order to correctly calculate the forces between the particles and thus evolve the system with time. In practice, the sphere of influence extends somewhat further than the r_{cut} value by a skin depth denoted as σ_s . This extension is crucial for tracking particles that are likely to approach within r_{cut} during the next few integration steps. Generally in such algorithms, whenever a particles moves a distance more than skin depth σ_s the Verlet list is updated [105].

The use of cell lists also works well for various cases, although this may be a slightly less elegant way to relieve much computational effort [9, 105, 133]. This method takes the simulation volume and cuts it into cubes of side lengths greater than r_{cut} . In this, all the particles present in a cube are collected into a list corresponding to that cube. The beauty of this approach becomes evident in larger simulations where the simulation volume is subdivided into a multitude of such cubes. To find the total force acting on a particle in each cube, we only need to look at possible interaction partners from the neighboring cubes that are conveniently stored as cell lists. This is advantageous as it helps to reduce computational cost with respect to considering all pairwise interactions while calculating short-ranged interactions and also makes the simulations more efficient, even in larger system sizes. However both these methods have large memory requirements for big systems.

3.3.3.2 Bounding Volume Hierarchies (LBVH)

Tree structures like bounding volume hierarchies (BVH), k-d trees, octrees are used in computer gaming and ray tracing [140, 305, 111, 164]. These methods are much more efficient to detect collisions and intersections than the grid search methods. These algorithms are able to group particle that are near to one another (in space) into a tree-like structure, which could be searched by simple intersection tests [140]. Many of these algorithm have already been implemented on a CPU to do neighbor searching for molecular simulations [216, 24, 16, 296]. Recently, few researchers proposed to use BVH algorithms to find neighbors in molecular simulation using GPUs [139]. A BVH partitions a system based on objects rather than space. The tree like structure is constructed such that the

objects are placed in **leaf** nodes, then these leaf nodes are placed together into **internal** nodes and finally these **internal** nodes ends at the **root** node at the very top of the tree.

To identify the neighbors of a specified particle, the algorithm checks whether the search volume intersects with the bounding volume of the node [139, 140]. This testing for overlap, starts at the root node possessing the largest bounding volume. Then the search progresses to the children of that node, if the algorithm detects an intersection or overlap; otherwise, that particular branch of the tree will be bypassed. Ultimately, the traversal arrives at a leaf node, where potentially more resource-intensive evaluations between the search volume and the object contained within the leaf can be executed if required.

HOOMD-blue uses linear bounding volume hierarchy (LBVH) [163] to search for neighbors. To build a LBVH the simulation box is divided into bins and the particles assigned into these bins, given a 30-bit Morton code [201] by interleaving the bin coordinates bitwise and finally sorted along Z order curve [140, 188]. The sorted particles are used to build the hierarchy. This involves recursively partitioning the set of particles and enclosing each subset within a bounding volume. The algorithm enclose the nodes in axis-aligned bounding boxes (AABBs) [290] because they are simple to construct, have a small memory footprint, and are easy to test for overlaps. Thus the tree structure is constructed such that there are $N - 1$ internal nodes for N nodes with each internal node having two children. Each particle conducts a search within the BVH by using a bounding volume centered around the particle. To account for periodic boundary conditions in molecular simulations, the search volume is shifted by appropriate combinations of lattice vectors, resulting in a total of 27 search volumes per particle for a three-dimensional periodic simulation box. Whenever the search volume intersects with an internal node, the traversal proceeds down to the left child of the node. Conversely, if there is no overlap, the traversal continues to reach the next node and thus continuing the search. The traversal is finally terminated as it reaches or passes the root node.

3.3.3.3 Coarse grained potentials

For the simulation of interacting particles, it is necessary to calculate the pair-wise force at any integration step. Here we will mainly discuss the pair-wise interactions (bonded and non-bonded) used in our system, followed by interactions used to maintain stiffness and model rotation around a bond in a molecule. All of them can be calculated as the

gradient to the radially symmetric potential:

$$\vec{F} = -\vec{\nabla}\phi(r) \quad (3.2)$$

Weeks Chandler Anderson Force (WCA): The Lennard-Jones potential aims to model the interactions of noble gases like Helium, Neon, Argon etc. This pair potential was originally named after its creator Lennard-Jones after his landmark publications [154, 153]. The potential shows a strong repulsion at distances smaller than the diameter of the considered atoms and a small attractive region at larger distances. The WCA [313] interaction is similar to the Lennard-Jones interaction, but it is cutoff at a distance corresponding to the minimum of the potential and shifted such that the minimum lies at zero.

$$\begin{aligned} V_{WCA} &= 4\epsilon \left[\left(\frac{\sigma}{r}\right)^{12} - \alpha \left(\frac{\sigma}{r}\right)^6 \right] + \epsilon & r < (2/\alpha)^{1/6}\sigma \\ &= 0 & r \leq (2/\alpha)^{1/6}\sigma \end{aligned} \quad (3.3)$$

Here ϵ is the interaction strength, σ the diameter and α the strength for the attractive part.

Finite-Extensible-Nonlinear-Elastic: This represents a bonded potential, which can break at finite distance (R_0) between two particles [152, 311].

$$V_{FENE} = -0.5K R_0 \ln \left[1 - \left(\frac{r}{R_0}\right)^2 \right] \quad (3.4)$$

Here K represents the strength of the potential, R_0 the maximum possible extension of the bonds.

Other than these short ranged interactions, we make use of dihedral and angular potentials in our simulations which mainly impose certain constraints to the particles and to the bonded beads.

Dihedral Potential : A dihedral potential [198] characterizes the energy profile as a function of the dihedral angle (torsional angle) between four atoms, usually forming a sequence within a molecule. Dihedral potentials are used to study and model the conformational flexibility of molecules [75]. They help understand, how different conformations or rotational states of a molecule relate to its energy and stability. Although different variations of dihedral potential are available, the one we will be using in our work has the

following forms:

$$V_{\text{dihed}} = \frac{K_{\text{dihed}}}{2} \left[1 + d \cos(\phi - \phi_0) \right] \quad (3.5)$$

$$V_{\text{tors}} = K_{\text{tors}} \sin^2(\phi - \phi_{\text{ref}}) \quad (3.6)$$

Here K_{dihed} and K_{tors} represents the dihedral constant which controls the heights of these potential. Here d is a sign factor that can take the value 1 or -1 , ϕ_0 and ϕ_{ref} refers to the phase shift angle.

Angular Potential : The angular potential or valence angle potential [198] characterizes the energy associated with the bending or deformation of chemical bonds, such as bond angles within a molecule. They try to maintain the structural integrity of molecules. Here in our simulations we use the angular potential of the following form to maintain a structural integrity.

$$V_{\text{Bend}} = \frac{K_{\text{Bend}}}{2} (\theta - \theta_0)^2 \quad (3.7)$$

Here θ is the angle between two vectors (mostly consecutive in their arrangement) and θ_0 , the angle constraint set by the user to prevent bending of the molecules beyond a point. K_{stiff} is the strength of stiffness set by the user.

3.3.4 Rigid Molecules

Molecules are intricate structures made of atoms which interacts via inter-molecular or intra-molecular forces. Considering the entire molecule has a single coarse-grained bead would simplify the dynamics, however this would give us results which are far away from reality. Hence preserving the structure of a molecule is important. This led to the use of classical MD simulation techniques, where a molecule is represented as a collection of such beads linked together by bonds. However, classical techniques would require very small timesteps in order to capture features like bond-vibration of the molecule. These timesteps would lead to an unfeasible simulations routines. One possibility of preserving structure and having feasible simulation time would be to suppress the degrees of freedom that are unimportant, for example inter-molecular vibrations. Methods like RATTLE [14] and SHAKE [253] are typical iterative methods which could achieve this by adding constraints to the equations of motion. Although this is a standard way to model molecules with fixed

bond lengths and bending angles but flexible dihedral angles, rigid body dynamics [80, 218, 219, 196] is more suitable as it is computationally more efficient and handles constraints implicitly. Here we will focus on rigid-body dynamics, emphasizing quaternions over Euler angles for numerical applications.

3.3.4.1 Euler Angles and Quaternions

The motion of rigid bodies can be broken down into two entirely independent components: the translation of the center of mass and the rotation around the center of mass. Translation is governed by the net force acting upon an object, while rotation depends on the total torque [105, 9]. As such, we can study rotational dynamics separately.

The Euler angles are defined in terms of a sequence of rotations of a set of Cartesian coordinate axes about the origin [243]. Although many conventions exist for Euler angles, the one described here follows the Z-X'-Z'' (also known as the 3-1-3) convention. The z -axis first rotates through an angle ϕ , followed by a x -axis rotation of θ . A final rotation of ψ around the new z -axis then occurs. The complete rotation matrix \mathbf{R} results from multiplying the individual rotation matrices in the described order [105].

$$\mathbf{R} = \mathbf{R}(\psi)\mathbf{R}(\theta)\mathbf{R}(\phi) \quad (3.8)$$

So we can use the rotation matrix to express the components of vector \mathbf{r}' in the rotated coordinate system $\mathbf{r} = \mathbf{R}\mathbf{r}'$. Alternatively, we can start with \mathbf{r} and apply the opposite rotation in reverse order using the transpose of \mathbf{R} , resulting in the rotated vector $\mathbf{r}' = \mathbf{R}^T\mathbf{r}$.

Another useful method to describe rotation is in terms of quaternions, which can be expressed in terms of Euler angles as follows [116, 105, 243]:

$$\begin{aligned} q_1 &= \sin(\theta/2) \cos((\phi - \psi)/2) \\ q_2 &= \sin(\theta/2) \sin((\phi - \psi)/2) \\ q_3 &= \cos(\theta/2) \cos((\phi + \psi)/2) \\ q_4 &= \cos(\theta/2) \sin((\phi + \psi)/2) \end{aligned} \quad (3.9)$$

The components are normalized:

$$\sum_m q_m^2 = 1 \quad (3.10)$$

The inverse relations are [105, 242]:

$$\begin{aligned} \sin \theta &= 2\sqrt{(q_1^2 + q_2^2)(1 - q_1^2 - q_2^2)} \\ \cos \theta &= 1 - 2(q_1^2 + q_2^2) \\ \sin \phi &= 2(q_1 q_3 + q_2 q_4) / \sin \theta \\ \cos \phi &= 2(q_1 q_4 - q_2 q_3) / \sin \theta \\ \sin \psi &= 2(q_1 q_3 - q_2 q_4) / \sin \theta \\ \cos \psi &= 2(q_1 q_4 + q_2 q_3) / \sin \theta \end{aligned} \quad (3.11)$$

We get a singularity in this relation when $\theta = 0$ or π , i.e., when two of the axes coincide. To remove any ambiguity, we set $\psi = 0$ [105].

Another definition inspired by rotations around a fixed point is [9, 105]:

$$\mathbf{r}' = \mathbf{r} \cos \beta + (\mathbf{n} \cdot \mathbf{r})\mathbf{n}(1 - \cos \beta) + (\mathbf{n} \times \mathbf{r}) \sin \beta \quad (3.12)$$

where \mathbf{n} is a unit vector specifying the axis of rotation and β is the rotation angle. Thus we can define quaternion as a set of 4 scalar parameters based on the unit vector \mathbf{n} and rotation angle β as follows [22, 105, 116]:

$$q_m = \begin{cases} n_m \sin(\beta/2), & m = 1, 2, 3 \\ \cos(\beta/2), & m = 4 \end{cases} \quad (3.13)$$

Equation (3.12) can now be rewritten as:

$$\mathbf{r}' = (2q_4^2 - 1)\mathbf{r} + 2(\mathbf{q} \cdot \mathbf{r})\mathbf{q} + 2q_4\mathbf{q} \times \mathbf{r} \quad (3.14)$$

This leads to the rotation matrix having the form [11, 22, 105, 173, 34]:

$$\mathbf{R} = 2 \begin{pmatrix} q_1^2 + q_4^2 - \frac{1}{2} & q_1 q_2 + q_3 q_4 & q_1 q_3 - q_2 q_4 \\ q_1 q_2 - q_3 q_4 & q_2^2 + q_4^2 - \frac{1}{2} & q_2 q_3 + q_1 q_4 \\ q_1 q_3 + q_2 q_4 & q_2 q_3 - q_1 q_4 & q_3^2 + q_4^2 - \frac{1}{2} \end{pmatrix} \quad (3.15)$$

Quaternions can also be defined as the sum of a scalar and a vector, using complex number notation [105, 11]:

$$\tilde{q} = q_4 + i\mathbf{q} \quad (3.16)$$

The product of two quaternions is [22, 11, 173, 105]:

$$\tilde{q}\tilde{q}' = q_4q_4' - \mathbf{q} \cdot \mathbf{q}' + i(q_4\mathbf{q}' + \mathbf{q}q_4' + \mathbf{q} \times \mathbf{q}') \quad (3.17)$$

Rotation can be described by choosing a vector \mathbf{r} , defining two quaternions $\tilde{r} = 0 + i\mathbf{r}$ and $\tilde{r}' = 0 + i\mathbf{r}'$, and using the relation $\tilde{r}' = \tilde{q}\tilde{r}\tilde{q}^*$.

3.3.4.2 Equation of motion of rigid bodies - quaternion representation

Rigid-body dynamics involves two reference frames: a stationary space frame and a body frame aligned with the rotating body's principal axes [105, 243, 34]. The angular velocity (ω') in the body frame using Euler angles is [116, 105]:

$$\begin{pmatrix} \omega'_x \\ \omega'_y \\ \omega'_z \end{pmatrix} = \begin{pmatrix} \sin \theta \sin \phi & \cos \phi & 0 \\ \sin \theta \cos \phi & \sin \phi & 0 \\ \cos \theta & 0 & 1 \end{pmatrix} \begin{pmatrix} \dot{\phi} \\ \dot{\theta} \\ \dot{\psi} \end{pmatrix} \quad (3.18)$$

This matrix becomes singular when $\sin \theta = 0$. To avoid this issue, quaternions are used instead [105]:

$$\begin{pmatrix} \omega'_x \\ \omega'_y \\ \omega'_z \\ 0 \end{pmatrix} = 2\mathbf{W} \begin{pmatrix} \dot{q}_1 \\ \dot{q}_2 \\ \dot{q}_3 \\ \dot{q}_4 \end{pmatrix} \quad (3.19)$$

where,

$$\mathbf{W} = \begin{pmatrix} q_4 & q_3 & -q_2 & -q_1 \\ -q_3 & q_4 & q_1 & -q_2 \\ q_2 & -q_1 & q_4 & -q_3 \\ q_1 & q_2 & q_3 & q_4 \end{pmatrix} \quad (3.20)$$

Now in the space-fixed frame, the rate of change of angular momentum \mathbf{l} equals torque:

$$\tau = \frac{d\mathbf{l}}{dt} \quad (3.21)$$

Using the relation between time derivatives in space-fixed and body-fixed coordinates given below [116, 22, 243]

$$\left(\frac{d\mathbf{l}}{dt}\right)_{space} = \left(\frac{d\mathbf{l}}{dt}\right)_{body} + \boldsymbol{\omega} \times \mathbf{l} \quad (3.22)$$

we can express the body-fixed form as:

$$\tau_x = \dot{l}_x + \omega'_y l_z - \omega'_z l_y \quad (3.23)$$

In the body-fixed frame, $l_x = I_x \omega'_x$ (with I_x a component of the inertia tensor), so:

$$I_x \dot{\omega}'_x = \tau_x + (I_y - I_z) \omega'_y \omega'_z \quad (3.24)$$

Other components could also be similarly expressed.

These are the Euler equations describing the rotation of a rigid body. However we could express equation (3.24) in terms of quaternions alone [235, 242, 105, 22]. For this we use the quaternion acceleration Eq. (3.25) given below in matrix form combined with expression for $\boldsymbol{\omega}'$ given in Eq.(3.19).

$$\begin{pmatrix} \ddot{q}_1 \\ \ddot{q}_2 \\ \ddot{q}_3 \\ \ddot{q}_4 \end{pmatrix} = \frac{1}{2} \mathbf{W} \begin{pmatrix} \dot{w}'_x \\ \dot{w}'_y \\ \dot{w}'_z \\ -2 \sum \dot{q}_m^2 \end{pmatrix} \quad (3.25)$$

3.3.5 Integrating the equations of motion

Once the forces acting on each particle in the system are calculated in Molecular Dynamics, the next step is to integrate Newton's equations of motion numerically. Following points are considered when choosing an integrator for simulation [9]:

- **Efficiency and memory usage:**

- The integrator should be fast and have low memory requirements. While speed of an integrator is important, generally the time taken by an integrator to produce the consecutive position and velocities is less compared to the force calculation step in a MD simulation routine.

- **Allowance for a long integration timestep (Δt) :**
 - A good integrator should be able to take a long integration timestep. This is especially vital, because it would help save computational time, i.e., by employing larger time steps a given period of simulation time can be covered within a smaller number of integration steps [98].

- **Accuracy in following trajectories:**
 - An integrator should follow the exact trajectory as closely as possible [93]. Even the smallest perturbations and errors can be amplified exponentially in time and hence the computer generated trajectory would diverge from the classical trajectories produced through exact solutions [120]. As long as the integrator is producing states of the desired ensemble over long time periods, it is only important that the integrator closely replicate a specific trajectory only on time scales similar to the characteristic temporal correlations of the system.

- **Conservation Laws and Symplecticity:**
 - There are methods that exists for conservative Hamiltonian systems that preserves volume in phase space. These are termed "symplectic" methods and because of their phase space preservation property they tend to have certain invariants for the system [279]. Using a symplectic integration scheme would result in trajectories whose Hamiltonian would lie very close to the true Hamiltonian of the system, i.e., to say that the energy associated with that trajectory would be an order $O(\Delta t)^p$ away from initial value of the true Hamiltonian H [108, 120]. Here p refers to the order of the integrator. Thus unlike the non-symplectic approaches, these leads to favorable long-term performance like minor deviations around the initial value of H and absence of any consistent energy drift [85, 120].

Two of the commonly used integrator algorithm in MD simulation are the "Leap frog" and the "Velocity verlet" schemes, which will be discussed below.

3.3.5.1 Velocity Verlet and Leap-frog Integration Scheme

The **Velocity Verlet** integration scheme [302, 143, 295] is a fundamental numerical method used in molecular dynamics simulations to solve the equations of motion for

particles in a system. This algorithm is very well known for its accuracy and stability, making it a popular choice in computational chemistry and physics. This scheme updates the positions and velocities of particles in a two-step process. First, it advances the positions based on the current velocities and forces.

$$\vec{r}(t + \Delta t) = \vec{r}(t) + \vec{v}(t)\Delta t + \frac{\vec{f}(t)}{2m}(\Delta t)^2 \quad (3.26)$$

Then, it computes the velocity at half time step as in equation (3.27) and then uses this velocity and the forces from the new positions (calculated in equation (3.26)) to get the velocity at $t + \Delta t$ (see equation (3.28)).

$$\vec{v}(t + \Delta t/2) = \vec{v}(t) + \frac{\vec{f}(t)}{2m} \Delta t \quad (3.27)$$

$$\vec{v}(t + \Delta t) = \vec{v}(t + \Delta t/2) + \frac{\vec{f}(t + \Delta t)}{2m} \Delta t \quad (3.28)$$

Here \vec{x} , \vec{v} , \vec{f} are the position, velocity, and force respectively with Δt being the time step. Equation 3.28 and 3.27 can be combined in a single step to yield $v(t + \Delta t)$:

$$\vec{v}(t + \Delta t) = \vec{v}(t) + \frac{\vec{f}(t + \Delta t) + \vec{f}(t)}{2m} \Delta t \quad (3.29)$$

This symplectic integration method exhibits remarkable energy conservation properties, crucial for simulating the behavior of complex molecular systems over extended time periods. Its versatility and reliability have made the Velocity Verlet integration scheme an indispensable tool for researchers studying the dynamics and interactions of particles in various scientific disciplines.

The **Leapfrog** algorithm [120, 9] is fundamentally similar to the Velocity Verlet. Both Leapfrog and Velocity Verlet integrators yield trajectories that are equivalent. The difference lies in the time steps at which velocity calculations takes place. Here the calculation of velocities are not done at the same time steps as the positions are calculated. Instead, Leapfrog updates positions and velocities at interleaved time points, creating a staggered pattern resembling a "leapfrog" motion.

Velocity, position, and forces are calculated using the following algorithm:

- Use $v(t - \Delta t/2)$ and $f(t)$ to compute $v(t + \Delta t/2)$:

$$\vec{v}(t + \Delta t/2) = \vec{v}(t - \Delta t/2) + \frac{\vec{f}(t)}{m} \Delta t \quad (3.30)$$

- Use $r(t)$ and $v(t + \Delta t/2)$ to compute $r(t + \Delta t)$:

$$\vec{r}(t + \Delta t) = \vec{r}(t) + \vec{v}(t + \Delta t/2) \Delta t \quad (3.31)$$

3.3.6 Brownian Dynamics

Robert Brown in 1827 made the observation that the pollen grains submerged in water were under constant motion. The movement of these pollens were very random and it puzzled scientists of that time. This fascinating phenomenon, has been called Brownian motion ever since its discovery[306, 84, 178].

Our current understanding of the Brownian motion, is that it arises from unceasing collisions between the pollen particles and whatever surrounding fluid they happen to be in. Brown's first recognition of this incessant, irregular motion has since become a bedrock principle in physics and chemistry alike. The ever-changing environment of particles in a so-called solvent, as evidenced by Brownian motion, paints a vivid picture of molecular interactions and diffusion processes. Brown's important observation from over a century ago still impacts our understanding of the microscopic world and various scientific fields.

3.3.6.1 The Langevin Equations

The observation made by Brown is analytically written down as the Langevin Equations, which is a stochastic differential equation used to describe the motion of a particle in a viscous continuum. The equation is described as follows:

$$m \frac{d\vec{v}_i}{dt} = -\gamma \vec{v}_i + \vec{F}_{R_i} + \vec{F}_i \quad (3.32)$$

where m is the particle mass, \vec{v}_i is the velocity of particle i , $\gamma = 6\pi a\eta$ (for spherical particles) is the friction coefficient, η the viscosity, \vec{F}_{R_i} is a random force, and $\vec{F}_i = -\nabla U(\vec{r}_i)$ is the total direct force arising from, e.g., interactions between particle i and other particles.

The fundamental idea behind the Langevin equation is to implicitly model the solvent molecules which are in constant and random collision with the particles of interest. This

is done by introducing a stochastic force (represented by \vec{F}_{R_i}) and applying a frictional drag force to the solute particles. This implicit way of representing solvent particles decreases the computational cost of simulating our system since we do not have to deal with iterating through each of the solvent particles to calculate the forces. It also allows for the use of larger timesteps. This efficiency enables the study of phenomena occurring over more extended time periods.

3.3.6.2 Discretized Langevin equation

The Langevin integrator, integrates the particles based on the differential equation (3.32) which can be discretized based on the velocity verlet scheme. The magnitude of the random force is chosen via the fluctuation-dissipation theorem to be consistent with the specified drag and temperature, T . The stochastic random noise or random force has the following properties:

$$\langle \vec{F}_R \rangle = 0 \quad (3.33)$$

$$\langle F_{R_i}(t)F_{R_j}(t') \rangle = 2k_B T \gamma \delta(t - t') \delta_{ij} \quad (3.34)$$

where i and j refers to components of the vector. For integration purposes we can re-write equation (3.32) as follows, which can be used with the velocity Verlet scheme. Note that in equation (3.35) the stochastic term has been scaled by $1/\sqrt{\Delta t}$, where Δt is the time step. The rationale for this will not be explored here, as it falls outside the scope of this thesis. However this scaling is dimensionally correct since $\delta(t - t')$ has the dimension of time inverse.

$$\begin{aligned} \vec{F}^{\text{tot}}(t) &= \vec{F}(t) - \gamma \vec{v}_i + \sqrt{\frac{2k_B T \gamma}{\Delta t}} \vec{h}(t) \\ \langle \vec{h}(t) \rangle &= 0 \\ \langle h_i h_j(t) \rangle &= \delta_{ij} \end{aligned} \quad (3.35)$$

We can now easily generate this noise using a random number generator following Gaussian probability distribution. The discretized form for the translational part is as follows:

$$\begin{aligned}\vec{v}(t + \Delta t/2) &= \vec{v}(t) - \frac{\Delta t}{2} \left(\frac{\gamma}{m} \vec{v}(t) - \frac{\vec{F}(t)}{m} \right) + \frac{\hbar}{m} \sqrt{k_B T \gamma \Delta t} \\ \vec{r}(t + \Delta t) &= \vec{r}(t) + \vec{v}(t + \Delta t/2) \Delta t \\ \vec{v}(t + \Delta t) &= \vec{v}(t + \Delta t/2) - \frac{\Delta t}{2} \left(\frac{\gamma}{m} \vec{v}(t + \Delta t/2) - \frac{\vec{F}(t + \Delta t)}{m} \right) + \frac{\hbar}{m} \sqrt{k_B T \gamma \Delta t}\end{aligned}\tag{3.36}$$

The Langevin equation for the rotational degrees of freedom looks like the following:

$$I \frac{d\vec{L}}{dt} = -\gamma_r \cdot \vec{L} + \vec{\tau}_R + \vec{\tau}\tag{3.37}$$

Here I is the moment of inertia, $\vec{\tau}$ is the torque arising from all the interactions, $\vec{\tau}_R$ is the random torque term coming from the bath, \vec{L} is the angular momentum and γ_r is rotational drag. The random torque is again taken from the fluctuation dissipation theorem in-order to be consistent with the rotational drag and temperature T , giving the following correlations.

$$\langle \vec{\tau}_R \rangle = 0\tag{3.38}$$

$$\langle \tau_{R_i}(t) \tau_{R_j}(t') \rangle = 2k_B T \sqrt{\gamma_{r_i} \gamma_{r_j}} \delta(t - t') \delta_{ij}\tag{3.39}$$

Throughout equations (3.33) to (3.39), we use i or j to represent the different x, y or z components. For rigid bodies, the integration scheme follows what is described in [159]. However we won't discuss it any further here as it lies beyond the scope of this thesis.

3.4 Summary

In this chapter, we seek to provide an overview of essential methodologies and concepts related to computer simulations in our study. To begin, we introduce the HOOMD simulation package, offering insight into its brief history and evolving design. This establishes the context for delving into Molecular Dynamics simulations in depth. We start by outlining fundamental MD steps before describing commonly used barrier techniques and boundary conditions. The chapter then focuses on topics like force calculation and the ways to improve the order $O(N^2)$ method used to calculate them. This leads to the exploration of techniques like the Verlet list, cell list, and LBVH algorithms for expediting

force computations. Additionally, we mention several coarse-grained potentials applied in our simulations. Given the use of rigid bodies in our simulation protocol, we dedicate a subsection solely to rigid body dynamics. In this subsection we summarise the use of Euler angles and quaternions to represent the equation of motions of a rigid-body. Next, we briefly discuss the characteristics of a good integrator, followed by a discussion on common integrator schemes like this Velocity Verlet and Leapfrog methods. The chapter concludes by characterizing Brownian Dynamics and the Langevin equation, rounding up our comprehensive guide to simulation techniques used in our research.

Chapter 4

Structure and Dynamic Evolution of Interfaces between Polymer Solutions and Gels and Polymer Interdiffusion: A Molecular Dynamics Study

Note: This chapter reproduces the reference [303], with some additional explanations. Additional explanations or details are marked with light purple color. If the text or parts of the text are omitted, this has been marked as [...].

Contributions :

- **Simulation setup and execution :** I was responsible for initialization of the regular network and modeling of the diffusive interpenetration and the subsequent study.
- **Data analysis:** I wrote the analysis code and analyzed all the results presented here.
- **Figures :** I contributed to the plotting of all the figures, ensuring they clearly communicate the key findings.
- **Manuscript preparation :** I contributed to the writing of the original draft of the manuscript and revising it according to the feedback from supervisor.

Reprint Permission : "Reprinted (adapted) with permission from Jude Ann Vishnu, Torsten Gereon Linder, Sebastian Seiffert, and Friederike Schmid; Structure and Dynamic Evolution of Interfaces between Polymer Solutions and Gels and Polymer Interdiffusion: A Molecular Dynamics Study. *Macromolecules* 2024 57 (11), 5545-5559. DOI: 10.1021/acs.macromol.4c00459". Copyright 2024 American Chemical Society.

4.1 Introduction

Hydrogels are three-dimensional macromolecular networks, which are able to hold a large amount of water [294]. In recent years, stimuli-responsive hydrogels (smart gels) are attracting increasing interest, especially due to their large potential in biomedical applications [55, 239, 156, 56, 330, 325]. Such hydrogels respond to external stimuli (changes in pH, ionic strength, temperature, solvent composition) by changing their properties like swelling ratio and elastic modulus. One particularly attractive feature of smart polymers is reversibility: induced changes can very often be reversed by simply removing the environmental trigger that caused the response [136, 294]. The high sensitivity of hydrogels to small stimuli makes them appealing for a variety of applications, e.g., enhanced oil recovery and bio-processing industries, biomimetic actuators, chemical valves and thermoresponsive surfaces [227, 107, 238].

The responsive properties of hydrogels in the bulk and at surfaces are typically coupled to each other. For example, one of the most commonly studied thermo-sensitive polymers is poly(*N*-isopropylacrylamide) (pNIPAAm). pNIPAAm hydrogels in water undergo a volume phase transition from a swollen to a collapsed state if the temperature is increased above 34.3 °C [299, 2, 138]. Such swelling-deswelling transitions are accompanied by a change in both gel elasticity [236, 131, 123] and microgel interaction potential [320]. Although the simultaneous change of these properties can be useful for some applications [262, 86], it would often be desirable – e.g., in applications such as switchable cell substrates – if one could manipulate the gel’s elasticity without affecting its hydrophilicity [126]. As a strategy to overcome this problem, [...] [Sebastian Seiffert and co-workers have developed](#) core-shell microgels with a thermo-responsive core and non-thermosensitive shell [270][...] [and have thus shown](#) that it is possible, using droplet-based microfluidics, to fabricate core-shell microgels with sizes in the range of 60-100 μm that have a pNIPAAm core and a (thermo-insensitive) polyacrylamide (pAAm) shell. This was achieved by wrapping a pre-synthesized pNIPAAm core by a droplet of semidilute photo-crosslinkable pAAm solution, and later crosslinking the droplet by UV exposure. The properties of the resulting particles depend crucially on the connection between the core and the gel, which is in turn determined by the structure of the interface between the polymer solution and the gel at the time of crosslinking.

From a theory point of view, interfaces between polymer gels and solutions are unusual and fascinating because they combine aspects of liquid-liquid interfaces and elasticity. Computer simulations can give molecular insights into the structure of such interfaces

and the mechanisms of solvent diffusion into the gel. While there have been numerous theoretical [37, 54, 284, 215, 187] and simulation studies on polymer gels [283, 90, 91, 248, 190, 35, 323, 39, 280, 106, 264, 13, 202, 298], as well as computer models simulating various reaction methods to create micro-gels [327, 182, 112, 249, 213, 113], comparatively few studies have been dedicated to gel-liquid interfaces [88, 45, 46, 124]. At the same time, we are not aware of any work on interfaces between polymer networks and polymer solutions.

In this [.] study, we set out to close this gap. We use coarse-grained molecular dynamics simulations based on the Kremer-Grest model [167, 92] to study interfaces between a regular polymer network with diamond network topology[87] and semidilute polymer solutions with varying polymer concentrations. This choice of network topology was motivated by our experimental work mentioned above [270], where the core gel was synthesized by free radical polymerization[71] involving tetrafunctional crosslinkers (N,N' -methylenebisacrylamide). Although in free radical polymerization, it is very unlikely for all the 4 functional groups of the cross-linker to react to form chains or attach to chains, here we will discuss an idealized scenario. Hence our network will lack defects such as loops and uneven strand-length. Our model network could also represent tetra-PEG gels[275, 312], which consist of symmetrical tetrahedron-like (four-arm) PEG networks with excellent physical properties that are attributed to a high homogeneity of the network [289, 205, 147, 214, 308, 172, 244, 26, 180]. To study possible effects of elastic strain, we compare two cases: slabs of isotropic gels and slabs of anisotropic gels which have been deformed with a ratio very close to 2:1 in lateral direction.

The [...] chapter is organized as follows: in section 4.2 we introduce our simulation model, specify the interaction potentials, and describe the setup and the preparation of initial configurations. The results are presented in section 4.3. We first characterize the time evolution of the system after the gel and the solution has been brought into contact, discuss the percolation transition of free chains inside the gel, and then analyze the final equilibrated interface including the capillary wave fluctuations. We summarize and conclude in Section 4.4.

4.2 Model and Simulation Details

We consider solutions of n_l linear polymers of length $N_l = 102$ beads, which are brought in contact with a polymer gel, using a simple spring-bead model for polymers in implicit good solvent [167]. The gel is modeled as a regular polymer network with diamond

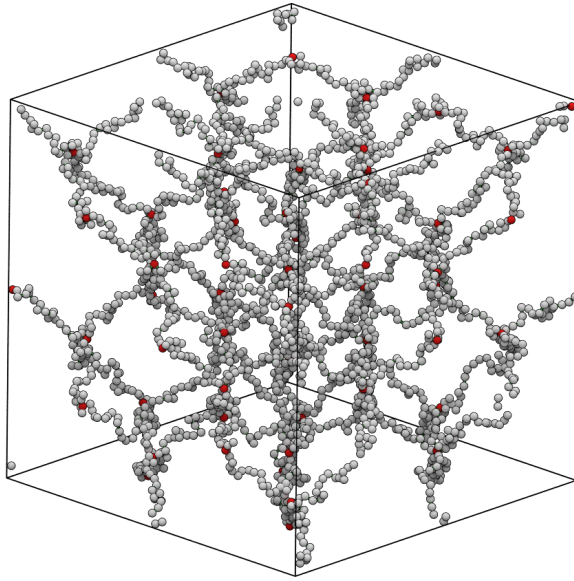


FIGURE 4.1: Example of a regular bulk diamond network structure, constructed as described in the main text and not yet relaxed by a NPT simulation. The red beads indicate the cross-linking units, regular beads are gray. The network shown here is crosslinked across periodic boundary conditions in all directions and is smaller than that used in our simulation.

network topology (see illustration in Figure 4.1) and consists of $n_s = 4464$ strands of length $N_s = 102$ beads that are connected by $n_c = 2304$ crosslinking beads in total. For simplicity, all beads ("monomers") are taken to be the same. They interact with purely repulsive Weeks-Chandler-Anderson (WCA) interactions[313] (Equation (4.1)). In addition, a Finite Extensible Nonlinear Elastic (FENE) potential connects beads that are linked to each other[152] (Equation (4.2)). The corresponding potentials are defined as

$$V_{\text{WCA}}(r) = \begin{cases} 4\epsilon \left[\left(\frac{\sigma}{r}\right)^{12} - \alpha \left(\frac{\sigma}{r}\right)^6 + \frac{\alpha^2}{4} \right] : & r < \left(\frac{2}{\alpha}\right)^{1/6} \\ 0 & \text{otherwise} \end{cases} \quad (4.1)$$

$$V_{\text{FENE}} = -\frac{k R_0^2}{2} \ln \left(1 - \left(\frac{r}{R_0}\right)^2 \right) \quad (4.2)$$

In the following, we will give all quantities in units of σ (length), ϵ (energy), and m (monomer mass). The basic unit of time is $\tau = \sqrt{m\sigma^2/\epsilon}$. The interaction strength for FENE bonds is set to $k = 30\epsilon/\sigma^2$ and the maximum extensibility of the bond to $R_0 = 1.5\sigma$. The parameter α in the WCA potential is chosen as $\alpha = 1$ for beads connected by FENE bonds and $\alpha = 2$ for all other pairs of beads.

Initial configurations for the simulations are prepared as follows: to construct the polymer network, n_c cross-linking beads are first placed in the form of a diamond lattice [...]. The diamond structure can be viewed as two interpenetrating face-centered cubic (FCC) lattices, where one lattice is shifted along the body diagonal of the unit cell by one-quarter of the length of the diagonal. Each atom in the diamond lattice has four nearest neighbors. Each of the n_c cross-linkers are then connected to each other via polymer strands. An example of the resulting small bulk gel structure is shown in Figure 4.1. To set up gel slabs, the network is cross-linked across the periodic boundaries in y and z direction, but not in the x direction (different from Figure 4.1). Then, to relax the strands, the system is simulated at constant pressure $P = 0.001\epsilon/\sigma^3$ over a time of $8 \times 10^3\tau$ using Martyna-Tobias-Klein integrator [192]. After the relaxation step, the linear dimensions of the simulation box are $L_x = (232.0 \pm 0.3)\sigma$, $L_y = L_z = (174.1 \pm 0.2)\sigma$. Next the simulation box is extended in the x direction on both sides of the gel slab up to a total length of $L_x = 697\sigma$. To create anisotropic gels, we then apply an affine deformation involving compression along the z direction and extension along the y direction over a time period of $10^3\tau$, and obtain a resized box with linear dimensions $L_z = 102\sigma$ and $L_y = 201\sigma$. This deformation step is omitted when preparing isotropic gel slabs. We note that the cross-sectional area of anisotropic gels is a bit lower than that of isotropic gels ($A = L_y \times L_z \sim 2 \times 10^4\sigma^2$ as opposed to $A \sim 3 \times 10^4\sigma^2$), which has a slight influence on some of the results.

[...] The final preparation step involves filling the empty spaces in the extended box with a free polymer solution. To do this, we place n_l fully stretched linear polymer chains along the z direction, so they occupy as much space as possible. The number n_l depends on the concentration of the polymer solution. Next, we insert temporary hard walls between the gel and solution regions and run NVT simulations of the solution at a temperature $k_B T = \epsilon$ for 160τ to allow the free chains to equilibrate. The hard walls interact with the polymer beads using WCA interactions (4.1) with a size parameter $\sigma_{\text{wall}} = 0.1\sigma$ and $\alpha = 1$. After the system has equilibrated, we remove the temporary walls and start the main simulation, where the free polymers chains from the solution are allowed to diffuse into the network.

The diffusion simulations (see Figure 4.2) were done in the NVT ensemble at temperature $k_B T = \epsilon$ using a Langevin thermostat. Typical total simulations times were $1.28 \times 10^6\tau$, with time step $\Delta t = 0.001\tau$. Quantities are averaged over ten independent runs for anisotropic gels and three independent runs for isotropic gels, starting from independently generated initial configurations. All simulations were performed using HOOMD

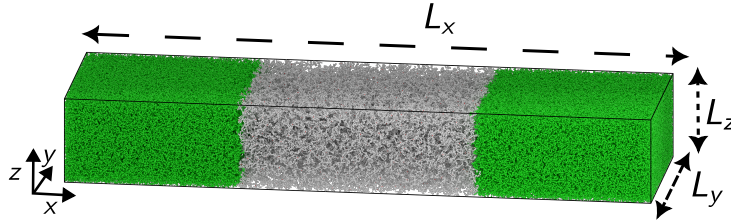


FIGURE 4.2: Setup of diffusive interpenetration study: A gel slab (gray) is sandwiched by free polymer chains (green) on either sides of it. The free chains permeate into the slab over time. The above snapshot is taken at 800τ at $\rho_{sol_f} = 0.168\sigma^{-3}$. The gel is anisotropic.

simulation package version 2.9.6 [17] and the simulation snapshots were produced using the fresnel package [1].

For future reference, we briefly characterize the main properties of the free polymers in our system. The squared radius of gyration of single polymers in dilute solution is $\langle R_g^2 \rangle = (53.3 \pm 0.7)\sigma^2$, and their diffusion constant is $D = (0.010 \pm 0.004)\sigma^2/\tau$. From these two values, one can estimate the characteristic chain relaxation time, i.e., the time it takes the polymer to diffuse over the distance of its own gyration radius, $\tau_d = \langle R_g^2 \rangle / D = 5.3 \times 10^3\tau$. Below, we usually present data in terms of rescaled times t/τ_d . From R_g , we can also estimate the overlap concentration ρ^* , i.e., the concentration where chains start to have significant contact with each other, via [77] $\rho^* \approx N_l / \frac{4}{3}\pi R_g^3 \sim 0.06\sigma^{-3}$. Figure A.1 in Appendix A demonstrates that this value indeed marks the crossover between the dilute and the semidilute regime. Alternatively, the overlap parameter can also be estimated from the equation of state of the free polymer solution, i.e., the relation between pressure and density. Fitting this relation to the theoretical expression [252] gives $\rho^* \sim 0.024\sigma^{-3}$, which is of the same order (see Figure A.2 in Appendix A).

4.3 Results

The behavior at interfaces is found to be very similar for isotropic and anisotropic gels. Therefore, with few exceptions, we will mostly present the data for anisotropic gels here; additional complementary data for the isotropic gel can be found in the Appendix A. We first characterize the evolution of the systems after bringing the gel and the solution into contact, and then analyze the properties of the final interface.

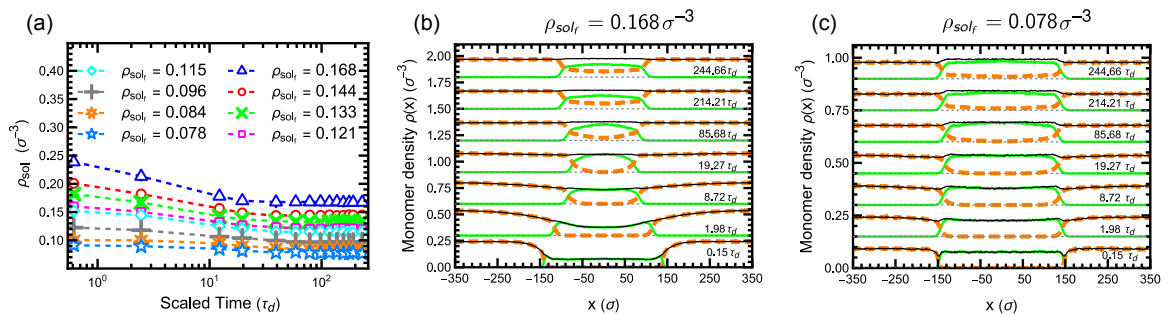


FIGURE 4.3: (a) Monomer density in the solution phase versus rescaled time t/τ_d for different final concentrations ρ_{sol_f} (in units of σ^{-3}) as indicated. (b,c): Monomer density profiles across the slab for free polymers (dashed orange), gel strands (solid green), and total (solid black) at different times as indicated for $\rho_{sol_f} = 0.168\sigma^{-3}$ (b) and $\rho_{sol_f} = 0.078\sigma^{-3}$ (c). Profiles corresponding to subsequent times are shifted upwards by $0.3\sigma^{-3}$ in (b) and $0.15\sigma^{-3}$ in (c). Thin dashed lines show corresponding baselines ($\rho = 0$). The gel is anisotropic. See Figure A.4 in the Appendix A for corresponding results for the isotropic gel.

4.3.1 Dynamic Evolution of Gel-Solution Interfaces

4.3.1.1 Monomer Density Profiles

After the gel and the polymer solution are brought into contact, polymers diffuse into the gel phase, which somewhat reduces the amount of polymers in the solution phase (see Figure 4.3a). In our simulations, the gel and the solution initially occupy similar volumes, and reductions of up to $2/3$ are observed at the highest concentrations. This could be similar in experimental microfluidics settings if the droplet that serves as precursor of the shell has a similar volume than the pre-synthesized core. In the following, we characterize solutions with different concentrations in terms of the final polymer density in solution phase ρ_{sol_f} , as calculated at the end of the simulation.

Figure 4.3b,c shows monomer density profiles for the gel and the free polymers along the direction perpendicular to the slab (the x -direction) for two choices of polymer concentration in the solution. Initially, the polymer solution compresses the gel slab along the x direction. The compression is caused by the osmotic pressure of the free polymers and is, hence, more pronounced for higher polymer concentrations. At the same time, polymers start to diffuse from the solution into the gel, and the gel swells. Both effects counteract each other, and eventually, once sufficiently many polymers have entered the gel region, the size of the gel increases again. However, the width of the gel slab remains smaller than the original width, due to the fact that the solvent quality of the polymer solution

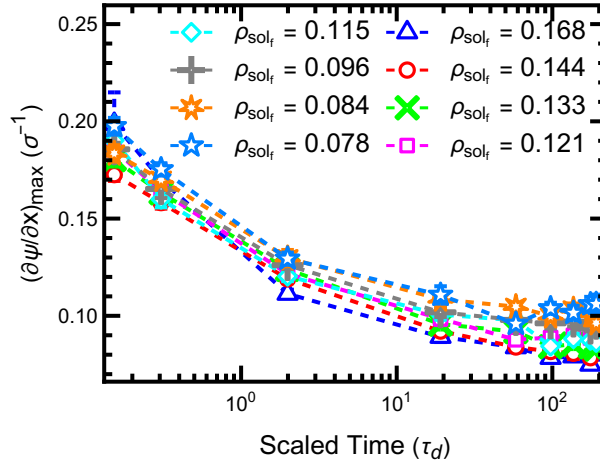


FIGURE 4.4: Maximum gradient of the rescaled monomer density difference profiles $\psi(x)$ at the interface (see Equation (4.3)) vs. rescaled time t/τ_d (orange lines in Fig. 4.3) for solutions with different concentrations ρ_{sol_f} as indicated. The gel is anisotropic.

is lower than that of pure (implicit) solvent. The interdiffusion leads to a broadening of the interface between the gel and the solution. This is demonstrated in Figure 4.4, which shows the value of the maximum slope of the rescaled difference ψ between the densities of monomers in free polymers ($\rho_l(x)$) and in strands ($\rho_s(x)$),

$$\psi(x) = \frac{\rho_l(x) - \rho_s(x)}{\rho_l(x) + \rho_s(x)} \quad (4.3)$$

It decreases and eventually saturates at times around $t \sim 100\tau_d$. We should note that the absolute values of the slopes, as reported in Figure 4.4, should not be taken literally because they are affected by capillary wave fluctuations and hence depend on the lateral system size. We will analyze this in more detail further below in Section 4.3.2.2.

In the concentrated regime, the profile of the final total monomer concentration is roughly constant across the whole system (Figure 4.3b, top profile). At lower concentrations close to the dilute regime, the final total monomer concentration in the gel is slightly higher than in the solution (Figure 4.3c, top profile), even if it is initially lower. This can be explained by the fact that free polymers gain translational entropy if they enter the gel.

The monomer densities at the center of the gel are shown as a function of rescaled time for different concentrations ρ_{sol_f} in Figure 4.5, separately for monomers belonging to free polymers (a), monomers belonging to the network (b), and all monomers (c). The figure reveals that none of the systems are fully equilibrated as a whole at the end of

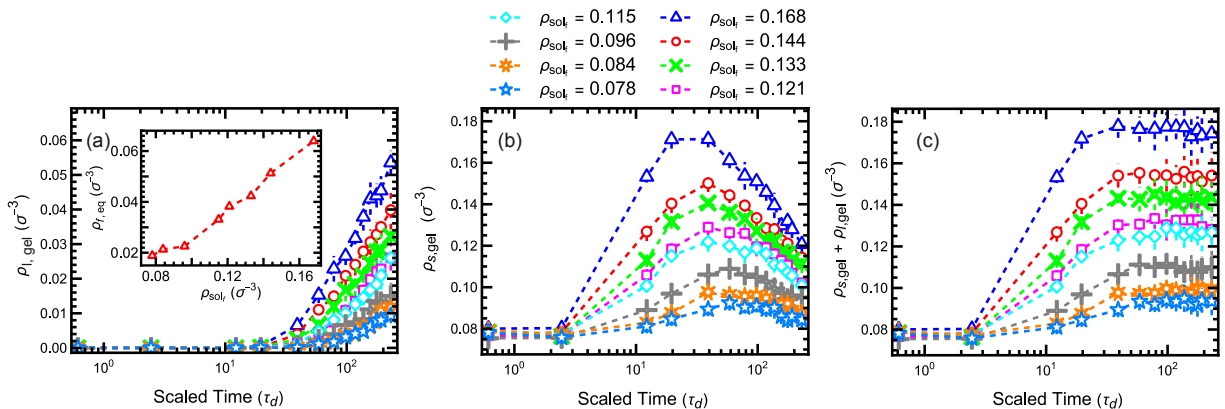


FIGURE 4.5: Monomer densities at the center of the gel slab versus rescaled time t/τ_d for (a) monomers belonging to free polymers, (b) gel monomers, and (c) all monomers, for different final concentrations in the outer solution ρ_{sol_f} (in units of σ^{-3}) as indicated. Inset in (a) shows equilibrium density of monomers belonging to free polymers inside the slab vs. ρ_{sol_f} , as extracted from a fit of the data in (a) to Eq. (4.4). The gel is anisotropic.

the simulation: the monomer density of free chains increases roughly logarithmically at late times, indicating that free polymers continue to diffuse into the gel. This logarithmic increase is compatible with the behavior expected from the solution of the one dimensional diffusion equation inside the gel with Dirichlet boundary conditions (see Section A.3 in Appendix A),

$$\frac{\rho_f(0, t)}{\rho_{f, \text{eq}}} \approx \frac{1}{2} \left[\tanh \left(\ln \left(\frac{Dt}{d^2} \right) + 2.357 \right) + 1 \right], \quad (4.4)$$

where d is the thickness of the gel slab and D the diffusion constant of free polymers. Fitting the data of Figure 4.5a to the approximate expression ((4.4)), we can estimate the final density $\rho_{f, \text{eq}}$ of monomers from free polymers in the final equilibrated state. The results are shown in the inset of Figure 4.5a.

The density of gel monomers (Figure 4.5b) first increases due to the initial compression the gel, and then decreases again as soon as the free polymers start moving in. Interestingly, the total density at the center of the gel saturates at a roughly constant value at times around $40 - 80\tau_d$. The predominant factor setting the overall density within the gel is the osmotic pressure exerted by the surrounding polymer solution on the polymer/gel interface. It depends on the densities of free polymers in the vicinity of the interface. Our findings thus suggest that the interface equilibrates much faster than the entire gel, and that it will be possible to analyze the local properties of interfaces.

4.3.1.2 Connection between gel and solution

Next, we characterize the interpenetration between free polymers and gel strands, which determines the strength of the connection between the two phases after cross-linking. As one measure of interpenetration, we evaluate the "Degree of Interfacial Integration" (DII), which has been introduced by Shi et al. [274] in studies of multilayer polymer films. It is defined as

$$\text{DII} = I/I_{\max} \quad \text{with} \quad I = [\dots] \langle d_p \rangle \cdot \langle S \rangle \quad (4.5)$$

and

$$S = \frac{n_{l_i}}{A}, \quad [\dots] d_p = \min \left(\sum_{j:x_j < 0} |x_j|, \sum_{j:x_j > 0} x_j \right). \quad (4.6)$$

here $A = L_y \cdot L_z$ is the area of the interface and n_{l_i} is the number of free polymers crossing the interface. The quantity $[\dots] d_p$ is evaluated for each of these polymers separately. The sum j runs over all monomers and x_j is the x -position of the monomer with respect to the position of the interface. Hence, S characterizes the areal density of free polymers stitching through the interface, and the "depth" of the stitch, $[\dots] d_p$, is largest if the polymer is fully stretched perpendicular to the interface with half of its monomers being on one side and the other half on the other side. The quantity DII is defined as the ratio of I and its maximal possible value I_{\max} for given polymer concentration ρ_{sol_f} in solution, i.e., $I_{\max} = [\dots] d_{p, \max} \times S_{\max}$ with

$$S_{\max} = \rho_{\text{sol}_f} r_0, \quad d_{p, \max} = r_0 N_l (N_l + 2) / 8, \quad (4.7)$$

where $r_0 = 0.97\sigma$ is the equilibrium bond length. This maximum value is reached in the very hypothetical case in which all free chains are fully stretched and oriented perpendicular to the surface. To get an estimate of a realistic range of I , we can also estimate the value of I for randomly distributed Gaussian coils with gyration radius $R_g^2 = r_0^2 N_l / 6$. In the x direction, the monomers of such a coil with the center of mass at x_{cm} are distributed according to [...]:

$$P(x) = \begin{cases} \mathcal{N}_c \exp(-3(x - x_{cm})^2 / 2R_g^2) & : |x - x_{cm}| < R_c \\ 0 & : |x - x_{cm}| \geq R_c \end{cases} \quad (4.8)$$

where R_c is the hypothetical cutoff for the maximum value of $|x - x_{cm}|$ and \mathcal{N}_c is the normalization factor. The normalization factor can be found by intergrating Equation 4.8 from $-R_c$ to R_c and equating to one. We can now easily obtain $\langle S_{\text{Gauss}} \rangle$ and $\langle d_{p, \text{Gauss}} \rangle$ using the general definition in Equation 4.6 and with the help of Equation 4.8

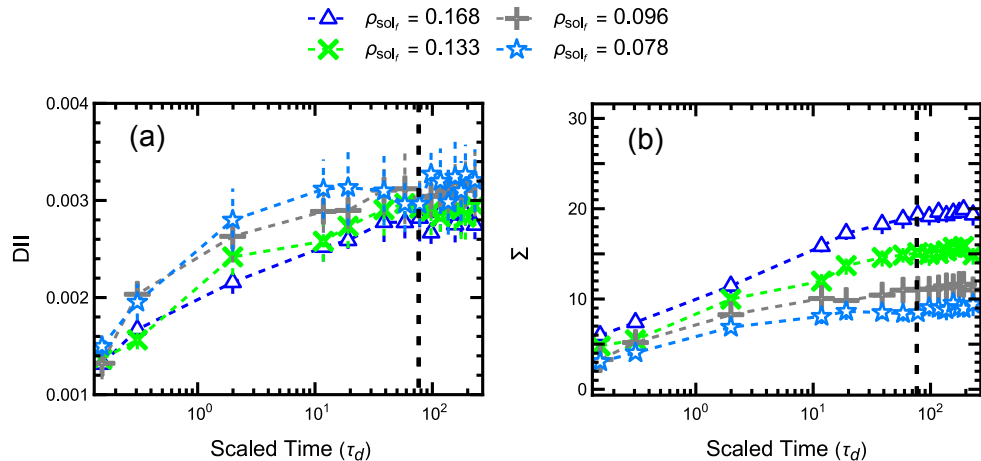


FIGURE 4.6: (a) DII vs scaled time t/τ_d for various concentrations ρ_{sol_f} . (b) Scaled areal density Σ of free chain monomers with connection to the interface vs scaled time t/τ_d . Dashed line indicates time after which Σ saturates. The gel is anisotropic.

$$\begin{aligned} \langle S_{\text{Gauss}} \rangle &= \frac{1}{A} \int_{-R_c}^{R_c} A \, dx \, \rho_{\text{poly}} = \frac{\rho_{sol_f}}{N_l} 2R_c, \\ \langle d_{p, \text{Gauss}} \rangle &= N_l \frac{1}{12} \frac{R_g^2}{R_c}, \end{aligned} \quad (4.9)$$

in the limit of large R_c ($R_c \gg 10R_g$). The DII for such a solution of non-interacting Gaussian coils would thus be given by

$$\text{DII}_{\text{Gauss}} = \frac{I_{\text{coil}}}{I_{\text{max}}} = \frac{2}{9} \frac{1}{N_l + 2} \approx 0.0024 \quad (4.10)$$

for chains of length $N_l = 102$.

The evolution of the DII with time in our system is shown in Figure 4.6a for anisotropic gels and 4.7a for isotropic gels. The behaviors in both cases is very similar. It increases and then saturates at a value around $\text{DII}=0.003$, which is slightly higher than the hypothetical value for randomly distributed Gaussian coils. Initially, the DII rises more rapidly if the solution is less concentrated, but the final value is independent of ρ_{sol_f} within the error. We should note that the absolute number of "stitches" of course increases with ρ_{sol_f} , therefore the figure also tells us that the strength of the connection between the two phases increases with increasing polymer concentration in the solution.

As a second measure to characterize the interface, we define the quantity Σ

$$\Sigma = \langle N_{li, \text{gel}} \rangle \cdot \langle S \rangle \langle R_g^2 \rangle, \quad (4.11)$$

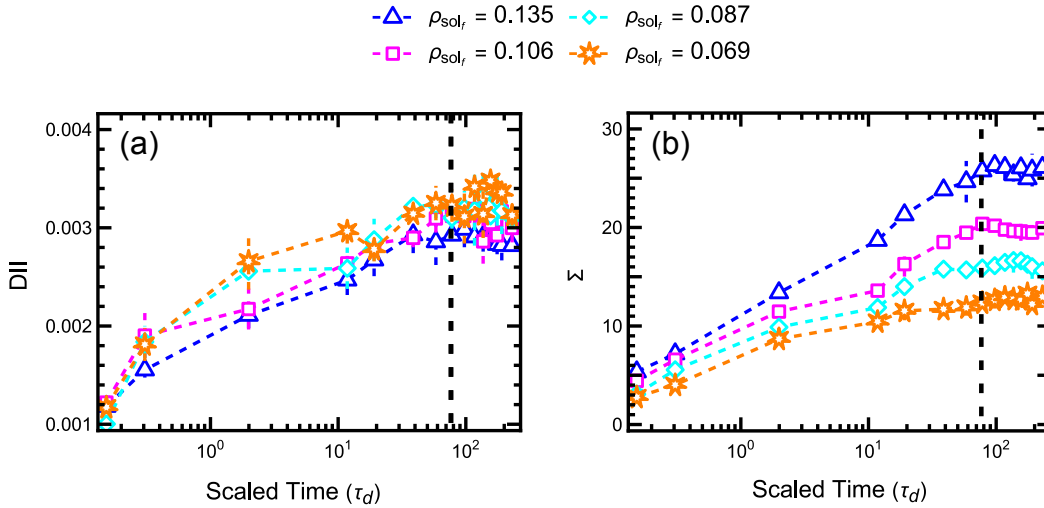


FIGURE 4.7: Same as Figure (4.6) for the isotropic gel.

where $\langle N_{li,gel} \rangle$ counts the number of monomers of a free polymer inside the gel, averaged over all polymers that cross the interface and $\langle R_g^2 \rangle$ is the mean squared radius of gyration of a chain in a dilute solution. Σ can be seen as number of monomers inside the gel within a lateral area R_g^2 that have some connection to the solution phase. This quantity is shown as a function of time in Figures 4.6b and 4.7b. It rises initially in a roughly logarithmic fashion (linear in a log-linear representation) and then levels off. Comparing Figure 4.6 with Figure 4.4, we notice that both, the DII and Σ , saturate at about the same time as the local monomer density profiles. The saturation time can be as long as $t_{sat} \sim 100\tau_d$. At late times beyond t_{sat} , the local density profiles and the local connectivity structure at the interface no longer change. We infer that for times $t > t_{sat}$, the interfaces can be considered to be at local equilibrium, even though polymers keep diffusing into the gel according to Figure 4.5.

We conclude that the best strategy to fabricate core-shell particles with given (pre-determined) connection between core and shell, using the droplet-based method sketched in the introduction, is to adjust the concentration of polymers in the solution. Unfortunately, this will likely also affect the structure of the shell network after irradiation, e.g., the density of crosslinking points. An alternative strategy is to adjust the time of crosslinking. Weak connectivities can be achieved by crosslinking shortly after the first polymer-core contact, and stronger connectivities will result if the crosslinking time is chosen in the long-time limit.

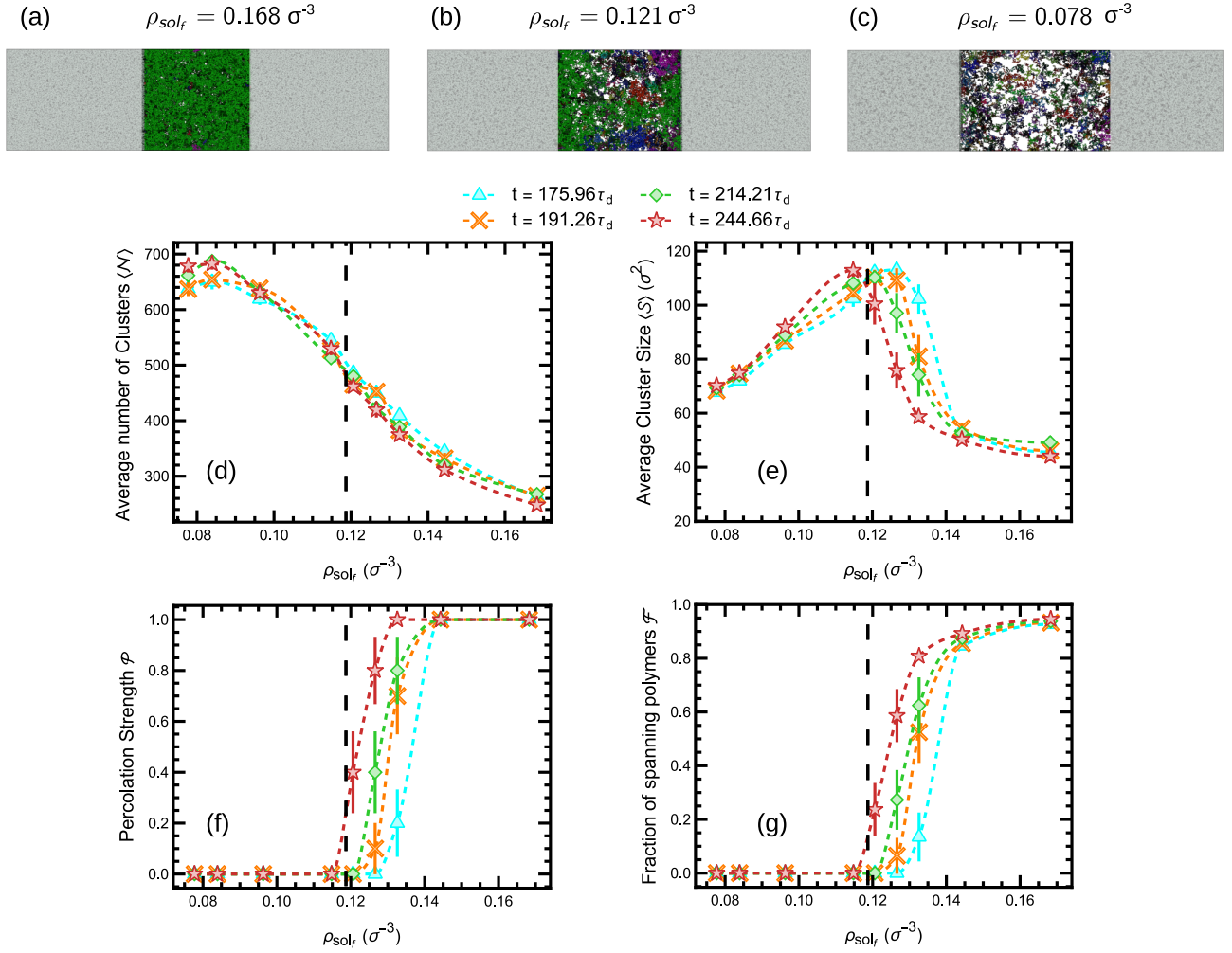


FIGURE 4.8: (a-c) Cluster formation of free chains within the gel region as viewed from top of the box (along z -axis) at different final polymer densities (ρ_{sol_f}) as indicated. Different clusters are colored differently in order to be distinguishable. The light gray color indicates solution region. (d-e) Characteristics of cluster distributions vs. (ρ_{sol_f}) at different times as indicated: (d) Average number of clusters; (e) Average cluster size (mean squared radius of gyration) of finite clusters; (f) Percolation strength (see text); (g) Fraction of free polymers inside gel that are part of the spanning cluster. The gel is anisotropic.

4.3.1.3 Percolation of free chains inside the gel

If the concentration of polymers in solution is sufficiently high, then one notices that the free polymers in the gel start to come in contact with each other and form clusters. Figure 4.8a-c shows examples of final configuration snapshots for different concentrations ρ_{sol_f} . Only the free polymer chains are shown; the gel region is singled out, and inside this region, chains belonging to different clusters are colored differently. Here, chains are

taken to belong to the same clusters if at least two monomers from different chains have a distance less than 2σ . The cluster analysis was performed using the freud-analysis package [241]. At low concentration ($\rho_{\text{sol}_f} = 0.078\sigma^{-3}$), some clusters form, but they are isolated. At higher concentration ($\rho_{\text{sol}_f} = 0.121\sigma^{-3}$), a spanning cluster emerges that connects both sides of the slab. [...] Further increase in ρ_{sol_f} leads to spanning clusters that contains almost all the free polymer chains within the gel region.

These findings suggest the existence of a percolation transition at some threshold density $\rho_{\text{sol}_f}^c$. The percolation transition is a well-known geometric transition [189, 276, 175, 217, 72, 332, 331] associated with critical exponents and universal power laws, which can be extracted, e.g., by performing a finite size analysis. Unfortunately, carrying out such an analysis is not possible for our system, because even the final configurations are not yet fully equilibrated as discussed earlier. Nevertheless, we can discuss typical aspects of percolation and monitor the onset of percolation with time.

Figure 4.8d-g shows a selection of quantities that characterize the distributions of clusters of free chains in the gel for different times, and as a function of the polymer concentration in solution, ρ_{sol_f} . The first quantity, shown in Figure 4.8d, is the average number of independent clusters $\langle \mathcal{N} \rangle$. The graph confirms the discussion above. At lower concentrations, the gel contains many scattered small clusters, which are not connected to each other. With increasing concentration, clusters start to merge and the total number of clusters decreases. The quantity $\langle \mathcal{N} \rangle$ decreases smoothly as a function of ρ_{sol_f} and shows no signature of a transition.

Next we plot the average cluster size $\langle \mathcal{S} \rangle$ of finite clusters as a function of ρ_{sol_f} in Figure 4.8e. Finite clusters are the ones which are not part of a spanning cluster. At lower concentrations, several isolated finite clusters coexist, and therefore, the average size ($\langle \mathcal{S} \rangle$) of the clusters is small. With increasing ρ_{sol_f} , clusters merge and grow in size, as can also be seen in the snapshots, Figure 4.8a,b. Above the percolation threshold, more and more larger clusters merge with the spanning cluster. The remaining clusters are small, hence $\langle \mathcal{S} \rangle$ decreases beyond the threshold concentration.

Figure 4.8f shows the so-called percolation strength $\mathcal{P} = \langle \chi \rangle$, where $\chi = 1$ if a configuration contains a spanning cluster, and $\chi = 0$ otherwise. The curves for \mathcal{P} versus ρ_{sol_f} strongly suggest the existence of a percolation transition, i.e., a jump from $\mathcal{P} = 0$ to $\mathcal{P} = 1$ at $\rho_{\text{sol}_f}^c \sim 0.12\sigma^{-3}$. The jump is smoothed out due to the finite size of the system. The onset of percolation, i.e., the concentration ρ_{sol_f} where percolation is observed, decreases with increasing time. This can be explained if we assume that percolation is only possible once the concentration of free chains inside the gel exceeds a certain value. Comparing

Figure 4.8e with Figure 4.5, we can estimate the threshold concentration inside the gel, $\rho_{i,\text{gel}}^c$, where percolation sets in. The data suggest $\rho_{i,\text{gel}}^c \sim 0.03\sigma^{-3}$, which is of the same order as the overlap concentration ρ^* . This seems low, but not unreasonable. Experiments have shown that the sol-gel transition in solutions of crosslinkable polymers – a transition similar to percolation – may set in at polymer concentrations as low $\rho^*/6$ [257].

Finally, we consider the fraction of free polymers in the gel that belong to the spanning cluster, \mathcal{F} . This quantity would typically be used as an order parameter for the transition. It is shown as a function of ρ_{sol_f} in Figure 4.8g. The curves show that \mathcal{F} increases beyond the transition, but less sharply than \mathcal{P} , indicating that the transition might be continuous in the limit of infinite systems.

In this section, we only show the data for anisotropic gels; the corresponding data for isotropic gels can be found in Appendix A, Section A.2.2. They are qualitatively similar, but percolation sets in at lower concentrations ρ_{sol_f} than in the anisotropic gel. We attribute this to the fact that our isotropic gels have a higher cross section area A and are hence less dense than the anisotropic gels; therefore, they can be more easily penetrated by free polymers. The density of monomers belonging to free polymers inside the gel at the percolation threshold is around $\rho_{i,\text{gel}}^c \sim 0.03\sigma^{-3}$, as in the anisotropic gel.

From a practical point of view, our results on the percolation transition of shell polymers inside the core might be relevant, because they give insight into the connection between the core and shell beyond the direct interfacial region. Submillimeter size core gels will typically not be fully invaded by shell polymers during the preparation time. However, once the shell polymer concentration exceeds ρ^* in a region close to the core surface, shell polymers may form large interconnected clusters which can be cross-linked and will further strengthen the connection between core and gel. The thickness of the region where these clusters occur depends upon the time duration during which shell chains are permitted to interdiffuse prior to being cross-linked.

4.3.2 Structure of equilibrated interfaces

Having studied the time evolution of the system after bringing the core gel and shell solutions into contact, we now investigate the properties of the final, locally equilibrated interfaces in more detail.

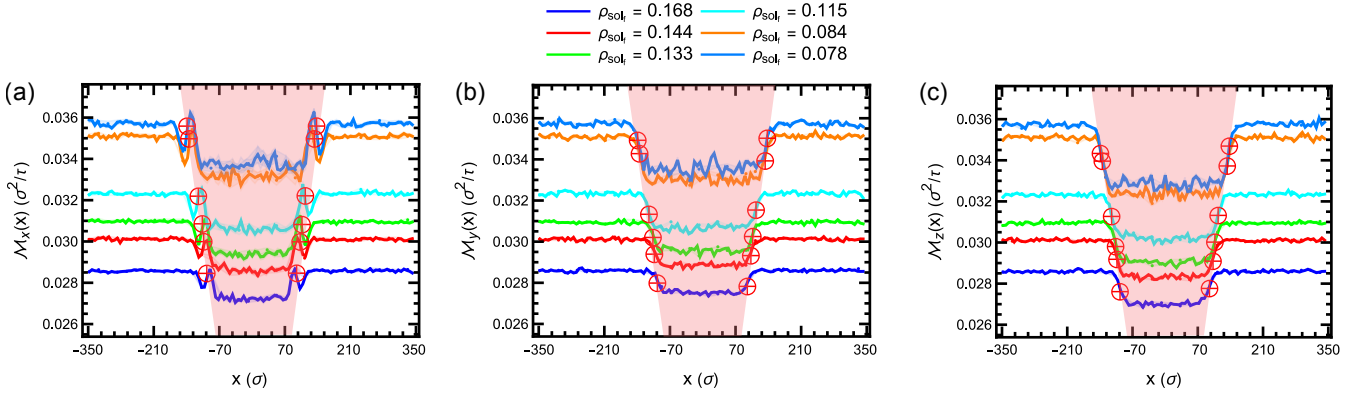


FIGURE 4.9: Profiles of monomer motion $\mathcal{M}_\alpha(x)$ in $\alpha = x$ (a), $\alpha = y$ (b) and $\alpha = z$ (c) direction vs. x -coordinate of monomers. The red symbols \oplus indicate the approximate position of interface, the red shading the gel regions. The gel is anisotropic.

4.3.2.1 Local monomer motion and chain conformations

To characterize the local motion of monomers, we calculate their mean squared displacements from every consecutive frames and define the quantity

$$\mathcal{M}_\alpha(x) = \frac{\langle (r_\alpha(t + \Delta t_s) - r_\alpha(t))^2 \rangle}{\Delta t_s}. \quad (4.12)$$

here $\alpha = x, y, z$, $r_\alpha(t)$ are the α th component of the position of the monomers at time t , and $\Delta t_s = 800\tau$ refers to the time interval between two consecutive frames /snapshots.

Figure 4.9 shows the profiles of \mathcal{M}_i across the slab for anisotropic gels. The corresponding results for isotropic gels can be found in Appendix A, Figure A.8. As one might expect, the local motion is reduced inside the gel, compared to the solution phase, due to the friction with the network. Furthermore, we also see that \mathcal{M}_α decreases with increasing ρ_{sol_f} due to the friction with other free polymers. Inside the gel, monomers move more in y direction than in z direction, which is a consequence of the anisotropy of the gel. The difference disappears in isotropic gels as shown in Appendix A, Figure A.8. In the x -direction, the value of \mathcal{M} inside the gel is intermediate between the values in y and z directions (identical in isotropic gels). More interestingly, the profile of $\mathcal{M}_x(x)$ features an oscillation close to the interface. Monomers just outside the gel move less than their neighbor monomers because the gel surface acts as a barrier to particle motion. Monomers just inside the gel move more than their neighbors because their moves take them into the gel-free region. The oscillation helps to maintain net zero monomer flux across the interface: Monomers just outside of the interface cross the interface less often,

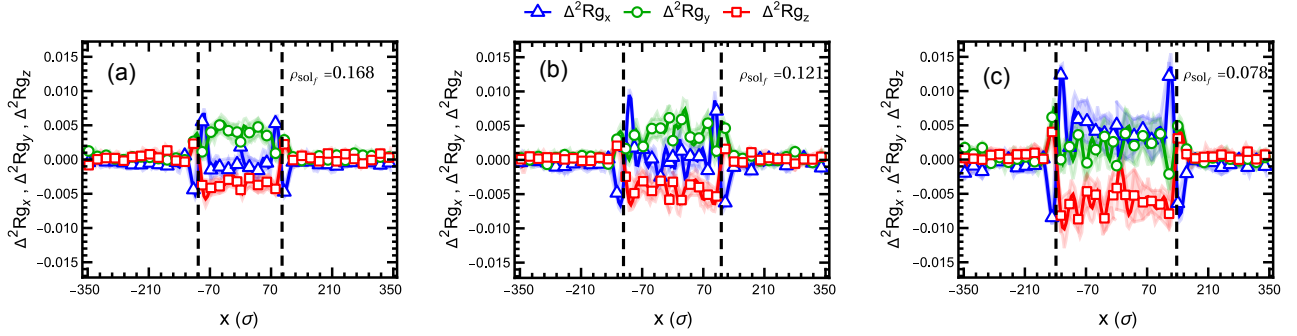


FIGURE 4.10: Profiles of chain conformation parameters $\Delta^2 R_{g_\alpha}$ (see text) across the gel slab for different concentrations ρ_{sol_f} as indicated. The x coordinate refers to the center of mass of chains. Black dashed line indicates the position of the interface, shaded bands represents the error. The gel is anisotropic

however, they have higher density. Monomers just inside cross the interface more often, but their density is lower.

Next we examine the conformations of the free polymers as a function of the x -position of the simulation box. Following Adhikari et al., [5, 6], we define anisotropy parameters of the gyration tensor as:

$$\Delta^2 R_{g_\alpha} = \frac{3\langle R_{g_\alpha}^2 \rangle - \langle R_g^2 \rangle}{2\langle R_g^2 \rangle}, \quad (4.13)$$

where $\alpha = x, y, z$ as before. Here $\langle R_g^2 \rangle \sim 42 - 47\sigma^2$ is the mean squared radius of gyration of free chains and $\langle R_{g_\alpha}^2 \rangle$ the corresponding component in the direction α . The value of $\Delta^2 R_{g_\alpha}$ is positive if chains orient or are elongated along the α direction, and negative if the chain orientation is orthogonal to that direction or if chains are squeezed. If $\Delta^2 R_{g_\alpha}$ is zero for all α , then the distribution of chain orientations and conformations is isotropic.

The resulting profiles for three different concentration values ρ_{sol_f} in solution are shown for anisotropic gels in Figure 4.10. Here, the x coordinate of a chain is taken to be the position of its center of mass. In the solution, the values of $\Delta^2 R_{g_\alpha}$ are zero for all α , indicating that the chain conformations are isotropic. Inside the gel, the conformations become anisotropic: $\Delta^2 R_{g_y}$ is positive and $\Delta^2 R_{g_z}$ is negative, indicating that the chains align in the direction in which the anisotropic gel has been stretched. Indeed, in the isotropic gel, these effect disappears and both $\Delta^2 R_{g_y}$ and $\Delta^2 R_{g_z}$ are zero within the error (see Figure A.9 in Appendix A). The value of $\Delta^2 R_{g_x}$ inside the gel is mostly zero, except at the lowest concentration, where it is positive, most likely due to the swelling of the gel.

Close to the interface, the profile of the perpendicular component of the gyration tensor, $\Delta^2 R_{g_x}$, exhibits an oscillation with a negative dip on the solution side and a positive dip on the gel side. This indicates that chains in solution are slightly squeezed close to the gel interface, similar to chains that are squeezed close to surfaces. On the gel side, the chains are slightly elongated due to a tendency to extend loops or chain ends into the solution region.

4.3.2.2 Interfacial width and interfacial tension

Finally, we discuss the fluctuations of the gel/solution interface. At finite temperatures, interfaces between liquids are not perfectly flat. They undulate due to thermal fluctuations. These undulations, also called capillary waves, significantly broaden the apparent interfacial profiles, such that the apparent width w grows indefinitely with the lateral system size L_{\parallel} , following $w^2 \sim L$ in two dimensions and $w^2 \sim \ln(L)$ in three dimensions [99, 267, 251]. For interfaces between demixed phases in homopolymer blends, the phenomenon has been studied intensely [316, 271, 195, 48], and it has been shown that a detailed analysis of the interfacial width broadening can be used to extract the interfacial tension. Our goal here is to use a similar approach to calculate the interfacial tension of gel/solution interfaces.

However, the situation is complicated by the elasticity of the gel. First, the notion of an interfacial tension is somewhat ambiguous when dealing with elastic interfaces. It can be defined in two different ways, i.e., (i) as the excess free energy per area at the surface, or (ii) as the work per area required to stretch the surface by a given amount. The first definition, also referred to as "surface energy" (σ), describes the free energy increase if the surface is enlarged by creating more interface, e.g., by cutting the gel up. The second definition, also referred to as "surface stress / tension" (γ), is related to the mechanical force that opposes stretching of the gel. At liquid/liquid interfaces, the two quantities are the same. At interfaces involving elastic materials, they are different, and related to each other via the so-called Shuttleworth relation [278, 315, 20]

$$\gamma = \sigma + A \frac{\partial \sigma}{\partial A}. \quad (4.14)$$

In the context of capillary wave fluctuations, interface fluctuate without adding/removing cross-links or strands in lateral direction; hence the relevant quantity is the surface stress γ .

A second complication arises from the fact that interface fluctuations are not only penalized by interfacial stress, but also by the elastic distortion of the gel perpendicular to the interface. Therefore, the standard capillary wave formalism must be modified accordingly.

Capillary wave fluctuations are typically described in terms of effective interface Hamiltonians. In our system, we have two interfaces, corresponding to the two surfaces of the slab. We assume that they are sufficiently far apart such that the coupling across the gel can be neglected. Hence, every surface can be described by an independent two-dimensional manifold which is coupled to an elastic medium. Neglecting overhangs, we describe the surface by a function $h(y, z)$ corresponding to its local position in x direction relative to its mean position. For simplicity, we ignore the fact that the interfacial tension γ might be anisotropic for anisotropic gels. The linearized interface Hamiltonian then reads

$$\mathcal{H}[h] = \int dy dz \left[\gamma \left(1 + \frac{1}{2} \left(\frac{\partial h}{\partial y} \right)^2 + \frac{1}{2} \left(\frac{\partial h}{\partial z} \right)^2 \right) + \frac{1}{2} B h^2 \right] \quad (4.15)$$

here B is an elastic coupling constant. Applying a two dimensional Fourier series expansion

$$h(z, y) = \frac{1}{\sqrt{A}} \sum_{\vec{q}} \tilde{h}(\vec{q}) \exp(-i\vec{q} \cdot \vec{r}) \quad (4.16)$$

to Equation (4.15) and then exploiting the generalized equipartition theorem, we can calculate the thermally averaged height correlations of the interface h in Fourier space as

$$\langle |\tilde{h}(\vec{q})|^2 \rangle = \frac{k_B T}{(B + \gamma q^2)}, \quad (4.17)$$

Now we use equation (4.17) to find the variance $\langle h^2 \rangle$ of the distribution of interface positions $\mathcal{P}(h)$ in a patch with lateral size L_{\parallel} . We assume that the apparent monomer density profile $\rho(z)$ at the interface can be written as the convolution of an "intrinsic" profile with $\mathcal{P}(h)$

$$\rho(z) = \int dh \mathcal{P}(h) \rho_{\text{int}}(z - h) \quad (4.18)$$

The interfacial broadening can then be approximated by [266, 317]

$$w^2 = w_{\text{int}}^2 + \frac{\pi}{2} \langle h^2 \rangle, \quad (4.19)$$

resulting in

$$w^2 = w_{\text{int}}^2 + \frac{k_B T}{8\gamma} \ln \left(\frac{1 + g b_{\text{int}}^2}{1 + g L_{\parallel}^2} \right) + \frac{k_B T}{4\gamma} \ln \left(\frac{L_{\parallel}}{b_{\text{int}}} \right) \quad (4.20)$$

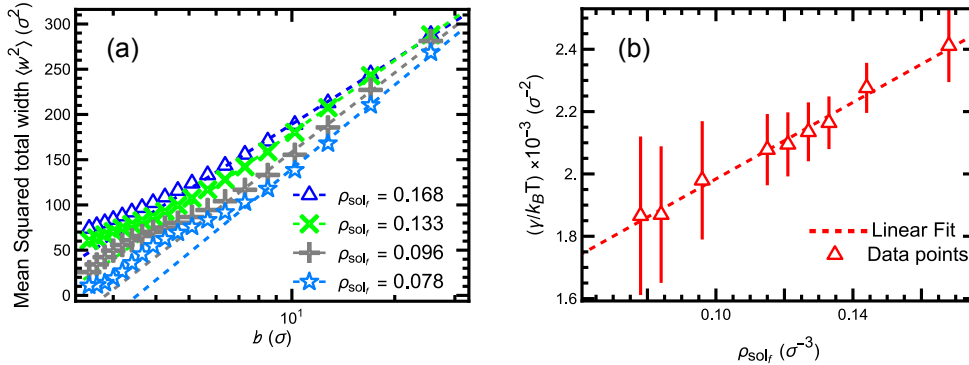


FIGURE 4.11: (a) Apparent squared interfacial width w^2 as a function of block size b (see text for explanation). The dashed lines represent the fit to Equation (4.20), see text for details. (b) Fitted value of interfacial tension γ vs polymer concentration ρ_{sol_f} . The dashed line shows a linear fit to the data. The gel is anisotropic.

where $g = B/4\pi^2\gamma$ and b_{int} is an intrinsic length scale. Details of the derivation can be found in section 4.5.2.

We now apply the relation (4.20) to analyze the gel–polymer interfaces. To this end, we divide the (L_y, L_z) surface of the simulation box into equal number of bins [316, 282, 204], such that we obtain n^2 sub-blocks with dimensions $b \times b \times L_x$. We determine the density profile within each of these sub-blocks, determine the interfacial width in the sub-block as described in section 4.5.1, and average over all sub-blocks and all configurations. The results are shown as a function of sub-block size in Figures 4.11a and 4.12a for the anisotropic and isotropic gel, respectively. For large sub-block sizes, the data are well described by Equation (4.20) (see below for details on the fitting procedure). At lower block sizes around $b \leq 10\sigma$, the curves deviate from the theory and bend upwards. In this regime, b becomes comparable to the radius of gyration of strands, and hence the description of the interface in terms of a simple interface Hamiltonian is bound to fail. The curves for the anisotropic gel exhibit some substructure for lower ρ_{sol_f} , see Figure 4.11a. This substructure is not observed in isotropic gels Figure 4.12a, indicating that the local interface structure is affected by gel anisotropy.

We note that it is not possible, just from looking at Figures 4.11a and 4.12a, to extract an obvious "intrinsic" block size b_{int} , which could be used to unambiguously determine the intrinsic width w_{int} . A similar observation was made in interfaces of homopolymer blends [316].

We have used Equation (4.20) to fit the interfacial width data for large block sizes b . The least square fitting procedure resulted in two different types of fits: one giving large values of the elastic parameter B , $B > 0.5 \epsilon/\sigma^4$ or higher, and one giving values of order

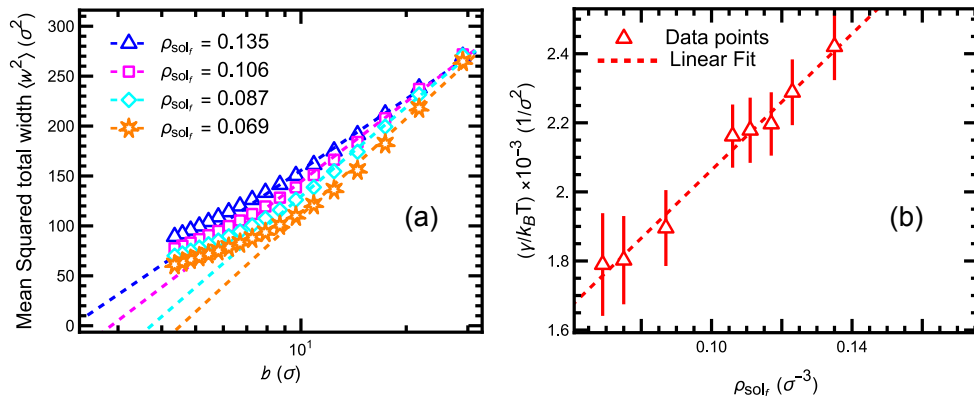


FIGURE 4.12: Same as Figure 4.11 for the isotropic gel.

$B \sim 10^{-9} \epsilon / \sigma^4$, i.e., B is zero within the error. Considering that the bulk modulus of bare gels is small (see Appendix A, Figure A.3), we consider the results of the first type of fit to be physically unreasonable, and selected the second type. The fitted values for w_{int}^2 and b_{int} had large errors, because they strongly depend on each other. However, if we applied constraints on one of these parameters, it only affected the other, and not the fit values of B and γ . Therefore, we infer that the fit values for γ are reliable, despite the fact that applying a four-parameter-fit to the curves in Figures 4.11a and 4.12a seems somewhat brash.

The results for the interfacial tension, $\gamma/k_B T$, are shown as a function of the concentration of polymers in solution, ρ_{sol_f} , in Figures 4.11b, 4.12b, respectively. The interfacial tension increases roughly linearly with increasing concentration ρ_{sol_f} . It grows a bit faster for the isotropic gel, which we attribute again to the fact that our isotropic gels are less dense; hence, the interfaces at the same bulk concentration ρ_{sol_f} contain a higher amount of free polymers. More importantly, Figures 4.11a and 4.12a clearly show that the "intrinsic width" itself, no matter how we define it – i.e., for which intrinsic block size b_{int} we evaluate it – also increases with increasing concentrations ρ_{sol_f} .

The positive correlation between the interfacial width and the interfacial tension stands in stark contrast with the conventional behavior seen at liquid-liquid interface, where these two quantities are typically anticorrelated: the interfacial tension increases with increasing incompatibility of the two components, whereas the interfacial width decreases. In Cahn Hilliard-type theories, the interfacial tension and the interfacial width are, in fact, predicted to be inversely proportional to each other. However, this does not hold true at the gel/solution interface, underscoring its peculiar nature. In our model system, the gel strands and the polymers in solution are not incompatible but are identical. The origin of interfacial tension lies in elasticity and entropy. As the polymer concentration

ρ_{sol_f} increases, the polymers swell the gel, leading to an increase of the interfacial width. On the other hand, the swollen gel stiffens, which also increases the interfacial tension.

4.4 Conclusions and outlook

In the current study, we have investigated the interdiffusion of polymers from solution into regular polymer networks. Even though the study was motivated by the practical problem of understanding physical processes during the preparation of core-shell particles by microfluidics, it also offers general insights into the structural properties of interfaces between polymer gels and solutions and the dynamics of interdiffusion.

Comparing the gel–solution interfaces to liquid–liquid interfaces between demixed homopolymer phases, we find several qualitative differences. First, the evolution of the interfacial region at the onset of interdiffusion is nonmonotonic due to interplay of two competing effects: the compression of the gel due to the osmotic pressure of the polymers in solution, and the swelling of the gel due to the penetration by polymers. As a result, the gel first shrinks and then expands again. A second remarkable difference is a positive correlation between the interfacial tension (the surface stress) and the interfacial width, which stands in contrast to interfaces between immiscible liquids, where these two quantities are inversely correlated.

From a practical point of view, our study can offer insights that might help to optimize experimental strategies for preparing multiphase polymer hydrogels by sequential crosslinking of layers. In good solvents, the connectivity between layers, as characterized by the "degree of interfacial integration" [274], saturates at values that are characteristic for randomly distributed Gaussian chains. However, we find that it takes a long time until saturation is reached. Even though entanglement effects are presumably not important in our system – even in dense melts, the entanglement length of flexible Kremer-Grest chains is of order $N_e \sim 50$ beads [291] – the saturation time is found to be orders of magnitude higher than the chain relaxation time. This suggests that it should be possible to tune the connectivity between the layers by tuning the time of crosslinking the solution after bringing it in contact with the gel. A second slow process that could be exploited in practical applications is the percolation of free polymers inside the gel. We have seen that percolation sets in as soon as the concentration of the free polymers inside the gel exceeds a threshold value which is of the order of the overlap concentration. Hence, the width of the region inside the gel where free polymers percolate should be driven by diffusion

and slowly increase with time. After crosslinking, these percolating polymers could form a network that interpenetrates the gel network and strengthens the connection between the two.

In the present work, we have studied an idealized case in which the free polymers and the gel polymers were taken to have the same chemical structures. In most applications, the two are chemically different, which will result in some incompatibility. Thus, the interfaces will be more similar to regular liquid-liquid interfaces of demixed phases. The interplay of incompatibility, elasticity, and entropy in such cases will be an interesting subject of future studies.

Another aspect which should have a significant impact on the properties of the interface is chain length disparity. Here, we have considered a special case where the free polymers and the strand polymers have equal lengths. In the future, it will be interesting to look at situations where the free polymers are much shorter, leading to increased swelling of the gel, or much longer, leading to slower diffusion, but also, possibly, an enhanced percolation probability. Furthermore, we have considered regular networks here. Real networks are disordered and have a distribution of mesh sizes, which will also lead to interesting novel phenomena.

4.5 Appendix

4.5.1 Determination of interfacial width

To calculate the interfacial width in a given sub-block of the system, we employ python3 alongside with packages such as "derivative" [162] and "statsmodel" [263] and proceed as follows:

- First we divide the density profiles of the gel and the polymers into the left and right halves symmetrically at $x = 0$. This gives four density curves.
- We then determine the derivative of these curves at each point (the instantaneous slope) and determine the maximum of the absolute value of this slope $\left| \frac{\partial \rho}{\partial x} \right|_{\max}$ for each curve. In addition, we determine the maximum and minimum density values for each curve.

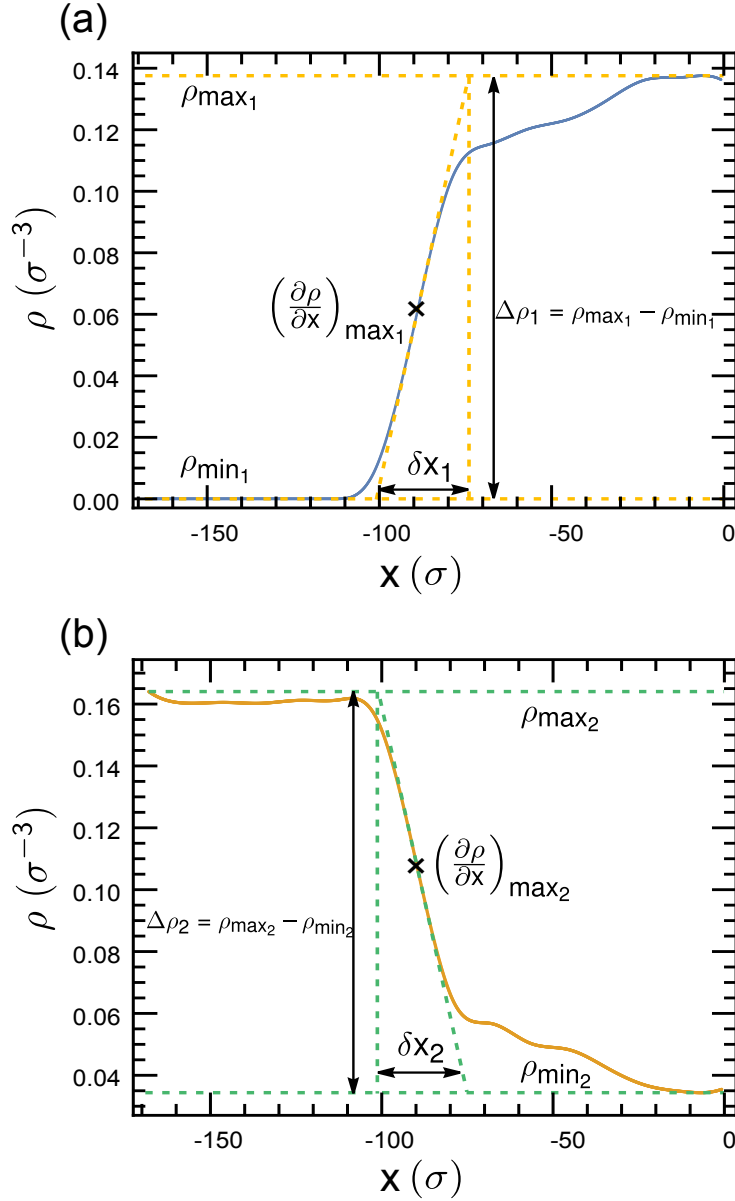


FIGURE 4.13: Schematics of the method use for extracting the total interfacial width from the gel monomer density profiles (a) and from the monomer density profiles for free polymers (b). After extracting δx_1 and δx_2 , we average over them to get w .

- From these numbers, we determine the interfacial width δx_i for each of the four profiles via [21]

$$\delta x = \frac{\rho_{\max} - \rho_{\min}}{\left| \left(\frac{\partial \rho}{\partial x} \right)_{\max} \right|} \quad (4.21)$$

This definition is illustrated in Figure 4.13.

- Finally, we average over these four numbers to obtain the total interfacial width $w = \frac{1}{4} \sum_{i=1}^4 \delta x_i$.

4.5.2 Theoretical expression for capillary wave broadening

Starting from the effective interface Hamiltonian, Equation (4.15), we first perform a Fourier transform according to (4.16). In Fourier representation, the Hamiltonian reads

$$\mathcal{H}[\tilde{h}(\vec{q})] = \gamma A + \sum_{\vec{q}} \frac{1}{2} (B + \gamma q^2) \tilde{h}(\vec{q}) \tilde{h}(-\vec{q}) \quad (4.22)$$

Now to calculate the correlations, we use the generalized equipartition theorem $\langle x_i \frac{\partial \mathcal{H}}{\partial x_j} \rangle = k_B T \delta_{ij}$. Here the x_i are generalized coordinates. Since the height h is a real function its Fourier coefficient $\tilde{h}(\vec{q})$ is complex conjugate to $\tilde{h}(-\vec{q})$. Exploiting this relation yields

$$\langle |\tilde{h}(\vec{q})|^2 \rangle = \frac{k_B T}{(B + \gamma q^2)}, \quad (4.23)$$

From (4.23), we can calculate the variance of the position of the interface h in real space as

$$\begin{aligned} \langle h(y, z)^2 \rangle &= \frac{1}{A} \sum_{\vec{q}} \langle |\tilde{h}(\vec{q})|^2 \rangle \\ &= \frac{1}{4\pi^2} \int 2\pi q \, dq \langle |\tilde{h}(\vec{q})|^2 \rangle \\ &= \frac{k_B T}{2\pi} \int dq \frac{q}{(B + \gamma q^2)}. \end{aligned} \quad (4.24)$$

The integral in Equation (4.24) can easily be solved by substitution of $p = (B + \gamma q^2)$ to get the following expression for $\langle h^2 \rangle$:

$$\langle h^2 \rangle = \frac{k_B T}{4\pi\gamma} \left[\ln \left(\frac{g b_{int}^2 + 1}{g L_{||}^2 + 1} \right) + 2 \ln \left(\frac{L_{||}}{b_{int}} \right) \right] \quad (4.25)$$

with $g = \frac{B}{4\pi^2\gamma}$.

Chapter 5

Molecular Motor gels

5.1 Introduction

Molecular motors can be natural or synthetic and their main task is to produce mechanical motion by converting energy from one form to another. Natural motors operate on nanometer length scales and their movements helps in the functioning of a variety of systems, from singled celled organisms, muscle fibers and bacterial flagella [300, 33, 197]. The potential applications of molecular motors are vast, and ongoing research in both biological and synthetic systems are aimed at unlocking their full potentials. The biological motors are typically made of proteins and nucleic acids and use ATP or proton gradients for energy. Some examples of biological motors are myosin, kinesin and dyneins, which are crucial for muscle contraction and intracellular transport, whereas ATP synthase and bacteria flagellar motor helps in rotary movements [258]. Additionally, RNA polymerase and ribosomes act as linear motors on nucleic acid tracks, providing support for gene expression and protein synthesis. Biological motors are capable of doing complex tasks, however, they are associated with many disadvantages like their inherent instability which can limit their reliability and efficiency, as well as the restrictions imposed by the specific environmental conditions required for their effective functioning [4].

The idea of fully synthetic molecular motor systems in itself is fascinating and the use of such motors to develop complex nanomachinery offers significant advantages as they can operate in a wide range of environmental conditions compared to biological machines. The ambition to construct entirely artificial motors and nanoscale machines, inspired by

Feynman's bottom-up approach [185, 97] introduced decades ago, has fueled efforts to tackle the challenges presented by these molecular devices. Typically they use chemical, electrochemical and photo-chemical processes as fuel source to generate mechanical-like movements of their submolecular components. This field has evolved from initial proof-of-concept studies to more advanced research exploring real-world applications. The Nobel prize winning works by Jean-Pierre Sauvage, Fraser Stoddart, and Ben Feringa, where they created molecular machines underscored the conceptual and technological significance of this research [259, 287, 95]. Over the years, various types of synthetic motors have been developed. These include linear motors, such as the rotaxane linear motor, which utilizes a molecular rotor threaded through a molecular ring to generate linear motion along a molecular dumbbell [150, 36, 10]. Other types include rotor motors, which achieve repetitive 360° rotation with energy consumption and directional control, as well as propeller motors, walkers, and shuttles [10].

Controlling these motors through light is very attractive as it allows for spatiotemporal control, does not produce waste products, and also due to its renewable nature. Since having a precise control over the thermal and photochemical rearrangement processes that dictates the rotors behaviour is difficult, creating such photochemically driven motors becomes challenging. Because molecular motors operate through repeated cycles, the reactions must be reversible, clean, and resistant to fatigue [66]. Consequently, only a few photochemical reactions have been used, primarily photoinduced electron-transfer and photoisomerization [66, 30, 65, 121]. One of the important discovery was the unidirectional light-driven rotatory motor based on an overcrowded alkene developed in the group of Ben Feringa [199, 166, 233, 297]. The integration of photo-induced isomerization and thermal helix inversion processes leads to unidirectional rotary cycles. Building on this discovery, different generations of molecular rotors have been engineered, by altering the structure of these first generation motors [247, 199]. Their distinctive motions have been harnessed for various potential applications, including transporters like molecular nanocars [168], supramolecular assemblies [304], responsive materials [82], functional surfaces [57], chiral catalysts [309], and bio-hybrid systems [186]. Thus these synthetic systems along with their biological counterparts are collectively called molecular machines.

Here we focus on "machines in polymers" particularly the molecular motor gels, an example of which has been created by Giuseppone and co-workers [179]. The previously mentioned paper illustrates the advancements in light-driven molecular motor. They employed the unidirectional rotation of overcrowded alkene motors to braid polymer chains together, leading to the contraction of a toluene submerged polymer gel. Further systematic experiments were done by Xuyang Yao and co-workers [326] where they changed the

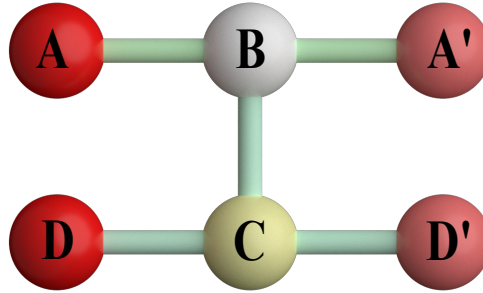


FIGURE 5.1: Coarse grained representation of molecular motor. A-B-A' and D-C-D' represents the two rigid bodies which forms the molecular motor. The axis A-B-A' and D-C-D' rotates along B-C opposite to each other, such that relative cumulative angle between them in each half cycle is 180°

molecular weights of the gel strand in a quasi-ideal tetrahedron like networks and studied its effect on contraction. Lifting experiments were also performed using these gels which produced fascinating results. The assumption at that time was that the motors creating the braiding effect in the strands could not unwind. Based on this assumption we have developed a coarse-grained molecular dynamics model for the molecular motors, which have a very high activation barrier and hence would not unwind. Here in this chapter we will summarise how the model for the uni-directional rotor was developed. This will be followed by a short description of the model of the gel and the simulation details. Further down the line we will discuss results from our simulations.

5.1.1 Modeling and simulation details

5.1.1.1 The six bead rigid body motor model

The basic element of a molecular motor gel or Feringa gel is a molecular motor. In our particular case we were interested in studying a polymeric machine, created by inter-connecting second generation rotor molecules by polymers. Our model for the motor uses rigid bodies. Rigid bodies were used because we were not interested in the oscillation of bonds within the molecule, but only on the overall rotation of the molecule. A rigid body is defined by a single **central particle** and a number of **constituent particles**. All of these are particles in the simulation state, and can interact with other particles via forces. The mass and the moment of inertia of the central particle sets the full mass and moment of inertia of the rigid body (constituent particle mass is ignored). The central particle is

placed in the center of mass of the rigid body and the other particles in the rigid-body system are placed relative to this center. The central particle's orientation, given as a quaternion defines the rotation from the body space into the simulation box. In the body space the center of mass of the rigid body is given a coordinate $(0, 0, 0)$. The position as well as the orientation of the constituent particles in the simulation box is set relative to the central particle's position and orientation.

We use a model of six beads which are part of two rigid bodies in-order to simulate the rotor molecule (see Figure 5.1). Each rigid body consists of three particles, a central particle and two constituent particles. The central particles of the two rigid bodies that forms the molecule are connected via FENE bond. In the initial simulation state, the central particles of the two rigid bodies that forms the molecule, are placed 0.6σ from each other along the z axis (B-C). Here σ is the diameter of the monomers of a polymer strand, which will be discussed further in the coming section. Similarly, constituent particles of the rigid bodies (A, A' and D, D'), in the initial state are placed 0.85σ from their respective central particles (B and C) along the x direction. Thus the particles of a rigid body lies on a straight line (A-B-A' and D-C-D'). Other than the central beads (B and C) which interacts via FENE (equation (5.2)) and WCA (equation (5.1)) interactions, no other particles have any non-bonded pair interactions between them to allow for smooth rotation.

$$V_{\text{WCA}} = 4\epsilon \left[\left(\frac{D_0}{r} \right)^{12} - \left(\frac{D_0}{r} \right)^6 \right] + \epsilon \quad r < 2^{1/6} D_0$$

$$= 0 \quad r \geq 2^{1/6} D_0 \quad (5.1)$$

$$V_{\text{FENE}} = -0.5 K_{\text{FENE}} R_0 \ln \left[1 - \left(\frac{r}{R_0} \right)^2 \right] \quad (5.2)$$

Here r is the current distance between monomers of any particles, $R_0 = 1.5D_0$ is the maximum bond distance and D_0 the closest possible distance between any two particles. D_0 for the bonded central particles of the rigid body is chosen to be 0.85σ . However, the particles do experience intermolecular non-bonded interactions via WCA. Additionally in order to keep the upper and lower rigid-bodies of the molecule parallel to one another, an angular potential (see equation (5.3)) constraining the angle between the particles A-B-C', D-C-B, A'-B-C and D'-C-B, to $\theta_0 = \frac{\pi}{2}$ radians or 90° is used.

$$V_{\text{Bend}} = 0.5 K_{\text{Bend}} \left(\theta - \theta_0 \right)^2 \quad (5.3)$$

5.1.1.2 Modeling uni-directional rotation

The six bead model above is a good representation of our molecule. However the molecule has to rotate uni-directionally without any backward flip. We initially approached this by using a constant torque model. A positive torque to the rigid center B was applied along direction B-C and a negative torque was applied to C along the same direction. This made the two rigid-bodies rotate relative to each other in order to create a positive rotation angle ϕ . The rotation angle ϕ is defined between the normals formed by the vectors A'-B, B-C and B-C, C-D'. This motor was incorporated as cross-linkers into a gel with diamond like topology. We then allowed for the continuous rotation of these motors in the free gel. The gel was able to contract in the continuous rotation model, but not all the molecules rotated uni-directionally for small torques. Increasing the applied torque on the motors allowed for a larger percentage of them to rotate uni-directionally, however this meant that we were continuously supplying more and more energy into the system, without giving any time for the thermostat (Langevin) to dissipate the energy gained. This led to the increase in the kinetic temperature of the system. So a conscious decision was made to add a period of time over which the system could relax after the application of torque. This also ensured that the simulation matched experimental conditions where the contraction of the gel was slow, typically in the order of minutes, and thus allowed for the relaxation of polymer strands naturally.

So the new strategy was to alternate between rotation and relaxation steps, thus allowing the strands to relax to the new state. A constant torque was applied to the motors during the rotation step and the torque was removed during the relaxation step. To determine the time interval for the torque to be applied, we took a free model-motor and applied a constant torque to it and noted the time taken by it to complete π radians or 180° . After their incorporation into the network, the motors were allowed to rotate for the same time interval as was determined for a free motor. However, these motors in the gel could not complete the 180° rotation in the same time interval as in the free motor case, due to the resistance coming from the attached chain pairs. Hence the rotation time period (τ_{rot}) and torque (M) was adjusted by keeping $M \times \tau_{\text{rot}}$ constant. After the rotation step, the relaxation step was enforced where the system equilibrated under the thermostat. Since we removed the constant torque in the relaxation period, many motors unwound/ backflipped during this time period. So necessary arrangements were made to fix the orientation of the motors, using a FENE interactions that used a shift factor Δ (see equation (5.4)). The shifted FENE interactions were added to the simulation state at the start of every relaxation step and removed at the end of every relaxation step. The

potential was applied between the particle pairs: A-D', A'-D', A-D and D-A' to fix their orientations.

$$V_{\text{FENE shift}} = -0.5k \ln \left[1 - \left(\frac{r - \Delta}{R_0} \right)^2 \right] \quad (5.4)$$

The value of Δ was chosen as the distance between the particle pairs mentioned above, just at the beginning of every relaxation step with $R_0 = 1.5\sigma$.

Initial simulation of the contraction of the free-gel using alternating rotation and relaxation step was done by applying small torques M . However for small torques, the motors were able to unwind. Although increasing the torque while maintaining $M\tau_{\text{rot}}$ constant, did result in uni-directional rotation for majority of motors, there were some of them which still unwound during the simulations. Further, increasing the torque did not make much sense as it felt unreasonably high; in orders of $200k_B T - 300k_B T$, i.e., such large torques were being applied at each time step. Although this was a good model, we had to abandon it to satisfy our assumption that our motors never unwind.

A newer model that used a two state dihedral potential (see Equation (5.5) and see Figure 5.2) was proposed. ϕ in eq.(5.5) is the dihedral angle defined between the normals formed by the vectors A'-B, B-C and B-C, C-D' and is the same as the rotation angle defined before. To induce rotation in the motors, an instability in the current dihedral angle state was created by flipping the value of n in eq.(5.5) from 1 to -1 and vice-versa. This ensured that the vectors A'-B and D'-C are antiparallel and parallel respectively, i.e. to say the molecules have a stable state when $\phi = 180^\circ$ and $\phi = 0^\circ$.

$$V_n = 0.5K_n \left[1 + n \cos(\phi) \right] \quad (5.5)$$

This method for inducing rotation in the coarse grained representation of molecular rotor was already introduced in the paper by J.D. Evans et al., [89] to study how the motor rotation affect the local and global transport properties of a confined fluid. In their model, one of the rigid-bodies forming the motor along with the axel (B-C) was fixed in space through out the simulations. The uni-directional nature to the motor rotation was imposed by applying a torque in the direction of the axel. The model is excellently suited to study scenarios where the motor is attached to a substrate, however in our studies the motors should be able to move freely. Hence, in our model all the particles making up the motors was free to move. Additionally a positive bias torque ($\sim 50k_B T$) on the rigid center B and an equal negative bias torque on C along direction vector of B-C was applied. The

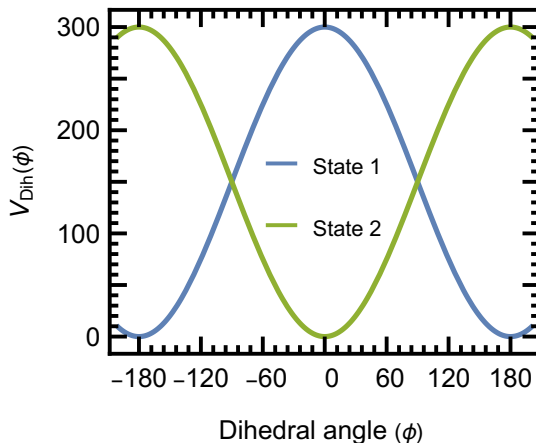


FIGURE 5.2: Two state switching potential as given by equation (5.5). State 1 corresponds to $n = -1$ and state 2 corresponds to $n = 1$.

applied torques helped create a specific direction for the rotation as the dihedral potential changed its state. Similar to our previous model, the simulation were done in alternating rotation and relaxation steps called rotation cycles. One rotation cycle consisted of two rotations and relaxations which are alternated between each other. The value of n was flipped at the beginning of every rotation step. In the relaxation step which followed, the same value of n is kept, which acts like a barrier preventing any backward flip. The model performed well, though there were occasional instances of the motor unwinding, during the rotation step, which our experimental collaborators had indicated should not occur. However, we later realized that this assumption is not correct, as shown by Gao, C, Jentsch, AV et al.[109]. In the next section we will discuss the current model for the motors which enables uni-directional rotation of the motors.

5.1.1.3 Current model for rotation

As mentioned in the introduction of this chapter, we will focus here on molecular motor gels with a very large activation barrier, such that the motors never flip backwards. We used a switching potential to create rotation, along with alternating rotation and relaxation steps (see Figure 5.4). The directionality for rotation was induced using another dihedral term of the form:

$$V_{\text{tors}} = 0.5K_{\text{tors}} \sin^2(\phi - \phi_{\text{ref}}) \quad (5.6)$$

Here ϕ_{ref} is the reference angle chosen just before every rotation and relaxation step. During the rotation step, the molecule experiences a dihedral force derived from the combined potential in equation (5.7)

$$V_{\text{dih}} = \begin{cases} 0.5K_{\text{tors}} \sin^2(\phi - \phi_{\text{ref}}) + 0.5K_n [1 + n \cos(\phi)] & \text{for } \phi < \phi_{\text{ref}} \\ 0.5K_n [1 + n \cos(\phi)] & \text{for } \phi \geq \phi_{\text{ref}} \end{cases} \quad (5.7)$$

Figure 5.3 (b) shows the combined potential (Eq. 5.7) for $\phi_{\text{ref}} = 0^\circ$. During the relaxation step, the molecule's orientation is fixed in its current state by using V_{tors} (see equation (5.6)), with ϕ_{ref} chosen at the beginning of every relaxation step (Figure 5.3 (a)).

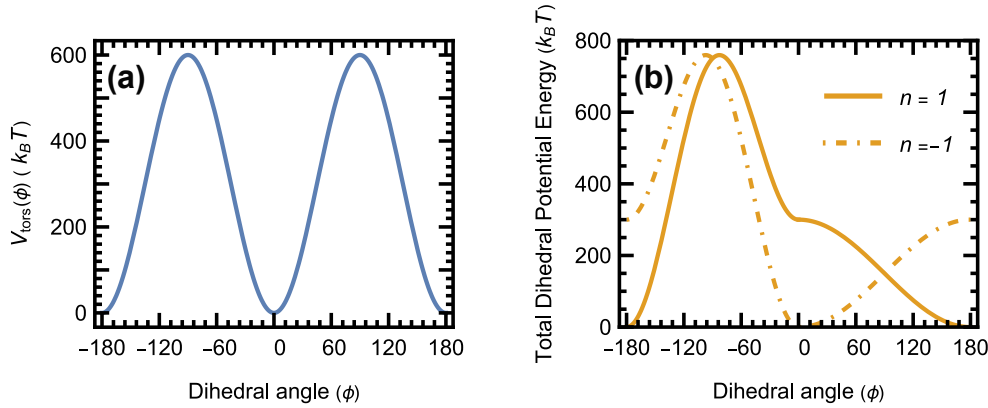


FIGURE 5.3: (a) Total dihedral potential energy in the relaxation step with $\phi_{\text{ref}} = 0$. (b) Total dihedral potential energy for rotation steps with $\phi_{\text{ref}} = 0$, for initially parallel subunits $n = 1$ (orange, solid) and anti-parallel sub-units $n = -1$ (orange, dot-dashed).

5.1.1.4 Gel model

Given that we want to study how the incorporation of these rotors into a polymer-matrix affect the physical properties of the gel through their cooperative motion, we initialised these motors in the form of a diamond lattice, similar to cross-linkers in Chapter 4. We then connected each of these motors by polymer chains to form the diamond structure. Figure 5.5 shows the initial structure of a small diamond network. The network in our case has 512 rotor molecules, meaning we have a system of 1024 rigid sub-units. Thus a total of 3072 particles makes up all the rotors. The strand length of the gel, in the current study are varied from 21 to 84. We used the strand lengths 21, 42, 62 and 84 to be approximately in the same range of arm lengths used in the experiments, which were 35, 41, 52, 84 and 144. The non-bonded monomers of the strands interact with purely

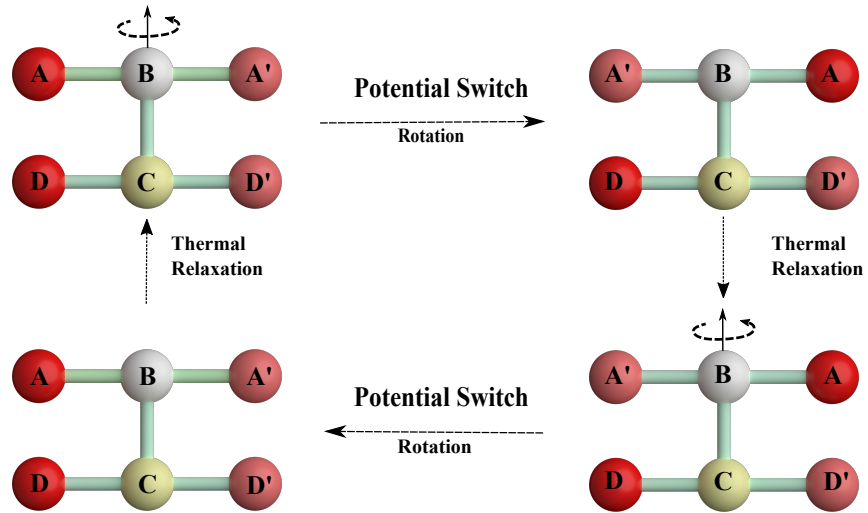


FIGURE 5.4: The four stages in the rotation cycle of a rotor molecule. The molecule rotates by switching the form of dihedral potential eq. (5.7), followed by thermal relaxation, then another potential switch and again a thermal relaxation. The bottom axis $D - C - D'$ is shown to be fixed in space, to facilitate the visualization of 180° rotation.

repulsive interactions (modeled via WCA), whereas the bonded monomers are modeled through FENE + WCA interactions. The interaction between the rotors and the strands are also given by WCA interactions. The value of D_0 and R_0 for these cases are chosen to be 1σ and 1.5σ respectively.

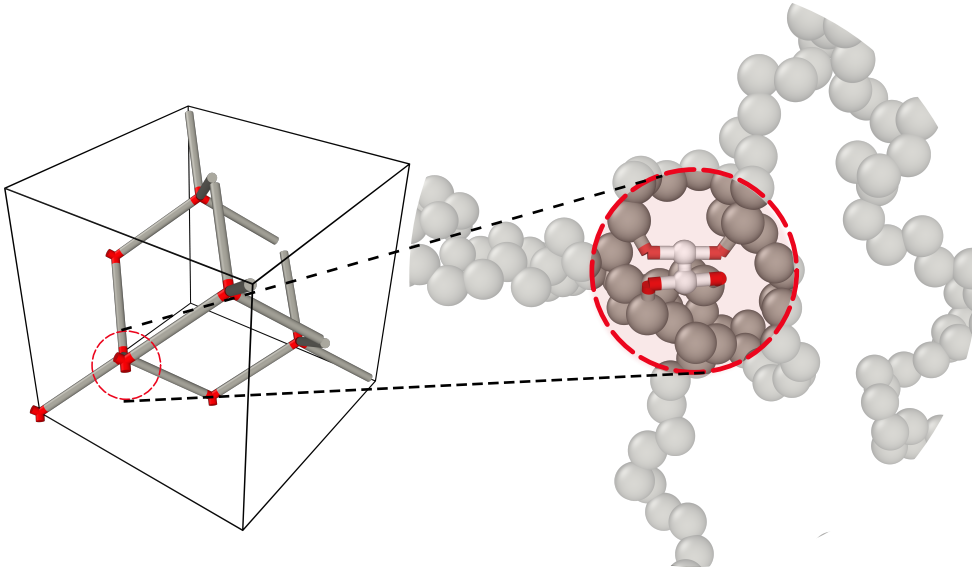


FIGURE 5.5: Initial structure of a small diamond network with 8 motors as crosslinkers

5.1.1.5 Simulation Details

Throughout this chapter we will express all quantities based on units of σ (length), $k_B T$ (energy) and the gel strand monomer mass m . We will use a derived unit τ for time, where $\tau = \sqrt{m\sigma^2/k_b T}$. The values of all the major parameters used in the potential is listed in table given below. Once the initial structure of the gel is set up, it is relaxed under a constant pressure of $0.001k_B T\sigma^{-3}$ and reduced temperature $k_B T = 1$ using the Martyna-Tobias-Klein (MTK) [192] thermostat and barostat for 15000τ . An integration time step of $\Delta t = 0.0005\tau$ is used. The temperature and pressure coupling constants are chosen here to be 0.05τ and 0.5τ respectively. In this chapter we will discuss the results of contraction of a free gel and a gel under different loads, focusing on the unwinding model of the motor.

As mentioned before, we impose alternating rotation and relaxation steps which makes up the rotation cycle. The molecules are allowed to undergo 220 such rotation cycles in the course of our simulation. Each rotation cycle is 40τ long and consist of 10τ long rotation steps and relaxation steps which are alternated. Clearly, 10τ is more than enough time for the chains to equilibrate, after motor rotation, as indicated by the auto-correlation functions of the radius of gyration of strands at different relaxation steps

Parameters	Value
$k_B T$	1
ϵ	$1k_B T$
σ	1
θ_0	$\frac{\pi}{2}$
n	1 or -1
r_0	1σ
R_0	$1.5D_0$
K_{FENE}	$200k_B T/\sigma^2$
K_n	300ϵ
K_{tors}	$600k_B T$
K_{Bend}	$1000k_B T$

TABLE 5.1: The table listing all the parameters used in our simulation

in Figure 5.6 (a)-(d). For our study, the angle turned by each molecule in both the relaxation and rotation cycles were also monitored. All these simulation were done using HOOMD version 3.7 [18], and some of the analysis in the result section used Freud Analysis package[240]. The Fresnel package was used in creating snap-shots of simulation.

5.2 Results

5.2.1 Contraction of free motor gel

To create a free gel, the cross-linkers or the motors are not connected across the periodic simulation box. As mentioned previously in 5.1.1.4, the gel is then relaxed under a pressure of $0.001k_B T\sigma^{-3}$ for about 15000τ . After this the polymer chains are unwrapped and the box is extended in the three directions such that the simulation box is 2.5 times the difference of the maximum and minimum coordinates in each direction. Once this has been done, the gel is equilibrated under a Langevin thermostat for 32τ at $k_B T = 1$. We then start the simulation by inducing rotation to the molecules by flipping the value of n from 1 to -1 , in the dihedral term of the equation (5.7). This causes the gel to contract as shown in the Figure 5.7.

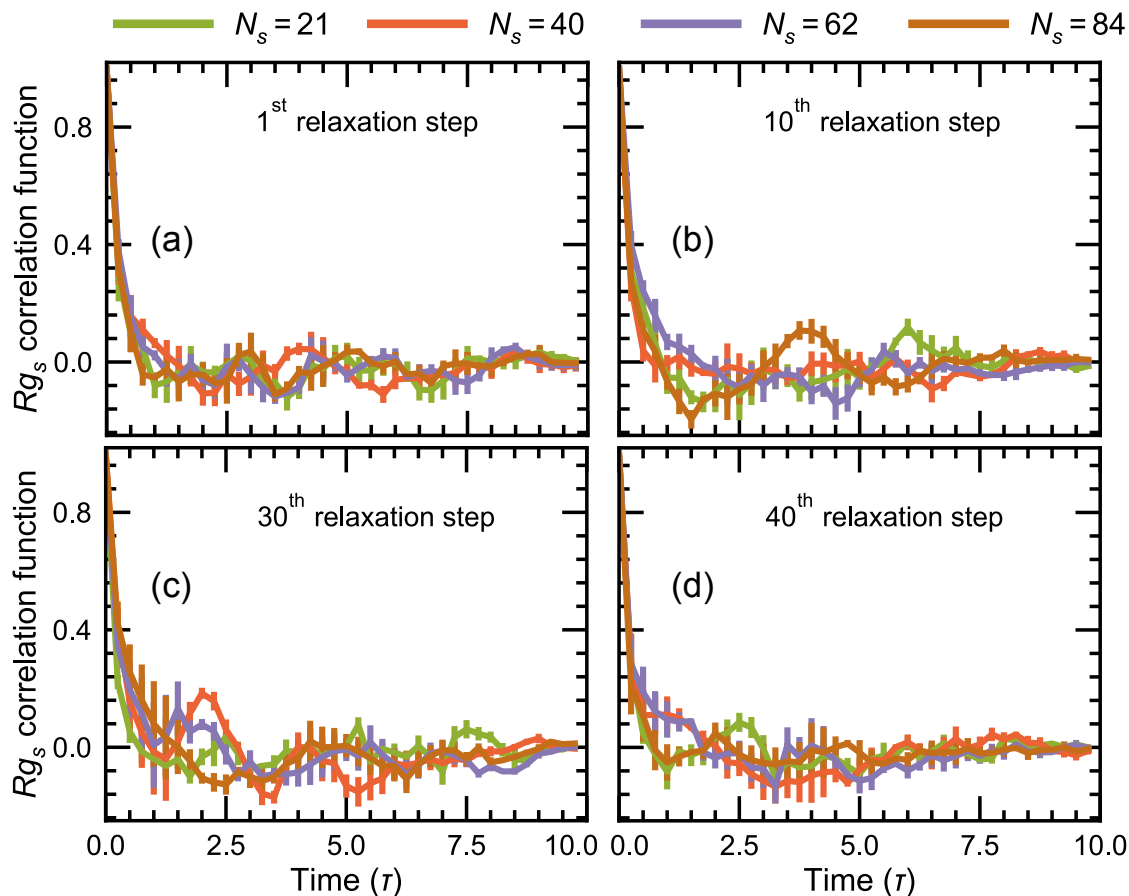


FIGURE 5.6: (a)-(d) Autocorrelation function for the radius of gyration of the strands (Rg_s), measured at different relaxation steps, for the various strand lengths used in our simulations.

5.2.1.1 Angle distribution and Size ratio

To verify the six-particle model for the rotor with the high activation barrier, (i.e., to check for backward flips), we plotted the distribution of the rotation angles during the free gel contractions at different simulation times. The plots in Figure 5.8 shows that initially almost all motors rotate by 180° , which is indicated by the peak at 180° in the Figure 5.8), slowly winding the polymer chain pairs attached to them. As time progresses the number of motors which can rotate 180° decreases, eventually approaching zero, as reflected by the peak at 0° . This is also visible in the plot showing the proportion of motors completing a 180° rotation during a half-cycle, with the x-axis representing time and the top axis showing the corresponding number of rotation cycles (see Figure 5.9 (a)), which drops from values close to 1 and approaches zero. The inability to rotate is attributed to the twisting of the chains attached to molecules, which leads to the creation of an internal

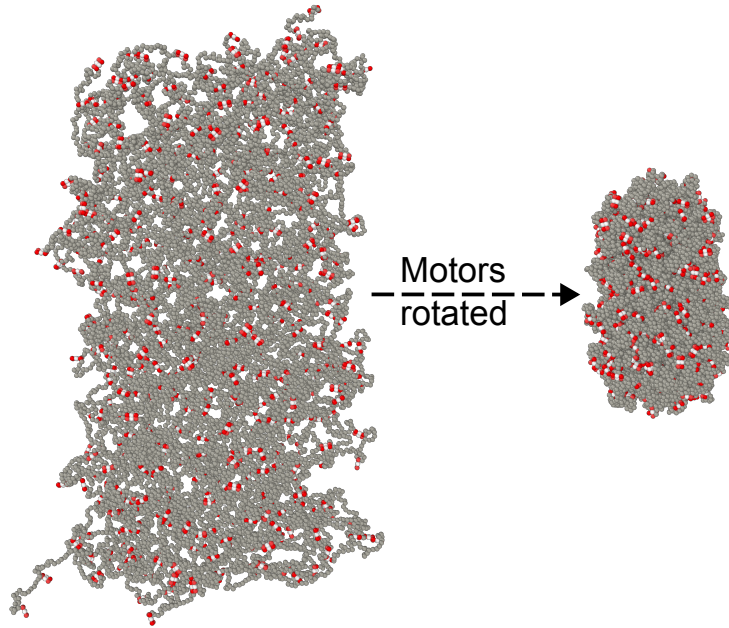


FIGURE 5.7: The swollen state of the gel on the left undergoes contraction as the molecules undergoes several rotation cycles to reach the contracted state on the right.

torque, ultimately neutralizing the rotational motion. Given the unidirectional nature of rotation of the motors, they halt in the long time limit.

One could also notice from Figure 5.9 (a) that for systems with shorter arms (meaning higher motor density), the motors tend to stall sooner. Conversely, in setups with longer arms and lesser motor density, stalling happens later. Even though these systems show comparable decay trends, their respective curves do not line up to form a unified master curve when rescaled or adjusted in time. Especially gels with smaller N_s shows deviations (see inset of Figure 5.10). This implies that the distinctions in topology caused by motor cross-links and the differences in the lengths of the polymer chains affect how the motors operate.

The motor rotation leads to twisting of the attached chain pairs around one another which further makes the chains come closer to each other. To study this effect on the entire gel system we plotted the size ratio defined as the ratio of the radius of gyration of the free gel at time t to that at $t = 0$, $(\langle Rg^2(t) \rangle / \langle Rg^2(0) \rangle)$. Figure 5.9 (b) shows this for gels with different strand lengths. The size ratio of all these system start at one and slowly decreases over time. The size ratio of gel systems with different strand lengths plateau to similar values in the long time limit. The observed behaviour is very much similar to what

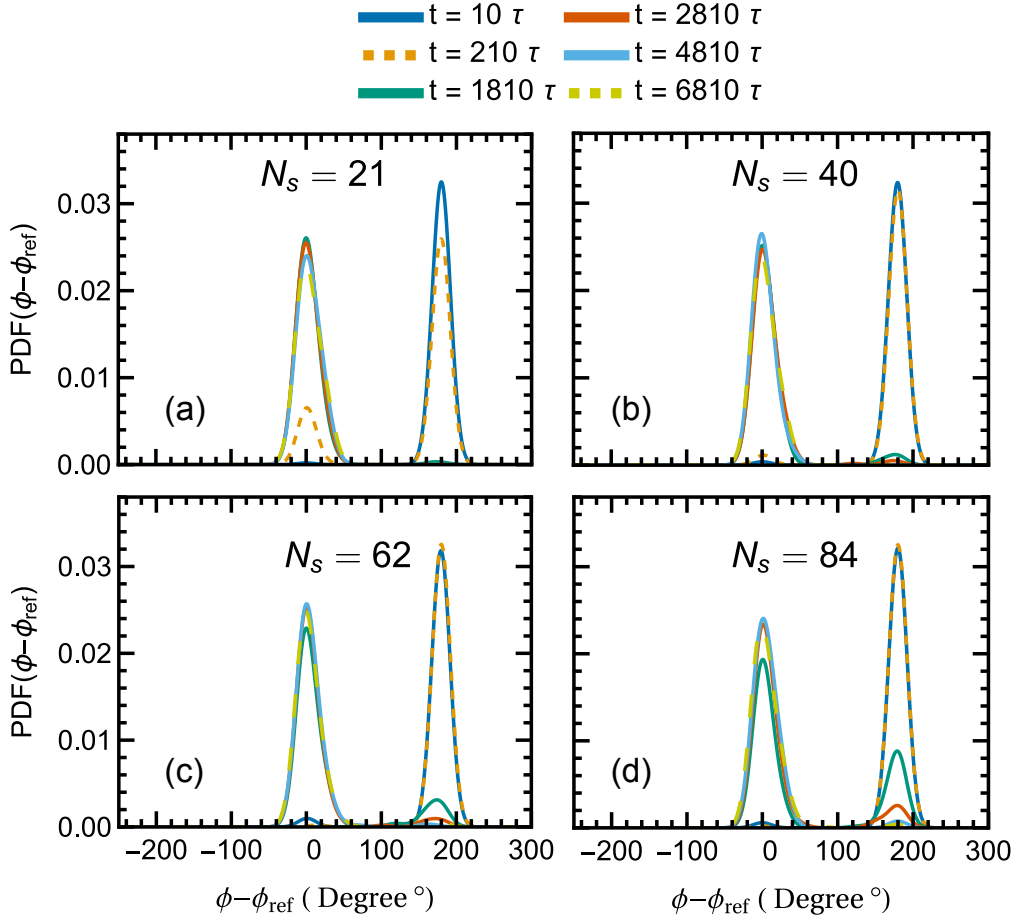


FIGURE 5.8: (a)-(d) Probability distribution of angle turned by the motors at the end of different rotation steps, for strand-length $N_s = 21 - 84$

we see in the experiments in the manuscript [326] (Figure 2e), although in the experiments, the contraction speed varies with the average strand length in a non-monotonic fashion, i.e., first an increase in contraction speed is observed followed by a decrease in the speed as average strand length increases. In the simulations, however, the contraction speed continuously increases as the strand length shortens. The reason for this difference lies in the fact that the simulations do not take into account the impact of increased optical density when motor concentration is high, which can reduce the penetration of light into the material.

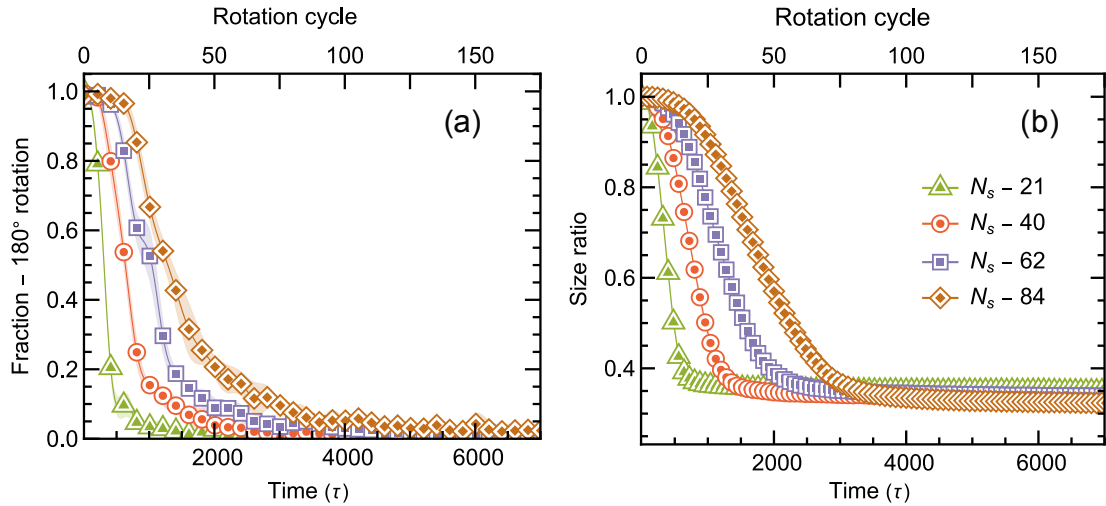


FIGURE 5.9: (a) Fraction of motors rotating by 180° and (b) radius of gyration ratio of the gel, both as a function of rotation cycle (top x-axis) and simulation time (bottom x-axis), for gels with different strand-lengths.

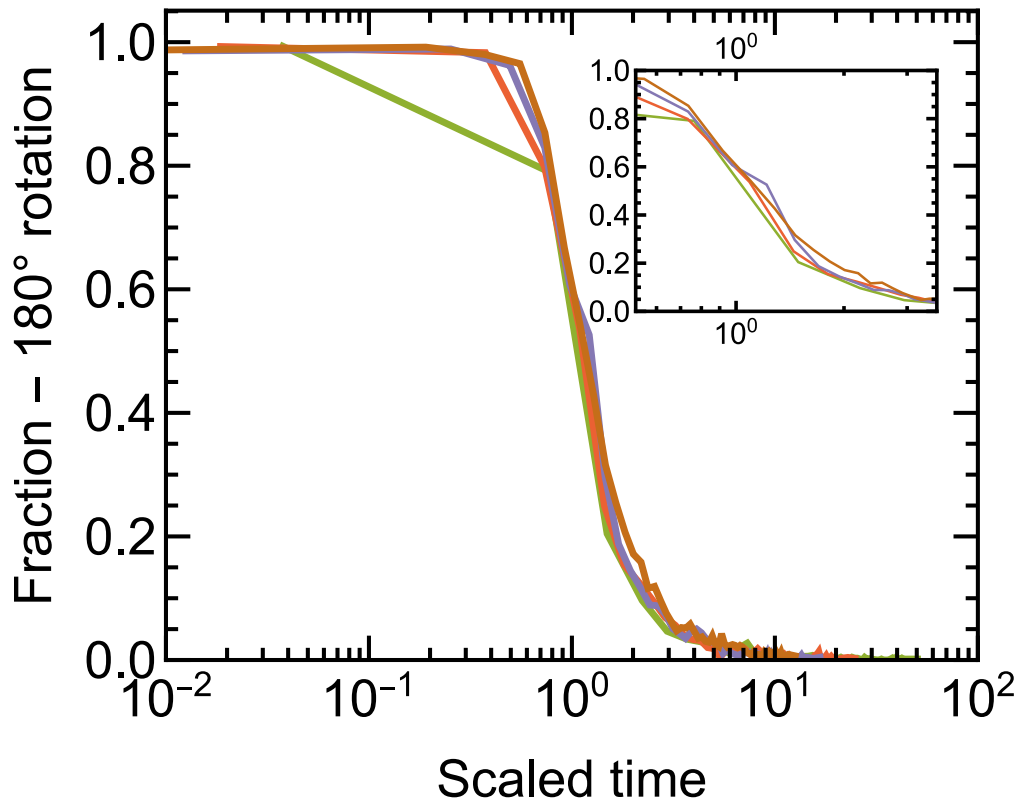


FIGURE 5.10: The same as Figure 5.9 (a) rescaled in time, with logscale representation of the x axis. The inset shows the zoomed in portion of the plot where data for the strands do not collapse onto a single master curve.

5.2.2 Contraction of motor-gel attached to loads

5.2.3 Initializing the gel with load

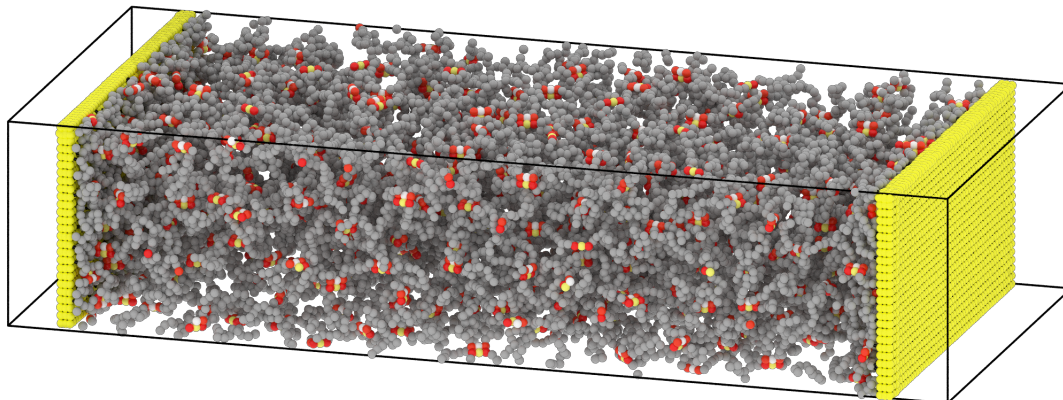


FIGURE 5.11: Represents the gel attached to yellow rigid structures made of harmonically bonded WCA beads. These rigid structures acts like loads, similar to the 1D contraction experiments.

Similar to the sections 5.1.1.4 and 5.2.1 on the initialization of the gel, here the regular network which has a diamond topology, is set up for studying 1D contractions. The gel is initialized to be cross-linked only across the y and z boundaries, with no cross-linking along the x direction boundaries. Then the system is equilibrated for 15000τ under a constant pressure similar to what we discussed in 5.1.1.4. Once the gel is equilibrated, we unwrap the gel in the x direction and centerize the slab. Then the length of the simulation box is extended in the x direction to be larger than the difference of the maximum and the minimum coordinates in x . Once this is done, we start adding 3 layers of particles on either of the x side of the slab (represented by yellow color in Figure 5.11). The particles in the same layer as well as consecutive layers are connected to each other via harmonic bonds with equilibrium bond-length $r_{\text{struct}} = 0.957\sigma$ and $k_{\text{struct}} = 1000k_B T/\sigma^2$. Thus forming rigid structures on either side. An attractive Lennard Jones interaction between the particles of the rigid structure and monomers of the gel-strands are added:

$$V_{\text{Harmonic-struct}} = k_{\text{struct}} \left(r - r_{\text{struct}} \right)^2 \quad (5.8)$$

$$\begin{aligned}
V_{LJ} &= 4\epsilon \left[\left(\frac{\sigma_{LJ}}{r} \right)^{12} - \left(\frac{\sigma_{LJ}}{r} \right)^6 \right] & r < 2.5\sigma \\
&= 0 & r \geq 2.5\sigma
\end{aligned} \tag{5.9}$$

The value of σ_{LJ} and ϵ in equation 5.9 is chosen to be $\sqrt{2}\sigma$ and $1k_B T$ respectively. We now equilibrate the system for 200τ by applying a constant pressure of $0.02k_B T\sigma^{-3}$ along the x direction while not allowing the other dimensions to rescale. This compresses the rigid structure to come closer to the the gel slab and the strand monomers gets attracted to the rigid structures. After this, another short equilibration run for 50τ is done with the help of Langevin integrator. The position of the rigid structures are then unwrapped in the x direction. Now harmonic bonds (similar equation to 5.8) are added between the monomers of the gel-strands, if they are at a distance of $\sqrt{2}\sigma$ from the rigid structure. The bonded interaction strength between these two types of particles are chosen to be $k_{\text{struct-monomer}} = 1000k_B T/\sigma^2$ and the equilibrium bond length to be $r_{\text{struct-monomer}} = \sqrt{2}\sigma$. After adding the bonds, the LJ interaction between the gel-strand monomers and the rigid structures are removed and the system is equilibrated with a Langevin thermostat for 400τ . This completes the setup for 1D contraction experiment with the load, as shown in Figure 5.11. Once the gel with the rigid structure is set up, we simulate the behaviour of a load by applying a constant force on each particle in the rigid structure. The net force by the particles of the rigid structure is taken to be the total force applied or the value of load in simulations of 1D contraction.

5.2.3.1 Properties of passive gel

To compare the gels before and after molecular motor rotation, we conducted separate simulations without rotating them. This allowed us to assess important mechanical properties of a reference gel with non-rotating crosslinkers. First, we conducted the extension test: the gel slab was allowed to relax initially for 15000τ without any load and without switching on the motor. Once it reached equilibrium, force was applied on either of the rigid structures to pull them. The pulling simulation lasted for 34000τ , which equilibrated the gel under the load. Simulation box was also extended in the x direction to create a free boundary for the purpose of extension test. In both the relaxation and pulling simulations a pressure $P = 0.0k_B T/\sigma^3$ was maintained in the lateral directions using MTK barostat and thermostat. Figure 5.12(a) presents the extension of a reference gel as a function of the applied load. Initially the gel follows a Hookean behavior, where extension is directly

proportional to the applied force, but then it saturates, remaining almost constant despite the increasing force. The one-dimensional contraction simulations described in the coming section uses force values from the Hookean region of this plot. In Figure 5.12(b), the density of the gel under compression is plotted against applied pressure. This figure is plotted as a result of the compression test, where we applied forces to the rigid structures to compress a gel with passive motors. The final density of the gel from this simulation is noted down and used for Figure 5.12(b). This density is only mildly affected by the strand length and can reach values exceeding $1\sigma^{-3}$, which is significantly higher than the density limit observed in the contraction simulations described below.

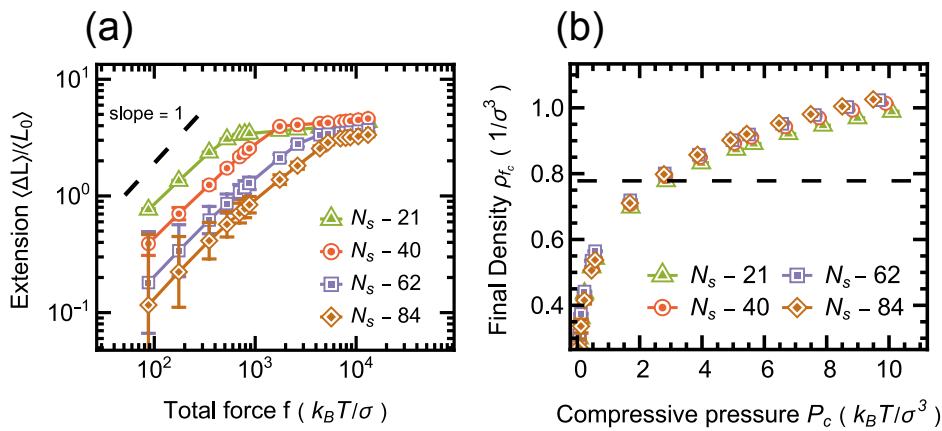


FIGURE 5.12: The relative extension $\langle \Delta L \rangle / \langle L_0 \rangle$ of the gel is plotted as a function of the applied load in the configuration illustrated in Figure 5.12 (a), where $\langle L_0 \rangle$ represents the initial extension of the gel. In panel (b), the density of gels under compression is shown as a function of compressive pressure. The dashed horizontal line represents the final density obtained in the one-dimensional contraction simulations after the molecular rotations were applied. In both panels (a) and (b), the simulations were conducted with molecular rotations turned off, while varying the strand lengths (N_s) as indicated.

5.2.3.2 Load Test

Before we start the rotation of the motors in the load test, the simulation box is extended along the x direction. In our simulations, we extended the box 200 times the initial box dimension along x . This creates an effect of free boundary conditions as described in Chapter 3. After extending the box along the x direction, the gel can be pulled and equilibrated under the applied force. (see Figure 5.13(a)). The equilibration of the gel with the load is done for a simulation time of 30000τ keeping the pressure along the lateral dimension at $0.0k_B T \sigma^{-3}$, using a MTK barostat. However, it has to be noted here that the

pressure along the lateral dimension is mostly set by the rigid structures, since the rigid structures can affect the resizing of the lateral dimensions of the simulation box during the application of the barostat. Thus, at the end of this process we have a gel system equilibrated under a particular load or force, to a length L_i . We vary the load applied to the gel from a value of $84k_B T \sigma^{-1}$ to $10^3 k_B T \sigma^{-1}$, i.e., in the Hookean regime of the force vs extension curve for the gel as seen in Figure 5.12(a). After equilibrating the system with the load, the motors are switched on and the contraction experiment is now done over a period of 220 rotation cycles, keeping the pressure along the lateral dimension to be $0.0k_B T \sigma^{-3}$, by enforcing a barostat. The rotation allows the gel to contract from an initial x dimension L_i , to a final x dimension L_f (see Figure 5.13(a)). Now from the displacement of the rigid-structures, we can calculate the 1D contraction ratio $\Delta x/L_i = 1 - L_f/L_i$, as a function of applied load (total force) for gels with different strand length N_s . Figure 5.13(b) demonstrates that the contraction ratio remains largely the same, regardless of the length of the strands, if the total forces acting on the gel is within the Hookean regime of the force vs extension curve. Once the forces exceeds the Hookean regime, the contraction ratio starts decreasing. This is likely due to the extended structures of the chains at high loads, which increases the difficulty of braiding the chain pairs. It is also to be noted that the values of the final relative contraction are significantly higher in the simulations compared to the experiments.

A key question arises: what physical effect restricts the relative contraction of the gel? An initial hypothesis might be that the gel's contraction is limited by excluded volume, suggesting that there is a critical density beyond which the gel cannot contract. To explore this, we plotted the monomer number density, ρ_f , in the gel's contracted state (Figure 5.13(c)). The density appears similar across various strand lengths and forces, though there is a higher variation in the limiting behaviour for shorter strand lengths.

To evaluate whether the density limit is set by excluded volume constraints, we examined the density as a function of compressive pressure in a gel with non-rotating crosslinking molecules (Figure 5.12(b)). These results indicated that the limiting density that we seen in the contraction experiment is not special; it is actually much lower than the maximum density achieved under high compression. Consequently, this suggests that excluded volume is not the major factor that limits gel contraction. Instead, it is more likely that the limitation arises from topological constraints, as previously proposed [103, 109] for a simpler, whirligig like systems.

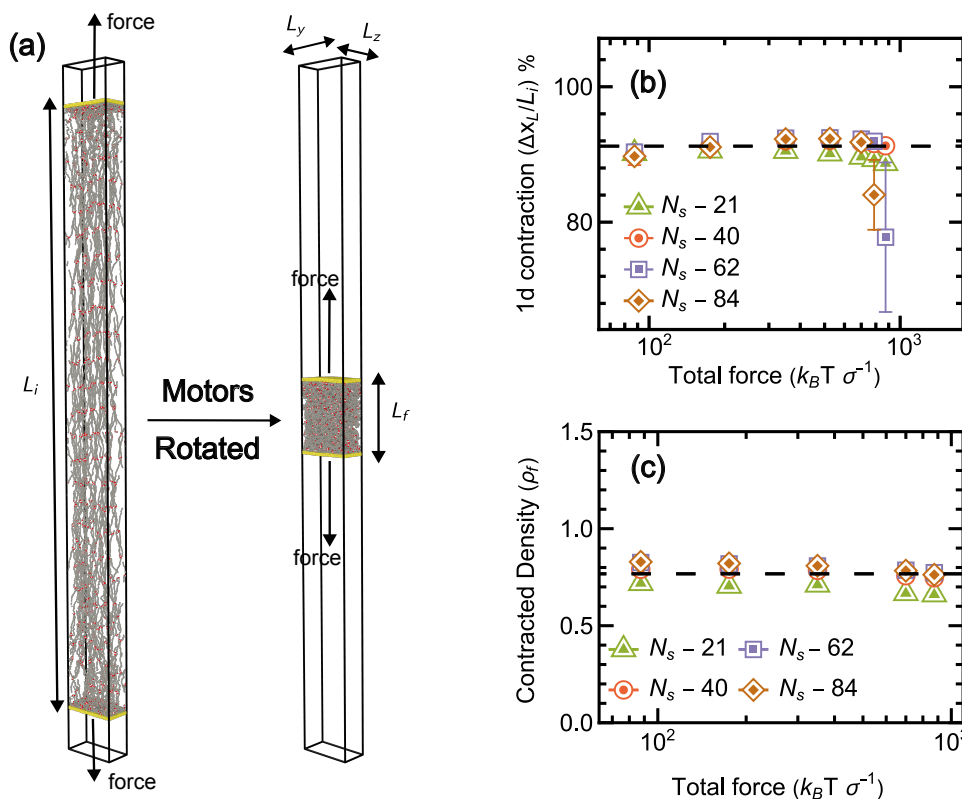


FIGURE 5.13: (a) Simulation snapshot showing the initial equilibrium extended state under load and contracted state after motor rotations. (b) Graphs illustrating one-dimensional contraction (as percentage) and (c) density in the contracted state, both plotted against applied loads. The simulation data are presented in units of $k_B T$ and bead size σ

5.2.3.3 Work and Torque

The work done in pulling the load is studied as a function of strand-length, using the setup mentioned above (see Figure 5.12(a)). We measure the displacement Δx of the rigid structures from the initially stretched configuration to the final contracted state in order to determine the work $f \cdot \Delta x$. Here f is the net force applied. Figure 5.14(a) shows that the work increases almost linearly with the strand-length of the gel, if the applied load is in the Hookean regime of the force-vs-extension curve. Initially the gels are stretched to their utmost limits prior to triggering the motor molecules, which prompt volume contraction. As a result, the effort exerted against the applied force is directly impacted by the elastic energy stored within the system. Given that the elastic energy is proportional to the polymer strand length, we observe a distinct linear correlation between the work performed and the length of the strands.

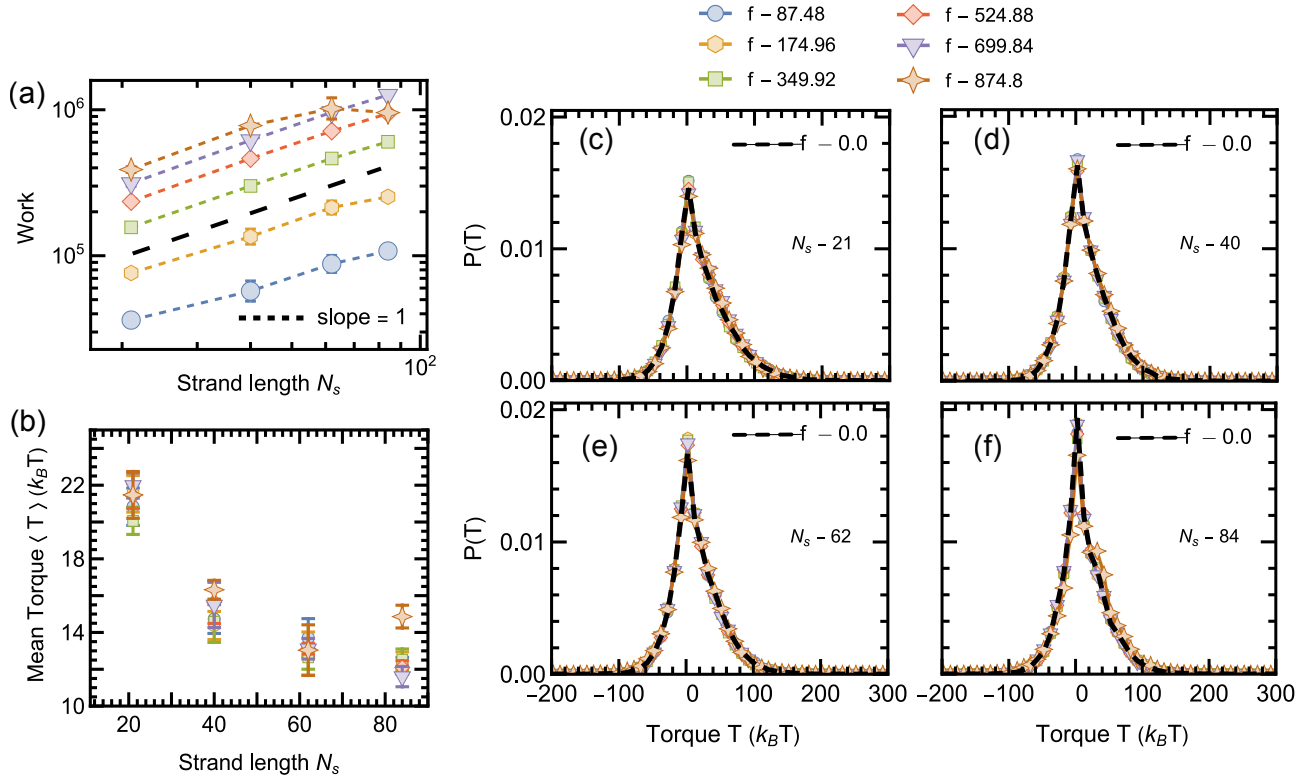


FIGURE 5.14: (a) The work done by the motors in pulling the load as a function of strand-length N_s , for different applied loads in Hookean regime. (b) The average torque applied by the motors in sustaining the contracted state as a function of N_s for different loads in Hookean regime. (c)-(f) shows the distribution of torques by the motor to sustain the system in the contracted state, for forces in the Hookean regime. The black dashed lines in (c)-(f) indicates the torque distribution at zero load.

Since we are using a model of rotors that do not unwind, we wanted to see the torque put up by the motors to sustain the contracted state for the different applied loads. The distributions, for the values of torque is shown in the Figure 5.14 (c)-(f). It shows that for all the forces in the Hookean regime, the torque distribution collapse onto one another. These overlapping distribution of torques, for different forces in the Hookean regime, implies that the loads have little to no effect on the torque given by the motors in this regime. This is confirmed by the torque distribution at zero load, which also overlaps with the other torque distributions (see Figure 5.14). The distributions of torques is clearly not Gaussian and shows a slightly wider spread among the positive torques. This implies that more motors want to unwind in the contracted state but is prevented due to the high activation barrier that provides a positive torque (since $\phi - \phi_{\text{ref}} < 0$). The negative values of torque means that $\phi - \phi_{\text{ref}} > 0$, i.e., the current configuration is oriented in the winding direction compared to the stable state ϕ_{ref} . So a negative torque is exerted to bring it

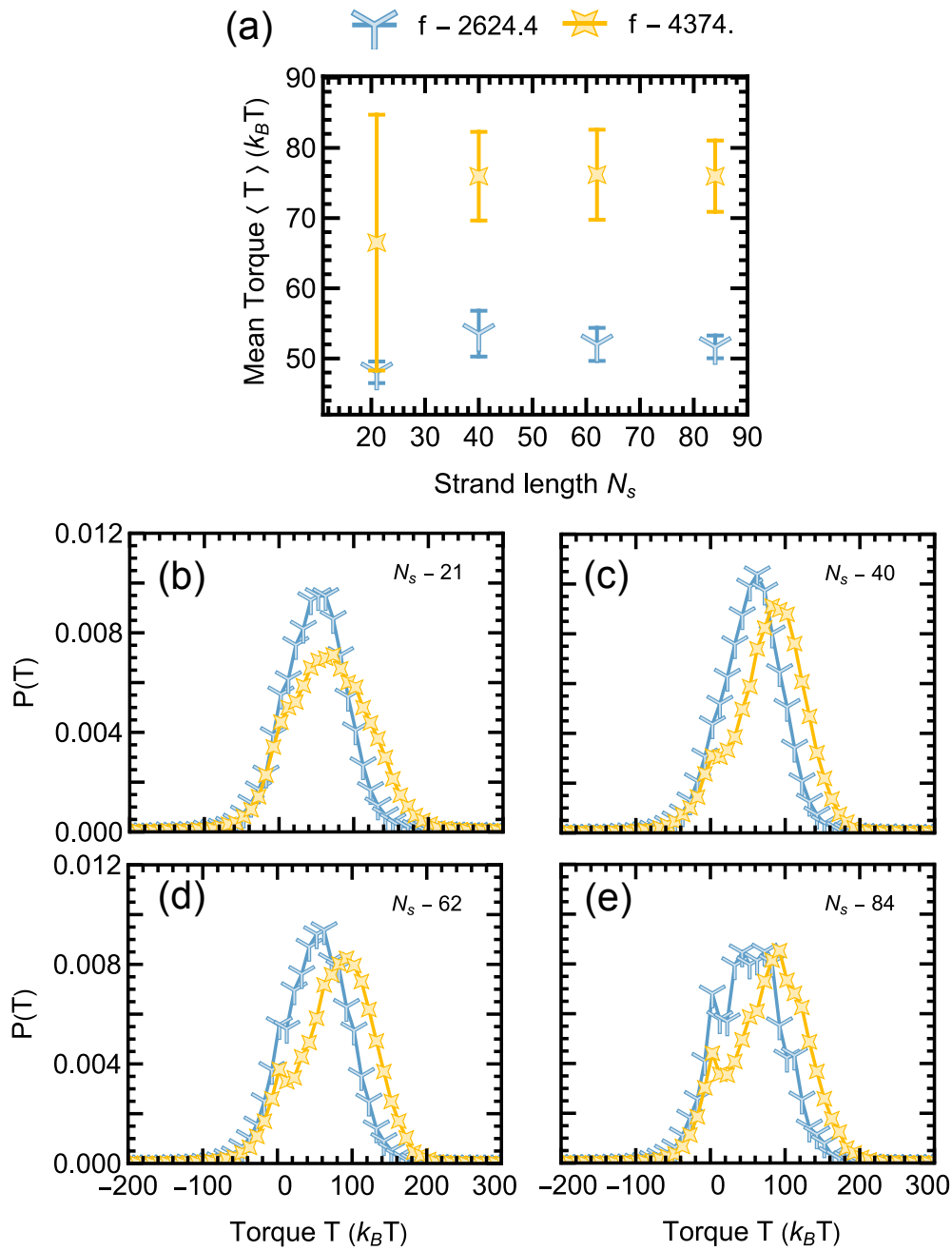


FIGURE 5.15: (a) Mean torque for the non-Hookean forces as a function of strand-length N_s . (b)-(e) The distribution of torques by the motor to sustain the system in the contracted state for the two forces in the non-Hookean regime.

back to the stable state. The torque distribution of motors when the loads are in the non-Hookean regime are shown in Figure 5.15 (b)-(e). The large values of load reduces the conformational entropy of the chains, because the number of possible configurations decreases as the chain becomes more extended. Hence it becomes increasingly difficult for the motors to create more braids in the chain pairs. The motors have the tendency to backflip as we observed previously under Hookean forces. The extended configuration of polymer chains due to the high loads, increases the motor's tendency to backflip even more. However, because our motor model does not allow for it to unwind, the motor generates larger torques to maintain its stable state, ϕ_{ref} . Hence the distribution of torques for non-Hookean forces, is centered around larger positive values. Figure 5.14(b) shows how the average torque in the contracted state varies with strand-length, we see that for the range of loads in the Hookean-regime, the torque increases with decreasing strand-length. A possible explanation could be that the shorter polymer strands have fewer entanglements compared to longer strands, as they cover less spatial volume and have fewer opportunities to intersect with neighboring chains. Hence for a larger N_s , the unwinding of molecules is already more difficult due to the higher number of links or entanglements between the chain pairs compared to smaller N_s . To overcome the ease with which the shorter chains can disentangle and thus unwind the motor, the motors attached to shorter strands will have to provide a larger positive torque in comparison to longer strands to prevent any unwinding and maintain the stable dihedral angle state ϕ_{ref} . In contrast to this we see that the average torque to sustain the contracted state is mostly independent of the strand-length, when the loads corresponds to the non-Hookean regime (see Figure 5.15 (a)). This is likely because the non-Hookean forces dictates the conformation of chains, and this has a greater impact on the braiding of the chains and the torque produced by the motors, in comparison to the strand length.

5.2.3.4 Measure of linking

The rotational motion causes twisting and bending in the attached polymer chains, which subsequently leads to the formation of entanglements between the chain pairs. In this subsection we will look at the entanglements of the system with loads. Normally one could use the concept of linking number for calculating the entanglements. The linking number, sums up the signed crossing (c_i) of the 2D projections of closed curves, to return an integer value for the degree of entanglement (see equation (5.10)).

$$L_k = \frac{1}{2} \sum_i c_i \quad (5.10)$$

However, applying this method to open chains necessitates creating a closing scheme [301, 47] for the chains, which would ultimately affect the value measured through equation (5.10), since different closing schemes would result in a different values. We utilize the Gaussian linking number (GLN), which eliminates the need for a closing scheme in its calculation. Consequently, we obtain a fractional value of the linking number, unlike the invariant values observed with closed links. The Gaussian linking number between two curves C_1 and C_2 was defined by Gauss [210] to be:

$$Lk_G(C_1, C_2) = \frac{1}{4\pi} \int_{C_1} \int_{C_2} d\vec{r}_1 d\vec{r}_2 \cdot \frac{\vec{r}_2 - \vec{r}_1}{|\vec{r}_2 - \vec{r}_1|^3} \quad (5.11)$$

Here \vec{r}_i refers to a point on the curve C_i . We use this concept to explore the entanglements between segments of chain pairs attached directly to the same rigid body of the motor. For this purpose, the integral in the above equation 5.11 was discretized by considering that the two curves are each composed of N piecewise straight segments:

$$Lk_G(C_1, C_2) = \frac{1}{4\pi} \sum_I^N \sum_J^N \Omega_{IJ} \quad (5.12)$$

where Ω_{IJ} is the solid angle formed by all those projections in which a pair of segments I and J appear to cross each other. Thus, for two straight segments $I, I+1$ and $J, J+1$, we can use the Van Oosterom and Strackee equality to obtain the solid angle formed by the vectors $\mathbf{k}, \mathbf{l}, \mathbf{m}$ and \mathbf{n} . Thus, the solid angle formed by the square pyramid made of vectors \mathbf{k}, \mathbf{l} and \mathbf{m} is given by:

$$\Omega(\mathbf{k}, \mathbf{l}, \mathbf{m}) = 2 \arctan \left(\frac{[\mathbf{k}, \mathbf{l}, \mathbf{m}]}{|\mathbf{k}||\mathbf{l}||\mathbf{m}| + \mathbf{k} \cdot \mathbf{l}|\mathbf{m}| + \mathbf{m} \cdot \mathbf{k}|\mathbf{l}| + \mathbf{l} \cdot \mathbf{m}|\mathbf{k}|} \right) \quad (5.13)$$

Here $[\mathbf{k}, \mathbf{l}, \mathbf{m}]$ is the scalar triple product of vectors $\mathbf{k}, \mathbf{l}, \mathbf{m}$ and $|\mathbf{k}|$ is the magnitude of the vector \mathbf{k} . Hence, the solid angle made by all those views in which two segments $(I, I+1)$ and $(J, J+1)$ apparently cross is given by:

$$\begin{aligned} \Omega_{IJ} = & 2 \arctan \left(\frac{[\mathbf{k}, \mathbf{l}, \mathbf{m}]}{|\mathbf{k}||\mathbf{l}||\mathbf{m}| + \mathbf{k} \cdot \mathbf{l}|\mathbf{m}| + \mathbf{m} \cdot \mathbf{k}|\mathbf{l}| + \mathbf{l} \cdot \mathbf{m}|\mathbf{k}|} \right) \\ & + 2 \arctan \left(\frac{[\mathbf{m}, \mathbf{n}, \mathbf{k}]}{|\mathbf{m}||\mathbf{n}||\mathbf{k}| + \mathbf{m} \cdot \mathbf{m}|\mathbf{k}| + \mathbf{k} \cdot \mathbf{m}|\mathbf{n}| + \mathbf{n} \cdot \mathbf{k}|\mathbf{m}|} \right) \end{aligned} \quad (5.14)$$

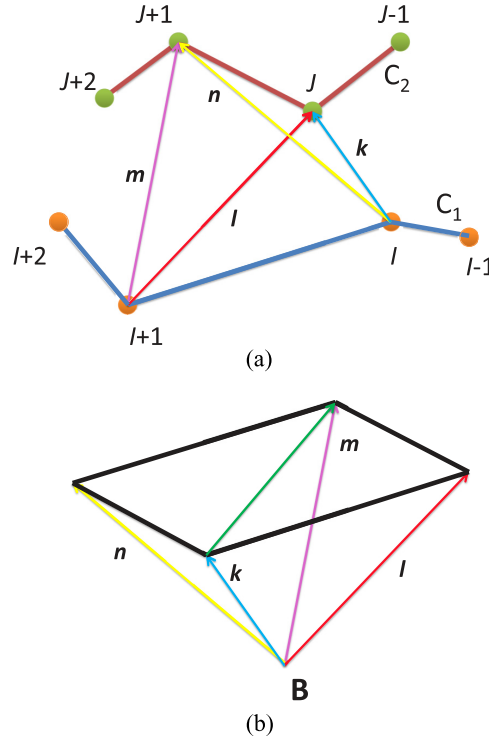


FIGURE 5.16: Calculation of the solid angle Ω_{IJ} between segments I and J , bounded by $I, I + 1$ and $J, J + 1$, respectively, involves the vectors $\mathbf{k}, \mathbf{m}, \mathbf{n}$, and \mathbf{l} shown in (a). The solid angle Ω_{IJ} formed at B in (b) is calculated using $\Omega(\mathbf{k}, \mathbf{l}, \mathbf{m})$ and $\Omega(\mathbf{k}, \mathbf{m}, \mathbf{n})$ as in Equation (5.14). "Reprinted figure with permission from Rasool Ahmad, Saptarshi Paul, and Sumit Basu, Phys. Rev. E, **101**, 022503(2020). Copyright (2020) by the American Physical Society." <https://doi.org/10.1103/PhysRevE.101.022503>.

We use equation (5.14) to determine the solid angle in order to determine the Gaussian linking number between segments of chain pairs directly attached to the same rigid-body forming the motor. Here we will use the method deployed by A. Rasool et al. in [7] for getting the local entanglements of these chain pairs.

In this method we first find the distance between the monomers of the chain pair. If the distance is less than $d_c = 2\sigma$, a predetermined threshold distance, the segments around these two points can potentially be entangled. This step helps us to disregard the pairs that are definitely not entangled and identify the one that are entangled. For example in Figure 5.17, A' and A are close. Thus we select the segments $B'-A'-C'$, and $B-A-C$ having approximately $2N_c$ atoms. Each of these segments $B-A$, $A-C$, $A'-C'$ except $B'-A'$ have N_c atoms. $B'-A'$ lying close to chain ends have less than N_c atoms (see Figure 5.17). The value of N_c was chosen after experimenting with various values of it, for all the strand lengths we used in the simulation. If N_c chosen was smaller than 3, the algorithm ended

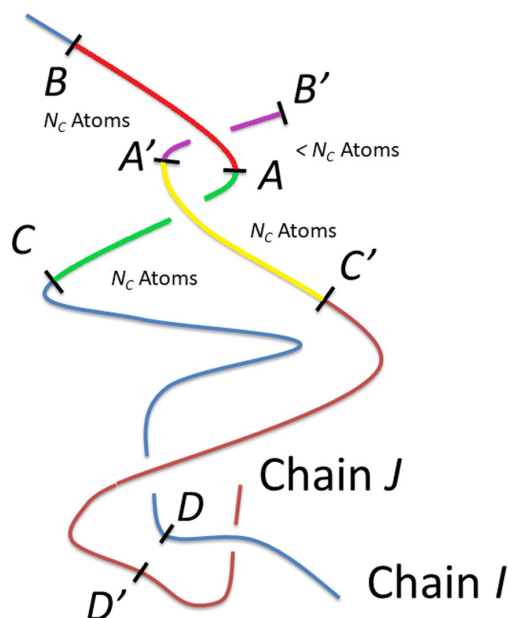


FIGURE 5.17: Definition of quantities involved in calculating Lk_G between segments of two chains I and J . "Reprinted figure with permission from Rasool Ahmad, Saptarshi Paul, and Sumit Basu, Phys. Rev. E, **101**, 022503(2020). Copyright (2020) by the American Physical Society." <https://doi.org/10.1103/PhysRevE.101.022503>.

up doing some redundant calculations. The redundant calculations happen because the segments of the chain pair, which should have formed a single entanglement gets divided into two or more entanglements due to the smaller value of N_c . When N_c was larger than 4 beads, it merged the entanglements that are located far apart along the two chains (which should not be done). Especially for smaller strand length $N_s = 21$, choosing $N_c = 5$ beads or above would mean considering more than half the chain length ($2N_c$) for every calculation of local GLN. Hence in our analysis we have chosen $N_c = 3$ beads, which is not too small nor too large. This way we find the local GLN values for all segments whose beads are below a cutoff distance d_c apart. Doing this for all the chain pairs attached to the molecules, we can get the local entanglement values. In Figure 5.18 we show a 2D plot for the local GLN values. The x and y axis are the bead ids (representing beads from the two chain pairs) with bead id coordinate $(0, 0)$ representing the attachment point of the chain pairs to the same rigid-body constituting the molecule.

The colors in this 2D plot represent the absolute value of local GLN obtained from our analysis described above. We average the absolute value of local GLNs for all chain pairs in the system, also averaging over different configuration. Figure 5.18 shows this for gels with strand length $N_s = 21$ (top) and $N_s = 84$ (bottom) under different loads.

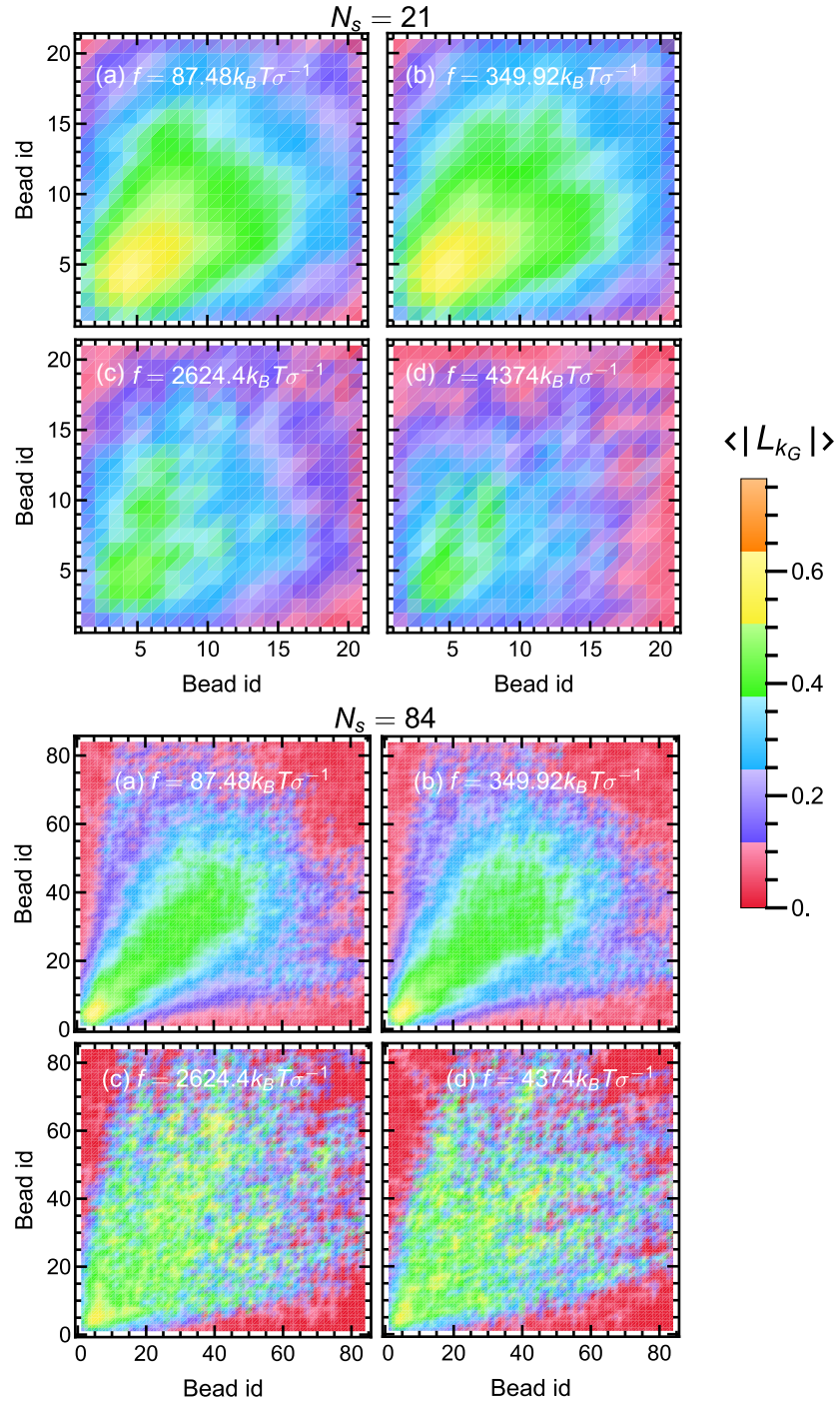


FIGURE 5.18: $\langle |L_{KG}| \rangle$ in the contracted state for different applied loads for gels with $N_s = 21$ (top) and $N_s = 84$ (bottom). Loads $f = 87.48, 349.92 k_B T \sigma^{-1}$ in (a)-(b) are in the Hookean regime, whereas loads $f = 2624.4, 4374 k_B T \sigma^{-1}$ in (d)-(c) are in the non-Hookean regime.

Comparing the local GLN values for $N_s = 21$ and $N_s = 84$, we see that the longer strands have more contact points and hence we see a wider spread for local GLN values across the bead-ids in Figure 5.18 (b). This is also in agreement with what we discussed in the previous subsection 5.2.3.3 about the longer strands having more entanglements. One can also notice that the stronger entanglements are found in the segments attached directly to the motor indicated by yellow color in Figure 5.18 (a)-(b) (top and bottom). This happens because of the high torsional force experienced by the segments near to the motors compared to others, forcing them to intertwine and entangle with the neighboring segments more, as compared to segments far away. We also noticed that for larger loads (total force f) in the non-Hookean regime, the entanglements become less strong, as indicated by the disappearance of the yellow color patch, and the presence of green and blue patches. This is as a result of strong pulling by the load which affects the chain conformations, as explained in the previous sub-section 5.2.3.3. This decrease in the local GLN values for larger loads are also reflected in the 1D contraction ratio.

5.2.4 Effect of stiffness on a free motor-gel

The following are preliminary results on the study of a free molecular motor gel, in which the stiffness of the polymer strands was varied. We will present the results in this subsection as a function of k_{stiff} , which is the strength of the bending potential (see eq. (5.15)) between consecutive triplets of beads in a polymer strand of the gel. Here $\theta_0 = \pi$ according to "HOOMD" conventions, such that straight configurations are energetically favored.

$$V_{\text{stiff}} = 0.5k_{\text{stiff}}(\theta - \theta_0)^2 \quad (5.15)$$

5.2.4.1 Size ratio

Figure 5.19 (a)-(d) shows the size ratio has a function of time for a given strand length N_s , with different values of stiffness parameter, k_{stiff} . The light blue colored circle marker in the plots, represent $k_{\text{stiff}} = 0$, i.e., chains that are highly flexible. The size ratio, has expected decreases with time for all values of stiffness parameters used and at later times it saturates. However we see that the value to which it has contracted to, for a given N_s , changes with the value of k_{stiff} in a non-monotonic fashion. This non-monotonic change in the size ratio as a function of k_{stiff} is shown in Figure 5.20 (a)-(d) for various strand lengths. All the systems with different strand lengths that we studied follows a

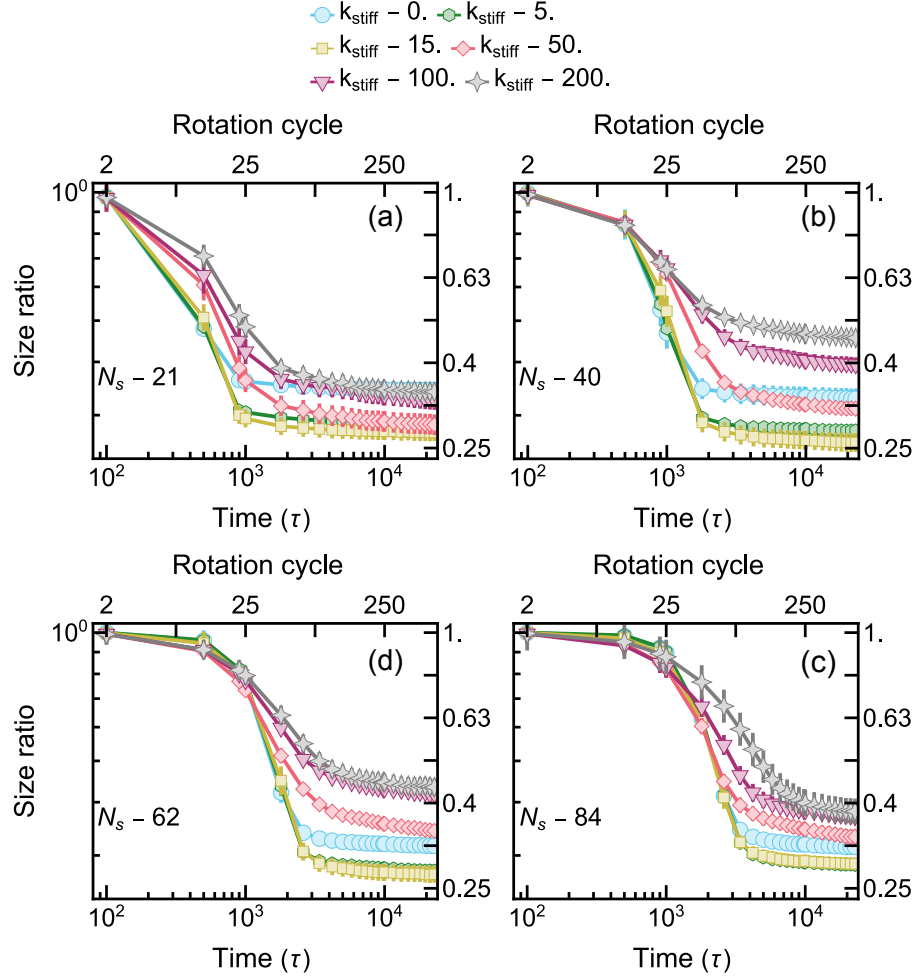


FIGURE 5.19: (a)-(d) Time evolution of the size ratio of free motor-gels with different stiffness parameter k_{stiff} for $N_s = 21, 40, 62, 84$ respectively.

similar trend: the size ratio decreases as k_{stiff} increases, but starts to rise again around $k_{\text{stiff}} = 10 - 15\epsilon$. Further increase of k_{stiff} only increased the size ratio. From Figure 5.20 we can see that, except for the shortest strand length $N_s = 21$, for all the other strand lengths, the increasing size ratio crosses the value of size ratio at $k_{\text{stiff}} = 0\epsilon$ (indicated by the black dashed lines) around $k_{\text{stiff}} = 50\epsilon$. For $N_s = 21$, increasing k_{stiff} simply brings the size ratio closer to what it is at $k_{\text{stiff}} = 0\epsilon$.

To see the underlying conformations of the polymer strands, we plotted the distribution of the normalized radius of gyration Rg_s/Rg_{s_0} of the gel strands as shown in Figure 5.21(a)-(h). Here Rg_{s_0} refers to the radius of gyration of an ideal chain of length N_s and if $Rg_s/Rg_{s_0} = 1$, it means that the strands are adopting an ideal chain conformation. Plots (a)-(d) illustrates the distribution of normalized radius of gyration ($P(Rg_s/Rg_{s_0})$) of these

strands before the motors started rotating, whereas (e)-(h) shows the distribution of the same strands in the contracted state. Clearly we see a decrease in the values of radius of gyration of the strands (Rg_s) after contraction for all values of k_{stiff} . $P(Rg_s/Rg_{s_0})$ for highly flexible chains is shown in Figure 5.21, and as indicated by the initial and the final $P(Rg_s/Rg_{s_0})$ for such strands, the peak of the distributions shifts from values greater than one to values more close to one. This indicates that some of the highly flexible strands adopts an ideal chain configuration after contraction. However, this shift in the

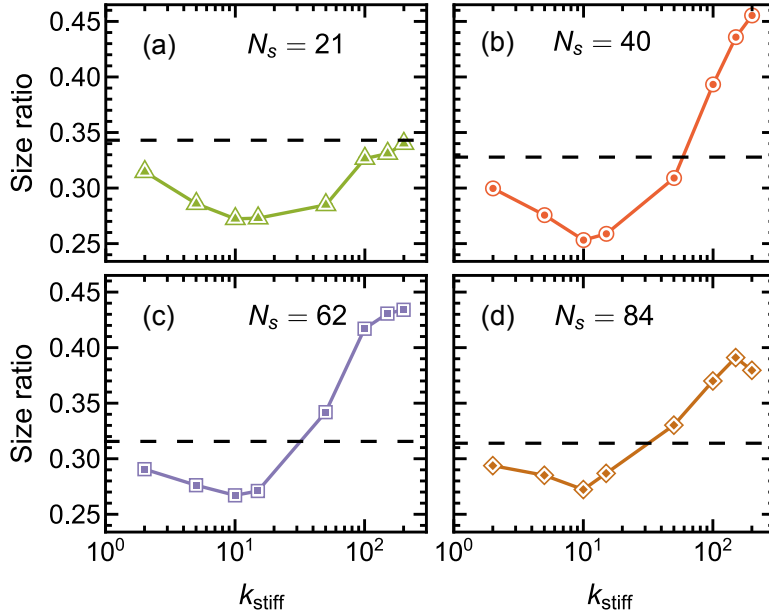


FIGURE 5.20: (a)-(d) shows the non-monotonic change of the final size ratio as a function k_{stiff} , for systems with different strand-length N_s . The x axis is in logscale. The black dashed lines represents the size ratio at $k_{\text{stiff}} = 0$ for a given N_s .

distribution for $k_{\text{stiff}} = 0\epsilon$ is smaller compared to what we observe for $k_{\text{stiff}} = 15\epsilon$. For example, for $k_{\text{stiff}} = 15\epsilon$, the peak of $P(Rg_s/Rg_{s_0})$ for all N_s shifts from values in the range $Rg_s/Rg_{s_0} = 3 - 5$ to values in the range $Rg_s/Rg_{s_0} = 1 - 1.2$, resulting in a final distribution that closely overlaps with that of highly flexible chains. This larger shift in the conformation of polymer strands likely contributes to the smaller saturated size ratio of the gel observed for $k_{\text{stiff}} = 2 - 15\epsilon$ compared to highly flexible strands (see Figure 5.20 or 5.19). For $k_{\text{stiff}} = 50\epsilon$, the initial $P(Rg_s/Rg_{s_0})$ sharply peaks at values larger than 1, but the distribution broadens after the gel contracts. However, the final configurations of the strands are still extended compared to the ideal chain configurations, as indicated by Figure 5.21, with the peak of the final distributions still lying at $Rg_s/Rg_{s_0} > 1$. Hence the size ratio of the gel as seen for $k_{\text{stiff}} = 50\epsilon$ in Figure 5.20 is larger compared to $k_{\text{stiff}} = 10 - 15\epsilon$. For $k_{\text{stiff}} = 100 - 200\epsilon$, the distribution only broadens after contraction of

the gel, with most of the strands lying in the extended configuration. Since most chains are still in the extended state as indicated by the distribution in Figure 5.21 (e)-(h), the size ratio is larger than or equal to the size ratio of the highly flexible chains.

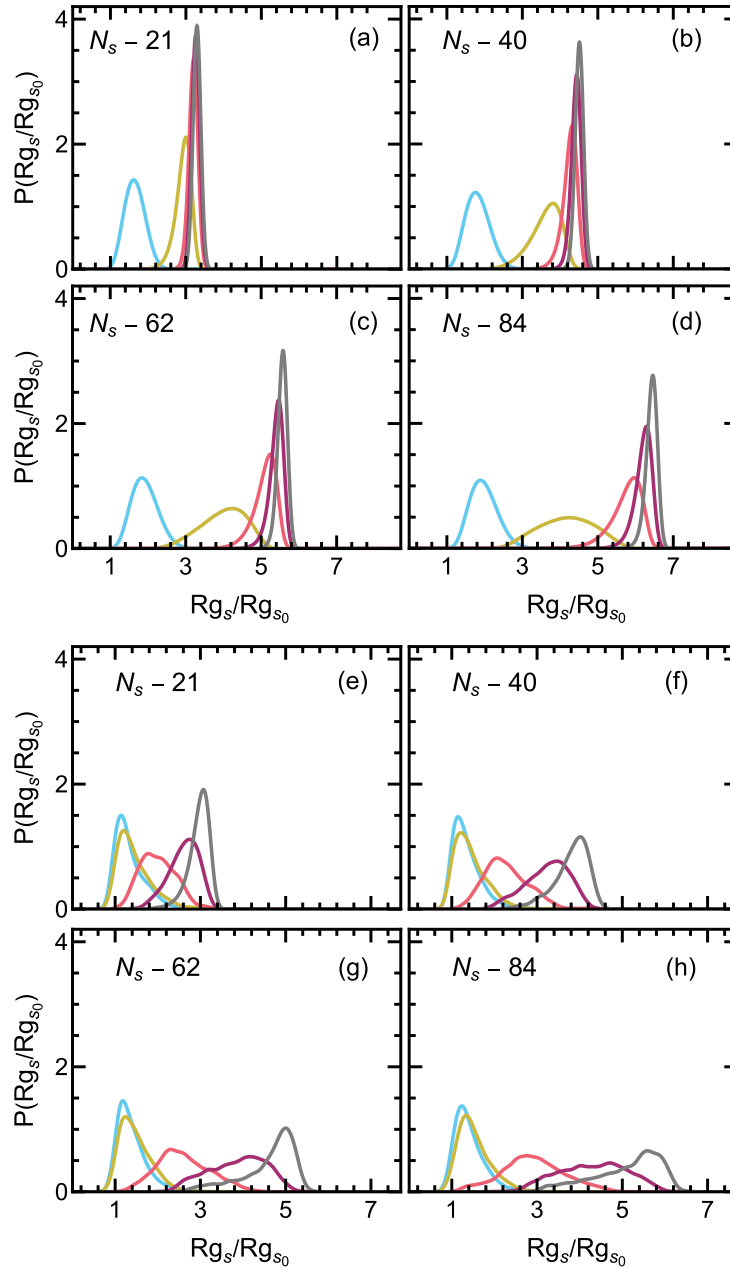


FIGURE 5.21: (a)-(d) Distribution of normalized radius of gyration of polymer strands of the gel before it starts contracting and (e)-(h) distribution of normalized radius of gyration of polymer strands of the gel before after the gel contraction, for different k_{stiff} for systems with different strand length N_s .

5.3 Conclusion and outlook

In conclusion, the advanced precision of our polymerization methodology allowed for the facile conversion of synthesized polymers into gels via standard cross-linking reactions. These techniques were able to produce gels that were quasi-ideal, which enabled us to understand the photo-driven contraction created by the twisting of the chain pairs attached to the molecular motors. The experimental investigation led by Dr. Yao revealed that, while similar total contraction ratios independent of degree of polymerization was achieved, the contraction speed exhibited non-linearity dependent on the motor density due to the compromise between optical density, light attenuation, and motor density. To have a deeper understanding, we developed a MD simulation framework that accurately captured the essence of light-induced contraction. A model for the rotor with a very high activation barrier was also created, just for this purpose. Thus imposing uni-directional rotation even under high strain or internal torque. The computer simulation showed an increased speed in volume contraction as the motor density increased, and thus helped to clarify that the experimentally observed non-linearity in contraction speed arises from sample thickness effects. In the simulations, we further extended the experiments by attaching loads to gel system. A variety of gel systems with varying strand lengths were selected for this load study, revealing that, irrespective of motor density/ strand length, the contraction ratio remains almost same for these system. This observation holds true for the present model of the motor that disallows unwinding. We further used simulations to infer that the excluded volume do not have a role to play for almost constant and consistent contraction behaviour that we see from the load test. This lead us to conclude that the topological limitations are in fact the cause of this constant contraction ratio.

Further, our analysis illustrated the linear increase in work by the motors, with increasing strand-length for any given force/load in the Hookean regime. One could conclude that the linear increase in work with strand-length, draws from the elastic energy harbored in the system. Additionally, the distributions of torques for different loads in the Hookean regime collapse on to one another. We see from the torque distributions that the number of molecules applying positive torque is slightly greater than the number of molecules applying negative torques, indicating that the molecules inherently wants to unwind, but is prevented by the large activation barrier which provides a positive torque to the counteract this unwinding tendencies of the molecules. Negative torques are fewer in number compared to the positive torques, implying that the dihedral angle state of such molecules are slightly greater than the value for stable state, i.e., ϕ_{ref} . Overall on an average, the molecules apply positive torque in-order to sustain contraction. This

torque, in the range $(10 - 22k_B T)$ is however very large compared to what is determined experimentally ($\approx 2k_B T$) [109]. This is probably a result of us choosing a non-backflipping model for the motor. Further, we notice that the average torque decreases with increasing strand-length, because there are larger points of contact between the chain pairs and hence more entanglement for longer strands. Thus the tendency to unwind, for motors attached to longer strands is lesser compared to those attached to shorter N_s . Hence, the motors connected to shorter strands apply a larger torque to maintain the stable dihedral state ϕ_{ref} . The stretch of entanglements/ windings for longer strands is also confirmed by the Gaussian linking number analysis. It also shows that the systems with loads in the non-Hookean regime experience weaker entanglements, spread unevenly through out the chain pairs. We then extended this study to "stiffer gels", i.e., free polymer gels having stiffer strands. Our preliminary analysis of the size ratio as a function of time, for stiffer gels confirmed the contraction of gels even when the stiffness parameter for the strands were quite high. However, the saturated size ratio showed a non-monotonic behaviour as we varied the stiffness. As the stiffness increased, the saturated size ratio decreased, i.e., the size ratio became lesser compared to the highly flexible chains, till a certain value of stiffness parameter is reached, after which it started increasing. With further increase in stiffness parameter, the size ratio grew, reaching values greater than or equal to the value for highly flexible chains. Our examination of the distributions of the "scaled radius of gyration" for the strands, indicates that the non-monotonic size ratios are probably due to how significantly these distributions changed, following contraction, in comparison to their original states. In other words, it depends on whether the strand distribution transitioned from an elongated state to a more condensed one or stayed closely resembling its initial state.

Here we studied an ideal network with an ideal motor as cross-linker, which would not unwind. However in a real motor-gel, the molecular motors can start unwinding due to the accumulation of internal torque as the chain pairs wind/ entangle with each other [109]. In the future work, we will be looking at motors with finite activation barrier of around $44k_B T$, instead of the very large activation barrier of around $450k_B T$ which was considered here. It will be interesting to know in such a case, whether the size ratio and contraction ratio will remain the same, or whether it will decrease because of the backflipping of the motors, creating chain unwinding. Furthermore, studying the effect of chain stiffness in the unwinding case will also be important to know how much the stiffness could actually effect the contraction ratio. Another potentially interesting factor is the volume of the polymer backbone. The gel strands in the experiment have side chains of three carbon atoms, therefore it would be important to investigate how varying the side

chain length affects the winding of the chains and hence the contraction ratio. It is also intriguing to explore gels possessing a higher polydispersity index and analyze how the gel's topology influences the entanglement of chain pairs.

Chapter 6

Tandem project - lab Work

6.1 Introduction

As part of the GRK-2516 program, PhD students were requested to complete a tandem project, fostering collaboration between simulators and experimentalists over a specified period. This chapter offers a concise overview of the project and details the procedures I followed during my tenure in Sebastian Seiffert's lab.

6.2 Brief explanation of Microfluidics

Microfluidics allows liquids to be precisely manipulated on minute scales [318]. Using integrated channels made from glass, polymers, or silicon – these instruments guide fluid movement to an accuracy of micrometers. A key application of microfluidics is the production of a single or double emulsion droplets. In a single emulsion [221, 61, 12] droplet an internal material is enveloped by a layer made from a different materials, where as in the case of a double emulsion [142, 174, 329] internal material is sandwiched between an enveloping layer and external shell. By regulating the flow rate and dimensional parameters, uniform droplets of targeted size, shape, and composition can be systematically synthesized. Subsequent treatment like cross-linking, evaporation of liquid contents, or photopolymerization hardens the encapsulating layers while removing interior fluids, resulting in solid core-shell constructs. These synthetic particles find broad use in drug delivery, micro-encapsulation, and chemical sensing. Therefore, by controlling fluids and

suspensions on a microscopic level, microfluidics enables generating multifaceted yet precisely specified particles applicable to fields including material science, biotechnology, and medicine.

6.3 Aim

The aim of this work was to produce sufficient quantities of core gel and shell polymers to later prepare the core-shell microgel particles. The procedure for the preparation of the shell polymers and the core gel particles along with core-shell particles will be mentioned below. Both the core and the core-shell particles are prepared through micro-fluidic experiments.

6.4 Methods

For creating the core-gel, shell polymers and core-shell particles, we followed the procedures given by Seuss et al., in the reference [270], with minute changes. The procedures for all of this will be given below:

6.4.1 Shell-polymer synthesis

We start by dissolving 7.93 g of acrylamide (AAm) (111.55 mmol) and 0.77 g of DMMI-AAm (3.45 mmol) in 250 mL of water to achieve a total concentration of 0.46 mol/L [265]. The resulting solution was purged with argon gas for 30 minutes at room temperature. To regulate the molecular weight of the polymers, 0.35 g of sodium formate was added as a chain transfer agent [96]. Then 4.6 mL of aqueous stock solutions of ammonium persulfate (APS) (0.2 mol/L) and tetramethylethylenediamine (TEMED) (0.5 mol/L) was introduced into the mixture. The reaction mixture was stirred under argon atmosphere at room temperature and samples were taken every 30 minutes after adding an excess amount of methanol to observe the precipitation of p(AAm-co-DMMIAAm). When the precipitation starts becoming visible (after around 120 minutes), the reaction was terminated by adding 750 mL of methanol. The precipitate was then filtered by adding 3 wt% hydrochloric acid (25 wt% HCl in water). The crude polymer obtained is now dissolved in water, then dialyzed against water for a week and finally freeze-dried. In the end, we will be left with a fluffy white solid which weigh 25% (2.18 g).

6.4.2 Fabrication of glass micro-fluidic device for core-gel preparation

To create the cores we used a glass-microfluidic device, the procedure for preparation of such a device will be given below.

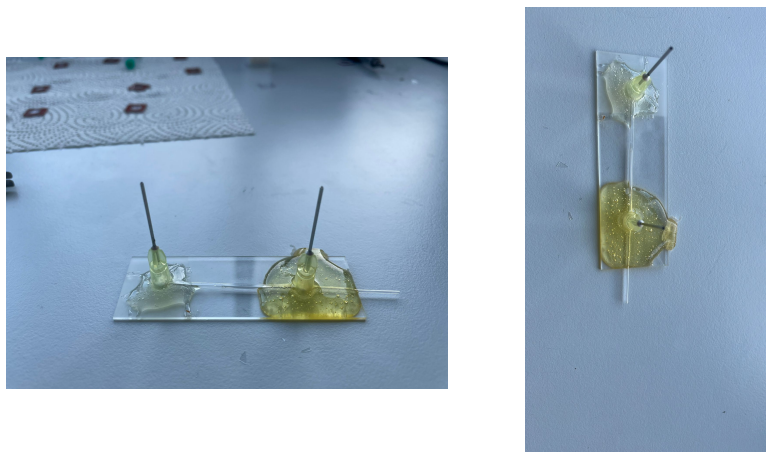


FIGURE 6.1: The in-house glass microfluidic device made for the core fabrication procedure.

A standard microscopic slide is used as a base for a simple single-emulsion glass capillary microfluidic device. We then take a microcapillary, with square cross-section having an inner 1.102 mm and outer diameter (1.35 mm) and scratch a breaking line into the middle of the capillary using a diamond scratcher. This is then placed on to the microscopic slide mentioned before. A glass capillary with circular cross-section having an inner and outer diameter of 0.58 mm and 1 mm respectively is placed inside a pipette pulling machine that can create two halves with tapered orifice each. Using one of these pulled capillary halves the device preparation can be continued. For this we extend the tapered orifice of the capillary half by rubbing it with sand-paper and removing the glass dust by blowing on it. After the smoothing procedure, we are left with a tip of the capillary having a diameter of $200\mu\text{m}$. Once the desired tip size for the circular capillary is achieved, the device is dipped in octadecyltrimethoxysilane. This process makes the silane react with the glass surface and cover it with hydrophobic octadecyl chains, thus making sure that only the respective outer phases in the microfluidic experiment wets the capillary walls, but not the inner phase, further helping the droplet formation. Chloroform is used to remove the excess reagents on the capillary walls, followed by a flushing of isopropanol and drying using air-flow. Now we place the tapered end of the round capillary at the

middle of the glass slide such that the un-tapered end is protruding out of the glass-slide's edge. Similarly the open end of the square capillary is placed 2 cm away from the round-capillary orifice. After this, two syringe tips on which a little cut has been made by a mini-grinding machines is used to inject the fluids into the device. These syringe tips are placed, one on the open end of the square capillary and the other on the little gap between square and the round-capillary. The placements of these syringe tips should cover the fluid inlets completely. Syringe tips are fixed and sealed using epoxy glue, first applying the glue from the sides and later at the cuts/ gates made on the syringe tips. The round capillary end sticking out of the glass-slide is also glued using epoxy mixture. This completes the single emulsion device, and it can now be used by injecting a continuous phase on the inlet at top of the gap between the two capillaries, whereas the dispersed phase can be injected into the inlet on the top of square capillary open end. The resulting emulsion will go through the round capillary, over whose end a piece of tubing may be put to collect the emulsion in a collection vial.

6.4.3 Microfluidic Fabrication of Core gel particles

A 10 mL solution comprising of NIPAAm monomers with 1 mol % of the cross-linker N,N'-methylene-bis(acrylamide) (BIS) formed the aqueous phase. The APS which is an initiator for the polymerization was also added to the aqueous phase at a concentration of 8g/L. A flow-focusing method was then used to emulsify the aqueous phase using an organic phase containing low viscous paraffin oil and 8 wt% Grindsted PGPR 90 Kosher as surfactant. The flow rates for NIPAAm-BIS solution and the organic phase was set to 1.5 mL/hr and 4 mL/hr. The droplets formed during this process was collected into a vessel containing TEMED and organic phase which would start the polymerization. This solution containing the droplets were stored for about 24 hours so that it could undergo complete polymerization. After this the solution was removed of the excess paraffin oil and other chemicals by rinsing with isopropanol and acetone. The product that remained after the clean up procedure was placed in distilled water creating swollen cores.

6.4.4 Microfluidic fabrication of core-shell particles

To create core-shell particles, we start by taking 100g L⁻¹ concentration of p(AAm-co-DMMIAAm) solution with a very low content of triplet photosensitizer sodium 2,7 - thioxanthonedisulfonate. This was later used to encapsulate the p(AAm-co-BIS) core

microgel. As a precaution to prevent any gelation of p(AAm-*co*-DMMIAAm) during the core-shell preparation due to the ambient light, the microfluidic device along with the tubings were wrapped in aluminium foil. Octadecyltrimethoxysilane was also coated on the tubing to make it hydrophobic. Using low viscous paraffin oil containing 10wt% of the modified polyetherpolysiloxane surfactant ABIL EM 90 as the continuous phase, core-shell premicrogel was created. During this process the flow rates of pNIPAAm microgels were continuously adjusted between $100\mu\text{L/h}$ to $1000\mu\text{L/h}$. The flow rates of pAAm-*co*-DMMIAAm and paraffin oil was chosen to be $200\mu\text{L/h}$ and $500\mu\text{L/h}$ respectively. After the droplets exited the device, they were exposed to UV light of wavelength 365nm using UV lamp (OmniCure series 1500) and collected in vial. The microgel emulsion collected in the collection vial, was washed thoroughly to remove the paraffin oil.

6.5 Result

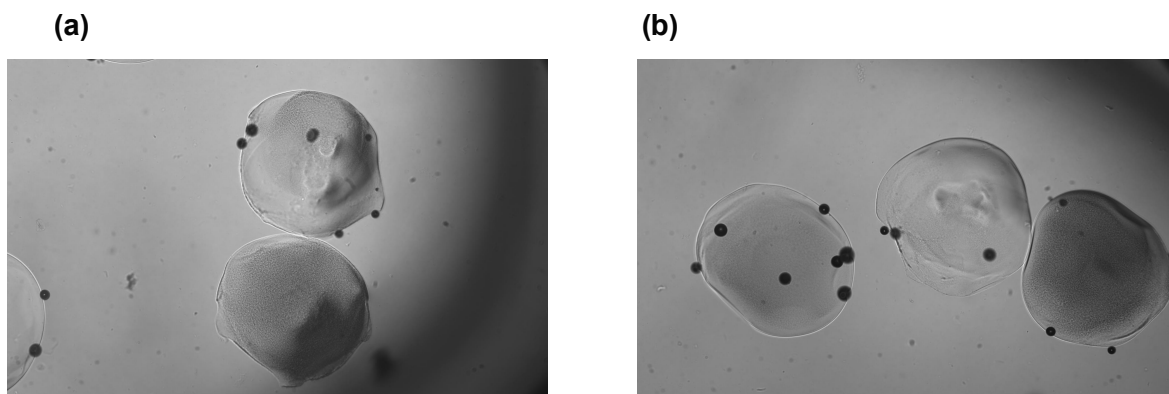


FIGURE 6.2: (a)-(b) Different sample cores of size approximately $700\mu\text{m}$ produced during the micro-fluidic experiments.

Sufficient quantity of shell polymers were prepared following the modified procedure mentioned in the subsection 6.4.1. To prepare the core particles we first created several iterations of glass-microfluidic devices using the procedure described in subsection 6.4.2. See Figure 6.1 showing a device which we created for core synthesis. Although some of these devices developed leaks, due to the improper gluing of the syringe tips with the glass-slides, about 90% of them could still be used for the fabrication of core particles. The device was thus able to produce a narrow size distribution of droplets with large yield owing to the high flow-rates. The high flow rates however also affected the shape of the cores, as it was not exactly spherical anymore. This is shown by the Figure 6.2 which

was roughly $700\mu\text{m}$ in diameter. We also tried to create core-shell microgels, however it resulted in failures as it either created particles with no core in it or multiple cores. We believe that this is caused by the flow-rates used for the core-shell synthesis.

6.6 Summary

We discuss the methods of preparation of non-thermoreponsive shell-polymers followed by the fabrication of glass micro-fluid device for core gel particle preparation. The method of preparation of core-shell particles are also discussed. Although the preparation of the shell polymer solution and the cores were successful, creation of core-shell particles did not work out. The problem might be stemming from flow-rates which is quite high and hence difficult to control. Thus the project enabled me to have an idea about the synthesis procedure of these particles and the typical problems that may arise during it's synthesis.

Chapter 7

Summary

Polymer gels are fascinating materials that combine the properties of both solids and liquids, making them incredibly versatile in various applications, from everyday products to advanced technologies. A subset of polymer gels include, the stimuli-responsive gels, which are created by cross-linking stimuli-responsive polymers or by integrating stimuli-responsive cross-linkers into a polymer matrix. Two popular choices of stimuli are temperature and light, because they offer precise and controllable ways to manipulate the properties of materials in real time. To this end, several innovative stimuli-responsive gels, for example core-shell microgels, where the core is thermo-responsive and shell is temperature insensitive, as well as molecular motor gels created by incorporating a polymer matrix with light responsive molecular motors have been synthesized. In this thesis, we first studied the interface between the polymer solution and the gel phase in the context of a core-shell microgel (in Chapter 4), which was followed by a study on volume contraction of a light-responsive molecular motor gel (in Chapter 5), both, using molecular dynamics simulations.

We first studied the interpenetration at the interface between the core gel and the shell polymer phase using the Kremer Grest model for free polymer chains and the gel strands. The core gel was represented by a regular network model with a diamond like topology and the interaction among all the particles were chosen to be the same to simplify our study. The density/ concentration of shell polymer phase was chosen to be in the semi-dilute regime, and was varied to observe its effect on interpenetration. When these two phases are made to come into contact with one another, we observed two time regimes for the core-shell diffusion: first, the gel becomes compressed as a result of osmotic pressure from the polymer solution, after which, the gel swells as the free polymer chains moves into the

gel. Analyzing the density profiles showed us that our polymer solution equilibrates locally after around $100\tau_d$, but the global equilibration of the system as a whole requires more time, depending on the thickness of the gel slab. The interpenetration of the shell polymers into the core gel was studied using quantities like "degree of interfacial integration" (DII) and "scaled areal density" (Σ) at the interface. When DII was plotted as a function of time, it increased faster for a smaller density of polymer solution, compared to a higher density of polymer solution but eventually stabilized at about the same saturation value for all concentrations. We observed that the DII saturated at a simulation time of around $100\tau_d$, indicating that the interface also achieved local equilibration around this time. The saturated value of DII observed in the simulations were very close to what was theoretically predicted for Gaussian polymer chains. Further, both areal density Σ and DII showed us that the connectivity between the two phases increased with shell polymer concentration, since the density of chains crossing the interface also increased with shell polymer concentration. This suggests that a well connected core-shell particle can be created using higher concentration of shell polymer solution. However, this might lead to the deformation of the core gel, due to the high osmotic pressure associated with denser polymer solution. Alternatively, we could play with the density of shell polymer solution and cross-link it with core-gel at different stages of polymer diffusion, in order to create a loosely connected to a well connected core-shell particle. We further observed the emergence of percolating clusters as the shell-polymer concentration exceeded a threshold concentration ρ^* , within the gel region. We inferred that, when the shell polymer concentration exceeds ρ^* in a region close to the interface, it can form large interconnected structures across the gel which can later be cross-linked and would be useful to strengthen the connection between the core and the shell. Further, a capillary wave model which accounts for gel elasticity was used to extract the dependence of interfacial broadening on concentration along with interfacial tension. Our study revealed a linear increase in interfacial tension with polymer concentration, indicating that these surface properties are affected by swelling of the gel due to the shell polymer concentration. Similarly the interfacial width was also seen to increase with shell polymer concentration. The observed positive correlation between interfacial width and tension sharply contrasted with the typical behavior at liquid-liquid interfaces, where these quantities are usually inversely related.

In the second work we focused on molecular motor gels, which used Feringa's second generation motors as cross-linkers. Thus, these cross-linkers formed the fundamental units that responded to external stimuli in such gels. We studied the limiting behaviour of such a gel using coarse grained molecular dynamics simulations. For simplicity and to replicate

the quasi-ideal experimental gels, we used a regular network with a diamond-like topology in our simulations. We worked under the assumption that the motors cannot unwind even under large strain or internal torque, and created a model motor that used a modified torsional potential to impart unidirectional rotation. The model enabled us to replicate the contraction of the experimental gels in our simulations. In our study we varied the strand length of the gel to systematically study its effect on the contraction of the gel. The size ratio of the free gel defined by the "gyration radius ratio" showed a systematic decrease with time as expected, and reached very similar contraction ratios independent of the strand length. The speed with which it reached the saturated value was dependent on the motor density in our simulation, i.e., to say that the gels with higher motor density/ shorter strands contracted faster compared to the ones with smaller motor density/ longer strands. This is different from what we observe in the experiments, in which case, the speed of contraction as a function of average strand length changes non-monotonically, probably due to the effects of increased optical density at high motor concentration, limiting the penetration of the light into the material. We also conducted simulations where the model gel was attached to a load and measured the contraction ratio as a function of this load. The 1D contraction ratios from these simulations showed a limiting value. This behaviour was qualitatively similar to those in the experiments. The compressive test in our simulation proved that the limiting behaviour is likely a consequence of topological limitation rather than the excluded volume effects. Further, we explored the work done by the motors to pull the loads which showed a linear increase with strand-length of the gel. The distributions of torques revealed overlapping statistics for all loads in the Hookean regime, even for zero loads, indicating that the loads in the Hookean regime do not affect the torque produced by the motors. The shape of the torque distribution, with more positive torques implied that, the motors have a tendency to unwind, but is prevented due to the high activation barrier of the torsion potential. Our study also revealed that the average torque to sustain the system in contracted state was highest for the gels with shorter strands, because of the lesser contact points for entanglements, which allowed for the motors to unwind easily compared to longer strands. Finally, in this study we explored the effect of stiffness of the polymer chains on the overall size ratio of the free gel. As stiffness increased, the long time size ratio, showed a non-monotonic behaviour, which first decreased with increasing stiffness and then started increasing again beyond a certain value of the stiffness parameter.

In conclusion, this work has provided significant insights into the interfaces of core-shell microgels and on the contraction behaviour of a molecular-motor gel. The results presented in this thesis could form the base for further studies on more realistic systems,

for example in studying the diffusive interpenetration of disordered networks or to study interfaces of polymer solution - gel systems with chemical disparities. Additionally the model for the molecular motor from the motor-gel simulations could be applied to a more non-ideal systems with strand length disparity or to a comb-like or hairy gels to see how the contraction behaviour changes with these defects in the gel. These results can be then compared to the case of an ideal network, which we have presented here. Thus the information from these simulations will serve as a foundation for guiding experimental efforts and developing new materials with amazing features as the field keeps growing.

Chapter A

Appendix A : Supporting information for Chapter 4

A.1 Properties of free polymer solutions

A.1.1 Gyration radius of free chains in solution

Figure A.1 shows the radius of gyration of free chains ($N = 102$) in solution as a function of monomer density. The theoretical value of the overlap concentration is around $\rho^* = 0.06\sigma^{-3}$. Even though the chains are quite short, the data are consistent with a crossover from a dilute regime, where R_g is independent of ρ , to a semidilute regime, where [252] $R_g \sim \rho^{-1/8}$.

A.1.2 Equation of state of the free solution and overlap concentration

Figure A.1 shows the pressure of the free polymer ($N = 102$) chains in a solution as a function of monomer density. We fit the data to de Gennes scaling equation [252]

$$\Pi \approx \left(\frac{\rho}{N}\right) \left[1 + \left(\frac{\rho}{\rho^*}\right)^{1.3}\right], \quad (\text{A.1})$$

using ρ^* as a fit parameter. A value of $\rho^* \approx 0.025\sigma^{-3}$ was obtained from the fit.

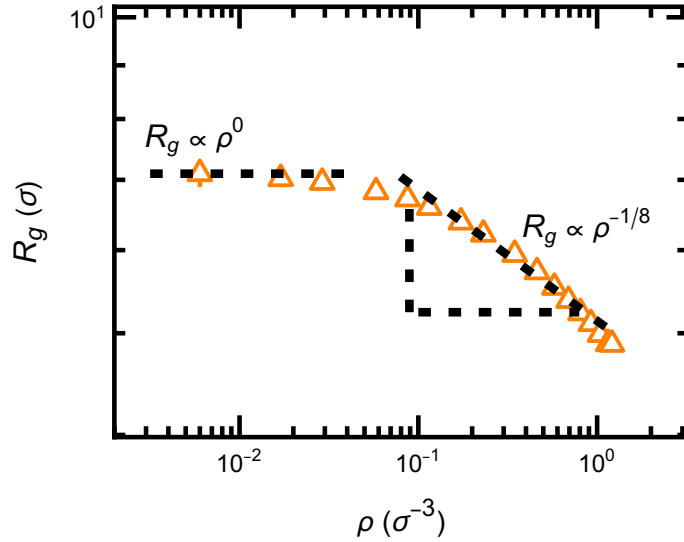


FIGURE A.1: Radius of gyration R_g of free polymers in solution vs. monomer density. Dashed lines indicates the expected power law scaling in the dilute regime ($R_g \propto \rho^0$) and in the semidilute regime ($R_g \propto \rho^{-1/8}$).

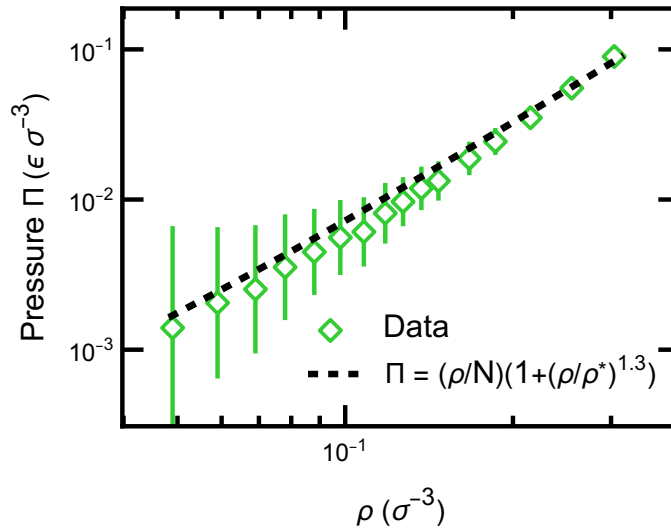


FIGURE A.2: Pressure of the free polymer Π solution vs. the solution density ρ . The dashed black lines shows a fit to the de Gennes scaling theory of polymers in a good solvent.

A.1.3 Bulk modulus of bare swollen gel

The elastic properties of bare gels (with no free polymers inside) are highly nonlinear. They are ultrasoft at small pressures and gradually stiffen at higher pressures. Figure A.3 shows the bulk modulus of a bare isotropic gel, as determined in a fully periodic system

where the gel is cross-linked across all three periodic boundaries. The bulk modulus is calculated as

$$K = k_B T \frac{\langle V \rangle}{\langle V^2 \rangle - \langle V \rangle^2} \quad (\text{A.2})$$

The figure shows that the modulus increases almost linearly with increasing pressure. At the pressures used to set up the gels in the simulations ($P \sim 0.001\epsilon\sigma^{-2}$), the bulk modulus is of order $K \sim 0.003\epsilon\sigma^{-3}$.

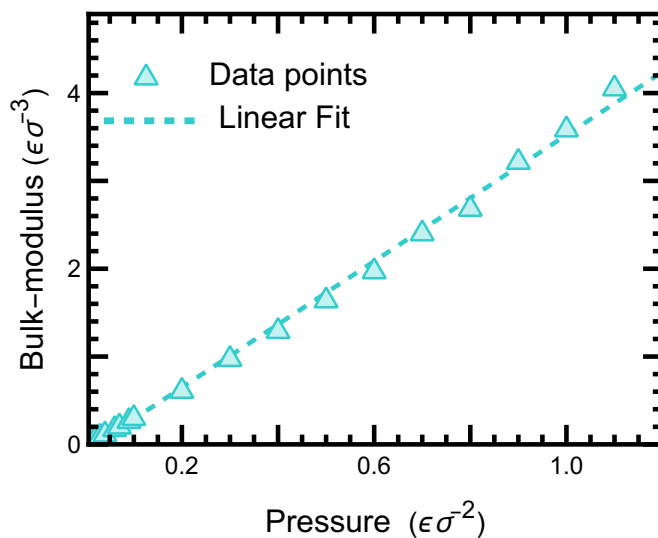


FIGURE A.3: Bulk-modulus as a function of applied pressure.

A.2 Additional data for isotropic gels

A.2.1 Monomer density profiles

Figure A.4 shows complementary data to Figure 4.3 in the main text: The time-dependent reduction of polymer concentration in the solution as the polymers diffuse into the gel (Figure A.4 (a)) and two selected sets of monomer density profiles across the slab, one at low concentration and one at high concentration. Figure A.5 (a)- (c) is complementary to Figure 4.5 (a)-(c) in the main text and shows the density of free polymers, the gel strand density and the total monomer density in the middle of the slab as a function of time in units of the chain relaxation time τ_d . The figure shows that the system as a whole does not reach equilibrium during the simulation time, as in the case of the anisotropic gel.

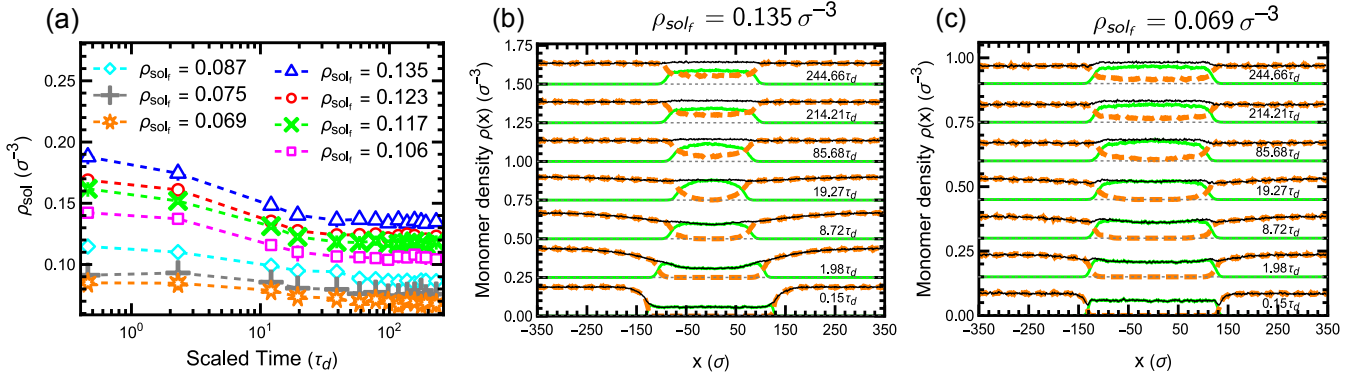


FIGURE A.4: (a) Time evolution of monomer density in the solution phase for different final concentrations ρ_{sol_f} (in units of σ^{-3}) as indicated. (b, c): Monomer density profiles across the slab for free polymers (dashed orange), gel strands (solid green), and total (solid black) at different times as indicated for different ρ_{sol_f} . For better readability, profiles corresponding to subsequent times are shifted upwards by $0.3\sigma^{-3}$ in (b) and $0.15\sigma^{-3}$ in (c). Thin dashed lines show corresponding baselines ($\rho = 0$). Data correspond to isotropic gels.

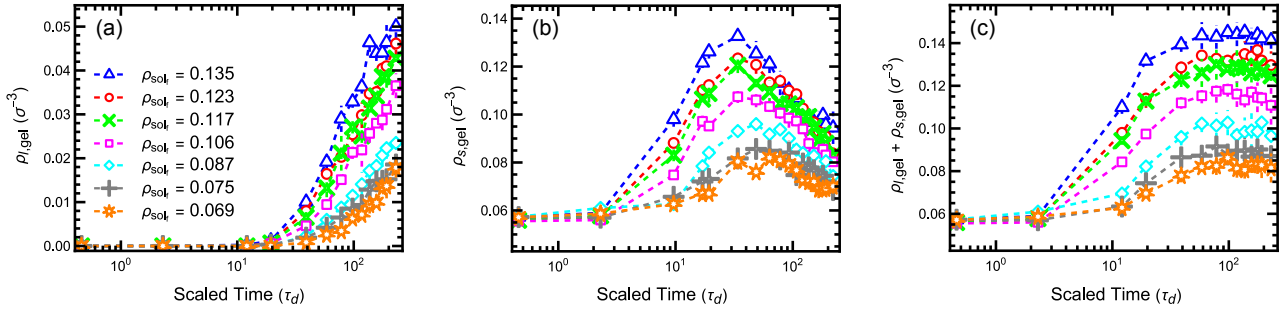


FIGURE A.5: Monomer densities at the center of the gel slab versus rescaled time t/τ_d for (a) monomers belonging to free polymers, (b) gel monomers, (c) all monomers, for different final concentrations in the outer solution ρ_{sol_f} (in units of σ^{-3}) as indicated. The gel is isotropic.

A.2.2 Percolation

Figures A.6 and A.7 show complementary snapshots and data to Figure 4.8 in the main text to characterize the cluster formation and the percolation of free chains inside the isotropic gel.

A.2.3 Monomer motion profiles

Figure A.8 shows complementary data for the isotropic gel to the profiles of local monomer motion in the anisotropic gel in Figure 4.9 in the main text. Different from Figure 4.9,

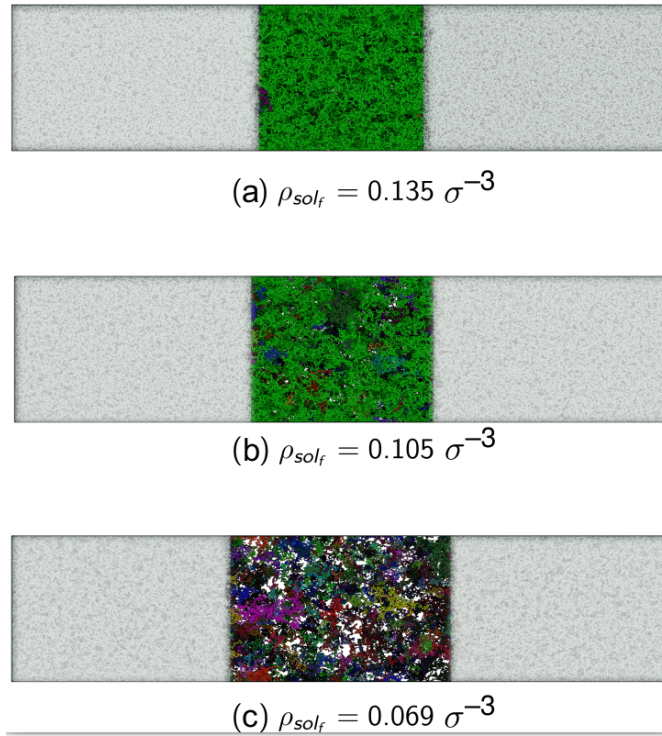


FIGURE A.6: (a-c) Snapshots showing cluster formation of free chains within the gel region as viewed from top of the box (along z -axis) at different final polymer densities (ρ_{sol_f}) as indicated. Different clusters are colored differently in order to be distinguishable. The light gray color marks the solution region. The gel is isotropic.

the profiles of $\mathcal{M}_z(x)$ and $\mathcal{M}_y(x)$ are the same. Inside the gel slab, the monomer motion is the same within the error in all three directions.

A.2.4 Chain conformation profiles

Figure A.9 shows complementary data for the isotropic gel corresponding to the profiles of chain conformation parameters $\Delta^2 R_{g_{x,y,z}}$ in anisotropic gels shown in Figure 4.10 in the main text. Different from the anisotropic gel, the chain conformations are isotropic within the error inside the gel. At the surface, a small change in chain orientation is observed for $\Delta^2 R_{g_x}$ as seen in the anisotropic gels.

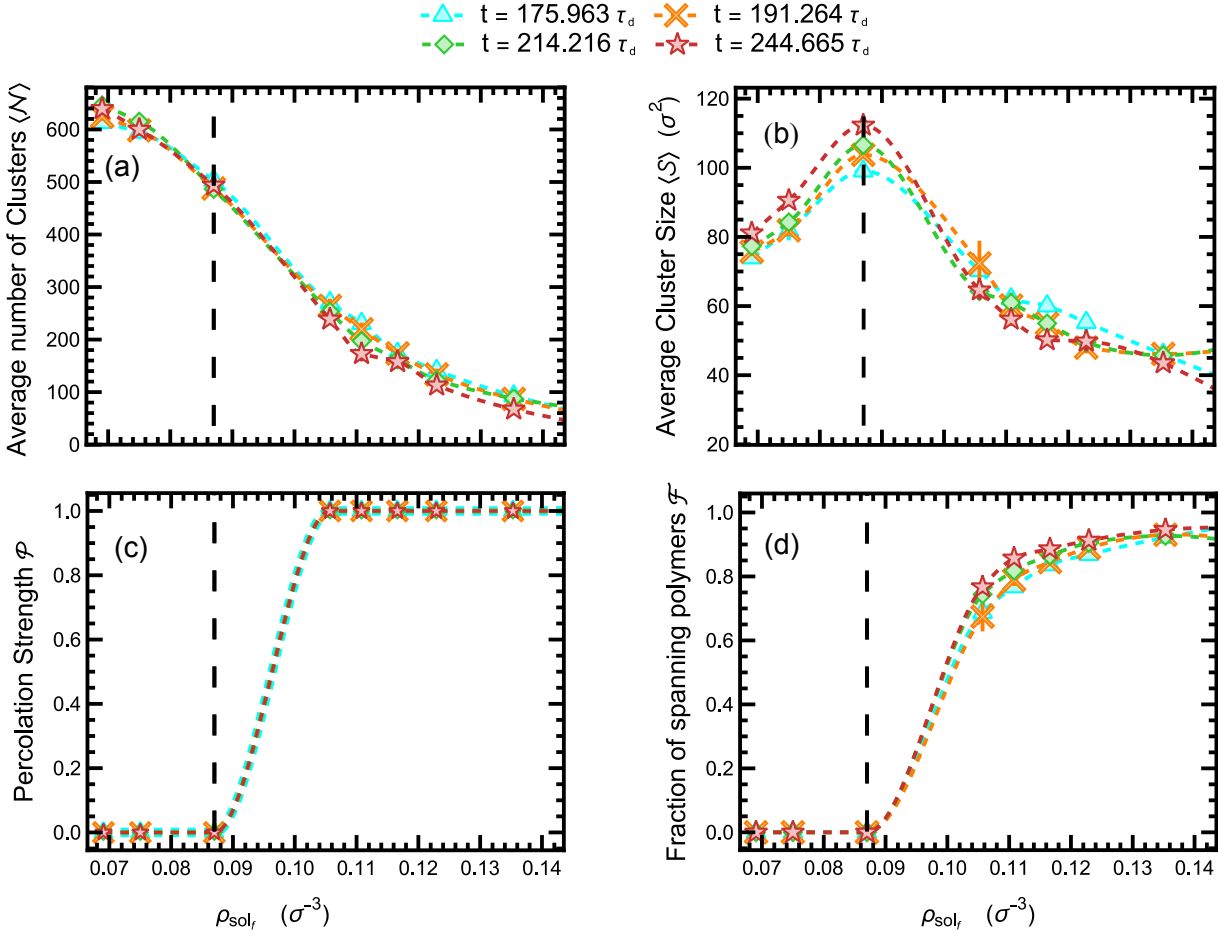


FIGURE A.7: Characteristics of cluster distributions vs. (ρ_{sol_f}) at different times as indicated: (a) Average number of clusters; (b) Average cluster size (mean squared radius of gyration) of finite clusters; (c) Percolation strength (see text); (d) Fraction of free polymers inside gel that are part of the spanning cluster. The gel is isotropic.

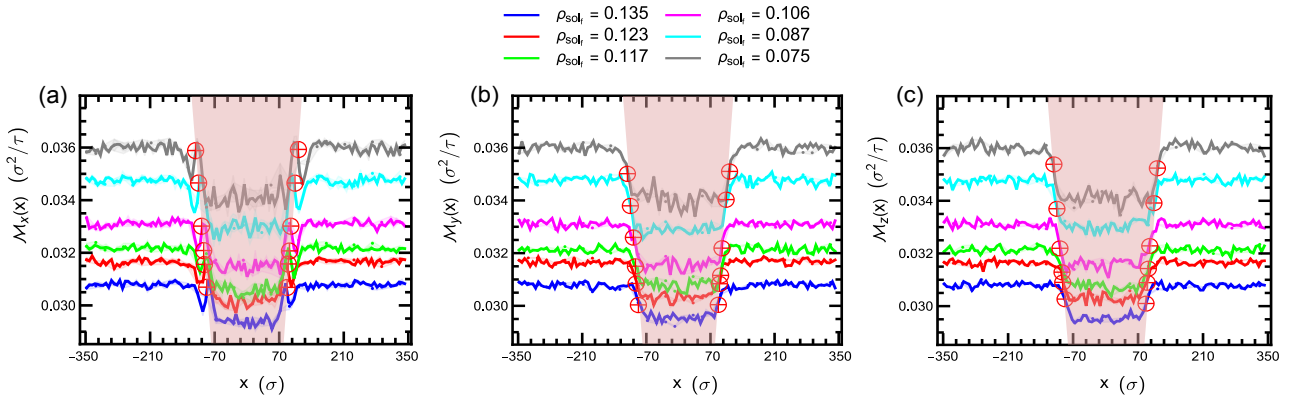


FIGURE A.8: Profiles of monomer motion $\mathcal{M}_\alpha(x)$ in $\alpha = x$ (a), $\alpha = y$ (b) and $\alpha = z$ (c) direction vs. x -coordinate of monomers. The red symbols \oplus indicate the approximate position of interface, the red shading the gel regions. The gel is isotropic.

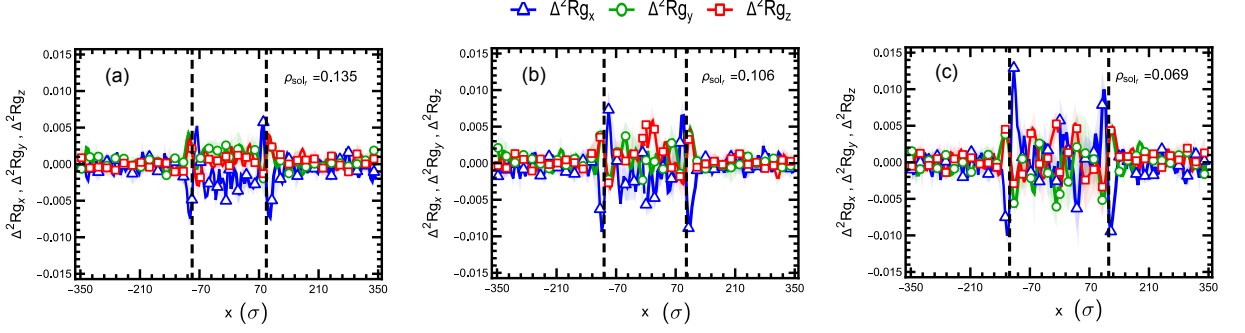


FIGURE A.9: Profiles of chain conformation parameters $\Delta^2 R_{g_\alpha}$ (see text) across the gel slab for different concentrations ρ_{sol_f} as indicated. The x coordinate refers to the center of mass of chains. Black dashed line indicates the position of the interface, shaded bands the error. The gel is isotropic.

A.3 Solution of diffusion equation for free polymers diffusing into a gel slab

To estimate the time scales required for the full equilibration of our system, we assume that the longest time scale is set by the diffusion of free polymers into the gel. We consider a system of polymers diffusing into a gel of thickness d from both sides with diffusion constant D . The gel is centered at $x = 0$, and the polymer density at the surface of the slab is set at $\rho_f(\pm d/2, t) \equiv \rho_{f,\text{eq}}$ (Dirichlet boundary conditions), where $\rho_{f,\text{eq}}$ is the equilibrium density of free polymers in the slab after equilibration. The solution of the one-dimensional diffusion equation ($\partial_t \rho = D \partial_{xx} \rho$) with these boundary condition at $x = \pm d/2$ and initial condition $\rho_f(x, t = 0) \equiv 0$ is

$$\begin{aligned} \rho_f(x, t) = \rho_{f,\text{eq}} & \left[1 - \frac{4}{\pi} \sum_{n=0}^{\infty} \frac{(-1)^n}{2n+1} \right. \\ & \times \cos\left(\frac{\pi}{d}(2n+1)x\right) \\ & \left. \times \exp\left(-D\left(\frac{\pi}{d}\right)^2(2n+1)^2 t\right) \right]. \end{aligned} \quad (\text{A.3})$$

This results in the time evolution equation

$$\frac{\rho_f(0, t)}{\rho_{f,\text{eq}}} = \left[1 - \varphi\left(\left(\frac{\pi}{d}\right)^2 D t\right) \right] \quad (\text{A.4})$$

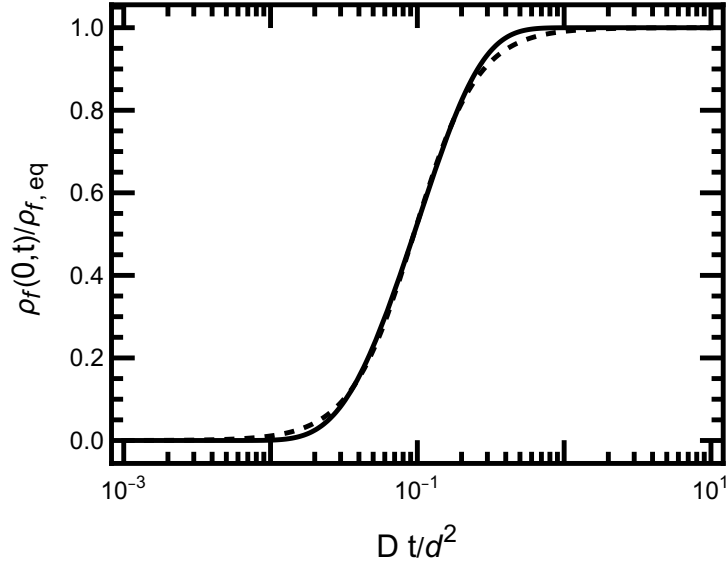


FIGURE A.10: Comparison of equation (A.4), describing the density of diffusing monomers at the center of the slab as a function of time (solid line), with the approximate expression Equation (A.5) (dashed line).

$$\text{with } \varphi(\tau) = \frac{4}{\pi} \sum_{n=0}^{\infty} \frac{(-1)^n}{2n+1} e^{-\tau(2n+1)^2}.$$

for $\rho_f(x,t)$ at the center of the slab. The function $\varphi(\tau)$ is initially close to zero up to $\tau \sim 0.1$, then it increases quasi logarithmically, until it finally saturates around $\tau \sim 5$. The time range between the initial discernible increase of free polymer density in the center of the gel, and the final saturation thus spans roughly 1.5 orders of magnitude. Numerically, the function $\rho_f(0,t)$ is reasonably well approximated by

$$\frac{\rho_f(0,t)}{\rho_{f,eq}} \approx \frac{1}{2} \left[\tanh \left(\ln \left(\frac{Dt}{d^2} \right) + 2.357 \right) + 1 \right], \quad (\text{A.5})$$

as shown in Figure A.10.

References

- [1] Fresnel: A visualization package for hoomd-blue. <https://github.com/glotzerlab/fresnel>.
- [2] Alexander A Abraham, Ruochong Fei, Gerard L Coté, and Melissa A Grunlan. Self-cleaning membrane to extend the lifetime of an implanted glucose biosensor. *ACS Appl. Mater. Interfaces*, 5(24):12832–12838, December 2013.
- [3] Farid F Abraham. On the fluctuation theory for the liquid—vapor interface. *Chem. Phys. Lett.*, 58(2):259–262, September 1978.
- [4] Robert T Abraham and Randal S Tibbetts. Cell biology. guiding ATM to broken DNA. *Science*, 308(5721):510–511, April 2005.
- [5] Narayan P Adhikari and Ekkehard Straube. Interfacial properties of asymmetric polymer mixtures. *Macromol. Theory Simul.*, 12(7):499–507, August 2003.
- [6] Narayan Prasad Adhikari, Rolf Auhl, and Ekkehard Straube. Interfacial properties of flexible and semiflexible polymers. *Macromol. Theory Simul.*, 11(3):315, March 2002.
- [7] Rasool Ahmad, Saptarshi Paul, and Sumit Basu. Characterization of entanglements in glassy polymeric ensembles using the gaussian linking number. *Phys. Rev. E.*, 101(2-1):022503, February 2020.
- [8] Ali A Al-Kinani, Ghada Zidan, Naba Elsaid, Ali Seyfoddin, Adam W G Alani, and Raid G Alany. Ophthalmic gels: Past, present and future. *Adv. Drug Deliv. Rev.*, 126:113–126, February 2018.
- [9] M P Allen and D J Tildesley. *Computer Simulation of Liquids*. Clarendon Press, Oxford, England, December 1987.

-
- [10] Alessio Altieri, Francesco G Gatti, Euan R Kay, David A Leigh, David Martel, Francesco Paolucci, Alexandra M Z Slawin, and Jenny K Y Wong. Electrochemically switchable hydrogen-bonded molecular shuttles. *J. Am. Chem. Soc.*, 125(28):8644–8654, July 2003.
- [11] Simon L Altmann. *Rotations, Quaternions, and Double Groups*. Dover Books on Mathematics. Dover Publications, Mineola, NY, November 2005.
- [12] E Amstad, S S Datta, and D A Weitz. The microfluidic post-array device: high throughput production of single emulsion drops. *Lab Chip*, 14(4):705–709, February 2014.
- [13] Mikhail V Anakhov, Rustam A Gumerov, and Igor I Potemkin. Stimuli-responsive aqueous microgels: properties and applications. *Mendeleev Commun.*, 30(5):555–562, September 2020.
- [14] Hans Christian Andersen. Rattle: A “velocity” version of the shake algorithm for molecular dynamics calculations. *Journal of Computational Physics*, 52:24–34, 1983.
- [15] Joshua A Anderson, M Eric Irrgang, and Sharon C Glotzer. Scalable metropolis monte carlo for simulation of hard shapes. *Comput. Phys. Commun.*, 204:21–30, July 2016.
- [16] Joshua A Anderson, M Eric Irrgang, and Sharon C Glotzer. Scalable metropolis monte carlo for simulation of hard shapes. *Comput. Phys. Commun.*, 204:21–30, July 2016.
- [17] Joshua A Anderson, Jens Glaser, and Sharon C Glotzer. HOOMD-blue: A python package for high-performance molecular dynamics and hard particle monte carlo simulations. *Comput. Mater. Sci.*, 173(109363):109363, February 2020.
- [18] Joshua A Anderson, Jens Glaser, and Sharon C Glotzer. HOOMD-blue: A python package for high-performance molecular dynamics and hard particle monte carlo simulations. *Comput. Mater. Sci.*, 173(109363):109363, February 2020.
- [19] Joshua A Anderson, Chris D Lorenz, and A Travesset. General purpose molecular dynamics simulations fully implemented on graphics processing units. *J. Comput. Phys.*, 227(10):5342–5359, May 2008.
- [20] Bruno Andreotti and Jacco H Snoeijer. Statics and dynamics of soft wetting. *Annu. Rev. Fluid Mech.*, 52(1):285–308, January 2020.

- [21] Alan J Ardell. Gradient energy, interfacial energy and interface width. *Scr. Mater.*, 66(7):423–426, April 2012.
- [22] M Arribas, A Elipe, and M Palacios. Quaternions and the rotation of a rigid body. *Celest. Mech. Dyn. Astron.*, 96(3-4):239–251, November 2006.
- [23] Karim Arroub, Isabel Gessner, Thomas Fischer, and Sanjay Mathur. Thermoresponsive poly (*N*-isopropylacrylamide)/polycaprolacton nanofibrous scaffolds for controlled release of antibiotics. *Adv. Eng. Mater.*, 23(9):2100221, September 2021.
- [24] Svetlana Artemova, Sergei Grudin, and Stephane Redon. A comparison of neighbor search algorithms for large rigid molecules. *J. Comput. Chem.*, 32(13):2865–2877, October 2011.
- [25] Asad Asadujjaman, Tiago Espinosa de Oliveira, Debashish Mukherji, and Annabelle Bertin. Polyacrylamide “revisited”: UCST-type reversible thermoresponsive properties in aqueous alcoholic solutions. *Soft Matter*, 14(8):1336–1343, 2018.
- [26] Hanako Asai, Kenta Fujii, Kengo Nishi, Takamasa Sakai, Koji Ohara, Yasuhiro Umebayashi, and Mitsuhiro Shibayama. Solvation structure of poly(ethylene glycol) in ionic liquids studied by high-energy x-ray diffraction and molecular dynamics simulations. *Macromolecules*, 46(6):2369–2375, March 2013.
- [27] Reda A I Azzam. Tailoring polymeric gels for soil reclamation and hydroponics. *Commun. Soil Sci. Plant Anal.*, 16(10):1123–1138, October 1985.
- [28] Vikram Baddam and Heikki Tenhu. Thermoresponsive polycations. *Polym. Chem.*, 14(32):3647–3678, 2023.
- [29] Rodrigue G M Badr, Lukas Hauer, Doris Vollmer, and Friederike Schmid. Cloaking transition of droplets on lubricated brushes. *J. Phys. Chem. B*, 126(36):7047–7058, September 2022.
- [30] Massimo Baroncini, Serena Silvi, and Alberto Credi. Photo- and redox-driven artificial molecular motors. *Chem. Rev.*, 120(1):200–268, January 2020.
- [31] Anchal Bassi, Garima Sharma, Parneet Kaur Deol, Ratna Sudha Madempudi, and Indu Pal Kaur. Preclinical potential of probiotic-loaded novel gelatin-oil vaginal suppositories: Efficacy, stability, and safety studies. *Gels*, 9(3):1–20, March 2023.
- [32] H Benkesntein, H Pagel, A Kullmann, W Kruger, and J Lehfeldt. Influence of a hydrophylic organic gel on soil properties and crop yield. *Archiv fur und acker*

- pflanzenbau und bodenkunde-archives of agronomy and soil science*, 31(2):111–115, 1987.
- [33] Howard C Berg. The rotary motor of bacterial flagella. *Annu. Rev. Biochem.*, 72(1):19–54, July 2003.
- [34] Peter Betsch and Ralf Siebert. Rigid body dynamics in terms of quaternions: Hamiltonian formulation and conserving numerical integration. *Int. J. Numer. Methods Eng.*, 79(4):444–473, July 2009.
- [35] David Beyer, Peter Košován, and Christian Holm. Simulations explain the swelling behavior of hydrogels with alternating neutral and weakly acidic blocks. *Macromolecules*, 55(23):10751–10760, December 2022.
- [36] Richard A Bissell, Emilio Córdova, Angel E Kaifer, and J Fraser Stoddart. A chemically and electrochemically switchable molecular shuttle. *Nature*, 369(6476):133–137, May 1994.
- [37] Santidan Biswas, Victor V Yashin, and Anna C Balazs. Dynamic behavior of chemically tunable mechano-responsive hydrogels. *Soft Matter*, 17(47):10664–10674, December 2021.
- [38] Max Born and Th. V. Kármán. Über Schwingungen in Raumgittern. (German) [On vibrations in space lattices]. *j-PHYSIKAL-Z*, 13(8):297–309, April 1912.
- [39] Monia Brugnoli, Andrea Scotti, Andrey A Rudov, Arjan P H Gelissen, Tobias Caumanns, Aurel Radulescu, Thomas Eckert, Andriy Pich, Igor I Potemkin, and Walter Richtering. Swelling of a responsive network within different constraints in multi-thermosensitive microgels. *Macromolecules*, 51(7):2662–2671, April 2018.
- [40] F P Buff, R A Lovett, and F H Stillinger. Interfacial density profile for fluids in the critical region. *Phys. Rev. Lett.*, 15(15):621–623, October 1965.
- [41] Brandon Butler, Vyas Ramasubramani, Joshua Anderson, and Sharon Glotzer. HOOMD-blue version 3.0 a modern, extensible, flexible, object-oriented API for molecular simulations. In *Proceedings of the 19th Python in Science Conference*, pages 24 – 31. SciPy, January 2020.
- [42] Gavin A Buxton and Nigel Clarke. Drug diffusion from polymer core-shell nanoparticles. *Soft Matter*, 3(12):1513–1517, November 2007.

-
- [43] John W Cahn and John E Hilliard. Free energy of a nonuniform system. i. interfacial free energy. *J. Chem. Phys.*, 28(2):258–267, February 1958.
- [44] Abdullah M Cakmak, Semra Unal, Ali Sahin, Faik N Oktar, Mustafa Sengor, Nazmi Ekren, Oguzhan Gunduz, and Deepak M Kalaskar. 3D printed polycaprolactone/gelatin/bacterial cellulose/hydroxyapatite composite scaffold for bone tissue engineering. *Polymers (Basel)*, 12(9):1962, August 2020.
- [45] Fabrizio Camerin, Miguel Ángel Fernández-Rodríguez, Lorenzo Rovigatti, Maria-Nefeli Antonopoulou, Nicoletta Gnan, Andrea Ninarello, Lucio Isa, and Emanuela Zaccarelli. Microgels adsorbed at liquid-liquid interfaces: A joint numerical and experimental study. *ACS Nano*, 13(4):4548–4559, April 2019.
- [46] Fabrizio Camerin, Nicoletta Gnan, José Ruiz-Franco, Andrea Ninarello, Lorenzo Rovigatti, and Emanuela Zaccarelli. Microgels at interfaces behave as 2D elastic particles featuring reentrant dynamics. *Phys. Rev. X.*, 10(3), July 2020.
- [47] Michele Caraglio, Cristian Micheletti, and Enzo Orlandini. Physical links: defining and detecting inter-chain entanglement. *Sci. Rep.*, 7(1):1156, April 2017.
- [48] C Carelli, R A L Jones, R N Young, R Cubitt, R Dalglish, F Schmid, and M Sferazza. Approaching criticality in polymer-polymer systems. *Phys. Rev. E Stat. Nonlin. Soft Matter Phys.*, 72(3 Pt 1):031807, September 2005.
- [49] Brian R Carrick, Steven Weigand, Claire L Seitzinger, and Timothy P Lodge. Concentration and temperature dependence of the interaction parameter and correlation length for poly(benzyl methacrylate) in ionic liquids. *Macromolecules*, 55(19):8899–8908, October 2022.
- [50] Nicolas Castrillon, Maria Echeverria, Heting Fu, Anurag Roy, and Joseph Toombs. Super absorbent polymer replacement for disposable baby diapers. Technical report, UC Berkley, 2019.
- [51] E Chacón and P Tarazona. Intrinsic profiles beyond the capillary wave theory: a monte carlo study. *Phys. Rev. Lett.*, 91(16):166103, October 2003.
- [52] Enrique Chacón and Pedro Tarazona. Characterization of the intrinsic density profiles for liquid surfaces. *J. Phys. Condens. Matter*, 17(45):S3493–S3498, November 2005.
- [53] Enrique Chacón, Pedro Tarazona, and José Alejandro. The intrinsic structure of the water surface. *J. Chem. Phys.*, 125(1):014709, July 2006.

- [54] Rayan Chatterjee, Santidan Biswas, Victor V Yashin, Michael Aizenberg, Joanna Aizenberg, and Anna C Balazs. Controllable growth of interpenetrating or random copolymer networks. *Soft Matter*, 17(30):7177–7187, August 2021.
- [55] Gong Chen, Wenwei Tang, Xiaohui Wang, Xueling Zhao, Cheng Chen, and Zhigang Zhu. Applications of hydrogels with special physical properties in biomedicine. *Polymers (Basel)*, 11(9):1420, August 2019.
- [56] Huangqin Chen, Xin Qiu, Tian Xia, Qing Li, Zhehan Wen, Bin Huang, and Yuesheng Li. Mesoporous materials make hydrogels more powerful in biomedicine. *Gels*, 9(3), March 2023.
- [57] Kuang-Yen Chen, Oleksii Ivashenko, Gregory T Carroll, Jort Robertus, Jos C M Kistemaker, Gábor London, Wesley R Browne, Petra Rudolf, and Ben L Feringa. Control of surface wettability using tripodal light-activated molecular motors. *J. Am. Chem. Soc.*, 136(8):3219–3224, February 2014.
- [58] Shengli Chen, Yuan Zhang, Ke Wang, Heng Zhou, and Wangqing Zhang. N-Ester-substituted polyacrylamides with a tunable lower critical solution temperature (LCST): the n-ester-substitute dependent thermoresponse. *Polym. Chem.*, 7(21):3509–3519, 2016.
- [59] Tai-Yu Chen, Yi-Jie Jiang, and Hsiu-Wen Chien. Developing transparent and conductive PolyHEMA gels using deep eutectic solvents. *Polymers (Basel)*, 15(12), June 2023.
- [60] Andrew Choi, Kyoung Duck Seo, Hyungjun Yoon, Seon Jin Han, and Dong Sung Kim. Bulk poly(n-isopropylacrylamide) (PNIPAAm) thermoresponsive cell culture platform: toward a new horizon in cell sheet engineering. *Biomater. Sci.*, 7(6):2277–2287, May 2019.
- [61] Iain C Clark, Kristina M Fontanez, Robert H Meltzer, Yi Xue, Corey Hayford, Aaron May-Zhang, Chris D’Amato, Ahmad Osman, Jesse Q Zhang, Pabodha Hettige, Jacob S A Ishibashi, Cyrille L Delley, Daniel W Weisgerber, Joseph M Replogle, Marco Jost, Kiet T Phong, Vanessa E Kennedy, Cheryl A C Peretz, Esther A Kim, Siyou Song, William Karlon, Jonathan S Weissman, Catherine C Smith, Zev J Gartner, and Adam R Abate. Microfluidics-free single-cell genomics with templated emulsification. *Nat. Biotechnol.*, 41(11):1557–1566, November 2023.
- [62] Claude Cohen-Tannoudji, Bernard Diu, and Franck Laloë. *Quantum mechanics, volume 3*. Blackwell Verlag, Berlin, Germany, 2 edition, October 2019.

- [63] Jean-Paul Collin, Valérie Heitz, Sylvestre Bonnet, and Jean-Pierre Sauvage. Transition metal-complexed catenanes and rotaxanes in motion: Towards molecular machines. *Inorg. Chem. Commun.*, 8(12):1063–1074, December 2005.
- [64] Hailin Cong, Liping Zhou, Qingye Meng, Yixin Zhang, Bing Yu, Youqing Shen, and Hao Hu. Preparation and evaluation of PAMAM dendrimer-based polymer gels physically cross-linked by hydrogen bonding. *Biomater. Sci.*, 7(9):3918–3925, September 2019.
- [65] Stefano Corra, Massimiliano Curcio, Massimo Baroncini, Serena Silvi, and Alberto Credi. Photoactivated artificial molecular machines that can perform tasks. *Adv. Mater.*, 32(20):e1906064, May 2020.
- [66] Stefano Corra, Massimiliano Curcio, and Alberto Credi. Photoactivated artificial molecular motors. *JACS Au*, 3(5):1301–1313, May 2023.
- [67] Carmelo Corsaro, Giulia Neri, Antonio Santoro, and Enza Fazio. Acrylate and methacrylate polymers’ applications: Second life with inexpensive and sustainable recycling approaches. *Materials (Basel)*, 15(1):282, December 2021.
- [68] Peter M Crapo and Yadong Wang. Small intestinal submucosa gel as a potential scaffolding material for cardiac tissue engineering. *Acta Biomater.*, 6(6):2091–2096, June 2010.
- [69] J Cui and A Del Campo. Photo-responsive polymers: properties, synthesis and applications. In *Smart Polymers and their Applications*, pages 93–133. Elsevier, 2014.
- [70] M Daoud, E Bouchaud, and G Jannink. Swelling of polymer gels. *Macromolecules*, 19(7):1955–1960, July 1986.
- [71] P. K Dass, N. N; Mahato. New perspective in free radical polymerization. *Indian J. Technol.*, June 1993.
- [72] Joaquim Elias de Freitas, Liacir dos Santos Lucena, and Stéphane Roux. Percolation as a dynamical phenomenon. *Physica A*, 266(1-4):81–85, April 1999.
- [73] P. G. de Gennes. *Scaling Concepts in Polymer Physics*. Cornell University Press, Ithaca, NY, 1979.
- [74] Cole A DeForest and Kristi S Anseth. Cytocompatible click-based hydrogels with dynamically tunable properties through orthogonal photoconjugation and photocleavage reactions. *Nat. Chem.*, 3(12):925–931, October 2011.

- [75] F Demydiuk, M Solar, H Meyer, O Benzerara, W Paul, and J Baschnagel. Role of torsional potential in chain conformation, thermodynamics, and glass formation of simulated polybutadiene melts. *J. Chem. Phys.*, 156(23):234902, June 2022.
- [76] Mitali Dewan, Arpita Adhikari, Koushik Dutta, and Dipankar Chattopadhyay. Impact of poly (vinyl alcohol) on the thermogelation property and drug release profile of ophthalmic formulations based on poloxamer 407. *ChemistrySelect*, 8(6), February 2023.
- [77] M Doi and S F Edwards. *The theory of polymer dynamics*. International Series of Monographs on Physics. Clarendon Press, Oxford, England, November 1988.
- [78] M Doi and Howard See. *Introduction to polymer physics*. Clarendon Press, Oxford, England, November 1995.
- [79] Masao Doi. *Soft Matter Physics*. Oxford University Press, London, England, June 2013.
- [80] Andreas Dullweber, Benedict Leimkuhler, and Robert McLachlan. Symplectic splitting methods for rigid body molecular dynamics. *J. Chem. Phys.*, 107(15):5840–5851, October 1997.
- [81] Karel Dušek and Miroslava Dušková-Smrčková. Volume phase transition in gels: Its discovery and development. *Gels*, 6(3):22, July 2020.
- [82] Rienk Eelkema, Michael M Pollard, Javier Vicario, Nathalie Katsonis, Blanca Serrano Ramon, Cees W M Bastiaansen, Dirk J Broer, and Ben L Feringa. Molecular machines: nanomotor rotates microscale objects. *Nature*, 440(7081):163, March 2006.
- [83] B E Eichinger. Rubber elasticity: Solution of the James-Guth model. *Phys. Rev. E Stat. Nonlin. Soft Matter Phys.*, 91(5):052601, May 2015.
- [84] A Einstein. Über die von der molekularkinetischen theorie der wärme geforderte bewegung von in ruhenden flüssigkeiten suspendierten teilchen. *Ann. Phys.*, 322(8):549–560, January 1905.
- [85] Robert D Engle, Robert D Skeel, and Matthew Drees. Monitoring energy drift with shadow hamiltonians. *J. Comput. Phys.*, 206(2):432–452, July 2005.
- [86] Adam J Engler, Shamik Sen, H Lee Sweeney, and Dennis E Discher. Matrix elasticity directs stem cell lineage specification. *Cell*, 126(4):677–689, August 2006.

- [87] Fernando A Escobedo and Juan J de Pablo. Molecular simulation of polymeric networks and gels: phase behavior and swelling. *Phys. Rep.*, 318(3):85–112, September 1999.
- [88] A C C Esteves, K Lyakhova, L G J van der Ven, R A T M van Benthem, and G de With. Surface segregation of low surface energy polymeric dangling chains in a cross-linked polymer network investigated by a combined experimental–simulation approach. *Macromolecules*, 46(5):1993–2002, March 2013.
- [89] Jack D Evans, Simon Krause, and Ben L Feringa. Cooperative and synchronized rotation in motorized porous frameworks: impact on local and global transport properties of confined fluids. *Faraday Discuss.*, 225:286–300, February 2021.
- [90] R Everaers and K Kremer. Topological interactions in model polymer networks. *Phys. Rev. E Stat. Phys. Plasmas Fluids Relat. Interdiscip. Topics*, 53(1):R37–R40, January 1996.
- [91] Ralf Everaers. Entanglement effects in defect-free model polymer networks. *New J. Phys.*, 1:12–12, August 1999.
- [92] Ralf Everaers, Hossein Ali Karimi-Varzaneh, Frank Fleck, Nils Hojdis, and Carsten Svaneborg. Kremer–grest models for commodity polymer melts: Linking theory, experiment, and simulation at the kuhn scale. *Macromolecules*, 53(6):1901–1916, March 2020.
- [93] Balázs Fábián. *Molecular Modeling of Interfacial Phenomena*. Theses, Université Bourgogne Franche-Comté ; Budapesti műszaki és gazdaságtudományi egyetem (Budapest), November 2018.
- [94] Arash Fattah-alhosseini, Razieh Chaharmahali, Sajad Alizad, Mosab Kaseem, and Burak Dikici. A review of smart polymeric materials: Recent developments and prospects for medicine applications. *Hybrid Advances*, 5(100178):100178, April 2024.
- [95] Ben L Feringa. The art of building small: from molecular switches to molecular motors. *J. Org. Chem.*, 72(18):6635–6652, August 2007.
- [96] Michael J Fevola, Roger D Hester, and Charles L McCormick. Molecular weight control of polyacrylamide with sodium formate as a chain-transfer agent: Characterization via size exclusion chromatography/multi-angle laser light scattering and determination of chain-transfer constant. *J. Polym. Sci. A Polym. Chem.*, 41(4):560–568, February 2003.

- [97] Richard Feynman. Nanotechnology. *Caltechs Eng. Sci.*, 23:22–36, 1960.
- [98] David Fincham. Choice of timestep in molecular dynamics simulation. *Comput. Phys. Commun.*, 40(2-3):263–269, June 1986.
- [99] E G Flekkoy and D H Rothman. Fluctuating hydrodynamic interfaces: Theory and simulation. *Phys. Rev. E Stat. Phys. Plasmas Fluids Relat. Interdiscip. Topics*, 53(2):1622–1643, February 1996.
- [100] P J Flory. *Principles of polymer chemistry*. The George Fisher Baker Non-Resident Lectureship in Chemistry at Cornell University. Cornell University Press, Ithaca, NY, December 1953.
- [101] Paul J Flory. Thermodynamics of high polymer solutions. *J. Chem. Phys.*, 10(1):51–61, January 1942.
- [102] Paul J Flory. Molecular theory of rubber elasticity. *Polym. J.*, 17(1):1–12, January 1985.
- [103] Justin T Foy, Quan Li, Antoine Goujon, Jean-Rémy Colard-Itté, Gad Fuks, Emilie Moulin, Olivier Schiffmann, Damien Dattler, Daniel P Funeriu, and Nicolas Giuseppone. Dual-light control of nanomachines that integrate motor and modulator subunits. *Nat. Nanotechnol.*, 12(6):540–545, July 2017.
- [104] Daan Frenkel. Colloidal systems. playing tricks with designer “atoms”. *Science*, 296(5565):65–66, April 2002.
- [105] Daan Frenkel, Berend Smit, and Mark A Ratner. *understanding molecular simulation: From algorithms to applications*. *Phys. Today*, 50(7):66–66, July 1997.
- [106] Cui-Liu Fu, Xue-Zhi Jia, Zhao-Yan Sun, and Li-Jia An. Effect of chain composition on the mechanical response of structural gel: A molecular dynamics simulation. *Polymer (Guildf.)*, 55(17):4538–4545, August 2014.
- [107] I Y Galaev and B Mattiasson. ‘smart’ polymers and what they could do in biotechnology and medicine. *Trends Biotechnol.*, 17(8):335–340, August 1999.
- [108] Jason Gans and David Shalloway. Shadow mass and the relationship between velocity and momentum in symplectic numerical integration. *Phys. Rev. E Stat. Phys. Plasmas Fluids Relat. Interdiscip. Topics*, 61(4):4587–4592, April 2000.
- [109] Chuan Gao, Andreas Vargas Jentzsch, Emilie Moulin, and Nicolas Giuseppone. Light-driven molecular whirligig. *J. Am. Chem. Soc.*, 144(22):9845–9852, June 2022.

-
- [110] Akash Garg, Rutvi Agrawal, Chetan Singh Chauhan, and Rohitas Deshmukh. In-situ gel: A smart carrier for drug delivery. *Int. J. Pharm.*, 652(123819):123819, March 2024.
- [111] Irene Gargantini. Linear octtrees for fast processing of three-dimensional objects. *Comput. Graph. Image Process.*, 20(4):365–374, December 1982.
- [112] Alexey A Gavrilov, Vladimir Yu Rudyak, and Alexander V Chertovich. Computer simulation of the core-shell microgels synthesis via precipitation polymerization. *J. Colloid Interface Sci.*, 574:393–398, August 2020.
- [113] Karen Geisel, Andrey A Rudov, Igor I Potemkin, and Walter Richtering. Hollow and core-shell microgels at oil-water interfaces: Spreading of soft particles reduces the compressibility of the monolayer. *Langmuir*, 31(48):13145–13154, December 2015.
- [114] Jens Glaser, Andrew S Karas, and Sharon C Glotzer. A parallel algorithm for implicit depletant simulations. *J. Chem. Phys.*, 143(18):184110, November 2015.
- [115] Jens Glaser, Trung Dac Nguyen, Joshua A Anderson, Pak Lui, Filippo Spiga, Jaime A Millan, David C Morse, and Sharon C Glotzer. Strong scaling of general-purpose molecular dynamics simulations on GPUs. *Comput. Phys. Commun.*, 192:97–107, July 2015.
- [116] Herbert Goldstein, Charles P Poole, and John L Safko. *Classical mechanics: Pearson new international edition*. Pearson Education, London, England, 3 edition, August 2013.
- [117] Pedro Gonnet. Pairwise verlet lists: combining cell lists and verlet lists to improve memory locality and parallelism. *J. Comput. Chem.*, 33(1):76–81, January 2012.
- [118] Alexander V Goponenko and Yuris A Dzenis. Role of mechanical factors in applications of stimuli-responsive polymer gels - status and prospects. *Polymer (Guildf.)*, 101:415–449, September 2016.
- [119] M Gordon. The physics of rubber elasticity (third edition). I. R. G. Treloar, Clarendon Press, Oxford. 1975 pp. xii + 370. price: £14.00. *Br. Polym. J.*, 8(1):39–39, March 1976.
- [120] Michael Griebel, Stephan Knapek, and Gerhard Zumbusch. *Numerical simulation in molecular dynamics*. Texts in Computational Science and Engineering. Springer, Berlin, Germany, 2007 edition, August 2007.

- [121] Jessica Groppi, Massimo Baroncini, Margherita Venturi, Serena Silvi, and Alberto Credi. Design of photo-activated molecular machines: highlights from the past ten years. *Chem. Commun. (Camb.)*, 55(84):12595–12602, October 2019.
- [122] Manuel Guentner, Monika Schildhauer, Stefan Thumser, Peter Mayer, David Stephenson, Peter J Mayer, and Henry Dube. Sunlight-powered khz rotation of a hemithioindigo-based molecular motor. *Nat. Commun.*, 6(1):8406, September 2015.
- [123] Marcos R Guilherme, Gilsinei M Campese, Eduardo Radovanovic, Adley F Rubira, Elias B Tambourgi, and Edvani C Muniz. Thermo-responsive sandwiched-like membranes of IPN-PNIPAAm/PAAm hydrogels. *J. Memb. Sci.*, 275(1-2):187–194, April 2006.
- [124] Rustam A Gumerov, Sergei A Filippov, Walter Richtering, Andrij Pich, and Igor I Potemkin. Amphiphilic microgels adsorbed at oil-water interfaces as mixers of two immiscible liquids. *Soft Matter*, 15(19):3978–3986, May 2019.
- [125] Shi-Jun Guo, Qing-Sheng Yang, X Q He, and K M Liew. Modeling of interface cracking in copper-graphite composites by MD and CFE method. *Compos. B Eng.*, 58:586–592, March 2014.
- [126] Raimo Hartmann, Marcel Weidenbach, Martin Neubauer, Andreas Fery, and Wolfgang J Parak. Stiffness-dependent in vitro uptake and lysosomal acidification of colloidal particles. *Angew. Chem. Int. Ed Engl.*, 54(4):1365–1368, January 2015.
- [127] G Heinrich, E Straube, and G Helmis. Rubber elasticity of polymer networks: Theories. In *Polymer Physics*, Fortschritte der Hochpolymeren-Forschung [Advances in polymer science], pages 33–87. Springer Berlin Heidelberg, Berlin, Heidelberg, 1988.
- [128] G Heinrich, E Straube, and G Helmis. Rubber elasticity of polymer networks: Theories. In *Polymer Physics*, Fortschritte der Hochpolymeren-Forschung [Advances in polymer science], pages 33–87. Springer Berlin Heidelberg, Berlin, Heidelberg, 1988.
- [129] W E Hennink and C F van Nostrum. Novel crosslinking methods to design hydrogels. *Adv. Drug Deliv. Rev.*, 64:223–236, December 2012.
- [130] M Heskins and J E Guillet. Solution properties of poly(n-isopropylacrylamide). *J. Macromol. Sci. - Chem.*, 2(8):1441–1455, December 1968.

-
- [131] Shunsuke Hirotsu. Elastic anomaly near the critical point of volume phase transition in polymer gels. *Macromolecules*, 23(3):903–905, February 1990.
- [132] M Hloucha and U K Deiters. Fast coding of the minimum image convention. *Mol. Simul.*, 20(4):239–244, March 1998.
- [133] Roger W Hockney and James W Eastwood. Fourier transforms, fourier series, and finite fourier transforms. In *Computer Simulation Using Particles*, pages 499–508. Taylor & Francis, January 1988.
- [134] Hannes Holey, Peter Gumbsch, and Lars Pastewka. Confinement-induced diffusive sound transport in nanoscale fluidic channels. *Phys. Rev. Lett.*, 131(8):084001, August 2023.
- [135] Thomas Hölzl, Hans L Trautenberg, and Dietmar Göritz. Monte carlo simulations on polymer network deformation. *Phys. Rev. Lett.*, 79(12):2293–2296, September 1997.
- [136] Ferenc Horkay, Jack F Douglas, and Emanuela Del Gado, editors. *Gels and other soft amorphous solids*. ACS symposium series. American Chemical Society. Oxford University Press, New York, NY, August 2019.
- [137] Robin Horstmann, Lukas Hecht, Sebastian Kloth, and Michael Vogel. Structural and dynamical properties of liquids in confinements: A review of molecular dynamics simulation studies. *Langmuir*, 38(21):6506–6522, May 2022.
- [138] Yaping Hou, Ruochong Fei, Jonathan C Burkes, Shin Duk Lee, Dany Munoz-Pinto, Mariah S Hahn, and Melissa A Grunlan. Thermoresponsive nanocomposite hydrogels: Transparency, rapid deswelling and cell release. *J. Biomater. Tissue Eng.*, 1(1), June 2011.
- [139] Michael P Howard, Joshua A Anderson, Arash Nikoubashman, Sharon C Glotzer, and Athanassios Z Panagiotopoulos. Efficient neighbor list calculation for molecular simulation of colloidal systems using graphics processing units. *Comput. Phys. Commun.*, 203:45–52, June 2016.
- [140] Michael P Howard, Antonia Statt, Felix Madutsa, Thomas M Truskett, and Athanassios Z Panagiotopoulos. Quantized bounding volume hierarchies for neighbor search in molecular simulations on graphics processing units. *Comput. Mater. Sci.*, 164:139–146, June 2019.

- [141] Kuikui Hu, Hui Shi, Ji Zhu, Dan Deng, Guangdong Zhou, Wenjie Zhang, Yilin Cao, and Wei Liu. Compressed collagen gel as the scaffold for skin engineering. *Biomed. Microdevices*, 12(4):627–635, August 2010.
- [142] Liyun Huang, Kui Wu, Shuhan Cai, Haosen Yu, Defei Liu, Wenbing Yuan, Xin Chen, and Hongbing Ji. Understanding the microfluidic generation of double emulsion droplets with alginate shell. *Colloids Surf. B Biointerfaces*, 222(113114):113114, February 2023.
- [143] Yanbin Huang, Igal Szleifer, and Nicholas A Peppas. A molecular theory of polymer gels. *Macromolecules*, 35(4):1373–1380, February 2002.
- [144] Maurice L Huggins. Thermodynamic properties of solutions of long-chain compounds. *Ann. N. Y. Acad. Sci.*, 43(1):1–32, March 1942.
- [145] Maurice L Huggins. Thermodynamic properties of liquids, including solutions. IX. thermodynamic properties of polymer solutions. *Polym. J.*, 4(5):502–510, May 1973.
- [146] Kazuhiko Ishihara, Xinfeng Shi, Kyoko Fukazawa, Tetsuji Yamaoka, George Yao, and James Yuliang Wu. Biomimetic-engineered silicone hydrogel contact lens materials. *ACS Appl. Bio Mater.*, 6(9):3600–3616, September 2023.
- [147] Asumi Ishikawa, Namie Ikeda, Shuichi Maeda, and Kenta Fujii. Polymer network formation mechanism of multifunctional poly(ethylene glycol)s in ionic liquid electrolyte with a lithium salt. *Phys. Chem. Chem. Phys.*, 23(31):16966–16972, August 2021.
- [148] Kazuhisa Iwaso, Yoshinori Takashima, and Akira Harada. Fast response dry-type artificial molecular muscles with [c2]daisy chains. *Nat. Chem.*, 8(6):625–632, June 2016.
- [149] Meyer B Jackson. *Molecular and Cellular Biophysics*. Cambridge University Press, Cambridge, England, May 2010.
- [150] Yi Jia and Junbai Li. Molecular assembly of rotary and linear motor proteins. *Acc. Chem. Res.*, 52(6):1623–1631, June 2019.
- [151] Cheng Jiang, Qihua Wang, and Tingmei Wang. Thermoresponsive PNIPAAm-modified cotton fabric surfaces that switch between superhydrophilicity and superhydrophobicity. *Appl. Surf. Sci.*, 258(11):4888–4892, March 2012.

-
- [152] Shi Jin and Lance R Collins. Dynamics of dissolved polymer chains in isotropic turbulence. *New J. Phys.*, 9(10):360–360, October 2007.
- [153] J E Jones. On the determination of molecular fields. —II. from the equation of state of a gas. *Proc. R. Soc. Lond. A Math. Phys. Sci.*, 106(738):463–477, October 1924.
- [154] J E Jones. On the determination of molecular fields.—i. from the variation of the viscosity of a gas with temperature. *Proc. R. Soc. Lond. A Math. Phys. Sci.*, 106(738):441–462, October 1924.
- [155] Richard A L Jones. Soft condensed matter. *Eur. J. Phys.*, 23(6):652–652, November 2002.
- [156] Jangwook P Jung, Joshua Z Gasiorowski, and Joel H Collier. Fibrillar peptide gels in biotechnology and biomedicine. *Biopolymers*, 94(1):49–59, June 2010.
- [157] Duyoun Ka, Myungeun Seo, Hyungsam Choi, Eun Hee Kim, and Sang Youl Kim. Physical gelation of polar aprotic solvents induced by hydrogen bonding modulation of polymeric molecules. *Chem. Commun. (Camb.)*, 46(31):5722–5724, August 2010.
- [158] Jørgen Kalckar. *Foundations of Quantum Physics II (1933-1958)*. Elsevier, 2013.
- [159] H Kamberaj, R J Low, and M P Neal. Time reversible and symplectic integrators for molecular dynamics simulations of rigid molecules. *J. Chem. Phys.*, 122(22):224114, June 2005.
- [160] Natasha Kamerlin. *Computer Simulations of Polymer Gels : Structure, Dynamics, and Deformation*. PhD thesis, Uppsala University, Physical Chemistry, 2017.
- [161] Natasha Kamerlin and Christer Elvingson. Deformation behavior of homogeneous and heterogeneous bimodal networks. *Macromolecules*, 50(23):9353–9359, December 2017.
- [162] Alan Kaptanoglu, Brian de Silva, Urban Fasel, Kadierdan Kaheman, Andy Goldschmidt, Jared Callahan, Charles Delahunt, Zachary Nicolaou, Kathleen Champion, Jean-Christophe Loiseau, J Kutz, and Steven Brunton. PySINDy: A comprehensive python package for robust sparse system identification. *J. Open Source Softw.*, 7(69):3994, January 2022.
- [163] Tero Karras and Timo Aila. Fast parallel construction of high-quality bounding volume hierarchies. In *Proceedings of the 5th High-Performance Graphics Conference*, page 89–99, New York, NY, USA, July 2013. ACM.

-
- [164] Laurens R A Kessener, Frans J Peters, and Marloes L P van Lierop, editors. *Data structures for raster graphics*. Focus on Computer Graphics. Springer, Berlin, Germany, 1986 edition, February 1986.
- [165] Hideki Kobayashi and Roland Winkler. Structure of microgels with Debye–Hückel interactions. *Polymers (Basel)*, 6(5):1602–1617, May 2014.
- [166] N Koumura, R W Zijlstra, R A van Delden, N Harada, and B L Feringa. Light-driven monodirectional molecular rotor. *Nature*, 401(6749):152–155, September 1999.
- [167] Kurt Kremer and Gary S Grest. Dynamics of entangled linear polymer melts: A molecular-dynamics simulation. *J. Chem. Phys.*, 92(8):5057–5086, April 1990.
- [168] Tibor Kudernac, Nopporn Ruangsapapichat, Manfred Parschau, Beatriz Maciá, Nathalie Katsonis, Syuzanna R Harutyunyan, Karl-Heinz Ernst, and Ben L Feringa. Electrically driven directional motion of a four-wheeled molecule on a metal surface. *Nature*, 479(7372):208–211, November 2011.
- [169] Werner Kuhn. Beziehungen zwischen molekülgröße, statistischer molekülgestalt und elastischen eigenschaften hochpolymerer stoffe. *Colloid Polym. Sci.*, 76(3):258–271, September 1936.
- [170] Flavia Laffleur and Benedikt Strasdat. Gelatin-based formulations for dermal application. *Eur. Polym. J.*, 118:542–550, September 2019.
- [171] Peter T Landsberg. *Thermodynamics and statistical mechanics*. Oxford University Press, London, England, June 1979.
- [172] Frank Lange, Konrad Schwenke, Manami Kurakazu, Yuki Akagi, Ung-Il Chung, Michael Lang, Jens-Uwe Sommer, Takamasa Sakai, and Kay Saalwächter. Connectivity and structural defects in model hydrogels: A combined proton NMR and monte carlo simulation study. *Macromolecules*, 44(24):9666–9674, December 2011.
- [173] Pierre Larochelle. Visualizing quaternions (a.j. hanson; 2006) [bookshelf]. *IEEE Control Syst.*, 28(4):104–105, August 2008.
- [174] Ali Lashkaripour, David P McIntyre, Suzanne G K Calhoun, Karl Krauth, Douglas M Densmore, and Polly M Fordyce. Design automation of microfluidic single and double emulsion droplets with machine learning. *Nat. Commun.*, 15(1):83, January 2024.

-
- [175] W. Lebrecht and M. I. Gonzalez. Discreet percolation in tridimensional networks. *Rev. Mex. Fis.*, 57(4):344–349, August 2011.
- [176] Swen Lehmann, Sebastian Seiffert, and Walter Richtering. Diffusion of guest molecules within sensitive core-shell microgel carriers. *J. Colloid Interface Sci.*, 431:204–208, October 2014.
- [177] Jean-Marie Lehn. Conjecture: imines as unidirectional photodriven molecular motors-motional and constitutional dynamic devices. *Chemistry*, 12(23):5910–5915, August 2006.
- [178] Don S Lemons and Anthony Gythiel. Paul langevin’s 1908 paper “on the theory of brownian motion” [“sur la théorie du mouvement brownien,” c. r. acad. sci. (paris) 146, 530–533 (1908)]. *Am. J. Phys.*, 65(11):1079–1081, November 1997.
- [179] Quan Li, Gad Fuks, Emilie Moulin, Mounir Maaloum, Michel Rawiso, Igor Kulic, Justin T Foy, and Nicolas Giuseppone. Macroscopic contraction of a gel induced by the integrated motion of light-driven molecular motors. *Nat. Nanotechnol.*, 10(2):161–165, February 2015.
- [180] Tzyy-Shyang Lin, Rui Wang, Jeremiah A Johnson, and Bradley D Olsen. Topological structure of networks formed from symmetric four-arm precursors. *Macromolecules*, 51(3):1224–1231, February 2018.
- [181] Wei Liu, John M. Prausnitz, and Harvey W. Blanch. Amyloid fibril formation by peptide lys (11-36) in aqueous trifluoroethanol. *Biomacromolecules*, 5(5):1818–1823, 2004.
- [182] Ya Liu, Joanna Aizenberg, and Anna C Balazs. Using dissipative particle dynamics to model effects of chemical reactions occurring within hydrogels. *Nanomaterials (Basel)*, 11(10):2764, October 2021.
- [183] Aude Livoreil, Jean-Pierre Sauvage, Nicola Armaroli, Vincenzo Balzani, Lucia Flamigni, and Barbara Ventura. Electrochemically and photochemically driven ring motions in a disymmetrical copper [2]-catenate. *J. Am. Chem. Soc.*, 119(50):12114–12124, December 1997.
- [184] Rayleigh Lord. XX. on the theory of surface forces.—II. compressible fluids. *Lond. Edinb. Dublin Philos. Mag. J. Sci.*, 33(201):209–220, February 1892.

- [185] Cedric Loretan and Andreas Müller. Nano, bits, and feynman’s dream: There’s plenty of room at the (molecular) bottom. *J. Chem. Educ.*, 100(3):1366–1370, March 2023.
- [186] Anouk S Lubbe, Qing Liu, Sanne J Smith, Jan Willem de Vries, Jos C M Kistemaker, Alex H de Vries, Ignacio Faustino, Zhuojun Meng, Wiktor Szymanski, Andreas Herrmann, and Ben L Feringa. Photoswitching of DNA hybridization using a molecular motor. *J. Am. Chem. Soc.*, 140(15):5069–5076, April 2018.
- [187] A Lucantonio, P Nardinocchi, and L Teresi. Transient analysis of swelling-induced large deformations in polymer gels. *J. Mech. Phys. Solids*, 61(1):205–218, January 2013.
- [188] J David MacDonald and Kellogg S Booth. Heuristics for ray tracing using space subdivision. *Vis. Comput.*, 6(3):153–166, May 1990.
- [189] Shane Macleod and Naeem Jan. Large lattice simulation of random site percolation. *Int. J. Mod. Phys. C*, 09(02):289–294, March 1998.
- [190] B. A. Mann, C. Holm, and K. Kremer. Swelling of polyelectrolyte networks. *Journal of Chemical Physics*, 122:154903, 2005.
- [191] James E Mark. *Physical properties of polymers handbook*. Springer, New York, NY, 2 edition, December 2006.
- [192] Glenn J Martyna, Douglas J Tobias, and Michael L Klein. Constant pressure molecular dynamics algorithms. *J. Chem. Phys.*, 101(5):4177–4189, September 1994.
- [193] James Clerk Maxwell. *Capillary Action*, page 541–591. Cambridge Library Collection - Physical Sciences. Cambridge University Press, 2011.
- [194] Sergey N Medyanik and Shuai Shao. Strengthening effects of coherent interfaces in nanoscale metallic bilayers. *Comput. Mater. Sci.*, 45(4):1129–1133, June 2009.
- [195] A Milchev and K Binder. Momentum-dependent interfacial tension in polymer solutions. *EPL*, 59(1):81–86, July 2002.
- [196] T F Miller, III, M Eleftheriou, P Pattnaik, A Ndirango, D Newns, and G J Martyna. Symplectic quaternion scheme for biophysical molecular dynamics. *J. Chem. Phys.*, 116(20):8649–8659, May 2002.
- [197] Alex Mogilner. Mechanics of motor proteins and the cytoskeleton. *Phys. Today*, 55(3):63–64, March 2002.

- [198] Bernard Monasse and Frédéric Boussinot. Determination of forces from a potential in molecular dynamics, January 2014.
- [199] Anirban Mondal, Ryojun Toyoda, Romain Costil, and Ben L Feringa. Chemically driven rotatory molecular machines. *Angew. Chem. Int. Ed Engl.*, 61(40):e202206631, October 2022.
- [200] M A Moore. Theory of semi-dilute polymer solutions. *Journal Phys.*, 38(3):265–271, 1977.
- [201] Guy M. Morton. A computer oriented geodetic data base and a new technique in file sequencing. *Phys. Plasmas*, 1966.
- [202] Ahmed Mourran, Yaodong Wu, Rustam A Gumerov, Andrey A Rudov, Igor I Potemkin, Andrij Pich, and Martin Möller. When colloidal particles become polymer coils. *Langmuir*, 32(3):723–730, January 2016.
- [203] Rolf Müllhaupt. Hermann staudinger and the origin of macromolecular chemistry. *Angew. Chem. Int. Ed Engl.*, 43(9):1054–1063, February 2004.
- [204] Marcus Müller and Friederike Schmid. Monte carlo simulations of interfaces in polymer blends. In *Annual Reviews of Computational Physics VI*, pages 59–127. WORLD SCIENTIFIC, March 1999.
- [205] Tomoya Murakami, Sujin Hoshi, Fumiki Okamoto, Takamasa Sakai, Takuya Katashima, Mitsuru Naito, and Tetsuro Oshika. Analysis of the sustained release ability of bevacizumab-loaded tetra-PEG gel. *Exp. Eye Res.*, 223(109206):109206, October 2022.
- [206] Christopher Stephen Andrew Musgrave and Fengzhou Fang. Contact lens materials: A materials science perspective. *Materials (Basel)*, 12(2):261, January 2019.
- [207] Arun K Nair, Edward Parker, Peter Gaudreau, Diana Farkas, and Ronald D Kriz. Size effects in indentation response of thin films at the nanoscale: A molecular dynamics study. *Int. J. Plast.*, 24(11):2016–2031, November 2008.
- [208] Masamichi Nakayama, Teruo Okano, Takanari Miyazaki, Fukashi Kohori, Kiyotaka Sakai, and Masayuki Yokoyama. Molecular design of biodegradable polymeric micelles for temperature-responsive drug release. *J. Control. Release*, 115(1):46–56, September 2006.

- [209] Ruth Naomi, Hasnah Bahari, Pauzi Muhd Ridzuan, and Fezah Othman. Natural-based biomaterial for skin wound healing (gelatin vs. collagen): Expert review. *Polymers (Basel)*, 13(14):2319, July 2021.
- [210] Charles Nash. Topology and physics – a historical essay. In *History of Topology*, pages 359–415. Elsevier, 1999.
- [211] A Nazir, A Asghar, and A Aslam Maan. Food gels: Gelling process and new applications. In *Advances in Food Rheology and Its Applications*, pages 335–353. Elsevier, 2017.
- [212] A Nazir, A Asghar, and A Aslam Maan. Food gels: Gelling process and new applications. In *Advances in Food Rheology and Its Applications*, pages 335–353. Elsevier, 2017.
- [213] S Nikolov, A Fernandez-Nieves, and A Alexeev. Mesoscale modeling of microgel mechanics and kinetics through the swelling transition. *Appl. Math. Mech.*, 39(1):47–62, January 2018.
- [214] Yusaku Nomoto, Takuro Matsunaga, Takamasa Sakai, Masatoshi Tosaka, and Mitsuhiro Shibayama. Structure and physical properties of dried Tetra-PEG gel. *Polymer (Guildf.)*, 52(18):4123–4128, August 2011.
- [215] Giovanni Noselli, Alessandro Lucantonio, Robert M McMeeking, and Antonio DeSimone. Poroelastic toughening in polymer gels: A theoretical and numerical study. *J. Mech. Phys. Solids*, 94:33–46, September 2016.
- [216] Alessandra Nurisso, Antoine Daina, and Ross C Walker. A practical introduction to molecular dynamics simulations: Applications to homology modeling. In *Methods in Molecular Biology*, Methods in molecular biology (Clifton, N.J.), pages 137–173. Humana Press, Totowa, NJ, January 2011.
- [217] Pawel Okal. NAP 2020 content volume 2. In *2020 IEEE 10th International Conference Nanomaterials: Applications & Properties (NAP)*. IEEE, November 2020.
- [218] Igor P Omelyan. On the numerical integration of motion for rigid polyatomics: The modified quaternion approach. *Comput. Phys.*, 12(1):97–103, January 1998.
- [219] Igor P Omelyan. A new leapfrog integrator of rotational motion. the revised angular-momentum approach. *Mol. Simul.*, 22(3):213–236, May 1999.

- [220] Dmitri A Ossipov and Jöns Hilborn. Poly(vinyl alcohol)-based hydrogels formed by “click chemistry”. *Macromolecules*, 39(5):1709–1718, March 2006.
- [221] Mehrnaz Oveysi, Vahid Bazargan, Amir Nejat, and Marco Marengo. Exploring the stability of single emulsion created by microfluidics and its use in the production of core–shell microparticles. *Microfluid. Nanofluidics*, 28(5):1–27, May 2024.
- [222] Sergei Panyukov and Yitzhak Rabin. Statistical physics of polymer gels. *Phys. Rep.*, 269(1-2):1–131, May 1996.
- [223] Sergey Panyukov. Theory of flexible polymer networks: Elasticity and heterogeneities. *Polymers (Basel)*, 12(4):767, April 2020.
- [224] George Pasparakis and Constantinos Tsitsilianis. LCST polymers: Thermoresponsive nanostructured assemblies towards bioapplications. *Polymer (Guildf.)*, 211(123146):123146, December 2020.
- [225] D Patterson. Free volume and polymer solubility. a qualitative view. *Macromolecules*, 2(6):672–677, November 1969.
- [226] Yong Pei, Jei Chen, Liming Yang, Lili Shi, Qiong Tao, Baojun Hui, and Jian Li. The effect of ph on the LCST of poly(n-isopropylacrylamide) and poly(n-isopropylacrylamide-co-acrylic acid). *J. Biomater. Sci. Polym. Ed.*, 15(5):585–594, 2004.
- [227] N A Peppas, P Bures, W Leobandung, and H Ichikawa. Hydrogels in pharmaceutical formulations. *Eur. J. Pharm. Biopharm.*, 50(1):27–46, July 2000.
- [228] Virgil Percec, editor. *Hierarchical macromolecular structures: 60 years after the Staudinger Nobel prize I*. Advances in Polymer Science. Springer International Publishing, Basel, Switzerland, 2013 edition, January 2014.
- [229] J K Percus. Free energy models for nonuniform classical fluids. *J. Stat. Phys.*, 52(5-6):1157–1178, September 1988.
- [230] P Pincus. Excluded volume effects and stretched polymer chains. *Macromolecules*, 9(3):386–388, May 1976.
- [231] Nikolai A Platé, Tamara L Lebedeva, and Lev I Valuev. Lower critical solution temperature in aqueous solutions of n-alkyl-substituted polyacrylamides. *Polym. J.*, 31(1):21–27, January 1999.

- [232] S D Poisson. Nouvelle théorie de l'action capillaire. *Ann. Phys.*, 101(6):270–287, January 1832.
- [233] Daisy R S Pooler, Anouk S Lubbe, Stefano Crespi, and Ben L Feringa. Designing light-driven rotary molecular motors. *Chem. Sci.*, 12(45):14964–14986, November 2021.
- [234] Catherine B Potter, Mark T Davis, Ahmad B Albadarin, and Gavin M Walker. Investigation of the dependence of the Flory-Huggins interaction parameter on temperature and composition in a drug-polymer system. *Mol. Pharm.*, 15(11):5327–5335, November 2018.
- [235] JG Powles, WAB Evans, E McGrath, KE Gubbins, and S Murad. A computer simulation for a simple model of liquid hydrogen chloride. *Molecular Physics*, 38(3):893–908, 1979.
- [236] G L Puleo, F Zulli, M Piovanelli, M Giordano, B Mazzolai, L Beccai, and L Andreozzi. Mechanical and rheological behavior of pNIPAAm crosslinked macrohydrogel. *React. Funct. Polym.*, 73(9):1306–1318, September 2013.
- [237] Fatih Puza, Yijun Zheng, Lu Han, Lulu Xue, and Jiayi Cui. Physical entanglement hydrogels: ultrahigh water content but good toughness and stretchability. *Polym. Chem.*, 11(13):2339–2345, 2020.
- [238] Y Qiu and K Park. Environment-sensitive hydrogels for drug delivery. *Adv. Drug Deliv. Rev.*, 53(3):321–339, December 2001.
- [239] Mani Rajasekar and Manivannan Lavanya. Gel scaffolds and emerging applications in biomedicine. *RSC Adv.*, 12(25):15925–15949, May 2022.
- [240] Vyas Ramasubramani. `freud`: A software suite for high throughput analysis of particle simulation data, September 2020.
- [241] Vyas Ramasubramani, Bradley D Dice, Eric S Harper, Matthew P Spellings, Joshua A Anderson, and Sharon C Glotzer. `freud`: A software suite for high throughput analysis of particle simulation data. *Comput. Phys. Commun.*, 254(107275):107275, September 2020.
- [242] D C Rapaport. Molecular dynamics simulation using quaternions. *J. Comput. Phys.*, 60(2):306–314, September 1985.

- [243] D C Rapaport. Preface to the first edition. In *The Art of Molecular Dynamics Simulation*, pages ix–xi. Cambridge University Press, Cambridge, April 2004.
- [244] Ralph Reid, Miriam Sgobba, Barak Raveh, Giulio Rastelli, Andrej Sali, and Daniel V Santi. Analytical and simulation-based models for drug release and gel-degradation in a tetra-PEG hydrogel drug-delivery system. *Macromolecules*, 48(19):7359–7369, October 2015.
- [245] G Rickayzen. Molecular theory of capillarity. *Phys. Bull.*, 34(10):437–438, October 1983.
- [246] Jessica Rodríguez-Fernández, Michael Fedoruk, Calin Hrelescu, Andrey A Lutich, and Jochen Feldmann. Triggering the volume phase transition of core-shell au nanorod-microgel nanocomposites with light. *Nanotechnology*, 22(24):245708, June 2011.
- [247] Diederik Roke, Sander J Wezenberg, and Ben L Feringa. Molecular rotary motors: Unidirectional motion around double bonds. *Proc. Natl. Acad. Sci. U. S. A.*, 115(38):9423–9431, September 2018.
- [248] Dana R Rottach, John G Curro, Joanne Budzien, Gary S Grest, Carsten Svaneborg, and Ralf Everaers. Molecular dynamics simulations of polymer networks undergoing sequential cross-linking and scission reactions. *Macromolecules*, 40(1):131–139, January 2007.
- [249] Lorenzo Rovigatti, Nicoletta Gnan, Letizia Tavagnacco, Angel J Moreno, and Emanuela Zaccarelli. Numerical modelling of non-ionic microgels: an overview. *Soft Matter*, 15(6):1108–1119, February 2019.
- [250] J S Rowlinson. Translation of j. d. van der waals’ ‘the thermodynamik theory of capillarity under the hypothesis of a continuous variation of density?’ *J. Stat. Phys.*, 20(2):197–200, February 1979.
- [251] J. S. Rowlinson and B. Widom. *Molecular theory of capillarity*. Oxford University Press, 1989.
- [252] Michael Rubinstein and Ralph H Colby. *Polymer physics*. Oxford University Press, June 2003.
- [253] Jean-Paul Ryckaert, Giovanni Ciccotti, and Herman J C Berendsen. Numerical integration of the cartesian equations of motion of a system with constraints: molecular dynamics of n-alkanes. *J. Comput. Phys.*, 23(3):327–341, March 1977.

- [254] Dipjyoti Saha and Suwendu Bhattacharya. Hydrocolloids as thickening and gelling agents in food: a critical review. *J. Food Sci. Technol.*, 47(6):587–597, December 2010.
- [255] Srinivas Sahanam and Dhar Sandipan. Advances in diaper technology. *Ind. J. Paediatr. Derm.*, 17(2):83, 2016.
- [256] Hiromu Saito, Daisuke Tsutsumi, and Takashi Inoue. Temperature dependence of the Flory interaction parameter in a Single-Phase mixture of poly(hydroxy ether of bisphenol-a) and poly(ether sulfone). *Polym. J.*, 22(2):128–134, February 1990.
- [257] Takamasa Sakai, Takuya Katashima, Takuto Matsushita, and Ung-Il Chung. Sol-gel transition behavior near critical concentration and connectivity. *Polym. J.*, 48(5):629–634, May 2016.
- [258] Gadiel Saper and Henry Hess. Synthetic systems powered by biological molecular motors. *Chem. Rev.*, 120(1):288–309, January 2020.
- [259] Jean-Pierre Sauvage. From chemical topology to molecular machines (nobel lecture). *Angew. Chem. Int. Ed Engl.*, 56(37):11080–11093, September 2017.
- [260] Lothar Schafer. *Excluded volume effects in polymer solutions*. Springer, Berlin, Germany, October 2011.
- [261] H G Schild. Poly(N-isopropylacrylamide): experiment, theory and application. *Prog. Polym. Sci.*, 17(2):163–249, January 1992.
- [262] Stephan Schmidt, Michael Zeiser, Thomas Hellweg, Claus Duschl, Andreas Fery, and Helmuth Möhwald. Adhesion and mechanical properties of PNIPAM microgel films and their potential use as switchable cell culture substrates. *Adv. Funct. Mater.*, 20(19):3235–3243, October 2010.
- [263] Skipper Seabold and Josef Perktold. Statsmodels: Econometric and statistical modeling with python. In *Proceedings of the 9th Python in Science Conference*. SciPy, June 2010.
- [264] David Sean and Gary W Slater. Langevin dynamics simulations of driven polymer translocation into a cross-linked gel. *Electrophoresis*, 38(5):653–658, March 2017.
- [265] Sebastian Seiffert, Wilhelm Prof Dr Oppermann, and Kay Saalwächter. Hydrogel formation by photocrosslinking of dimethylmaleimide functionalized polyacrylamide. *Polymer*, 48:5599–5611, 2007.

- [266] A N Semenov. Theory of block copolymer interfaces in the strong segregation limit. *Macromolecules*, 26(24):6617–6621, November 1993.
- [267] Sanjib Senapati and Max L. Berkowitz. Computer simulation study of the interface width of the liquid/liquid interface. *Phys. Rev. Lett.*, 87:176101, October 2001.
- [268] Soumyadipta Sengupta and Alexey V Lyulin. Molecular dynamics simulations of substrate hydrophilicity and confinement effects in capped nafion films. *J. Phys. Chem. B*, 122(22):6107–6119, June 2018.
- [269] Jan Seuring and Seema Agarwal. Polymers with upper critical solution temperature in aqueous solution. *Macromol. Rapid Commun.*, 33(22):1898–1920, November 2012.
- [270] Maximilian Seuss, Willi Schmolke, Astrid Drechsler, Andreas Fery, and Sebastian Seiffert. Core-shell microgels with switchable elasticity at constant interfacial interaction. *ACS Appl. Mater. Interfaces*, 8(25):16317–16327, June 2016.
- [271] M. Sferrazza, C. Xiao, R. A. L. Jones, D. G. Bucknall, J. Webster, and J. Penfold. Evidence for capillary waves at immiscible polymer/polymer interfaces. *Phys. Rev. Lett.*, 78:3693–3696, May 1997.
- [272] Shuai Shao and Sergey N Medyanik. Dislocation-interface interaction in nanoscale fcc metallic bilayers. *Mech. Res. Commun.*, 37(3):315–319, April 2010.
- [273] Shubham Shende, Bhagyashri Meshram, Ms. Heera Karemore, Prashant Gaikwad, Hemlata More, Lalchand Devhare, and Ankur Srivastava. Development and characterization of glycerogelatin suppositories for enhanced efficacy. *Eur. J. Pharm. Med. Res*, 10:522–528, 06 2023.
- [274] Meinong Shi, Youchen Zhang, Lisheng Cheng, Zhiwei Jiao, Weimin Yang, Jing Tan, and Yumei Ding. Interfacial diffusion and bonding in multilayer polymer films: A molecular dynamics simulation. *J. Phys. Chem. B*, 120(37):10018–10029, September 2016.
- [275] Mitsuhiro Shibayama. Exploration of ideal polymer networks. *Macromol. Symp.*, 372(1):7–13, April 2017.
- [276] Kazuhito Shida, Ryoji Sahara, M N Tripathi, Hiroshi Mizuseki, and Yoshiyuki Kawazoe. Conductivity percolation on a square lattice with core-shell particles. *Mater. Trans.*, 51(4):771–774, 2010.

- [277] Xiao Zheng Shu, Shama Ahmad, Yanchun Liu, and Glenn D Prestwich. Synthesis and evaluation of injectable, in situ crosslinkable synthetic extracellular matrices for tissue engineering. *J. Biomed. Mater. Res. A*, 79(4):902–912, December 2006.
- [278] R Shuttleworth. The surface tension of solids. *Proc. Phys. Soc.*, 63(5):444–457, May 1950.
- [279] Robert D Skeel. Numerical hamiltonian problems (j. m. Sanz-Serna and m. p. calvo). *SIAM Rev. Soc. Ind. Appl. Math.*, 37(2):277–279, June 1995.
- [280] Yelena R Sliozberg, Randy A Mrozek, Jay D Schieber, Martin Kröger, Joseph L Lenhart, and Jan W Andzelm. Effect of polymer solvent on the mechanical properties of entangled polymer gels: Coarse-grained molecular simulation. *Polymer (Guildf.)*, 54(10):2555–2564, April 2013.
- [281] Andrey V Smagin, Viktor I Budnikov, Nadezhda B Sadovnikova, Anatoly V Kirichenko, Elena A Belyaeva, and Victoria N Krivtsova. Gel-forming soil conditioners of combined action: Laboratory tests for functionality and stability. *Polymers (Basel)*, 14(21):4665, November 2022.
- [282] Jan Smrek and Kurt Kremer. Interfacial properties of active-passive polymer mixtures. *Entropy (Basel)*, 20(7):520, July 2018.
- [283] Jens-Uwe Sommer. Structural properties and swelling behavior of randomly crosslinked polymer networks: A monte carlo study. *Macromol. Symp.*, 81(1):139–152, April 1994.
- [284] K P Sonu, Le Zhou, Santidan Biswas, John Klier, Anna C Balazs, Todd Emrick, and Shelly R Peyton. Strain-stiffening hydrogels with dynamic, secondary cross-linking. *Langmuir*, 39(7):2659–2666, February 2023.
- [285] Noel T Southall, Ken A Dill, and A D J Haymet. A view of the hydrophobic effect. *J. Phys. Chem. B*, 106(3):521–533, January 2002.
- [286] H Staudinger. Über polymerisation. *Ber. dtsh. Chem. Ges. A/B*, 53(6):1073–1085, June 1920.
- [287] J Fraser Stoddart. Mechanically interlocked molecules (MIMs)-molecular shuttles, switches, and machines (nobel lecture). *Angew. Chem. Int. Ed Engl.*, 56(37):11094–11125, September 2017.

-
- [288] Gert R Strobl. *The physics of polymers*. Springer, Berlin, Germany, 3 edition, August 2007.
- [289] Asumi Sugimura, Makoto Asai, Takuro Matsunaga, Yuki Akagi, Takamasa Sakai, Hiroshi Noguchi, and Mitsuhiro Shibayama. Mechanical properties of a polymer network of Tetra-PEG gel. *Polym. J.*, 45(3):300–306, March 2013.
- [290] Hamzah Asyrani Sulaiman, Abdullah Bade, and Mohd Harun Abdullah. Computing distance using internal axis-aligned bounding-box for nearly intersected objects. In *Proceedings of the 3rd international conference on mathematical sciences*. AIP Publishing LLC, 2014.
- [291] Carsten Svaneborg and Ralf Everaers. Characteristic time and length scales in melts of kremer–grest bead–spring polymers with wormlike bending stiffness. *Macromolecules*, 53(6):1917–1941, March 2020.
- [292] Lloyd D Taylor and Leon D Cerankowski. Preparation of films exhibiting a balanced temperature dependence to permeation by aqueous solutions—a study of lower consolute behavior. *J. Polym. Sci. Polym. Chem. Ed.*, 13(11):2551–2570, November 1975.
- [293] M Joan Taylor, Paul Tomlins, and Tarsem S Sahota. Thermoresponsive gels. *Gels*, 3(1):4, January 2017.
- [294] Vijay Kumar Thakur and Manju Kumari Thakur, editors. *Hydrogels*. Gels Horizons: From Science to Smart Materials. Springer, Singapore, Singapore, 1 edition, September 2018.
- [295] Jos Thijssen. *Computational Physics*. Cambridge University Press, Cambridge, England, 2 edition, March 2007.
- [296] Maxime M C Tortora and Jonathan P K Doye. Hierarchical bounding structures for efficient virial computations: Towards a realistic molecular description of cholesterics. *J. Chem. Phys.*, 147(22):224504, December 2017.
- [297] Ryojun Toyoda, Nong V Hoang, Kiana Gholamjani Moghaddam, Stefano Crespi, Daisy R S Pooler, Shirin Faraji, Maxim S Pshenichnikov, and Ben L Feringa. Synergistic interplay between photoisomerization and photoluminescence in a light-driven rotary molecular motor. *Nat. Commun.*, 13(1):5765, September 2022.

- [298] Dimitrios G Tsalikis, Mihai Ciobanu, Costas S Patrickios, and Yuji Higuchi. Model amphiphilic polymer conetworks in the bulk: Dissipative particle dynamics simulations of their self-assembly and mechanical properties. *Macromolecules*, November 2023.
- [299] Faheem Ullah, Muhammad Bisyrul Hafi Othman, Fatima Javed, Zulkifli Ahmad, and Hazizan Md Akil. Classification, processing and application of hydrogels: A review. *Mater. Sci. Eng. C Mater. Biol. Appl.*, 57:414–433, December 2015.
- [300] Ronald D Vale. The molecular motor toolbox for intracellular transport. *Cell*, 112(4):467–480, February 2003.
- [301] Sudarkodi Venkatesan and Sumit Basu. Investigations into crazing in glassy amorphous polymers through molecular dynamics simulations. *J. Mech. Phys. Solids*, 77:123–145, April 2015.
- [302] Loup Verlet. Computer “experiments” on classical fluids. i. thermodynamical properties of Lennard-Jones molecules. *Phys. Rev.*, 159(1):98–103, July 1967.
- [303] Jude Ann Vishnu, Torsten Gereon Linder, Sebastian Seiffert, and Friederike Schmid. Structure and dynamic evolution of interfaces between polymer solutions and gels and polymer interdiffusion: A molecular dynamics study. *Macromolecules*, 57(11):5545–5559, June 2024.
- [304] Jana Volarić, Wiktor Szymanski, Nadja A Simeth, and Ben L Feringa. Molecular photoswitches in aqueous environments. *Chem. Soc. Rev.*, 50(22):12377–12449, November 2021.
- [305] AG Voloboi. Compact storage for octrees in a fast ray-tracing algorithm. *Prog. & Comp. Softw.*, 18(1):8–13, Jan-Feb 1992.
- [306] M von Smoluchowski. Zur kinetischen theorie der brownschen molekularbewegung und der suspensionen. *Ann. Phys.*, 326(14):756–780, January 1906.
- [307] Chenyu Wang, Bozhong Lin, Haopeng Zhu, Fei Bi, Shanshan Xiao, Liyan Wang, Guangqing Gai, and Li Zhao. Recent advances in phenylboronic acid-based gels with potential for self-regulated drug delivery. *Molecules*, 24(6):1089, March 2019.
- [308] Endian Wang and Fernando Escobedo. Swelling and tensile properties of tetrapolyethylene glycol via coarse-grained molecular models. *Macromol. Theory Simul.*, 26(3):1600098, May 2017.

- [309] Jiaobing Wang and Ben L Feringa. Dynamic control of chiral space in a catalytic asymmetric reaction using a molecular motor. *Science*, 331(6023):1429–1432, March 2011.
- [310] Shuping Wang, Shui Guan, Jianqiang Xu, Wenfang Li, Dan Ge, Changkai Sun, Tianqing Liu, and Xuehu Ma. Neural stem cell proliferation and differentiation in the conductive PEDOT-HA/Cs/Gel scaffold for neural tissue engineering. *Biomater. Sci.*, 5(10):2024–2034, 2017.
- [311] Harold R Warner, Jr. Kinetic theory and rheology of dilute suspensions of finitely extendible dumbbells. *Ind. Eng. Chem. Fundam.*, 11(3):379–387, August 1972.
- [312] Takaichi Watanabe and Shoji Takeuchi. Microfluidic formation of monodisperse tetra-PEG hydrogel microbeads for cell encapsulation. In *2016 IEEE 29th International Conference on Micro Electro Mechanical Systems (MEMS)*. IEEE, January 2016.
- [313] John D Weeks, David Chandler, and Hans C Andersen. Role of repulsive forces in determining the equilibrium structure of simple liquids. *J. Chem. Phys.*, 54(12):5237–5247, June 1971.
- [314] Menglian Wei and Michael J Serpe. Temperature-light dual-responsive Au@PNIPAm core-shell microgel-based optical devices. *Part. Part. Syst. Charact.*, 36(1):1800326, January 2019.
- [315] Joost H Weijts, Jacco H Snoeijs, and Bruno Andreotti. Capillarity of soft amorphous solids: a microscopic model for surface stress. *Phys. Rev. E Stat. Nonlin. Soft Matter Phys.*, 89(4):042408, April 2014.
- [316] A. Werner, F. Schmid, M. Müller, and K. Binder. “intrinsic” profiles and capillary waves at homopolymer interfaces: A monte carlo study. *Phys. Rev. E*, 59:728–738, January 1999.
- [317] Andreas Werner, Friederike Schmid, Marcus Müller, and Kurt Binder. Anomalous size-dependence of interfacial profiles between coexisting phases of polymer mixtures in thin-film geometry: A monte carlo simulation. *J. Chem. Phys.*, 107(19):8175–8188, November 1997.
- [318] George M. Whitesides. The origins and the future of microfluidics. *Nature*, 442(7101):368–373, July 2006.
- [319] Gibbs J Willard. *Scientific Papers of J. Willard Gibbs*. Forgotten Books., 1901.

- [320] Jianzhong Wu, Bo Zhou, and Zhibing Hu. Phase behavior of thermally responsive microgel colloids. *Phys. Rev. Lett.*, 90(4):048304, January 2003.
- [321] Weitai Wu and Shuiqin Zhou. Responsive materials for self-regulated insulin delivery. *Macromol. Biosci.*, 13(11):1464–1477, November 2013.
- [322] Mohammadreza Yaghoobi and George Z Voyiadjis. Effect of boundary conditions on the MD simulation of nanoindentation. *Comput. Mater. Sci.*, 95:626–636, December 2014.
- [323] JM Yang, XL Cao, KL Zhang, XW Song, F Qiu, and YZ Xu. Monte carlo simulation of the gelation process of the aqueous polymer weak gel. *Chem. J. Chin. Univ. (Chin.)*, 27(3):579–582, March 2006.
- [324] Lei Yang, Xiaoguang Fan, Jing Zhang, and Jia Ju. Preparation and characterization of thermoresponsive poly(n-isopropylacrylamide) for cell culture applications. *Polymers (Basel)*, 12(2):389, February 2020.
- [325] Shuangchun Yang, Zhenye Liu, Yi Pan, Jian Guan, Peng Yang, and Muratbekova Asel. A review of research progress on the performance of intelligent polymer gel. *Molecules*, 28(10), May 2023.
- [326] Xuyang Yao, Jude Ann Vishnu, Claudius Lupfer, Daniel Hoenders, Oliver Skarsetz, Weixiang Chen, Damien Dattler, Alexis Perrot, Wen-Zhi Wang, Chuan Gao, Nicolas Giuseppone, Friederike Schmid, and Andreas Walther. Scalable approach to molecular motor-polymer conjugates for light-driven artificial muscles. *Adv. Mater.*, 36(28):e2403514, July 2024.
- [327] Xin Yong, Olga Kuksenok, and Anna C Balazs. Modeling free radical polymerization using dissipative particle dynamics. *Polymer (Guildf.)*, 72:217–225, August 2015.
- [328] T Young. An essay on the cohesion of fluids. *Abstr. Pap. Print. Philos. Trans. R. Soc. Lond.*, 1(0):171–172, December 1832.
- [329] Reza Yousofvand and Kasra Ghasemi. A novel microfluidic device for double emulsion formation: The effects of design parameters on droplet production performance. *Colloids Surf. A Physicochem. Eng. Asp.*, 635(128059):128059, February 2022.
- [330] Zhiang Yuan, Junjie Ding, Yu Zhang, Bin Huang, Zhaohui Song, Xiangxin Meng, Xintao Ma, Xuyang Gong, Zixu Huang, Songmei Ma, Shidong Xiang, and Wenlong Xu. Components, mechanisms and applications of stimuli-responsive polymer gels. *Eur. Polym. J.*, 177(111473):111473, August 2022.

-
- [331] Cheng Zhang, Ping Wang, Chun-An Ma, Guozhang Wu, and Masao Sumita. Temperature and time dependence of conductive network formation: Dynamic percolation and percolation time. *Polymer (Guildf.)*, 47(1):466–473, January 2006.
- [332] Han Zhang, Emiliano Bilotti, Wei Tu, Chun Yee Lew, and Ton Peijs. Static and dynamic percolation of phenoxy/carbon nanotube nanocomposites. *Eur. Polym. J.*, 68:128–138, July 2015.
- [333] Jian-Yong Zhang, Li-Hua Zeng, and Juan Feng. Dynamic covalent gels assembled from small molecules: from discrete gelators to dynamic covalent polymers. *Chin. Chem. Lett.*, 28(2):168–183, February 2017.
- [334] Shuxin Zhang, Yangyang Peng, Ran Jiang, Wenqiang Liu, Huanlei Yang, Na Yun, and Xinsheng Chai. Predicting the swelling behavior of acrylic superabsorbent polymers used in diapers. *Adv. Polym. Technol.*, 2021:1–7, December 2021.
- [335] Chuanzhuang Zhao, Zhiyuan Ma, and X X Zhu. Rational design of thermoresponsive polymers in aqueous solutions: A thermodynamics map. *Prog. Polym. Sci.*, 90:269–291, March 2019.

List of Publications and Conferences

Articles Published in International/National Journals

1. J. A. Vishnu, T. G. Linder, S. Seiffert, and F. Schmid. Structure and Dynamic Evolution of Interfaces between Polymer Solutions and Gels and Polymer Interdiffusion: A Molecular Dynamics Study. *Macromolecules*. **57**, 5545-5559 (2024). <https://doi.org/10.1021/acs.macromol.4c00459>
2. X. Yao, J. A. Vishnu, C. Lupfer, D. Hoenders, O. Skarsetz, W. Chen, D. Dattler, A. Perrot, W. Wang, C. Gao, N. Giuseppone, F. Schmid, A. Walther. Scalable Approach to Molecular Motor-Polymer Conjugates for Light-Driven Artificial Muscles. *Adv. Mater.* **36**, e2403514 (2024). <https://doi.org/10.1002/adma.202403514>

Presentations and Proceedings in International/National Conferences

1. Poster - PNG Conference 2021
2. Poster - DPG Conference 2022
3. Presentation - Mainz Nanotour Symposium 2023
4. Poster - ECIS Conference 2023
5. Presentation - APS Meeting 2024
6. Presentation - SoftComp annual meeting 2024

